Universidade do Minho
Escola de Ciências

Joana Margarida Fernandes da Silva Ribeiro

Transparent Thermoelectric Titanium Dioxide-based Thin Films for Thermal Energy Harvesting

setembro de 2024

Transparent Thermoelectric Titanium Dioxide-based Thin Films for Thermal Energy Harvesting
Joana Margarida Fernandes da Silva Ribeiro
UMinho | 2024

Universidade do Minho
Escola de Ciências

Joana Margarida Fernandes da Silva Ribeiro

Transparent Thermoelectric Titanium Dioxide-based Thin Films for Thermal Energy Harvesting

Tese de Doutoramento
Programa Doutoral em Física

Trabalho efetuado sob a orientação de
Professor Doutor Carlos José Macedo Tavares
Doutor Torben Boll

setembro de 2024

COPYRIGHT AND TERMS OF USE OF WORK BY THIRD PARTIES

ACKNOWLEDGEMENTS

This work is the result of a collective effort and would not have been possible without the support of several people and institutions to whom I express my deep and sincere gratitude.

First of all, I want to thank my supervisor Professor Carlos Tavares. A huge thank you for providing the opportunity to carry out this work at the University of Minho (UM), for the entrusted responsibility, for the scientific discussions, as well as for the wise advice and knowledge transmitted.

Thank you to my co-supervisor Torben Boll, for welcoming me at the Karlsruhe Institute of Technology (KIT), for enabling access to do APT measurements and for the help and patience in the discussion of results.

I want to thank the APT group at the Institute for Applied Materials (IAM-WK) at the KIT, for warmly welcoming me in Germany, especially to Michael Eusterholz, Delphine Chassaing and Samer Daradkeh for their extensive help with FIB and APT, and Oscar López-Galán for his DFT knowledge and calculations. Special thanks to Alexander Welle, from the Institute of Functional Interfaces (IFG) at the KIT, for the opportunity to perform TOF-SIMS analysis, for his availability, attentive training and extensive measurements. I would also like to thank Peter Weidler, also from the IFG-KIT, for his help availability in performing XRD measurements.

I want to thank Sebastian Reparaz and Professor Alejandro Goñi for hosting me at the Institute of Materials Science of Barcelona (ICMAB) and for the help with the FDTR measurements, as well as in the discussion of the results.

A special mention to the late Wolfgang Theiss for the help in interpreting and improving the SCOUT model.

I want to thank Professor Luís Rebouta, Professor Sandra Carvalho and Professor Luís Cunha, for their experience, knowledge and discussions.

A warm thank you to Edith Avila, responsible for the SEM images at the Materials Characterization Services of the University of Minho (SEMAT/UM), for giving me confidence and showing me that everything can be achieved even at a low point in life.

To my colleagues in the office, Juliana Marques, Marta Forte, Tiago Gomes, Rui Antunes, Joana Parente e Vânia Sousa, thank you for the company and many hours of small talk. To the students Luís Dias, Frederico Rodrigues, Hélder Faria, Gonçalo Martins and Bruno Fernandes, for developing my training skills and helping with my work. To my colleagues at the centre of Physics at the University of Minho, Luísa Fialho, Edgar Carneiro, José Castro, Maria José Lima and Abbas Alrjoub, for directly or

indirectly helping me in the development of this work. Thank you to my MAP-fis partners, Diana Meira, Celso Oliveira and Sérgio Veloso, for the fun times and help.

A special thanks to, my friend and colleague Filipe Correia, who was the best work partner I could have asked for. I appreciate the positive energy, the long hours spent over the sputtering chamber, the scientific discussion that made us grow a lot, and the good times we spent. Thank you for the help, advice and outlook on life, and for the encouragement in the most difficult times.

To my dear friend Nelssom Cunha, for sharing in my crazy ideas. I owe a deep thank you for the way in which he has always been willing to help me. I am also grateful to my dear friend and training partner Eduardo Brito for the kindness, words of encouragement and patience to hearing me vent many times.

A special thanks to my family and to my parents, without whom I would not be here today. I want to acknowledge the support, encouragement and for everything they have done for me.

Last but not the least, my deepest gratitude to the love of my life, João Oliveira, for his friendship, patience and support. He has been my support pillar in the hardest times throughout these years, and I couldn't have managed the courage to fight and persist without him.

To my cats Nyx, Scot, Haku and Yuki, thank you for lighting my way, especially in the darkest moments.

And thank you to whom, directly or indirectly, helped me in the development of this work and I have forgotten to include. I am grateful for all the opportunities that have allowed me to grow as a person and as a researcher, the support, the patience, the empathy, and above all else, the friendship.

To all, my most sincere gratitude...

I am grateful for the financial support received from TECMINHO – *Associação Universidade-Empresa Para o Desenvolvimento* and *Fundação Luso-Americana para o Desenvolvimento* (FLAD) (Papers@USA 2022/0090), without which it would not have been possible to participate in important international conferences and scientific trips. This work was also carried out with the support of the Helmholtz Association Research Centres: the German electron synchrotron (DESY, www.desy.de) and Karlsruhe Nano Micro Facility at KIT (KNMFi-KIT, www.knmf.kit.edu).

This work was funded by the *Fundação para a Ciência e Tecnologia* (FCT) under the PhD scholarship with the reference SFRH/BD/147221/2019.

STATEMENT OF INTEGRITY

I hereby declare having conducted this academic work with integrity. I confirm that I have not used plagiarism or any form of undue use of information or falsification of results along the process leading to its elaboration.

I further declare that I have fully acknowledged the Code of Ethical Conduct of the University of Minho.

RESUMO

Os materiais termoelétricos transparentes são uma tecnologia promissora para ecrãs sensíveis ao toque e aplicações em células solares, levando a uma alimentação sustentável do dispositivo. A modificação da estrutura atómica do TiO_2 através da introdução deliberada de defeitos aumenta em grande medida as suas propriedades elétricas e termoelétricas. Por outro lado, a introdução de um elemento mais pesado na sua matriz metal-óxido, dificulta a condução de calor mediada por fonões, consequentemente reduzindo a condutividade térmica, o que irá aumentar ainda mais a Figura de Mérito termoelétrica.

Este trabalho tem como objetivo compreender o papel da dopagem de Nb, pressão parcial reativa de oxigênio, temperatura de deposição e tratamento térmico pós-deposição nas propriedades de filmes finos opticamente transparentes de TiO_2 dopados com Nb com propriedades termoelétricas aprimoradas, depositados por pulverização reativa de magnetrão DC em alto vácuo.

Os filmes finos foram produzidos, cuidadosamente caracterizados e aplicados a um dispositivo termoelétrico transparente. A técnicas de Tomografia de Sonda Atómica e Espectrometria de Massa de Iões Secundários com análise de tempo do voo permitem a determinação da composição e homogeneidade inerente dentro dos filmes finos, bem como a investigação da segregação de iões para interfaces e fronteiras de grãos. Foi descoberto que o Nb encontra-se homogeneamente distribuído na matriz de TiO_2, sem limites de grãos visíveis.

A otimização dos parâmetros de produção resulta em filmes finos com espessura de aproximadamente 200 nm, transmitância ótica média de 76 % na faixa do visível, resistividade elétrica do tipo-n de 0,01 Ω·cm e um coeficiente de Seebeck absoluto de 226 $\mu V \cdot K^{-1}$, originando um Fator de Potência termoelétrica de 300 $\mu W \cdot m^{-1} \cdot K^{-2}$ e uma Figura de Mérito de 0,06.

O protótipo final com (25 × 25) mm^2 consiste numa matriz de 16 629 pilares microfabricados de TiO_2:Nb, isolados por SiO_2. Exibiu um aumento no coeficiente de Seebeck, (36 ± 1) $\mu V \cdot K^{-1}$, quando comparado a um filme contínuo de TiO_2:Nb, resultando num Fator de Potência termoelétrico de (10 ± 1) × 10^{-14} $W \cdot m^{-1} \cdot K^{-2}$ e uma Figura de Mérito de (1,9 ± 0,3) × 10^{-11}, mantendo 69 % de transparência no intervalo do visível.

Palavras-chave: Termoelétrico transparente, Filme fino, Semicondutor, Energia.

ABSTRACT

Transparent thermoelectric materials are a promising technology for touchscreen displays and solar cell applications, rendering a sustainable powering of the device. Modifying the atomic structure of TiO_2 by deliberately introducing defects enhances its electrical and thermoelectrical properties to a great extent. On the other hand, introducing a heavier element into the metal-oxide matrix hinders phonon mediated heat conduction, consequently reducing the thermal conductivity, which will further increase the thermoelectric Figure of Merit.

This work aims to understand the role of Nb doping, reactive oxygen partial pressure, deposition temperature and post-deposition annealing in the properties of optically transparent Nb-doped TiO_2 thin films with enhanced thermoelectric properties, deposited by reactive DC magnetron sputtering in high vacuum.

The thin films were produced, thoroughly characterized, and applied to a transparent thermoelectric device. Atom Probe Tomography and Time-of-Flight Secondary Ion Mass Spectrometry enables the determination of the composition and inherent homogeneity within the thin films, as well as the investigation of the segregation of ions to interfaces and grain boundaries. Nb was found to be homogeneously distributed in the TiO_2 matrix with no visible grain boundaries.

The optimization of the production parameters results in thin films with thickness of approximately 200 nm, optical transmittance averaged in the visible range of 76 %, n-type electrical resistivity of 0.01 Ω·cm and an absolute Seebeck coefficient of 226 $\mu V \cdot K^{-1}$, yielding a thermoelectric Power Factor of 300 $\mu W \cdot m^{-1} \cdot K^{-2}$ and Figure of Merit of 0.06.

The final (25 × 25) mm^2 prototype device consists of an array of 16 629 micro-fabricated pillars of TiO_2:Nb, isolated by SiO_2. It showed an increase in the Seebeck coefficient, (36 ± 1) $\mu V \cdot K^{-1}$, when compared to a continuous film TiO_2:Nb, leading to a thermoelectric Power Factor of (10 ± 1) × 10^{-14} $W \cdot m^{-1} \cdot K^{-2}$ and Figure of Merit of (1.9 ± 0.3) × 10^{-11}, while maintaining 69 % of transparency in the visible range.

Keywords: Transparent thermoelectric, Thin film, Semiconductor, Energy.

TABLE OF CONTENTS

COPYRIGHT AND TERMS OF USE OF WORK BY THIRD PARTIES ii
ACKNOWLEDGEMENTS iii
STATEMENT OF INTEGRITY v
RESUMO vi
ABSTRACT vii
TABLE OF CONTENTS viii
LIST OF FIGURES xi
LIST OF TABLES xxiii
LIST OF SYMBOLS, ABBREVIATIONS AND ACRONYMS xxv
CHAPTER I 1
1. Introduction 2
1.1. Motivation 2
1.2. Thermoelectricity 3
1.3. Transparent Thermoelectrics 8
1.4. Thin Film Deposition 11
1.5. Objectives 12
1.6. Dissertation Structure 14
CHAPTER II. 15
2. Materials and Methods 16
2.1. Titanium Dioxide 16
2.2. Reactive Magnetron Sputtering 19
2.3. Characterization Techniques 25
2.3.1. Morphology, Surface and Interface Analysis 25
2.3.1.1. X-ray Diffraction (XRD) and Reflectometry (XRR) 26
2.3.1.2. X-ray Photoelectron Spectroscopy (XPS) 27
2.3.1.3. X-ray Absorption Spectroscopy (XAS) 27
2.3.1.4. Scanning Electron Microscopy (SEM) 28
2.3.1.5. Transmission Electron Microscopy (TEM) 28
2.3.1.6. Time-of-Flight Secondary Ion Mass Spectrometry (TOF-SIMS) 29
2.3.1.7. Atom Probe Tomography (APT) 31
2.3.2. Optical Properties: Ultraviolet-Visible (UV-Vis) Spectrophotometry 36
2.3.3. Electrical Properties: Hall Effect 38
2.3.4. Thermal Properties: Frequency Domain Thermoreflectance (FDTR) 38
2.3.5. Thermoelectric Properties: Seebeck Coefficient 39
2.3.6. Mechanical Properties 41
2.3.6.1. Scratch Test 41
2.3.6.2. Nanoindentation 41
2.3.7. Data Analysis 42

2.3.7.1. Reverse Monte Carlo (RMC) 42
2.3.7.2. X-ray Absorption Near-edge Structure (XANES) 43
2.3.7.3. Density Functional Theory (DFT) 43

CHAPTER III. 46
3. Influence of Niobium-doping 47
3.1. Experimental details 47
3.1.1. Sample Fabrication 47
3.1.2. Sample Characterization 48
3.1.3. Data analysis 49
3.2. Results and Discussion 50
3.3. Partial Conclusions 64

CHAPTER IV. 66
4. Influence of the Oxygen Flow 67
4.1. Experimental Details 67
4.1.1. Sample Fabrication 67
4.1.2. Sample Characterization 69
4.2. Results and Discussion 71
4.3. Partial Conclusions 87

CHAPTER V. 90
5. Influence of the Deposition Temperature 91
5.1. Experimental Details 91
5.1.1. Sample Fabrication 91
5.1.2. Sample Characterization 94
5.2. Results and Discussion 96
5.3. Partial Conclusions 110

CHAPTER VI. 114
6. Morphology, Microstructure and Grain Boundary Characterization 115
6.1. Experimental Details 115
6.1.1. Sample Fabrication 115
6.1.2. Sample Characterization 117
6.2. Results and Discussion 118
6.3. Partial Conclusions 132

CHAPTER VII. 134
7. Application in a Thermoelectric Prototype 135
7.1. Introduction 135
7.2. Study of the Mechanical Properties 136
7.2.1. Experimental Details 136
7.2.1.1. Sample Fabrication 136
7.2.1.2. Sample Characterization 137
7.2.2. Results and Discussion 138
7.3. Design of a Transparent Thermoelectric Prototype 141
7.3.1. Experimental Details 144
7.3.1.1. Sample Fabrication 144
7.3.1.2. Sample Characterization 147
7.3.2. Results and Discussion 148
7.4. Partial Conclusions 152

CHAPTER VIII. 154
8. Final Remarks and Future Work 155
REFERENCES 161
APPENDIX A – SEM-EDX Analysis 176
APPENDIX B – XRR Analysis 179
APPENDIX C – XPS Spectra and Fits 181
APPENDIX D – Transmittance and Reflectance spectra 184
APPENDIX E – APT Analysis 186
E.1. Sample A 188
E.2. Sample B 191
E.3. Sample C 193
APPENDIX F – HAADF-STEM Analysis 208
APPENDIX G – Propagation of Uncertainty 213
APPENDIX H – Scientific Contribution 214
H.1. Articles Published in Scientific Journals 214
H.2. Oral presentations in international conferences 215
H.3. Poster communications in International Conferences 216
H.4. Schools and Training Courses 217
H.5. Patents 217
H.6. Awards 217

LIST OF FIGURES

Figure 1. Origin and flow of energy consumed in the United States of America in the year 2022, according to the Lawrence Livermore National Laboratory and Department of Energy [2]..... 3

Figure 2. Chronogram of prominent thermoelectric advancements over the course of history..... 4

Figure 3. Seebeck effect in an n-type **(a)** and p-type **(b)** semiconductor material, measured in an open circuit. 5

Figure 4. Peltier effect **(a)** and Seebeck effect **(b)** of a conventional thermoelectric device for Cooling and Power Generation, respectively, using n- and p-type semiconductors. 7

Figure 5. Research in thermoelectrics, thermoelectric thin films and transparent thermoelectrics over the years, a total of 99647, 6042 and 673 results, respectively, obtained through data from *www.scopus.com*, included in tittles, abstracts or keywords, considered from 1875 to 2023 at an international level. 8

Figure 6. Research in PVD processes (*grey*) over the years, obtained through data from *www.scopus.com*, with a total of 213387 results, included in tittles, abstracts or keywords, considered from 1870 to 2023 at an international level. Pie Chart relates to the Research and Application fields of PVD processes..... 12

Figure 7. Research and Application fields of TiO_2, a total of 267379 results obtained through data from *www.scopus.com*, included in tittles, abstracts or keywords, considered from 1861 to 2023 at an international level. 16

Figure 8. Crystalline phases and respective structures of TiO_2, anatase **(a)**, rutile **(b)** and brookite **(c)**. 17

Figure 9. Schematic of the reactive DC magnetron sputtering system used to deposit TiO_2:Nb thin films in planar configuration..... 19

Figure 10. New (unused) **(a)** and used **(b)** targets of Ti(96)Nb(4) wt.% with 99.9 % of purity (FHR) with 10 cm of diameter. 21

Figure 11. Hysteresis curves for increasing and decreasing O_2 flow during sputtering of a pure Ti target **(a)** and a new **(b)** and used **(c)** Ti(96)Nb(4) wt.% target, using 0.5 A, 0.75 A and 1 A applied to a 10 cm diameter target, at room temperature *(RT, blue)* and with heating applied atop the substrate *(HT, red)*. 23

Figure 12. Schematic of the characterization techniques used for surface, interface and depth analysis and their respective types of incident *(solid arrows)* and outgoing *(dotted arrows)* radiation..... 26

Figure 13. TEM sample preparation of TiO_2:Nb thin film **(a)** by FIB: deposition of a Pt protective layer **(b)**, sample erosion **(c)**, lamella lift-out **(d)**. Lamella polishing **(e,f)**..... 29

Figure 14. Schematic representation of a time-of-flight secondary ion mass spectrometer. 30

Figure 15. Schematic of the operation of a typical modern atom probe (based on the Local Electrode Atom Probe (LEAP). Atoms at the surface of a microtip are evaporated by field effect and are accelerated toward a detection system **(a)**, which determines (x,y) positions **(b)** and the chemical nature of each atom **(c)**, resulting in the mass spectrum of each element and 3D reconstruction of the sample **(d)**..... 32

Figure 16. Si coupon with microtip array for APT analysis **(a)** and preparation of a microtip of TiO_2:Nb by FIB: deposition of a protective Pt layer **(b)**, annular milling with a 30 KV Ga-beam **(c,d)**, final milling step with a 10 KV Ga-beam and final tip shape **(e,f)**..... 34

Figure 17. Schematic of the in-plane Seebeck coefficient measuring system at 1 Pa for an n-type thin film. P# indicates a pin connection. The power of the Peltier modules is individually adjusted, and the sample Voltage and thermistor temperatures are measured by the controller interface. 39

Figure 18. Schematic of the through-plane Seebeck coefficient measuring system at ambient pressure in voltage **(a)** and current **(b)** mode. 40

Figure 19. X-ray diffraction patterns of the as-deposited and annealed TiO_2:Nb thin films deposited on Kapton substrates. 51

Figure 20. XPS experimental *(exp.)* spectra and respective fits *(fit)* for a TiO_2:Nb thin film where Ti $2p$ (fitted with 2 components, C1 and C2) **(a)**, O $1s$ (fitted with 2 components, C1 and C2) **(b)** and Nb $3d$ core levels **(c)**; in these plots the background *(backgr.)* is also shown. Survey spectrum **(d)**. 52

Figure 21. Ti K-edges EXAFS $\chi kk2$ spectra **(a)** and their Fourier transforms (FTs) **(b)** at 18 K for rutile and anatase reference powders, and for as-prepared TiO_2:Nb thin film. Ti and Nb K–edges EXAFS $\chi kk2$ spectra **(c)** and their FT **(d)** at 300 K for as-deposited TiO_2:Nb thin film (Nb K–edge) and two reference powders – anatase TiO_2 (Ti K–edge) and Nb_2O_5 (Nb K–edge). 53

Figure 22. Experimental and calculated by RMC Ti K–edge EXAFS spectra $\chi kk2$ **(a,b)** and their Fourier **(c,d)** and Morlet wavelet **(e,f,g,h)** transforms for anatase TiO_2 reference powder at 18 K and 300 K. 54

Figure 23. Experimental and calculated by RMC Ti and Nb K–edge EXAFS spectra $\chi kk2$ **(a,b)** and their Fourier **(c,d)** and Morlet wavelet **(e,f,g,h)** transforms for TiO_2:Nb thin film at 300 K. 56

Figure 24. RDFs $G(R)$ calculated from the coordinates of atoms in a TiO_2 $5a \times 5b \times 2c$ supercell at 300 K, for 5 % **(a)** and 10 % **(b)** of dopant Nb atoms. Dashed (*black* and *red*) lines are for RDFs G(Ti–O) and G(Ti–Ti) in anatase TiO_2 at $T = 300$ K. Fragments of the RMC $5a \times 5b \times 2c$ supercells for 5 % **(c)** and 10 % **(d)** of Nb atoms..... 57

Figure 25. Experimental XANES spectra of TiO_2:Nb thin film at the Ti and Nb K–edges measured at 300 K. The Ti K–edge XANES spectrum *(dashed line)* of reference anatase TiO_2 powder is shown for comparison..... 58

Figure 26. Experimental and calculated XANES spectra of TiO_2:Nb thin film measured at the Ti **(a)** and Nb **(b)** K-edges at 300 K. The calculations were performed for varying atomic cluster sizes. The spectra are vertically shifted for clarity. 59

Figure 27. Experimental and calculated Nb K-edge XANES spectra of a TiO_2:Nb thin film. The calculations were performed for the cluster radius of 8.1 Å and two different core-level widths $\Gamma =$ 0.94 eV and $\Gamma = 4.14$ eV **(a)**. A comparison of the calculated XANES spectra at the Ti and Nb K-edges (top) with p-DOS for Ti and Nb (bottom) **(b)**. 60

Figure 28. Evolution of the Seebeck coefficient *(black circles)* and potential difference *(blue triangles)* with a thermal gradient across the surface of a (75 × 26) mm, for 150 nm **(a)** and 750 nm thick **(b)** TiO_2:Nb film on a glass substrate. 61

Figure 29. Frequency-dependent phase lag between the pump (405 nm) and probe (532 nm) lasers, for a 150 nm **(a)** and 750 nm thick **(b)** TiO_2:Nb thin film. The results from the fits are listed in

Table 6. Error curves *(blue)* represents ± 0.2 $W \cdot m^{-1} \cdot K^{-1}$ and ± 0.3 $W \cdot m^{-1} \cdot K^{-1}$ uncertainty in κ for (a) and (b), respectively. 62

Figure 30. Transmittance (T) and Reflectance spectra of a 150 nm **(a)** and 750 nm thick **(b)** TiO_2:Nb thin film deposited on glass and respective determination of the optical band-gap **(c,d)**. The ellipses show the regions within 95 % confidence for the linear regressions..... 63

Figure 31. Cathode (target) potential vs. reactive oxygen flow hysteresis curve for the deposition of TiO_2:Nb thin films..... 69

Figure 32. SEM cross-section micrographs from three TiO_2:Nb thin films deposited with reactive oxygen flow rates of 5.5 sccm, 7.5 sccm and 9.5 sccm, having thicknesses of 322 nm, 226 nm, 137 nm, respectively. 71

Figure 33. XPS spectra and respective fits for the O 1s core lines for as-deposited TiO_2:Nb thin film with a reactive oxygen flow rate of 7 sccm **(a)**, as-deposited TiO_2:Nb with 7.5 sccm **(b)**, TiO_2:Nb with 7.5 sccm after annealing (*) **(c)**, as-deposited TiO_2:Nb with 9 sccm **(d)** and as-deposited undoped TiO_2 with a reactive oxygen flow rate of 7.5 sccm..... 72

Figure 34. XRD for post-deposition annealed TiO_2:Nb thin films deposited with 6.5 sccm, 7.5 sccm, 8.5 sccm and 9.5 sccm of reactive oxygen flow rates, with corresponding Seebeck coefficient values (S, in $\mu V \cdot K^{-1}$). Lower portion shows XRD patterns for TiO_2 anatase JCPDS card 21-1272 and TiO_2 rutile JCPDS 21-1276 card. 76

Figure 35. XRD for TiO_2:Nb thin films deposited with 7.5 sccm of reactive oxygen flow rates, as-deposited *(Ad, blue)* and after annealing *(TT, red)*.The corresponding film thickness (d, in nm) and the Seebeck coefficient (S, in $\mu V \cdot K^{-1}$) is indicated in the legend of each diffractogram. 76

Figure 36. Weight fraction of rutile calculated from equation (13) as a function of the measured Seebeck coefficient for TiO_2:Nb thin films measured after annealing. 77

Figure 37. Transmittance *(full triangles)* and specular reflectance *(open triangles)* of the as-deposited TiO_2:Nb thin films, averaged from 400 sccm to 700 nm, as a function of the reactive oxygen flow rate during deposition..... 78

Figure 38. Transmittance and specular reflectance spectra **(a)** and Tauc plot **(b)** for an as-deposited TiO_2:Nb thin film deposited for 5 min with 7.5 sccm of oxygen flow rate. 79

Figure 39. Band-gap energies for TiO_2:Nb thin films as a function of the reactive oxygen flow rate used during deposition, as-deposited *(Ad, blue)* and after annealing *(TT, red)*..... 80

Figure 40. Electrical resistivity of TiO_2:Nb thin films as a function of oxygen flow rate during deposition, measured as-deposited *(Ad, blue)* and after thermal annealing at 500 °C *(TT, red)*. The *blue striped zone* refers to very resistive as-deposited films, unable to be measured. 81

Figure 41. Thermal conductivity of TiO_2:Nb thin films measured as-deposited by FDTR as a function of film thickness. Oxygen flow rate during deposition was set to 7.5 sccm. 82

Figure 42. Thermal conductivity of TiO_2:Nb thin films measured as-deposited by FDTR as a function of reactive oxygen flow rate during deposition. The data was fitted with two linear fits: for oxygen flow rates below 6.5 sccm *(navy dashed line)*; for oxygen flow rates above 6.5 sccm *(magenta dashed line)*. 82

Figure 43. Seebeck coefficient for TiO_2:Nb thin films as a function of the reactive oxygen flow rate during deposition, measured as-deposited *(Ad, blue)* and after annealing *(TT, red)*. 83

Figure 44. Seebeck coefficient of TiO_2:Nb thin films as a function of the film thickness. Oxygen flow rate was set at 7.5 sccm, measured as-deposited *(Ad, blue)* and after annealing *(TT, red)*. 84

Figure 45. Thermoelectric power factor for TiO_2:Nb thin films as a function of the reactive oxygen flow rate during deposition, calculated as-deposited *(Ad, blue)* and after annealing *(TT, red)*. 85

Figure 46. Thermoelectric figure of merit at 300 K for TiO_2:Nb thin films as a function of the reactive oxygen flow rate during deposition, calculated as-deposited *(Ad, blue)* and after annealing *(TT, red)*. 85

Figure 47. Figure of Merit values from **Figure 46** plotted as as-deposited *(Ad)* versus after annealing *(TT)* for TiO_2:Nb thin films. *Blue line* plots $y = x$ and *blue zone* refers to the as-deposited tendency of the data. 87

Figure 48. Temperature of the deposition chamber as a function of deposition time for samples deposited with *(HT, red)* and without *(RT, blue*) substrate heating. *Open circles* represent depositions with no Oxygen inside the chamber. 92

Figure 49. Cathode potential vs. reactive oxygen flow rate hysteresis curve for the deposition of TiO_2:Nb thin films with *(HT, red)* and without *(RT, blue*) substrate heating. *Crossed black line* refers to the chosen O_2 flow for the present study. 93

Figure 50. TOF-SIMS depth profiles of Nb^+, NbO^+ (positive polarity), NbO^- and NbO_2^- (negative polarity) normalized to maximum signal intensities in TiO_2:Nb thin films deposited without substrate heating *(RT)* **(a)** and with substrate heating *(HT)* **(b)**, measured as-deposited *(Ad, blue)* and after annealing at 500 °C *(TT, red)*. The interface with the Si substrate and beginning of film growth is indicated at $d = 0$ nm. 97

Figure 51. Relative ratio of $Nb^+$and NbO^+ signals calibrated on the $^{46}Ti^+$ and $^{46}TiO^+$ peak area signals, respectively, normalized to maximum signal intensities in TiO_2:Nb thin films deposited without substrate heating *(RT)* and with substrate heating *(HT)*, measured as-deposited *(Ad, open circles)* and after annealing at 500 °C *(TT, closed circles)*, obtained by TOF-SIMS in positive polarity with Oxygen beam erosion. 99

Figure 52. Average Transmittance (400 nm to 700 nm) **(a)** and average Specular Reflectance (400 nm to 700 nm) **(b)** of TiO_2:Nb thin films in relation to the chamber temperature during deposition, for films deposited with substrate heating *(HT, red)* and without substrate heating *(RT, blue)*, measured as-deposited *(Ad, open circles)* and after annealing at 500 °C *(TT, closed circles)*. 99

Figure 53. Band-gap Energy **(a)** and rutile phase content **(b)** of TiO_2:Nb thin films in relation to the chamber temperature during deposition, for films deposited with substrate heating *(HT, red)* and without substrate heating *(Ad, blue)*, measured as-deposited *(Ad, open circles)* and after annealing at 500 °C *(TT, closed circles)*. 100

Figure 54. Grazing Incidence X-ray diffractograms of TiO_2:Nb thin films deposited without substrate heating *(RT)* **(a)** and with substrate heating *(HT)* **(b)**, measured as-deposited *(Ad, blue)* and after annealing at 500 °C *(TT, red)*. *Dashed black lines* refer to the XRD patterns for TiO_2 anatase JCPDS card 21-1272 and TiO_2 rutile JCPDS 21-1276 card. 101

Figure 55. Structural model of TiO_2:Nb anatase ($3a \times 2b \times 1c$) **(a)** and rutile ($2a \times 2b \times 3c$) **(b)** supercells for 1.4 % Nb atoms visualised by VESTA. 102

Figure 56. Projected density of states for Nb *(red)*, Ti *(blue)* and O *(green)* for anatase **(a)** and rutile **(b)** unit cells (U_c) of undoped TiO_2 (Top) and supercells (S_c) of doped TiO_2:Nb. The Fermi level is located at 0 eV. 103

Figure 57. Band structures for undoped anatase **(a)** and rutile **(b)** TiO_2 unit cells and doped anatase **(c)** and rutile **(d)** TiO_2:Nb supercells. The Fermi level is located at 0 eV and band-gap energy in indicated in *red*. 103

Figure 58. Projected density of states per element, Nb *(red)*, Ti *(blue)*, and O *(green)*, per orbital for doped anatase **(a)** and rutile **(b)** TiO_2:Nb supercells. The Fermi level is located at 0 eV. The remaining contributions of the orbitals from Nb, Ti, and O remain negligible around the Fermi level (not plotted). The *dark yellow circles* point to the contribution arising from the interaction between the Ti and Nb d-orbitals around the Fermi level. 104

Figure 59. Seebeck Coefficient **(a)** and electrical resistivity **(b)** of TiO_2:Nb thin films in relation to the chamber temperature during deposition, for films deposited with substrate heating *(HT, red)* and without substrate heating *(RT, blue)*, measured as-deposited *(Ad, open circles)* and after annealing at 500 °C *(TT, closed circles)*. The *blue striped zone* refers to as-deposited thin films with extremely high electrically resistivity and are unable to be measured..... 105

Figure 60. Projected Seebeck coefficient **(a)**, electrical conductivity dependent of $\tau 0$ **(b)** and electronic component of the thermal conductivity dependent of $\tau 0$ **(c)** for the unit cells (U_c) of undoped anatase and rutile TiO_2 (top) and supercells (S_c) of anatase and rutile TiO_2:Nb (bottom). The anatase phase is indicated in *navy*, the rutile phase is indicated in *magenta* and the Fermi level is located at 0 eV..... 106

Figure 61. Charge carriers mobility **(a)** and concentration **(b)** of TiO_2:Nb thin films in relation to the chamber temperature during deposition, for films deposited with substrate heating *(HT, red)* and without substrate heating *(RT, blue)*, measured as-deposited *(Ad, open circles)* and after annealing at 500 °C *(TT, closed circles)*. The *blue striped zone* refers to as-deposited thin films with extremely high electrically resistivity and are unable to be measured..... 107

Figure 62. Calculated Power Factor of TiO_2:Nb thin films in relation to the chamber temperature during deposition, for films deposited with substrate heating *(HT, red)* and without substrate heating *(RT, blue)*, measured as-deposited *(Ad, open circles)* and after annealing at 500 °C *(TT, closed circles)*. The *blue striped zone* refers to as-deposited thin films with extremely high electrically resistivity and are unable to be measured..... 108

Figure 63. Projected thermoelectric Power Factor dependent of $\tau 0$ **(a)** and electronic Figure of Merit at 300 K **(b)** for the supercells of anatase *(top)* and rutile *(bottom)* TiO_2:Nb. The anatase phase is indicated in *navy*, the rutile phase is indicated in *magenta* and the Fermi level is located at 0 eV. 109

Figure 64. Representation and respective SEM cross-section of Sample A: Ti:Nb → TiO_2:Nb (11 sccm O_2) + Ti **(a)** and Sample B: TiO_2:Nb (11 sccm O_2) → Ti:Nb + Ti **(b)**, both measuring 700 nm of thickness. 118

Figure 65. TOF-SIMS depth profile of Sample A **(a)** and Sample B **(b)**, in positive polarity (sample erosion with Oxygen) – $^{LC}Ti^+$ (linear combination of $^{50}Ti^+$, $^{46}Ti^+$,$^{47}Ti^+$ and $^{49}Ti^+$), $^{LC}TiO^+$ (linear combination of $^{50}TiO^+$, $^{46}TiO^+$,$^{47}TiO^+$ and $^{49}TiO^+$), Nb^+, NbO^+ and $^{LC}Si^+$ (linear combination of $^{30}Si^+$ and $^{29}Si^+$) – and negative polarity (sample erosion with Cesium) – $^{18}O^-$, $^{LC}TiO^-$ (linear combination of $^{50}TiO^-$, $^{46}TiO^-$ and $^{49}TiO^-$), NbO^-, NbO_2^- and $^{LC}Si^-$ (linear combination of $^{30}Si^-$ and $^{29}Si^-$) – normalized to maximum signal intensities with 4 point binning in the x-axis. Note that both depth profiles from each sample were not recorded at the same spot. 119

Figure 66. Relative ratio of Nb^+, NbO^+ and NbO_2^+ signals calibrated on the $^{46}Ti^+$, $^{46}TiO^+$ and $^{46}TiO2^+$ peak area signals, respectively, plotted against the reactive oxygen flow during sputter deposition

over the depth of sample A, obtained by TOF-SIMS in positive polarity with Oxygen beam erosion. 120

Figure 67. 1D concentration profile in the z-axis (parallel to the film growth) for sample A **(a)**, analysed closer to the substrate, and sample B **(b)** obtained by APT. 121

Figure 68. Volume render of atomic Ti and O concentrations for tip M10* of sample A **(a)**, analysed closer to the substrate, and M9 of sample B **(b)**. Sample count threshold at 0 %, with confidence sigma of 0. Opacity is at half value and a darker colour value relates to a higher atomic concentration value. 122

Figure 69. Volume render of atomic Ti concentration **(a)** and density **(b)** for tip M10* of Sample A, analysed closer to the substrate, and atomic Ti concentration **(c)** and density **(d)** for tip M4 of Sample B. Sample count threshold at 0 %, with confidence sigma of 0. Opacity is at half value and a darker colour value relates to a higher atomic concentration/density value. 122

Figure 70. TOF-SIMS depth profile of a TiO_2:Nb thin film (Sample HT_B) measured as-deposited (Ad) **(a)** and after annealing at 500 °C (TT) **(b)**, in positive polarity – $^{LC}Ti^+$ (linear combination of $^{50}Ti^+$, $^{46}Ti^+$,$^{47}Ti^+$ and $^{49}Ti^+$), $^{LC}TiO^+$ (linear combination of $^{50}TiO^+$, $^{46}TiO^+$,$^{47}TiO^+$ and $^{49}TiO^+$), Nb^+, NbO^+ and $^{LC}Si^+$ (linear combination of $^{30}Si^+$ and $^{29}Si^+$) – and negative polarity – $^{18}O^-$, $^{LC}TiO^-$ (linear combination of $^{50}TiO^-$, $^{46}TiO^-$ and $^{49}TiO^-$), NbO^-, NbO_2^- and $^{LC}Si^-$ (linear combination of $^{30}Si^-$ and $^{29}Si^-$) – normalized to maximum signal intensities with 4 point binning in the x-axis. 123

Figure 71. 1D concentration profile in the z-axis (parallel to the film growth) of two tips of a TiO_2:Nb thin film (Sample C), M25 measured as-deposited *(Ad)* **(a)** and M28* measured after annealing at 500 °C *(TT)* **(b)**, obtained by APT. 124

Figure 72. APT profile viewed ionic maps of Ti, TiO_2, O and a combination of Nb, NbO and NbO_2 signals of the 3D reconstruction of a TiO_2:Nb thin film (Sample C), tip M25 measured as-deposited *(Ad)* and M28* measured after annealing at 500 °C *(TT)*. 125

Figure 73. APT profile views of the 3D reconstruction of a TiO_2:Nb thin film (Sample C), tip M25 measured as-deposited *(Ad)* and M28* measured after annealing at 500 °C *(TT)*, with decomposed atomic concentration iso-surfaces of Nb at 0.1 % **(a)** and Ti at 24 %, 32 % and 36 **(b)**. Sample count threshold at 1 % for Nb and 5 % for Ti, with confidence sigma of 1. 126

Figure 74. APT sliced top view of the 3D reconstruction of tip M27 (5113) of a TiO_2:Nb thin film (Sample C(Ad)), decomposed atomic Ti (*blue*, at 27 %, 29 % and 31 %), Si (*black*, at 7 %, 8 % and 11 %), O (*green*, at 47 %, 45 % and 43 %) and Nb (*red*, at 0.01 %, 0.1 % and 0.2 %) concentration iso-surfaces. Sample count threshold at 1 % for Si and Nb and 5 % for Ti and O, with confidence sigma of 1. 126

Figure 75. HAADF-STEM (ROI#1) **(a)** and respective Nb **(b)**, Ti **(c)** and O **(d)** EDX maps of a TiO_2:Nb thin film after thermal annealing at 500 °C (Sample C(TT)). 127

Figure 76. HAADF-STEM (ROI#53) **(a)** and respective Nb **(b)**, Ti **(c)** and O **(d)** EDX maps of a TiO_2:Nb thin film after thermal annealing at 500 °C (Sample C(TT)). 128

Figure 77. HAADF-STEM (ROI#53) of a TiO_2:Nb thin film (Sample C(TT)) **(a)** and zoomed-in amplification **(b)** represented by the white square on the main micrograph in (a). A direct measurement of the interplane distance (d) in indicated by the white arrow and intensity vs. position plot in (b). 129

Figure 78. HAADF-STEM (ROI#230) along [110] **(a)**, FFT **(b)** and Intensity Profiles **(c)** for an analysis zone in a TiO_2:Nb thin film (Sample C(TT)). The FFT is represented by the coloured square on the

main micrographs in (a) and yellow line in (b) represents plane orientation positions plotted in (c). 129

Figure 79. HAADF-STEM (ROI#22) **(a)** and FFTs **(b,c,d,e)** for four analysis zones in a TiO_2:Nb thin film (Sample C(TT)). The FFTs are represented by the white squares correspondingly identified on the main micrographs in (a). Plain orientation positions are indicated in orange. Analysis zone Z_e (e) is located around ROI#53. 130

Figure 80. HAADF-STEM (ROI#27) **(a)**, FFTs **(b,d,e)** and intensity profile **(c)** for three analysis zones in a TiO_2:Nb thin film (Sample C(TT)). The FFTs are represented by the white squares correspondingly identified on the main micrographs in (a). Plain orientation positions are indicated in orange and yellow line in (b) represents plane orientation positions plotted in (c). 130

Figure 81. HAADF-STEM (ROI#756) **(a)** and FFT **(b)** in a TiO_2:Nb thin film (Sample C(TT)). Plain orientation positions are indicated in orange. 131

Figure 82. HAADF-STEM (ROI#747) **(a)** and FFT for an analysis zone **(b)** in a TiO_2:Nb thin film (Sample C(TT)). The FFT is represented by the white square on the main micrographs in (a). Plain orientation positions are indicated in orange. 131

Figure 83. SEM cross section of two TiO_2:Nb films. Sample A measured 251 nm of thickness **(a)** and Sample B measured 1.73 μm of thickness **(b)**. 138

Figure 84. Transmittance and specular reflectance spectra for sample A (tdep=5 min) **(a)** and sample B **(b)**. 138

Figure 85. Tangential Force and Acoustic Emission in response to the tangential Force applied to a TiO_2:Nb thin film (sample A), measured with a Load between 5 N and 50 N and a scratch speed of 5.0 mm·min^{-1} **(a)** and a Load between 5 N and 25 N and a scratch speed of 2.5 mm·min^{-1} **(b)**. *Light grey* stands for a plain glass substrate, Lc1 and Lc2 are represented by dashed *magenta* and *navy* lines, while *grey dashed* lines represent the fracture points of the glass substrate. 139

Figure 86. Scratch channels on a TiO_2:Nb thin film (sample A), with a Load between 5 N and 50 N and a scratch speed of 5.0 mm·min^{-1} **(a)** and a Load between 5 N and 25 N and a scratch speed of 2.5 mm·min^{-1} **(b)**. $Lc1$ and $Lc2$ are represented in *magenta* and *navy* lines, while *grey* lines represent the fracture points of the glass substrate. 140

Figure 87. Applied Load vs. indentation depth for different nanoindentations on a TiO_2:Nb thin film (sample B) with 9.0 mN of maximum applied Load. *Magenta* and *navy* arrows refer to the load and unload stages of measurement, while the *grey dashed lines* refer to the maximum values read by the system. HV is the nano hardness and δ is the Young's modulus. 141

Figure 88. Schematic of three TiO_2:Nb-based thermoelectric prototype designs: a single TiO_2:Nb thin film (thermal gradient generated parallel to the film's surface) **(a)**, a 4-sectional TiO_2:Nb thin film horizontally connected by Ag painted contact (thermal gradient generated parallel to the film's surface) **(b)** and a 4-sectional TiO_2:Nb thin film connected by a bottom TCO contact layer (sputtered before) and an intercepting top layer (sputtered after the thermoelectric layer) (thermal gradient applied perpendicularly to the film's surface) **(c)**. TiO_2:Nb is represented in *blue*, electrical contacts in *orange* and substrate in *black*. 142

Figure 89. Schematic representation a thermal gradient applied perpendicularly to two thermoelectric prototypes, consisting of bottom (FTO) and top (AZO) electrode layers and thermoelectric layers of TiO_2:Nb. The parallel arrangement of the TiO_2:Nb micropillars (electrical and thermally insulated by SiO_2) in sample A **(a)** yields increased total generated electric current compared to a continuous

TiO_2:Nb layer in Sample B **(b)**, although sample B generates a higher voltage. TiO_2:Nb is represented in *blue*, AZO/FTO electrical contacts in *orange* and substrate in *black*. Middle figures represented in electrochemical equilibrium (electrons accumulated near the coldest regions). *Black arrows* in right-hand figures indicate the flow of electric current. 143

Figure 90. Schematic representation of Sample A **(a)** with micro-array of 16 629 TiO_2:Nb pillars and sample B **(b)** with a continuous TiO_2:Nb layer. 145

Figure 91. Two pulse representation *(navy)* **(a)** and cathode potential vs. reactive oxygen flow rate hysteresis curve for the deposition of TiO_2:Nb thin films with *(HT, in red)* and without *(RT, in blue)* substrate heating (*dashed grey line* refers to the chosen O_2 flow for the present study of 6.5 sccm) **(b)** of a pulsed power supply using an applied target current of 1 A. 146

Figure 92. Top-view SEM of Sample A and zoomed-in angled view *(white square)* of a cross section of a TiO_2:Nb micropillar **(a)**, zoomed-in angled view *(black square)* at the interface between the TiO_2:Nb micropillar and the SiO_2 layer **(b)**, and cross section side view of Sample B **(c)**. 148

Figure 93. Transmittance spectra for Sample A, measured as-deposited *(Ad)* and after annealing at 500 °C *(TT)*, Sample B, a control sample with empty wells and a control sample of SiO_2. 149

Figure 94. Electric potential plotted against temperature gradient **(a)** and electric current **(b)** for Sample A, measured as-deposited *(Ad)* and after annealing at 500 °C *(TT)*, and Sample B. Seebeck coefficient and electric resistance were obtained by the slope of the linear fit for each sample, for (a) and (b), respectively. 149

Figure A 1. EDX analysis of the Ti, Nb and O atomic concentration in TiO_2:Nb thin films, deposited with 7.5 sccm, 8 sccm, 8.5 sccm and 9 sccm of reactive Oxygen flow, and the used Ti(96)Nb(4) wt.% target (99.9 % of purity, FHR) (*black*). 176

Figure A 2. EDX analysis of the Ti, Nb and O atomic concentration in Ti:Nb (no Oxygen, *lined columns*) and TiO_2:Nb (7 sccm of reactive Oxygen flow, *full columns*) thin films, deposited without substrate heating *(RT, blue)* and with substrate heating *(HT, red)* and using a new (previously unused) target *(HT, black)*. 177

Figure A 3. EDX analysis of the Nb atomic concentration in Ti:Nb (no Oxygen, *open circles*) and TiO_2:Nb (7 sccm of reactive Oxygen flow, *closed circles*) thin films deposited on Al foil without substrate heating *(RT, blue)* and with substrate heating *(HT, red)* and with a new target *(HT, black)* **(a)**, carried out in 5 different substrate zones **(b)**..... 178

Figure B 1. XRR measurement results and fits of a TiO_2 **(a)** and TiO_2:Nb **(b)** thin film, deposited for 2 min with a reactive oxygen flow of 6 sccm. 179

Figure C 1. XPS spectra and respective fits for the Nb 3d core lines for as-deposited TiO_2:Nb thin film with a reactive oxygen flow rate of 7 sccm **(a)**, as-deposited TiO_2:Nb with 7.5 sccm **(b)**, TiO_2:Nb with 7.5 sccm after annealing (*) **(c)** and as-deposited TiO_2:Nb with 9 sccm **(d)**..... 181

Figure C 2. XPS spectra and respective fits for the Ti 2p core lines for as-deposited TiO_2:Nb thin film with a reactive oxygen flow rate of 7 sccm **(a)**, as-deposited TiO_2:Nb with 7.5 sccm **(b)**, TiO_2:Nb with 7.5 sccm after annealing (*) **(c)**, as-deposited TiO_2:Nb with 9 sccm **(d)** and as-deposited undoped TiO_2 with a reactive oxygen flow rate of 7.5 sccm **(e)**. 182

Figure C 3. Survey XPS spectra for as-deposited TiO_2:Nb thin film deposited with a reactive oxygen flow rate of 7 sccm **(a)**, as-deposited TiO_2:Nb with 7.5 sccm **(b)**, TiO_2:Nb with 7.5 sccm after annealing (*) **(c)**, as-deposited TiO_2:Nb with 9 sccm **(d)** and as-deposited undoped TiO_2 with a reactive oxygen flow rate of 7.5 sccm **(e)**..... 183

Figure D 1. Transmittance **(a)** and specular reflectance spectra **(b)** for as-deposited TiO_2:Nb thin films deposited for 5 min with varying oxygen flow rates. 184

Figure D 2. Transmittance **(a)** and specular reflectance spectra **(b)** for TiO_2:Nb thin films deposited for 5 min with 7.5 sccm of oxygen flow rate measured as-deposited *(Ad, blue)* and after annealing *(TT, red)*. 185

Figure E 1. APT microtip array. The fiducials are used as references for sample positioning during measurements. 186

Figure E 2. 1D concentration profiles of all analysed tips in the z-axis (parallel to the film growth) of a Ti:Nb/TiO_2:Nb film (Sample A), obtained by APT. 188

Figure E 3. APT profile viewed ionic maps of Ti **(a)**, TiO **(b)**, TiO_2 **(c)**, Si **(d)**, O **(e)** and Nb **(f)** signals of the 3D reconstruction of tip M4* (16758) of a Ti:Nb/TiO_2:Nb film (Sample A). 189

Figure E 4. APT profile viewed ionic maps of Ti **(a)**, TiO **(b)**, TiO_2 **(c)**, Si **(d)**, O **(e)** and Nb **(f)** signals of the 3D reconstruction of tip M10* (16760) of a Ti:Nb/TiO_2:Nb film (Sample A). 189

Figure E 5. APT profile viewed ionic maps of Ti **(a)**, TiO **(b)**, TiO_2 **(c)**, Si **(d)**, O **(e)** and Nb **(f)** signals of the 3D reconstruction of tip M11* (16772) of a Ti:Nb/TiO_2:Nb film (Sample A). 190

Figure E 6. Volume rendered side-views of decomposed atomic Ti concentration **(a)**, O concentration **(b)**, Ti density **(c)** and O density **(d)** for tip M10* (16760) of a Ti:Nb/TiO_2:Nb film (Sample A). Sample count threshold at 0 %, with confidence sigma of 0. Opacity is at half value and a darker color value relates to a higher atomic concentration/density value. 190

Figure E 7. 1D concentration profile of all analysed tips in the z-axis (parallel to the film growth) of a Ti:Nb/TiO_2:Nb film (Sample B), obtained by APT. 191

Figure E 8. APT profile viewed ionic maps of Ti **(a)**, TiO **(b)**, TiO_2 **(c)**, Si **(d)**, O **(e)** and Nb **(f)** signals of the 3D reconstruction of tip M4 (16677) of a Ti:Nb/TiO_2:Nb film (Sample B)..... 192

Figure E 9. APT profile viewed ionic maps of Ti **(a)**, TiO **(b)**, TiO_2 **(c)**, Si **(d)**, O **(e)** and Nb **(f)** signals of the 3D reconstruction of tip M11 (16679) of a Ti:Nb/TiO_2:Nb film (Sample B). 192

Figure E 10. APT profile viewed ionic maps of Ti **(a)**, TiO **(b)**, TiO_2 **(c)**, Si **(d)**, O **(e)** and Nb **(f)** signals of the 3D reconstruction of tip M9 (16680) of a Ti:Nb/TiO_2:Nb film (Sample B)..... 193

Figure E 11. APT volume rendered side-views of decomposed atomic Ti concentration **(a)**, O concentration **(b)**, Ti density **(c)** and O density **(d)** for tip M9 (16680) of a Ti:Nb/TiO_2:Nb film (Sample B). Sample count threshold at 0 %, with confidence sigma of 0. Opacity is at half value and a darker color value relates to a higher atomic concentration/density value. 193

Figure E 12. Atomic concentration of Ti, O and Nb in a TiO_2:Nb thin film (sample C) obtained by APT, over 3 tip measurements as-deposited *(Ad, in blue)* and 3 after annealing at 500 °C *(TT, in red)*. 194

Figure E 13. 1D concentration profile in the z-axis (parallel to the film growth) of Ti, O and Nb in a TiO_2:Nb thin film (sample C) obtained by APT, over 3 tip measurements as-deposited *(Ad)* **(a)** and 3 after annealing at 500 °C *(TT)* **(b)**. 195

Figure E 14. APT profile viewed ionic maps of Ti **(a)**, TiO **(b)**, TiO_2 **(c)**, Si **(d)**, O **(e)** and a combination of Nb, NbO and NbO_2 **(f)** signals of the 3D reconstruction of tip M25 (5112) of a TiO_2:Nb thin film (Sample C(Ad)). 195

Figure E 15. APT profile viewed ionic maps of Ti **(a)**, TiO **(b)**, TiO_2 **(c)**, Si **(d)**, O **(e)** and a combination of Nb, NbO and NbO_2 **(f)** signals of the 3D reconstruction of tip M27 (5113) of a TiO_2:Nb thin film (Sample C(Ad)). 196

Figure E 16. APT profile viewed ionic maps of Ti **(a)**, TiO **(b)**, TiO_2 **(c)**, Si **(d)**, O **(e)** and a combination of Nb, NbO and NbO_2 **(f)** signals of the 3D reconstruction of tip M29 (5116) of a TiO_2:Nb thin film (Sample C(Ad)). 196

Figure E 17. APT profile viewed ionic maps Ti **(a)**, TiO **(b)**, TiO_2 **(c)**, Si **(d)**, O **(e)** and a combination of Nb, NbO and NbO_2 **(f)** signals of the 3D reconstruction of tip M26* (15394) of a TiO_2:Nb thin film measured after annealing at 500 °C (Sample C(TT)). 197

Figure E 18. APT profile viewed ionic maps of Ti **(a)**, TiO **(b)**, TiO_2 **(c)**, Si **(d)**, O **(e)** and a combination of Nb, NbO and NbO_2 **(f)** signals of the 3D reconstruction of tip M28* (15395) of a TiO_2:Nb thin film measured after annealing at 500 °C (Sample C(TT)). 197

Figure E 19. APT profile viewed ionic maps of Ti **(a)**, TiO **(b)**, TiO_2 **(c)**, Si **(d)**, O **(e)** and a combination of Nb, NbO and NbO_2 **(f)** signals of the 3D reconstruction of tip M33* (153401) of a TiO_2:Nb thin film measured after annealing at 500 °C (Sample C(TT)). 198

Figure E 20. APT profile view of the 3D reconstruction of tip M25 (5112) of a TiO_2:Nb thin film (Sample C(Ad)), with decomposed atomic concentration iso-surfaces of Ti at 20 %, 24 %, 28 %, 32 %, 34 % and 36 % **(a)**, Si at 1 %, 3 %, 5 %, 7 %, 11 % and 15 % **(b)**, O at 41 %, 43 %, 45 %, 47 %, 49 % and 51 % **(c)** and Nb at 0.01 %, 0.1 %, 0.2 %, 0.3 %, 0.4 % and 0.5 % **(d)**. Sample count threshold at 1 % for Si and Nb and 5 % for Ti and O, with confidence sigma of 1. 199

Figure E 21. APT sliced top view of the 3D reconstruction of tip M25 (5112) of a TiO_2:Nb thin film (Sample C(Ad)), decomposed atomic Ti (*blue*, at 28 %, 30 % and 32 %), Si (*black*, at 13 %, 15 % and 17 %), O (*green*, at 47 %, 45 % and 43 %) and Nb (*red*, at 0.01 %, 0.1 % and 0.2 %) concentration iso-surfaces. Sample count threshold at 1 % for Si and Nb and 5 % for Ti and O, with confidence sigma of 1. 200

Figure E 22. APT profile view of the 3D reconstruction of tip M27 (5113) of a TiO_2:Nb thin film (Sample C(Ad)), with decomposed atomic concentration iso-surfaces of Ti at 20 %, 24 %, 28 %, 32 %, 34 % and 36 % **(a)**, Si at 1 %, 3 %, 5 %, 7 %, 11 % and 15 % **(b)**, O at 41 %, 43 %, 45 %, 47 %, 49 % and 51 % **(c)** and Nb at 0.01 %, 0.1 %, 0.2 %, 0.3 %, 0.4 % and 0.5 % **(d)**. Sample count threshold at 1 % for Si and Nb and 5 % for Ti and O, with confidence sigma of 1. 201

Figure E 23. APT sliced top view of the 3D reconstruction of tip M27 (5113) of a TiO_2:Nb thin film (Sample C(Ad)), decomposed atomic Ti (*blue*, at 28 %, 30 % and 32 %), Si (*black*, at 13 %, 15 % and 17 %), O (*green*, at 47 %, 45 % and 43 %) and Nb (*red*, at 0.01 %, 0.1 % and 0.2 %) concentration iso-surfaces. Sample count threshold at 1 % for Si and Nb and 5 % for Ti and O, with confidence sigma of 1. 202

Figure E 24. APT profile view of the 3D reconstruction of tip M29 (5116) of a TiO_2:Nb thin film (Sample C(Ad)), with decomposed atomic concentration iso-surfaces of Ti at 20 %, 24 %, 28 %, 32 %, 34 %

and 36 % **(a)**, Si at 1 %, 3 %, 5 %, 7 %, 11 % and 15 % **(b)**, O at 41 %, 43 %, 45 %, 47 %, 49 % and 51 % **(c)** and Nb at 0.01 %, 0.1 %, 0.2 %, 0.3 %, 0.4 % and 0.5 % **(d)**. Sample count threshold at 1 % for Si and Nb and 5 % for Ti and O, with confidence sigma of 1..... 203

Figure E 25. APT profile view of the 3D reconstruction of tip M29 (5116) of a TiO_2:Nb thin film (Sample C(Ad)), with decomposed atomic concentration iso-surfaces of Ti (*blue*, 27 %) and Si (*black*, 4 %) **(a)**, Ti (35 %) and Si (8 %) **(b)**, Ti (35 %) and Si (10 %) **(c)** and Ti (35 %) and O (*green*, 45) **(d)**. Sample count threshold at 1 % for Si and 5 % for Ti and O, with confidence sigma of 1..... 204

Figure E 26. APT sliced top view of the 3D reconstruction of tip M29 (5116) of a TiO_2:Nb thin film (Sample C(Ad)), decomposed atomic Ti (*blue*, at 28 %, 33 % and 35 %), Si (*black*, at 5 %, 9 % and 11 %), O (*green*, at 47 %, 45 % and 43 %) and Nb (*red*, at 0.01 %, 0.1 % and 0.2 %) concentration iso-surfaces. Sample count threshold at 1 % for Si and Nb and 5 % for Ti and O, with confidence sigma of 1..... 204

Figure E 27. APT profile view of the 3D reconstruction of tip M26* (15394) of a TiO_2:Nb thin film after annealing at 500 °C (Sample C(TT)), with decomposed atomic concentration iso-surfaces of Ti at 20 %, 24 %, 28 %, 32 %, 34 % and 36 % **(a)**, Si at 1 %, 3 %, 5 %, 7 %, 11 % and 15 % **(b)**, O at 41 %, 43 %, 45 %, 47 %, 49 % and 51 % **(c)** and Nb at 0.01 %, 0.1 %, 0.2 %, 0.3 %, 0.4 % and 0.5 % **(d)**. Sample count threshold at 1 % for Si and Nb and 5 % for Ti and O, with confidence sigma of 1. 205

Figure E 28. APT profile view of the 3D reconstruction of tip M28* (15395) of a TiO_2:Nb thin film after annealing at 500 °C (Sample C(TT)), with decomposed atomic concentration iso-surfaces of Ti at 20 %, 24 %, 28 %, 32 %, 34 % and 36 % **(a)**, Si at 1 %, 3 %, 5 %, 7 %, 11 % and 15 % **(b)**, O at 41 %, 43 %, 45 %, 47 %, 49 % and 51 % **(c)** and Nb at 0.01 %, 0.1 %, 0.2 %, 0.3 %, 0.4 % and 0.5 % **(d)**. Sample count threshold at 1 % for Si and Nb and 5 % for Ti and O, with confidence sigma of 1. 206

Figure E 29. APT profile view of the 3D reconstruction of tip M33* (15401) of a TiO_2:Nb thin film after annealing at 500 °C (Sample C(TT)), with decomposed atomic concentration iso-surfaces of Ti at 20 %, 24 %, 28 %, 32 %, 34 % and 36 % **(a)**, Si at 1 %, 3 %, 5 %, 7 %, 11 % and 15 % **(b)**, O at 41 %, 43 %, 45 %, 47 %, 49 % and 51 % **(c)** and Nb at 0.01 %, 0.1 %, 0.2 %, 0.3 %, 0.4 % and 0.5 % **(d)**. Sample count threshold at 1 % for Si and Nb and 5 % for Ti and O, with confidence sigma of 1. 207

Figure F 1. HAADF-STEM of the TiO_2:Nb thin film (after thermal annealing at 500 °C) lamella **(a)**. **(b)** and **(d)** are zoomed-in magnifications of b-ROI and d-ROI in (a), **(c)** is a magnification of the c-ROI (b) and **(e)** and **(f)** (ROI#1) are magnifications of the e-ROI and f-ROI in (d), indicated by their respective coloured squares. 208

Figure F 2. HAADF-STEM (ROI#2) **(a)** and respective Nb **(b)**, Ti **(c)** and O **(d)** EDX maps of a TiO_2:Nb thin film after thermal annealing at 500 °C. 209

Figure F 3. HAADF-STEM (ROI#3) **(a)** and respective Nb **(b)**, Ti **(c)** and O **(d)** EDX maps of a TiO_2:Nb thin film after thermal annealing at 500 °C. 209

Figure F 4. HAADF-STEM (ROI#240) **(a)** and respective Nb **(b)**, Ti **(c)** and O **(d)** EDX maps of a TiO_2:Nb thin film after thermal annealing at 500 °C. 210

Figure F 5. HAADF-STEM (ROI#4) **(a)** and respective Nb **(b)**, Ti **(c)** and O **(d)** EDX maps of a TiO_2:Nb thin film after thermal annealing at 500 °C. 210

Figure F 6. HAADF-STEM (ROI#36) **(a)** and respective Nb **(b)**, Ti **(c)** and O **(d)** EDX maps of a TiO_2:Nb thin film after thermal annealing at 500 °C. 211

Figure F 7. HAADF-STEM EDX spectra for ROI#1 **(a)**, ROI#2 **(b)**, ROI#3 **(c)** and ROI#4 **(d)** of a TiO_2:Nb thin film after thermal annealing at 500 °C. 211

Figure F 8. HAADF-STEM EDX spectra for ROI#53 **(a)**, ROI#240 **(b)**, ROI#43 **(c)** and ROI#36 **(d)** of a TiO_2:Nb thin film after thermal annealing at 500 °C. 212

Figure F 9. Atomic concentration of Ti, O and Nb in a TiO_2:Nb thin film after thermal annealing at 500 °C obtained by STEM-EDX, over measurements in 4 zones: ROI#36, ROI#43, ROI#53 and ROI#240. 212

LIST OF TABLES

Table 1. Transparent and semi-transparent devices that use thermoelectric effects. 9

Table 2. Seebeck coefficient (S), electrical conductivity (σ), electronic and lattice thermal conductivity (κe and κp) and thermoelectric figure of merit (ZT) for six TCOs with thermoelectric properties at 800 K in the study by Spooner et al. [40]. 10

Table 3. Crystalline phases and respective parameters of TiO_2. Based on [37,57]..... 17

Table 4. Summary of samples, presented and discussed in their respective chapters..... 25

Table 5. XPS fitting parameters for as-deposited TiO_2:Nb thin film. 51

Table 6. Thermoelectric, thermal, electrical and optical properties of TiO_2:Nb film for different thickness: Seebeck coefficient (S); thermoelectric power factor (PF) and figure of merit (ZT); thermal conductivity (κ); electrical conductivity (σ), carrier concentration (ne) and mobility (μe); optical band-gap (Eg)..... 60

Table 7. Composition of the as-deposited TiO_2:Nb and TiO_2 thin films as a function of reactive oxygen rate (in sccm) during deposition; * denotes a post-deposition thermal annealed sample at 500 °C in vacuum..... 73

Table 8. Ti 2p core level XPS fitting parameters for the samples listed in Table 7. 73

Table 9. O 1s core level XPS fitting parameters for the samples listed in Table 7..... 73

Table 10. Nb 3d core level XPS fitting parameters for the samples listed in Table 7. 74

Table 11. Summary of results for Transmittance (Tvis) averaged in the (400 to 700) nm range, Band-Gap Energy (Eg), Seebeck coefficient (S), electrical conductivity (σ), thermal conductivity (κ) and calculated Power Factor (PF) and Figure of Merit (ZT) at 300 K of TiO_2:Nb thin films deposited with different reactive oxygen flow rates, measured as-deposited (Ad) and after annealing at 500 °C (TT)..... 85

Table 12. Summary of samples A, B, C, D and E, deposited with and without substrate heating. 96

Table 13. Resulting lattice parameters for the anatase and rutile unit cells (U_c) and supercells (S_c) models..... 102

Table 14. Summary of results for Transmittance (Tvis) averaged in the (400 to 700) nm range, Band-Gap Energy (Eg), fraction of Rutile phase (WR), Seebeck coefficient (S), electrical conductivity (σ) and calculated Power Factor (PF) of TiO_2:Nb thin films deposited with (HT) and without (RT) substrate heating, measured as-deposited (Ad) and after annealing at 500 °C (TT), with different deposition temperatures (Tdep). The Figure of Merit (ZT) at 300 K was estimated by considering $\kappa = (1.5 \pm 0.1)$ W·m^{-1}·K^{-1} [146]..... 110

Table 15. Deposition conditions for sample A, sample B and sample C. The different deposition times were used to compensate for the lower deposition rate for higher Oxygen flows. 116

Table 16. Relative atomic Ti, O and Nb composition of a TiO_2:Nb thin film (Sample C) as-deposited (Ad) and after annealing at 500 °C (TT), obtained by APT (APPENDIX E – APT Analysis), SEM-EDX (APPENDIX A – SEM-EDX Analysis), STEM-EDX (APPENDIX F – HAADF-STEM Analysis) and XPS (Section 3.2). 124

Table 17. Summary of measured electric potential (V), electric current (I) and efficiency (η) for Sample A, measured as-deposited (Ad) and after annealing at 500 °C (TT) and Sample B, for an applied temperature difference (ΔT) of 5.5 °C. 150

Table 18. Summary of results for Transmittance ($T\mathrm{vis}$), averaged in the (400 to 700) nm range, electrical Conductivity (σ), Seebeck coefficient (S) and calculated Power Factor (PF) of the thermoelectric devices. Sample A was measured as-deposited (Ad) and after annealing at 500 °C (TT). To estimate the Figure of Merit (ZT) at 300 K, a thermal conductivity value of (1.5 ± 0.1) $W{\cdot}m^{-1}{\cdot}K^{-1}$ was considered [146]. 151

Table 19. Summary of results for Transmittance ($T\mathrm{vis}$), averaged in the (400 to 700) nm range, electrical Conductivity (σ), Seebeck coefficient (S) and calculated Power Factor (PF) and Figure of Merit (ZT) at 300 K of the best samples from each chapter, measured as-deposited (Ad) and after annealing at 500 °C (TT). 159

Table B 1. Thickness (d), roughness and density (D), obtained by XRR, and average transmittance in the (400 to 700) nm range, obtained by UV-vis, for as-deposited TiO_2 and TiO_2:Nb thin films with varying deposition times and reactive oxygen flows. 180

Table E 1. APT tip measurements for sample A, B and C measured in a local electrode atom probe (LEAP 4000X HR) in UV-laser mode with variable laser energy ($E\mathrm{laser}$), pulse frequency (f), temperature ($T\mathrm{A}$ and $T\mathrm{B}$) and detection rate (DR). 187

LIST OF SYMBOLS, ABBREVIATIONS AND ACRONYMS

A	Area	$[m^2]$
A_r°	Standard atomic weight	
a, b, c	Crystalline structure parameters	[Å]
V_c	Volume of a crystalline cell	$[Å^3]$
d_{hkl}	Interplanar distance	[Å]
D	Density	$[g \cdot cm^{-3}]$
m	Mass	[Kg]
m/z	Mass-to-charge ratio	[Da]
m^*	Effective mass	[Kg]
Z	Number of atoms per unit cell	$[atom \cdot cell^{-1}]$
A_A	Main anatase peak integrated area	
A_R	Main rutile peak integrated area	
W_A	Weight fraction of anatase	
W_R	Weight fraction of rutile	
E	Energy	[J]
E_F	Energy at the Fermi level	[eV]
E_g	Band-gap energy	[eV]
E_k	Kinetic Energy	[J]
α	Absorption coefficient	
β	Constant of proportionality	
R	Optical Reflectance	[%]
Rs	Optical Specular Reflectance	[%]
$\overline{Rs}_{VIS}$	Specular Reflectance averaged in the visible (400 to 700) nm range	[%]
T	Optical Transmittance	[%]
$\bar{T}_{VIS}$	Transmittance averaged in the visible (400 to 700) nm range	[%]
τ	Relaxation-time	[s]
v	Velocity	$[m \cdot s^{-1}]$
ν	Phonon frequency	[Hz]
f	Frequency	$[s^{-1}]$
ω	Angular frequency	$[rad \cdot s^{-1}]$
ω_p	Plasma frequency	$[rad \cdot s^{-1}]$
λ	Wavelength	[nm]
k_p	Wavenumber	$[cm^{-1}]$
k_f	Field reduction factor	
ϵ_τ	Relative permittivity or dielectric constant	$[F \cdot m^{-1}]$
ϵ_{optic}	Dielectric constant below the interband absorption edge	$[F \cdot m^{-1}]$
Γ_τ	Damping rate	$[s^{-1}]$
$\Gamma_{\tau,high}$	Damping constant at high frequencies	
$\Gamma_{\tau,low}$	Damping constant at low frequencies	
$\Gamma_{\tau,crossover}$	Crossover parameter at the transition region	
$\Gamma_{\tau,width}$	Width parameter at the transition region	

n_e	Charge carriers concentration	$[cm^{-3}]$
μ_e	Charge carriers mobility	$[m^2 \cdot V^{-1} \cdot s^{-1}]$
σ	Electrical conductivity	$[\Omega^{-1} \cdot m^{-1}]$
ρ	Electrical resistivity	$[\Omega \cdot m]$
K	Thermal conductance	$[W \cdot K^{-1}]$
κ	Thermal conductivity	$[W \cdot m^{-1} \cdot K^{-1}]$
κ_e	Electronic contribution to the thermal conductivity	$[W \cdot m^{-1} \cdot K^{-1}]$
κ_p	Phonon/lattice contribution to the thermal conductivity	$[W \cdot m^{-1} \cdot K^{-1}]$
B	Magnetic field	$[T]$
I	Electric current	$[A]$
j	Current density	$[A \cdot m^{-2}]$
ε	Electric field	$[V \cdot m^{-1}]$
V	Electric potential	$[V]$
V_{DC}	Standing voltage	$[V]$
V_{HF}	High frequency voltage	$[V]$
V_H	Hall voltage	$[V]$
R	Electrical resistance	$[\Omega]$
P	Electric power	$[J \cdot s^{-1}]$
W	Generated electric power	$[J]$
χ_e	Electric susceptibility	
μ	X-ray absorption coefficient	
S_0^2	Amplitude reduction factor	
t_{dep}	Deposition time	$[s]$
T	Absolute temperature	$[K]$
T_C	Absolute temperature in the coldest side of a material	$[K]$
T_{dep}	Deposition temperature	$[K]$
T_H	Absolute temperature in the hottest side of a material	$[K]$
T_b	Boiling point	$[K]$
T_m	Melting point	$[K]$
C_p	Heat capacity	$[J \cdot K^{-1}]$
$\dot{Q}_P$	Peltier heat per unit of time	$[W]$
$\dot{q}_T$	Thomson heat per unit of time and unit of volume	$[W \cdot m^{-3}]$
Q_{HC}	Heat flow from the hot to the cold side	$[J \cdot s]$
S	Seebeck coefficient	$[V \cdot K^{-1}]$
Π	Peltier coefficient	$[V\ K^{-1}]$
$\mathcal{K}$	Thomson coefficient	$[V\ K^{-1}]$
ZT	Figure of Merit	
PF	Power factor	$[W \cdot m^{-1} \cdot K^{-2}]$
η	Thermoelectric efficiency	$[\%]$
d	Thickness	$[m]$
r	Radius	$[m]$
r_0	APT tip apex curvature radius	$[m]$
α_0	APT tip apex shank	$[°]$
θ	Detector angle	$[°]$
U	Hubbard parameter	$[eV]$
Y	Sputtering Yield	$[atom \cdot ion^{-1}]$
H_V	Hardness	$[GPa]$
δ	Young modulus	$[GPa]$

Lc	Critical load	$[\mathrm{N}]$
Δ	Difference	
∇	Gradient	
ϵ_0	Vacuum permittivity ($\approx 8.8542 \times 10^{-12}$)	$[\mathrm{F{\cdot}m^{-1}}]$
e	Electron charge ($\approx 1.6022 \times 10^{-19}$)	$[\mathrm{C}]$
h	Planck constant ($\approx 6.6261 \times 10^{-34}$)	$[\mathrm{J{\cdot}Hz^{-1}}]$
$\hbar$	Reduced Planck constant ($\approx 1.0546 \times 10^{-34}$)	$[\mathrm{J{\cdot}s}]$
$\mathrm{P_{amb}}$	Ambient pressure (≈ 1.0133)	$[\mathrm{bar}]$

A

AC	Alternate current
AC-STEM	Aberration-corrected scanning transmission electron microscopy
Ad	As-deposited
AEMIS	Advanced Electron Microscopy, Imaging & Spectroscopy
APT	Atom probe tomography

B

$BaSnO_3$	Barium stannate
BF-STEM	Bright field scanning transmission electron microscopy
bcc	Body-centred cubic
Bi_2Te_3	Bismuth telluride

C

CAE	Constant analyser energy mode
CB	Conduction band
CdO	Cadmium oxide
CF-UM-UP	Physics Centre of Minho and Porto Universities
CH_4	Methane
CuI	Copper iodide
CVD	Chemical vapour Deposition

D

DC	Direct current
DESY	German electron synchrotron
DFT	Density functional theory
DOS	Density of states
DWL	Direct write laser

E

EA	Evolutionary algorithm
EDS / EDX	Energy-dispersive X-ray spectroscopy
ESZM	Extended Structure Zone Model
EXAFS	Extended X-ray absorption fine structure

F

FDM	Finite difference method

FDTR	Frequency-domain thermo-reflectance
FEG	Field emission gun
FFT	Fast Fourier transform
FIB	Field ion beam
FIM	Field ion microscopy
FT	Fourier transform
TO:F / FTO	Fluorine-doped tin oxide
FWHM	Full width at half maximum

G

GGA	Generalized gradient approximation
GIXRD	Grazing incidence x-ray diffraction

H

H_2O_2	Hydrogen peroxide
H_2SO_4	Sulfuric acid
HAADF	Annular dark field
HASYLAB	Hamburg Synchrotron Radiation Laboratory
HCB	High current bunched
HF	High frequency
HREM	High resolution electron microscopy
HT	Substrate/chamber heating
HV	High vacuum (10^{-3} mbar to 10^{-8} mbar)

I

ICDD	International Centre for Diffraction Data
ICMAB	Institute of Materials Science of Barcelona
In_2O_3:Sn / ITO	Tin-doped indium oxide
IAM-WK-KIT	Institute for Applied Materials – Materials Science and Engineering, at the KIT
IFG-KIT	Institute of Functional Interfaces, at the KIT
INL	International Iberian Nanotechnology Laboratory

J

JCPDS	Joint Committee on Powder Diffraction Standard

K

KFM	Kelvin probe force microscopy
KIT	Karlsruhe Institute of Technology
KNMFi	Karlsruhe Nano Micro Facility for Information-driven Material Structuring and Characterization

L

LEAP	Local Electrode Atom Probe
LMIG	Liquid metal ion gun
LSI	Large-scale-integrated
LV	Low vacuum (1000 mbar to 1 mbar)

M

MCP	Microchannel plate
MS	Multiple-scattering
MT	Muffin-tin
MV	Medium vacuum (1 mbar to 10^{-3} mbar)

N

Nb_2O_5	Niobium pentoxide

O

OJL	O'Leary-Johnson-Lm

P

PBC	Periodic boundary conditions
PBE	Perdew–Burke–Ernzerhof
PDOS	Projected density of states
PECVD	Plasma-enhanced chemical vapour deposition
PIPS	Passivated implanted planar silicon
PLD	Pulse-laser deposition
PVD	Physical vapor deposition

Q

R

RDF	Radial distribution functions
RIE	Reactive ion etching
ROI	Region of interest
RMC	Reverse Monte Carlo
RT	Room temperature/no substrate heating
RTG	Radioactive Thermoelectric Generator

S

S_c	Supercell
SEM	Scanning electron microscopy
SEMAT/UM	Materials Characterization Services of the University of Minho
SiO_2	Silicon dioxide
SIMS	Secondary ion mass spectrometry
SLG	Soda-lime glass
SnO_2	Tin oxide
SnSe	Tin selenide
SZM	Structure zone model

T

TCO	Transparent conductive oxide
TEC	Thermo-electric cooler
TEG	Thermo-electric generator
TEM	Transmission electron microscopy
TiO_2	Titanium dioxide
TiO_2:Nb	Nb-doped titanium dioxide

TOF	Time-of-flight
TOF-SIMS	Time-of-flight secondary ion mass spectrometry
TT	Thermal treatment/annealing

U

U_c	Unit cell
UHV	Ultra-high vacuum (10^{-8} mbar to 10^{-12} mbar)
UM	University of Minho
UV-Vis-NIR	Ultraviolet-visible-near-infrared

V

VB	Valence band

W

WT	Wavelet transform

X

XAS	X-ray absorption spectroscopy
XANES	X-ray absorption near-edge structure
XPS	X-ray photoelectron spectroscopy
XRD	X-ray diffraction
XRR	X-ray reflectometry/reflectivity

Y

Z

ZnO	Zinc oxide
ZnO:Al / AZO	Aluminium-doped zinc oxide
ZnO:Ga / GZO	Gallium-doped zinc oxide

CHAPTER I.

INTRODUCTION

1. Introduction

In this chapter, the problem is briefly framed and described in the scope of this work, giving a state of the art in the area of thermoelectric materials and technologies. Different approaches are presented and discussed, as are the motivation and objectives. Lastly, the structure of the dissertation is presented.

1.1. Motivation

Energy is a key part of human life. The increasing growth of human population and its technological advancements, creates one of the biggest challenges for the world's population: meeting energy demand - predicted to be 34 % more in 2050 - in an economically effective and ecologically responsible way [1]. An estimated 66 % of all generated energy is wasted as heat, produced and released either via radiation, cooling fluid, exhaust gas or air. **Figure 1** presents a 2022 diagram of the Lawrence Livermore National Laboratory and Department of Energy [2], in which 67.3 % of the energy produced in the United States is wasted. Approximately 10 % to 25 % of this wasted heat is theoretically recoverable through one of the many waste heat usage technologies [3,4]. These facts illustrate the importance of controlling energy sources and efficiency. Furthermore, the demand for reliable, affordable, sustainable and cleaner energy is ever-growing due to global warming and increasing cost of the conventionally used fossil fuel sources.

Thermoelectric-based devices such as generators have drawn much attention as a new energy source for their reliability, durability, simple structure and no moving parts. Thermoelectric materials transform heat into electricity (or vice versa) and are promising candidates for this task [4]. Thermoelectric generators (TEG) have been widely used in space probes and other specific space applications for many years. Some, in the specific case of the Voyager I probe, launched in the mid-seventies of the last century, are still in perfect working condition, and should remain so until 2025. Thermoelectric technology based on the Seebeck effect, one of the thermoelectric phenomena, may play a relevant role in the production of electricity. Matsubara et al. (2002) [5] and Yang et al. (2006) [6] present a concrete record of the application of thermoelectrics for the recovery of wasted thermal energy in gasoline thermal combustion vehicles, such as the use of thermoelectrics for cooling seats in expensive cars.

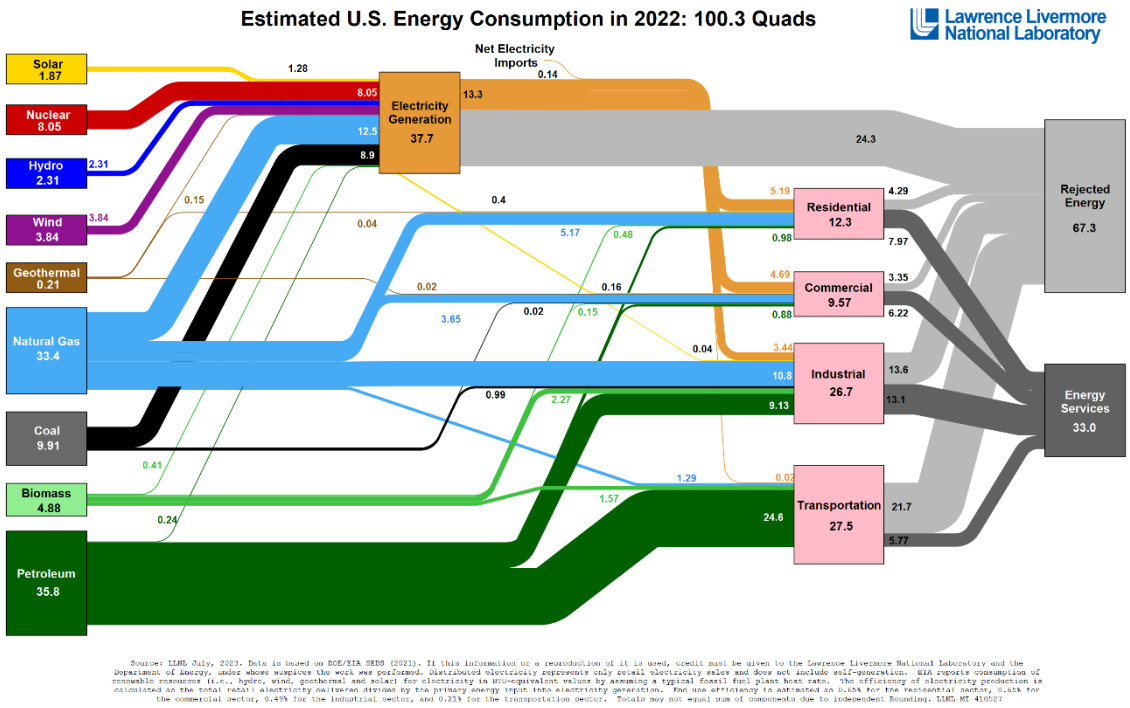

Figure 1. Origin and flow of energy consumed in the United States of America in the year 2022, according to the Lawrence Livermore National Laboratory and Department of Energy [2].

The design of a transparent material with thermoelectric properties is a desired technology to produce electrical energy by harvesting the generated heat in transparent devices, such as photovoltaics, thermovoltaics and touch displays, thus rendering a more sustainable powering of the device.

1.2. Thermoelectricity

The direct energy conversion between the transport of heat and electric charge based on thermoelectric effects has been a topic of long-standing interest in condensed matter materials science for over half a century [7]. The chronogram in **Figure 2** features the most important markers in the long history of thermoelectrics in providing simple and reliable power generation solutions [8,9]. The three important phenomena relating to the thermoelectric effects were discovered during the 19th century: the Seebeck effect, the Peltier effect and the Thomson effect [8]. The discovery of these effects paved the way for the research and implementation of thermoelectric energy conversion processes.

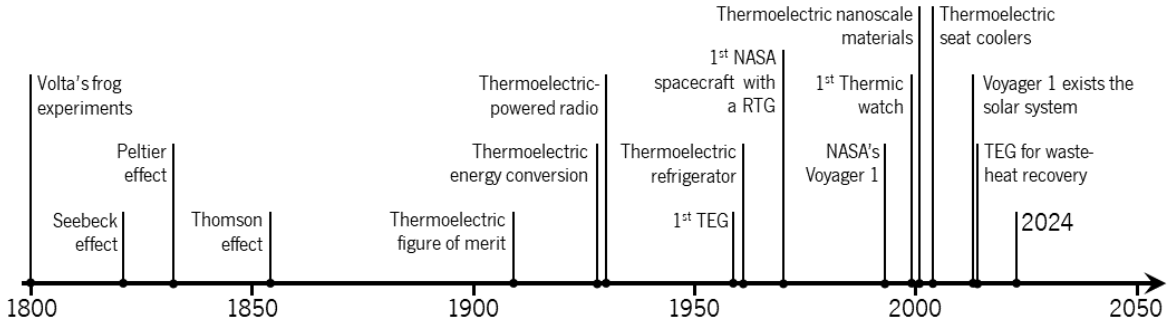

Figure 2. Chronogram of prominent thermoelectric advancements over the course of history.

Although the Seebeck effect was reported by Johann Seebeck in 1821 [10], it was first observed by Alessandro Volta over 20 years earlier [11], through his experiments with frogs, that led to the invention of the battery. The Seebeck effect is the phenomenon in which an electromotive force is generated from a temperature gradient ∇T applied to two dissimilar materials and is expressed by the thermopower, or Seebeck coefficient (S) as

$$\mathbf{j} = -\sigma \boldsymbol{\nabla} V - \sigma S \boldsymbol{\nabla} T \,, \tag{1}$$

where j is the current density, σ is the electrical conductivity, ∇V is the voltage gradient.

The free electrons or holes (vacancies left by electrons) in a thermoelectric material are responsible for charge and heat transport. Similar to the motion of a gas, in the absence of an electric field, charge carriers will move in random directions through a conductor, but an electric field applied to the system will cause the free charge carriers to drift parallel to it. An increase in temperature increases the potential energy of the charge carriers, and, if there is a temperature difference, this creates a charge flux towards the colder edge of the material (**Figure 3**), before it reaches electrochemical equilibrium. In materials where electrons are the main charge carriers, a negative potential will be generated at the cold side, contrary to the temperature gradient. When the charge carriers are mainly positively charged holes, the current will flow contrary-wise to the temperature gradient, as holes also tend to move towards the cold side.

Owing to their band-gap energy E_g, semiconductors offer higher Seebeck coefficients than metals, which are typically around (1-10) $\mu V \cdot K^{-1}$. Semiconductors can exhibit either electron (n-type, negative thermopower) or hole (p-type, positive thermopower) conduction, but it is necessary to dope with either donor or acceptor states to allow for extrinsic conduction [12].

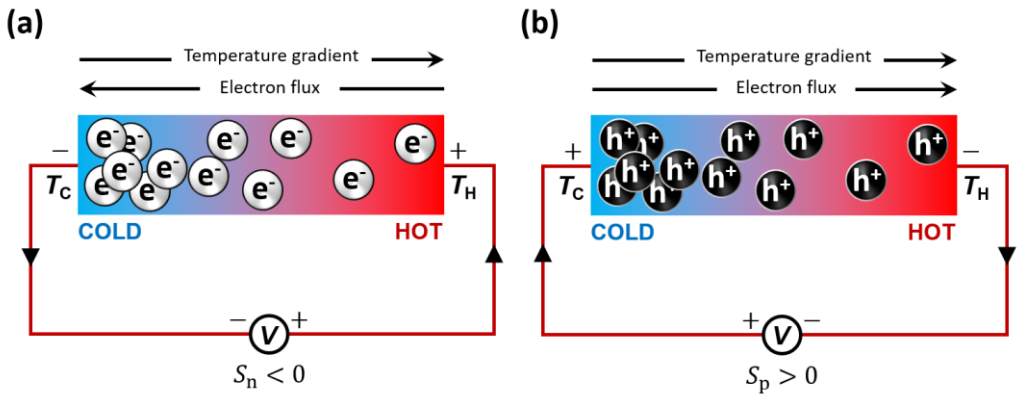

Figure 3. Seebeck effect in an n-type **(a)** and p-type **(b)** semiconductor material, measured in an open circuit.

The most common way to measure the Seebeck coefficient, is with an open circuit (**Figure 3**), where the current density is zero, resulting in charge accumulation near the cold edge, and S can be expressed by

$$\Delta V = -S\Delta T\,, \tag{2}$$

where $\Delta T = T_{\mathrm{H}} - T_{\mathrm{C}}$ is a small temperature difference between the hot (H) and cold (C) edges, with $T_{\mathrm{C}} < T_{\mathrm{H}}$, and ΔV is the generated electrical potential difference [9].

Correspondingly, the Peltier effect (1834) consists in the release and absorption of additional heat when an electric current is forced across the materials and is quantified by the Peltier coefficient (Π) through the relation

$$\dot{Q}_{\mathrm{P}} = \Pi I\,, \tag{3}$$

where $\dot{Q}_{\mathrm{P}}$ is the heat released or absorbed per time Δt at the junction and I is the electric current flowing through the junction [9].

Finally, the amount of exchanged heat is proportional to both the electric current and the temperature gradient, and their mutual direction determines if the heat is absorbed or released, named the Thomson effect (1851), and is expressed by the Thomson coefficient ($\mathcal{K}$), expressed by

$$\mathcal{K} = \frac{\dot{q}_{\mathrm{T}}}{\mathbf{j}\cdot\boldsymbol{\nabla}T}\,, \tag{4}$$

where q_{T} is the absorbed or released heat per unit of time [9]. The Thomson effect connects both the Seebeck and Peltier effect [9], for which William Thomson derived

$$\mathcal{K} = T\frac{\mathrm{d}S}{\mathrm{d}T} \tag{5}$$

and

$$\Pi = ST\,. \tag{6}$$

The dimensionless thermoelectric figure of merit of a material [13] is the fundamental parameter used to compare different thermoelectric materials at a given temperature. ZT equates the relation between the electronic transport and thermal transport, given by

$$ZT = \frac{S^2\sigma}{\kappa}T\,, \tag{7}$$

where κ is the thermal conductivity, which is the sum of the electronic (κ_e) and lattice (κ_l) thermal conductivities. Traditional thermoelectric materials operating at room temperature (300 K) show an average $ZT \approx 1$ [14].

The thermoelectric Power Factor (PF), given by

$$PF = S^2\sigma T\,, \tag{8}$$

is crucial to evaluate the performance, and while it is also sometimes used as a quantifier, where the thermal conductivity is not considered, it offers its own limitations [7,12].

The typical thermoelectric junction (**Figure 4**) consists of a p-type and n-type semiconductor and a heat sink that absorbs heat from the hot side and dissipates heat related to the cold side. An electric current is generated when two closed circuit junctions of dissimilar materials are at different temperatures.

The efficiency of a thermoelectric junction (η, in %) is derived from the Carnot efficiency and is expressed by

$$\eta = \frac{W}{Q_{HC}}\,, \tag{9}$$

where W is the generated electric power and Q_{HC} is the heat flow from the hot side (heat source) to the cold side (heat sink) [12,15,16]. η is directly related to the figure of merit, obtaining

$$\eta = \frac{T_H - T_C}{T_H}\cdot\frac{\sqrt{1+Z\bar{T}}-1}{\sqrt{1+Z\bar{T}}+\frac{T_C}{T_H}}\,, \tag{10}$$

were T_H and T_C are the highest (hot side, heat source) and lowest (cold side, heat sink) temperatures and $\bar{T}$ is the average absolute temperature at which the device is operating, given by

$$\bar{T} = \frac{T_H + T_C}{2}. \tag{11}$$

Taking equations **(7)** and **(11)**, the thermoelectric efficiency can be established by

$$\eta = \frac{T_H - T_C}{T_H} \cdot \frac{\sqrt{1 + \frac{S^2\sigma(T_H + T_C)}{2\kappa}} - 1}{\sqrt{1 + \frac{S^2\sigma(T_H + T_C)}{2\kappa}} + \frac{T_C}{T_H}}. \tag{12}$$

Thermoelectric modules typically generate power in the range of (1 to 125) W, with modularly enhancing power to approximately 5 kW, and operate in two modes: a TEG generates electricity from a temperature difference, based on the Seebeck effect (**Figure 4(b)**); while a Thermoelectric Cooler (TEC) converts a direct current into a temperature difference, based on the Peltier effect (**Figure 4(a)**) [4].

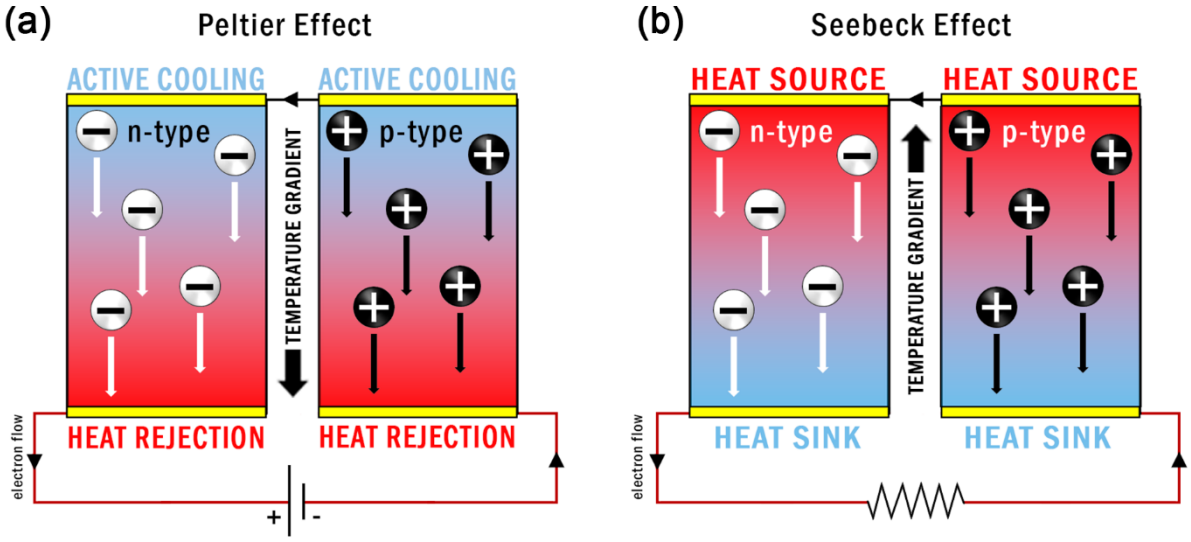

Figure 4. Peltier effect **(a)** and Seebeck effect **(b)** of a conventional thermoelectric device for Cooling and Power Generation, respectively, using n- and p-type semiconductors.

One of the first commercial TEGs, based on ZnSb thermocouples was built in 1947 [17], while TECs were introduced in 1954 [18]. Radioactive Thermoelectric Generators (RTGs), invented in 1954 [19], use the Seebeck effect to convert heat released by the decay of a radioactive material into electricity. RTGs are ideal for use in remote and harsh environments and enabled the launch of the Navy Transit 4A, the first spacecraft equipped with a RTG, to orbit Earth as a navigational satellite in 1961.

Further advancements in the thermoelectric sector were steered by the development of nanotechnology, in hopes of increasing energy conversion efficiency and ZTs. Today's worldwide energy issues provide the opportunity to combine TEGs with conventional engines to reduce heat-related energy

losses. In particular, scaled-down generators, such as micro-thermoelectric generators (μTEGs), are designed to operate at room temperature to substitute typical batteries in low power electronics [20,21].

The current challenge stands in increasing performance, reducing fabrication cost and increasing sustainability, but the range of application possibilities of thermoelectric technology is seemingly unlimited.

1.3. Transparent Thermoelectrics

The continued development of thermoelectrics continues to rise (**Figure 5**). More recently, transparent or semi-transparent devices that use thermoelectric effects has seen interesting research over the years.

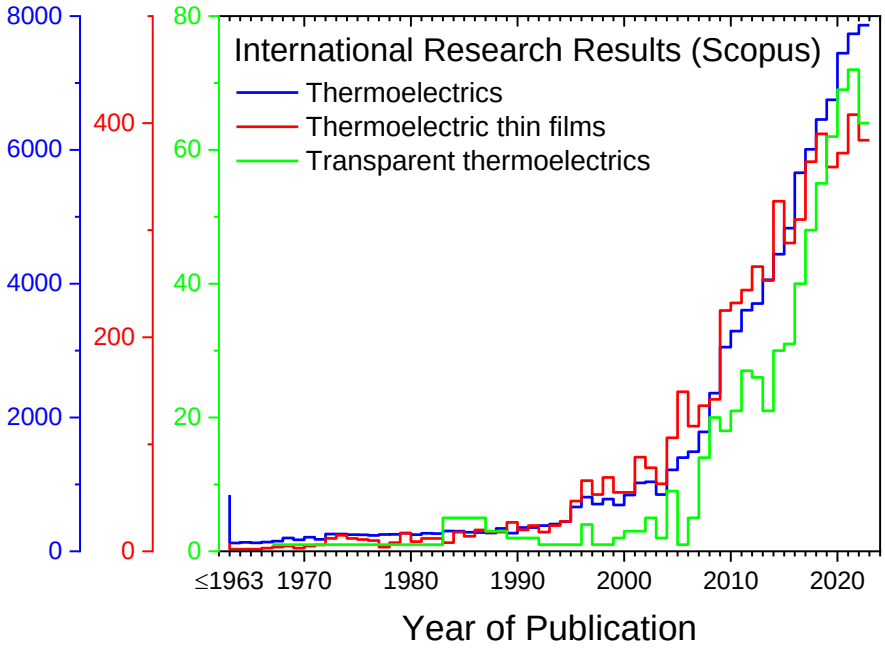

Figure 5. Research in thermoelectrics, thermoelectric thin films and transparent thermoelectrics over the years, a total of 99647, 6042 and 673 results, respectively, obtained through data from *www.scopus.com*, included in tittles, abstracts or keywords, considered from 1875 to 2023 at an international level.

Table 1 highlights a few transparent or semi-transparent devices recently investigated. Klochko et al. (2019) [22] developed a thin film-based TEG for low power/wearable devices due to absorption of low-potential heat. The device contains a flexible p-type CuI thin film with a transmission of (60 to 85) % in the visible spectral range, output power of 17.1 $\mu W \cdot m^{-2}$ at a temperature difference $\Delta T = 35$ K and a ZT of 0.21 at 300 K. A semi-transparent ZnO/FTO solar nTEG for energy efficient glazing was also

developed [23]. Yang et al. (2017) [24] also developed a transparent and flexible thermoelectric thin film based on CuI with a $ZT = 0.21$ at 300 K.

Table 1. Transparent and semi-transparent devices that use thermoelectric effects.

Reference	Material	Application	Transparency
[25]	ZnO:Al thin film	Functional sensor	Transparent
[26]	ITO thin film	TEG	Transparent
[27]	TiO_2 thin film	Photoelectric/photothermal	Transparent
[24]	CuI thin film	Low-power TEG	Transparent
[28]	Bi_2Te_3	TEG	Semi-transparent
[22]	CuI thin film	TEG	Semi-transparent
[29]	GZO–CuI p–n module	TEG	Transparent
[23]	ZnO nanorods	nTEG	Semi-transparent

Karimov et al. (2020) [28] developed a semi-transparent thermoelectric cell (TEC) used for water heating. Koskinen and co-authors (2020) [25] developed a functional sensor material, where each contact pad allows the probing of the Seebeck voltage at that location with respect to the reference contact located at the edge of the sample. A hybrid device that combines photoelectric and photo-thermal methods in one cell to fully utilizing solar energy was developed by Wang et al. (2011) [27]. Coroa et al. (2019) [29] developed a transparent flexible device consisting of a (1 × 1) cm^2 GZO–CuI p–n module that generates a maximum $V = 0.43$ mV and $I = 1.16$ μA for a $\Delta T = 20$ K. The authors reported ZT values of 0.29 and 0.07 for p-type CuI and n-type GZO, respectively.

Because the ZT (equation **(7)**) remains the main indicator of thermoelectric performance, the materials must have a high Seebeck coefficient, high electrical conductivity and low thermal conductivity. This relation is challenging and requires very fine tuning of the production process parameters [30–32]. The higher the Seebeck coefficient, the greater the electromotive force generated per unit of temperature. Hence, the greater the current, the greater the output electrical power supplied. The higher the electrical conductivity, the less work performed on the electrons inside the device, meaning less energy loss through the Joule effect and more current is generated. Finally, the lower the thermal conductivity, the greater the thermal difference for the same heat flow and a higher generated potential difference.

Transparent conducting oxides (TCOs) are electrically conductive materials with high transparency in the visible range. TCOs have been investigated for a wide range of applications in optoelectrical devices including photovoltaics, displays, optoelectrical interfaces and window glass

technologies [33,34]. Touch-screen and solar cell applications require TCO coatings with high transparency (transmissivity $>$ 85 %, averaged from 400 to 1100 nm), combined with useful electrical conductivity ($>$ 50 $\Omega^{-1}\cdot cm^{-1}$) [34,35].

The most utilized TCO, tin-doped indium oxide (ITO), although easy to fabricate and possesses good conductive properties, presents scarcity, poor chemical stability in hydrogen atmosphere and toxicity. Potential alternatives to ITO include doped ZnO and SnO_2 but there is a huge interest to explore new materials [33,36,37]. IDTechEx's research [38] forecasts that transparent conductive films alternative to ITO will reach a combined market value of $220 million and new market opportunities will grow to represent nearly 45 % of the total TCF market in 2027. On the other hand, the market for thermoelectric energy harvesters is estimated to reach over $1.5 billion by 2028 [39]. A good opportunity presents itself for using TCOs as thermoelectrics.

In **Table 2**, Spooner et al. (2020) [40] used hybrid density functional theory to study the thermoelectric efficiency of known TCOs and analyse their limitations as thermoelectrics. The authors demonstrated that reducing the lattice thermal conductivity ($<$ 4 $W\cdot m^{-1}\cdot K^{-1}$) is vital for improving the thermoelectric efficiency of a TCO. It was found to be the most variable parameter, making it a decisive factor in the ZT. This is due to the very long phonon mean free paths, making them strong candidates for nano structuring to increase performance. This reveals that the PF, sometimes used as an alternative screening metric for ZT, is not enough to evaluate the thermoelectric efficiency of these materials.

Table 2. Seebeck coefficient (S), electrical conductivity (σ), electronic and lattice thermal conductivity (κ_e and κ_p) and thermoelectric figure of merit (ZT) for six TCOs with thermoelectric properties at 800 K in the study by Spooner et al. [40].

Material	S ($\mu V\cdot K^{-1}$)	σ ($\Omega^{-1}\cdot cm^{-1}$)	κ ($W\cdot m^{-1}\cdot K^{-1}$)		ZT
			κ_e	κ_p	
$BaSnO_3$	-230	127	0.19	1.4	0.3
CdO	-204	150	0.23	3.0	0.2
SnO_2	-243	159	0.20	13.0	0.1
ZnO	-203	95	0.14	17.4	0.04
SnSe	350	100	0.05	0.3	1.9
$AgPb_{18}SbTe_{20}$	-370	200	1.1		2.1

Although a wide range of thermoelectric materials had been explored, a high ZT value remains associated with bulk materials which, due to their small band-gap, tend to be optically opaque [41,42].

While TCOs are well understood and widely used commercially, their thermoelectric performance is far below that needed for industrial deployment [40], making them best suited for low-power applications.

Since the field of optically transparent TCOs still has a lot to be explored, this work aims to develop a transparent thermoelectric that is, in terms of thermoelectric properties, as efficient as other known TCOs, but is more environmentally friendly and is less expensive to produce, while being able to harvest thermal energy from the environment.

1.4. Thin Film Deposition

Transparent thermoelectrics can be fabricated in the form of thin films (**Figure 5**) and will be the focus of this work. Thin films have been used for over half a century and have become an intrinsic part of everyday life, by depositing atoms/molecules/ions of a material on a substrate, with thicknesses typically less than several micron-meters, but their properties often differ radically from bulk materials and are greatly influenced by the fabrication conditions [43,44].

The method of choice to deposit thin films for a specific application is not always obvious, nonetheless, the typical methods can be divided in two major groups: Physical processes, composed of the Physical Vapour Deposition (PVD) processes; and Chemical processes, encompassing the Chemical Vapour Deposition (CVD) processes and chemical solvent deposition. The importance and increased attention given to PVD and thin film technology research over the years is emphasized in **Figure 6**.

In PVD processes, particles of the material are vaporized by a physical process, either by thermal evaporation (resistivity heating or energetic electron beams) or sputtering (bombardment with energetic particles) [43,45–47]. The particles (now in vapour form) are then transported to the substrate through a low pressure gaseous environment, and deposited by condensation in the form of a thin film [48–50].

The ability of these types of atomistic deposition process to produce high-quality, uniform, durable and functional metal, alloy, semiconductor and insulator thin films [45,46], justifies their use in a wide range of applications, such as bio-compatible sensors for medical applications, decorative and/or hard coatings, functional multilayers with optical and microelectronics purposes, among several others [44,51–54]. Furthermore, thin films can be grown on temperature sensitive substrates, such as polymers, conceding the flexibility and simplicity of automating the process [55,56].

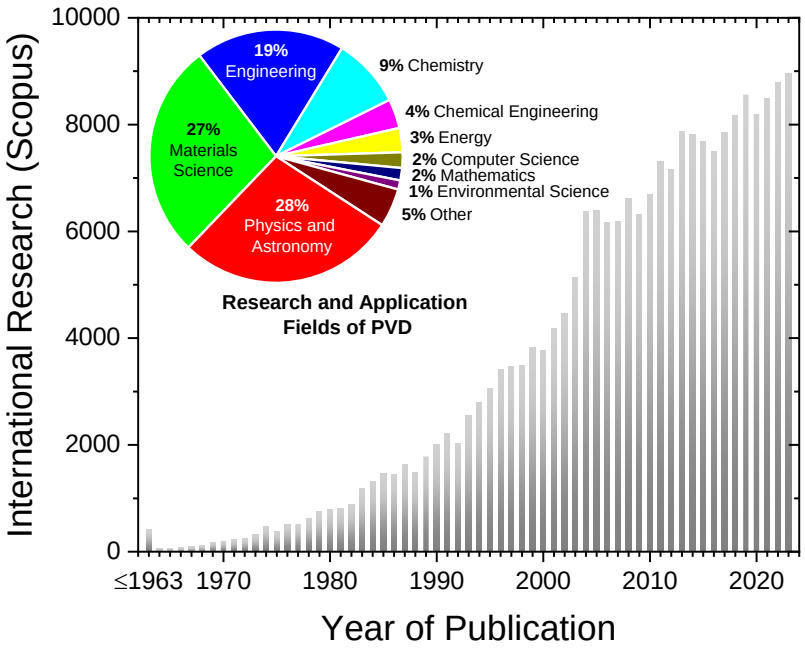

Figure 6. Research in PVD processes (*grey*) over the years, obtained through data from *www.scopus.com*, with a total of 213387 results, included in tittles, abstracts or keywords, considered from 1870 to 2023 at an international level. Pie Chart relates to the Research and Application fields of PVD processes.

1.5. Objectives

From an environmental and social point of view, the main goal of this work is the development of a clean and environmentally sound thermal energy harvesting technology. The focus is the preparation, characterization, optimization and application of thin films of Nb-doped TiO_2. In ideal settings, the proposed technology is able to generate electrical energy through a thermal difference in the environment and can replace current energy generating practices that involve more hazardous and polluting methods and integrate in heating/cooling processes.

This dissertation has greatly benefited from a cooperation between Portugal, University of Minho (UM), Germany, Karlsruhe Institute of Technology (KIT) and German Electron Synchrotron (DESY), and Spain, Institute of Materials Science of Barcelona (ICMAB). The majority of the work was done at the Centre of Physics of Minho and Porto Universities (CF-UM-UP), campus of Azurém, Guimarães.

This work follows the development of an optically transparent electrically conductive, thermoelectric thin film that is inexpensive to produce, non-toxic, durable and applicable in a variety of thermoelectric devices. To perform the cationic doping of TiO_2, Nb-doped TiO_2 thin films were sputtered from an alloy target in reactive mode and thermally annealed. A plethora of characterization techniques

were used to study the composition, microstructure, electric, thermal, thermoelectric and optical properties of these films.

The optimization of the processing conditions define the first set of objectives, where the thin films must be transparent, electrically conductive, thermally resistive and possess thermoelectric properties.

I. Effect of doping on TiO_2 with (1 to 5) at.% of Nb.

II. Optimization of the film production parameters through reactive magnetron sputtering, such as the deposition time, reactive gas (O_2) flow, temperature and target current density.

III. Effects of annealing and/or heat treatments processes on the Seebeck coefficient, optical properties and electrical properties of the thin films.

IV. Produce thin films with low surface roughness and with a thickness of around (100 to 300) nm, optical transparency above 70 %, Seebeck coefficient values in the range of 200 $\mu V \cdot K^{-1}$, electrical resistivity lower than 10^{-2} $\Omega \cdot cm$ and thermal conductivity below 2 $W \cdot m^{-1} \cdot K^{-1}$.

V. Obtain a thermoelectric power factor of around 350 $\mu W \cdot K^{-2} \cdot m^{-1}$ and figure of merit close to 0.1, making these films ideal for energy harvesting applications.

The second set of objectives seeks to understand what is happening in the grain boundaries of the thin films through the Atom Probe Tomography (APT) technique, which was done at the KIT. This understanding involves monitoring of segregation of host and dopant ions, oxide phases development, electron and phonon scattering mechanisms, and enables the fine tuning of the production method of the thin films and further the relation between the production parameters and the properties of the thin films. This method does not yet exist in Portugal, but its role in understanding the role of doping in the properties of these materials is undeniable.

VI. Attain proficiency in the technique of APT, aptitude with the hardware and software, be able to prepare and analyse a variety of samples and efficiently interpret the resulting data.

VII. With the use of APT, understand the role of the grain boundaries and dopants in the properties and further optimization of the produced thin films.

Finally, the last objective is to envisage a working thermoelectric device prototype in which to apply the developed transparent thermoelectric thin films. The thin films will be integrated into a thermoelectric device.

VIII. Design of a working prototype using the developed films on a thermoelectric and/or TCO module device.

1.6. Dissertation Structure

The dissertation is divided into 8 chapters, in order to provide a logical sequence to understand the development of the deposition of TiO_2:Nb thin films, their characterization and consequent application. Some chapters are based on collaborative papers published in peer-reviewed international journals, in the process of submission, and/or in dissertation works.

CHAPTER I. Introduction introduces the topic of the thesis, giving some contextualization, motivation and main objectives of this work. This chapter also offers an overview of the literature, introducing important concepts and giving insight on the main topics of this study and the current state of the art of transparent thermoelectrics.

CHAPTER II. Materials and Methods introduces the materials and experimental fabrication and characterization techniques used throughout this work, while offering contextualization based on the state of the art.

In Chapters III to VII, the results of material synthesis, characterization and application are presented and thoroughly discussed, resulting in the fine-tuning of the production process parameters.

CHAPTER III. Influence of Niobium-doping studies the impact of Nb when doping TiO_2 thin films deposited by DC reactive magnetron sputtering, as a way to increase the thermoelectric properties of the thin films.

CHAPTER IV. Influence of the Oxygen Flow focuses on the effect of the Oxygen flow used during the production method on the properties of the TiO_2:Nb thin films.

CHAPTER V. Influence of the Deposition Temperature concentrates on the effect of the temperature during the sputtering process on the properties of the TiO_2:Nb thin films. Interest is also given to the anatase/rutile phase changes further aided by the post-deposition annealing.

CHAPTER VI. Morphology, Microstructure and Grain Boundary Characterization relates to the use of atomic tomography and spectroscopy techniques in ascertaining homogeneity and ion segregation inside the TiO_2:Nb thin films. The influence of the Oxygen flow during reactive sputtering and post-deposition annealing in the incorporation of Nb and atomic content variation is also studied.

CHAPTER VII. Application in a Thermoelectric Prototype focuses on incorporating the TiO_2:Nb film in a working thermoelectric prototype capable of generating electrical energy from a temperature difference. The mechanical properties are also presented and discussed.

Lastly, **CHAPTER VIII. Final Remarks and Future Work** gives an overall conclusion and final considerations of this thesis and discusses the possible future research perspectives.

CHAPTER II.

MATERIALS AND METHODS

2. Materials and Methods

This chapter follows the materials, fabrication methods and characterization techniques used throughout this work, providing a background and description of the experimental methodologies.

2.1. Titanium Dioxide

Titanium dioxide is one of the most stable and with the highest melting point (> 1700 °C) of the transition metal oxides [57]. Traditionally used as a white pigment, it quickly grew to incorporate a variety of fields and applications (**Figure 7**). The interesting structural, optical, electronic and photocatalytic properties of TiO_2 have been extensively documented in the literature [57–59], making it a very versatile material and an appropriate choice for this work.

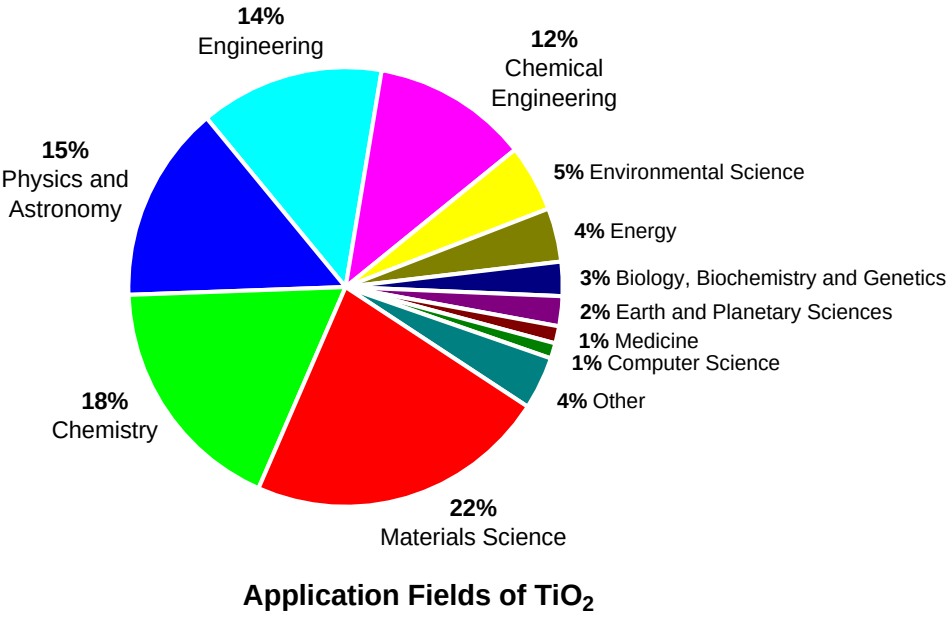

Figure 7. Research and Application fields of TiO_2, a total of 267379 results obtained through data from *www.scopus.com*, included in tittles, abstracts or keywords, considered from 1861 to 2023 at an international level.

TiO_2 naturally occurs in the five forms but the three most known crystalline phases, rutile, anatase and brookite, are displayed in **Table 3** and **Figure 8**. Rutile TiO_2 is thermally stable at high temperature,

has a higher density, higher refractive index (2.72, at a wavelength of 500 nm), than that of anatase TiO_2 (2.52), and has a high dielectric constant ($\geq$ 100), making it usable as a dielectric layer in capacitors for large-scale-integrated (LSI) devices [60]. Rutile is considered to be the most stable form of TiO_2, as on certain heating conditions both anatase and brookite irreversibly transform to rutile. Rutile is the simpler structure of TiO_2 and can be derived from a distorted hexagonal close packed arrangement of oxygen atoms, while anatase is derived from distorted cubic close-packed oxygen arrangements, both with half the octahedral voids filled by titanium atoms [57].

Table 3. Crystalline phases and respective parameters of TiO_2. Based on [37,57].

	Anatase	**Rutile**	**Brookite**
Crystalline Structure	Body-centred Tetragonal	Tetragonal	Body-centred Tetragonal
a **(Å)**	3.784	4.594	9.184
b **(Å)**	3.784	4.594	5.447
c **(Å)**	9.515	2.959	5.145
Z **(atom/cell)**	4	2	8
V_c **(Å^3)**	136.2	62.4	257.4
D **(g·cm^{-3})**	3.79	4.13	3.79
E_g **(eV)**	3.2	3.0	3.2

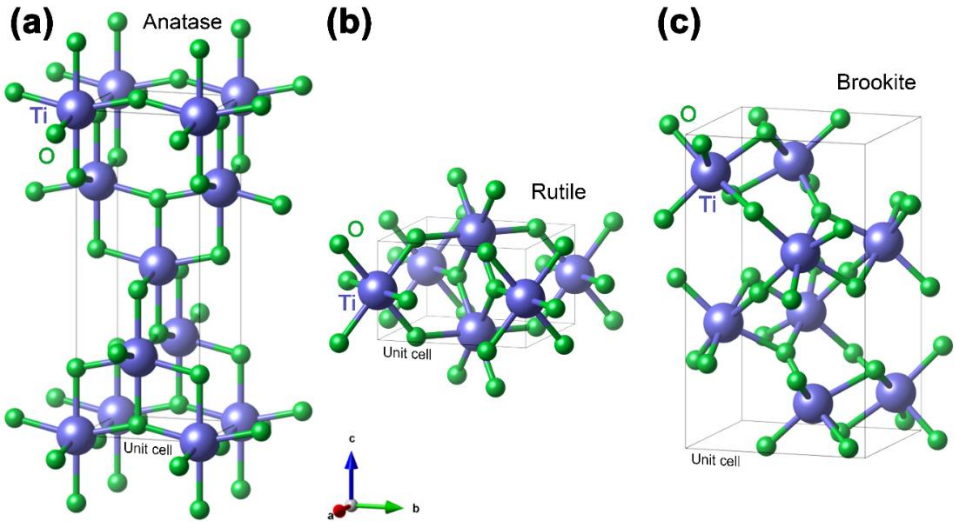

Figure 8. Crystalline phases and respective structures of TiO_2, anatase **(a)**, rutile **(b)** and brookite **(c)**.

The two main phases of TiO_2, anatase and rutile, have a bang-gap of 3.2 eV and 3.0 eV, respectively [61], which can be increased to up to 3.5 eV with cationic doping, due to the Burstein-Moss (**section 2.3.2**) effect [62,63]. A cationic doping of TiO_2 has been documented to improve its electrical

conductivity [64–68]. The optical properties of the films are strongly dependent on the dopant type and concentration [35,69–71]. From preliminary studies, an optically transparent thin film (< 100 nm) of Nb-doped TiO_2, shows great promise in this field [72,73].

The choice of Nb for a pentavalent dopant is two-fold. First, it is expected that heavier pentavalent and hexavalent ions added through doping, such as Nb, Ta, Mo or Bi in TiO_2, will inhibit the propagation of phonon vibration modes. The ionic radius of Nb^{5+} (0.64 Å) is slightly greater than that of Ti^{4+} (0.61 Å), thus suitable to create more phonon scattering, without introducing too much stress into the crystalline structure. This process will reduce the phononic component of the thermal conductivity and increase the thermoelectric power and ZT.

Second, when Nb^{5+} substitutes Ti^{4+} in the TiO_2 lattice below the level of solubility, it creates a charge unbalancing, resulting in an increase of charge carrier concentration and thus in electrical conductivity. Other pentavalent ions such as vanadium and tantalum have a larger ionic mismatch and are prone to produce other oxides that will compete and inhibit the formation of a stable TiO_2 doped film.

Liu et al. (2008) [70] calculated the electronic structure and optical properties of Nb-doped TiO_2 and undoped TiO_2. The authors found that for undoped TiO_2 the Fermi level is located in the gap, typical of an insulator, while for TiO_2:Nb the Fermi level shifts upward into the conduction band, showing a typical n-type metallic characteristic in its electronic structure.

Various authors reported on the transparent conducting properties of polycrystalline TiO_2:Nb anatase films, revealing that grain crystallinity and boundaries play key roles in conductive films [74–77]. Hitosugi et al. (2010) [37] deposited polycrystalline (0.06 at.%)Nb-doped TiO_2 films by sputtering at room temperature with of $6.4 \times 10^{-4}\ \Omega$ cm and transmittance of 60 % to 80 % in the visible range. Sato et al. (2008) [78] obtained transparent conducting TiO_2:Nb films utilizing direct current (DC) sputtering. Using Nb concentrations up to 6.4 at.% and post-annealing in a vacuum (400 °C at 6×10^{-4} Pa), the authors obtained resistivities of $1.3 \times 10^{-3}\ \Omega$ cm, carrier concentrations of 1.3×10^{21} cm^{-3}, with transparency of over 60 % to 70 % in the visible range.

There is little doubt on the suitability of TiO_2 as a TCO, but its role as a thermoelectric still has a lot to be explored.

2.2. Reactive Magnetron Sputtering

In this work, thin films of Titanium dioxide and Niobium-doped Titanium dioxide were produced by DC magnetron sputtering (also known as sputter ion plating) in a high vacuum custom sputtering equipment (schematised in **Figure 9**), available at the CF-UM-UP, Portugal. Magnetron sputtering has become established as the PVD process of choice for the deposition of a wide range of industrially important coatings [55]. It provides higher currents for relatively low voltage discharges, making it more accessible when compared to the basic sputtering mode, while lower pressures prevent gas phase collisions and scattering, increasing the deposition rates [55,56,79].

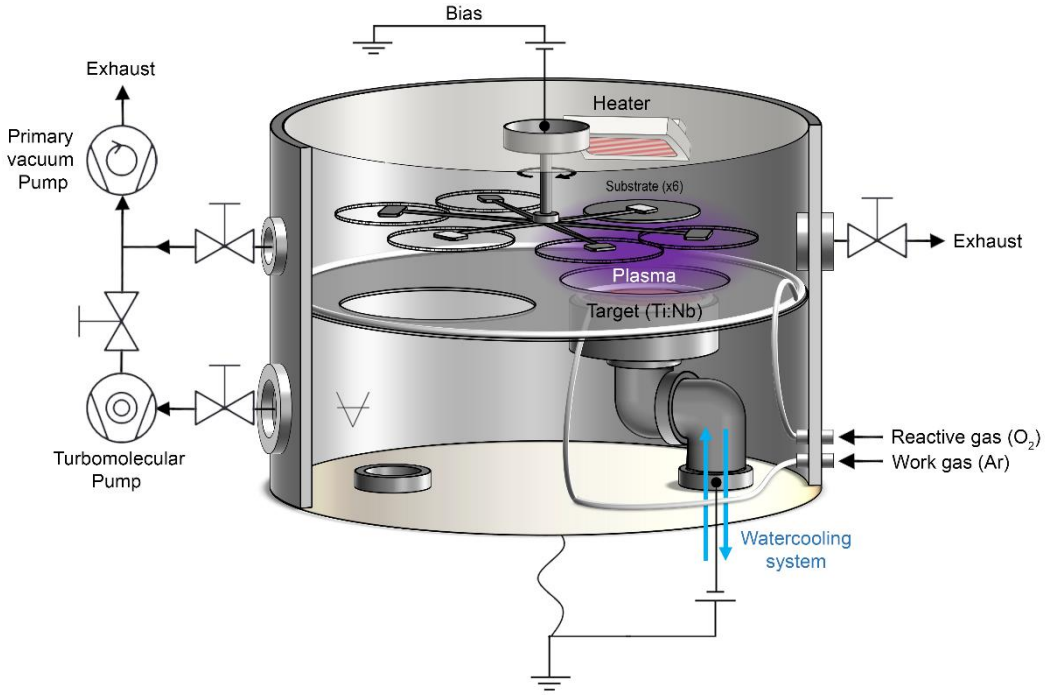

Figure 9. Schematic of the reactive DC magnetron sputtering system used to deposit TiO_2:Nb thin films in planar configuration.

Sputtering is a typical multiple collision process that consists in the ejection of particles from the surface of a solid material target due to the momentum exchange with energetic projectile particles impacting on its surface, usually ions of a noble gas [56,80]. A sputter deposition is conducted in a vacuum atmosphere (**Figure 9**), which is vital to increase the mean free path of the gas molecules and to reduce vapour contamination during the deposition process. A substrate holder (anode) is placed facing the target (cathode), to intercept the flux of sputtered atoms. A discharge voltage is applied between the electrodes, partially ionizing a gas (e.g. Ar) at low-pressure and originating a plasma [56].

The positively charged ionized gas particles (Ar^+ ions) are accelerated by the generated electric field towards the negatively charged cathode target. When the ions impact the surface atoms in the target with enough energy to overcome the surface binding energy, it results in sputtering and emission of atoms from the cathode material, as well as newly ejected (secondary) electrons [54,56]. The ejected atoms move through the plasma until they reach and get deposited onto the substrate. The energy transferred during the collision with the surface of the target will determine the number of atoms ejected from a target surface per incident ion, or sputtering yield (Y) [44,56,80,81]. Finally, the energetic secondary electrons are accelerated into the plasma, acquiring sufficient energy to ionize further gas atoms, making them the primary energy source to sustain the plasma [44,49,56,82].

In magnetron sputtering, the cathode is submitted to non-uniform electric ($\boldsymbol{\varepsilon}$) and magnetic ($\mathbf{B}$) fields to confine the movement of secondary electrons in the surrounding area of the surface of the target [83]. The electric field is established by the electric cover between the plasma and the cathode, making $\boldsymbol{\varepsilon}$ perpendicular to the cathode and increase with target surface approximation. The magnetic field lines have a circular symmetry between the poles, created by the magnets permanently positioned behind the target, at its central axis and along its outer edge. This makes $\mathbf{B}$ parallel to the target at unique points [47]. The $\mathbf{B} \times \boldsymbol{\varepsilon}$ drift force is thus parallel to the target and forces the secondary electrons to follow circular paths around the target surface, acting as an electron trap. This confinement of electrons closer to the cathode results in a high-density plasma sustained at lower pressures and considerably increases the ionization efficiency [79,84].

Magnetron sputtering can also be used in reactive mode by adding reactive gases (such as O_2, N_2, CH_4, etc.) together with the inert working gas, where they can chemically interact with the sputtered material and develop a complex compound on the substrate [54,84]. Throughout this pathway, the collisions with the other particles present in the plasma can change the energy, direction and momentum of the sputtered atoms. The flux of incoming particles, and their energies, will thus be essential to the crystalline structure and morphology of the growing film [84].

The Structure Zone Model (SZM) proposed by Thornton (2000) [85] and reviewed by Petrov and co-authors (2003) [86] highlights gas pressure and the homologous temperature[1] as important deposition parameters that can influence the microstructure and morphology of the deposited film [55,84,87]. The Extended Structure Zone Model (ESZM), introduced by Mahieu et al. (2006) [87] provides further insights into sputter deposited thin film growth. The structure (crystallographic orientation) and morphology of a

[1] The homologous temperature is characterized by the quotient between the substrate temperature (T_{dep}) and the melting temperature of the coating material (T_{m}).

film is influenced by the energy and mobility of both the arriving sputtered particles (adatoms) and other particles (photons, atoms, molecules, electrons and ions) [84,87].

In the case of this work, experimental details concerning certain deposition variables were already optimized in previous works using similar conditions [72]. A target of Ti(96)Nb(4) wt.% with 99.9 % of purity (**Figure 10**), fabricated by FHR Anlagenbau GmbH (Germany), with 10 cm of diameter, was used in planar configuration. The major drawback of the magnetron configuration is the heterogeneous erosion on the target, due to the electron confinement and the concentration of the plasma in a small region of the target area. Consequently, the sputtering of material occurs preferentially in a specific region of the target, leading to a formation of an extended and prominent "racetrack" or erosion trench (**Figure 10(b)**). For a standard planar magnetron configuration, the target material utilization is in general less than 30 % [56,88].

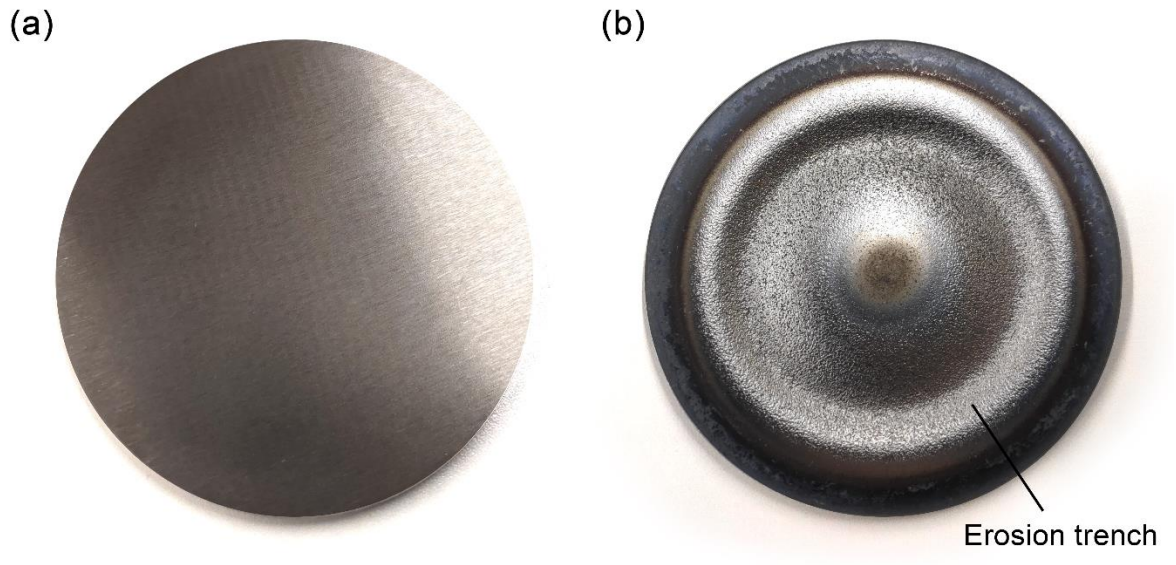

Figure 10. New (unused) **(a)** and used **(b)** targets of Ti(96)Nb(4) wt.% with 99.9 % of purity (FHR) with 10 cm of diameter.

The films were deposited on (76 × 26 × 1) mm^3 glass substrates from Normax Lda (Portugal), (10 × 10 × 0.5) mm^3 Si substrates, cut from P/B doped Si-wafer <100>, from Siegert Wafers GmbH (Germany) and (15 × 15 × 0.05) mm^3 Kapton® film. To maximize the adhesion at the film/substrate interface, the substrates were cleaned with isopropyl alcohol (2-Propanol) and acetone in an ultrasonic bath, for 15 min each, removing contaminants on the surface of the substrates that may arise during storage and handling [89,90]. The substrate-holders were mounted onto a rotating 6-position support

controlled by a motor (used either in continuous rotation or to exchange samples over the magnetron), with a target-substrate distance kept in the range of 6.5 cm to 10 cm.

The chamber was evacuated prior to the depositions with a primary rotary pump and a turbo molecular pump to achieve a base pressure of around 10^{-4} Pa. At this stage, prior to the deposition, an etching voltage of 500 V can be applied to the substrates, for 3 min, at a pressure of 1.8 Pa and in continuous rotation of the substrate holders. Research grade Ar with 99.999 % purity was used as working gas (50 sccm) to enable plasma formation. This process removes oxides and impurities possibly accumulated and retained on the surface of the substrates and creates atomic defects in the substrate, enabling better nucleation of the film during deposition.

A dummy deposition of (2 to 3) min for target cleaning (burn) was typically used in the first position of the substrate holder, followed by the deposition of one to five samples in a single batch. The target current was turned off between depositions to increase consistency and enable a precise control of the position and deposition parameters for the succeeding substrate holders. During a continuous deposition, the temperature inside the chamber inherently increases due to the plasma, which can be useful to further control the deposition temperature. Target current density was varied in the range of (3.2 to 12.7) mA·cm^{-2} and the deposition temperature up to 450 K (**Figure 11**). For all depositions, 40 sccm of Ar flow was used and a pulsed bipolar electrical potential was applied to the substrates (substrate bias), at 100 kHz of frequency, a 70 % work cycle at –60 V and 30 % reverse cycle at +16 V. This ensures the level of ion bombardment that will initiate nucleation of the adatoms on the film growth front. These deposition conditions enable an effective content of up to 2 at.% of Nb substitutional doping in the TiO_2 cell (**Figure A 1**) [72,91].

O_2 was used as the reactive gas with flow rates in the range of (0 to 16) sccm, with partial pressures in the range of (0.01 to 2) Pa, in order to avoid target poisoning and have films with a dense microstructure. One of the most important process parameters during reactive sputtering to obtain conductive oxide films is the control of the oxygen stoichiometry [37]. Okimura (2021) [60] obtained rutile TiO_2 thin films by sputtering at temperatures below 300 °C and showed that the rutile phase forms under conditions of higher currents in incident ion species, such as O^+, Ar^+ and Ti^+.

The cathode potential hysteresis curve (**Figure 11**) was obtained by varying the reactive O_2 flow, ascending and descending, using the same processing conditions as previously described, with 5 min of stabilization time for each step, using either a pure Ti or a composite Ti:Nb target in the usual configuration at 6.4 mA·cm^{-2}, 9.5 mA·cm^{-2} and 12.7 mA·cm^{-2}, corresponding to 0.5 A, 0.75 A and 1 A, respectively, applied to the target. The latter was chosen due to the higher voltage and broader curve,

enabling a more precise control of the O_2 flow. In this case, the metal mode is registered for oxygen flow rates below 3 sccm, while the oxide mode is achieved for oxygen flow rates above 8.5 sccm. The transition region seems to be between 6 sccm and 8 sccm, which will be important when discussing the results in the following chapters.

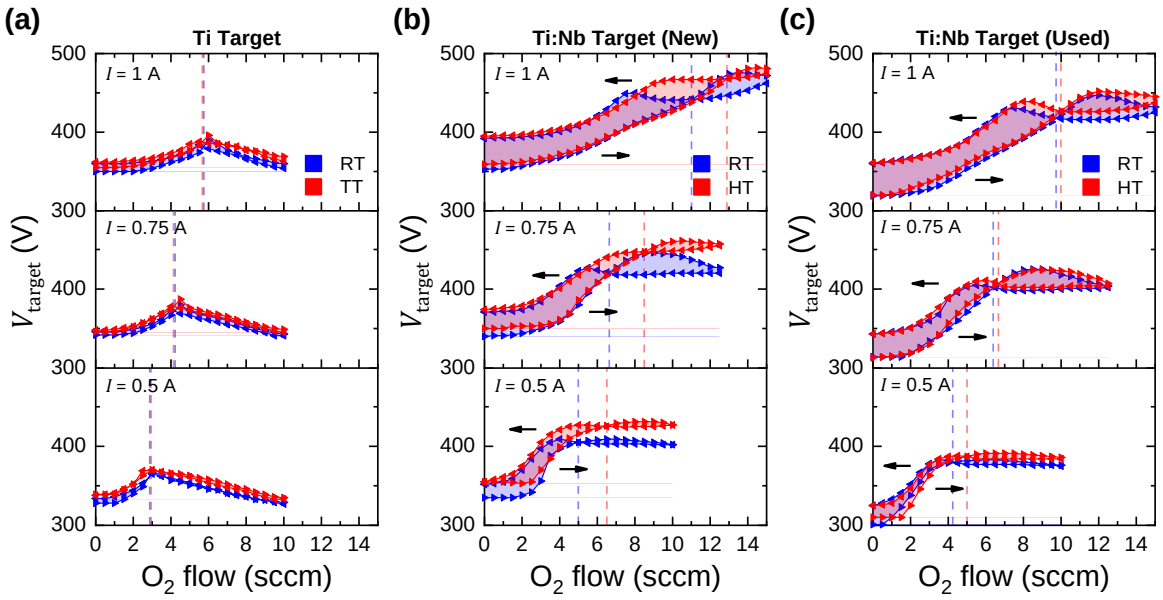

Figure 11. Hysteresis curves for increasing and decreasing O_2 flow during sputtering of a pure Ti target **(a)** and a new **(b)** and used **(c)** Ti(96)Nb(4) wt.% target, using 0.5 A, 0.75 A and 1 A applied to a 10 cm diameter target, at room temperature *(RT, blue)* and with heating applied atop the substrate *(HT, red)*.

Additionally, a bipolar pulsed power supply with a lower applied current was used in **Chapter 7** due to the need to reduce sample stress when sputtering a TiO_2:Nb layer on a microfabricated device. The films were deposited using 0.8 A of applied target current (current density of 10.2 mA·cm^{-2}) and alternating between 70 V and -292 V with a frequency of a 150 kHz (**Figure 91(a)**). The hysteresis curve is shown in **Figure 91(b)** and the experimental conditions are detailed in **section 7.3.1**.

Subsequently, several as-deposited TiO_2:Nb films were heat treated to enhance their microstructure and electrical properties [37,75,76,78,92], in a custom vacuum furnace at the CF-UM-UP, at 10^{-3} Pa. The temperature was increased from room temperature to 500 °C in 90 min and maintained at 500 °C for 1 h, followed by a natural cooling stage to room temperature for 6 h. The films deposited onto Kapton film (**Chapter 3**) were annealed in ambient pressure at a lower temperature of 400 °C for 1 h, as other authors reported on insulating films by annealing in air at 600 °C [37].

A considerable number of thin films were produced, but

Table 4 presents a summary of the samples chosen and presented throughout this work.

Table 4. Summary of samples, presented and discussed in their respective chapters.

	Conditions	Chapter III	Chapter IV	Chapter V	Chapter VI	Chapter VII
Substrate	Glass	☑	☑	☑	☑	☑
	Si	☑	☑	☑	☑	☑
	Kapton	☑	☒	☒	☒	☒
	APT coupon	☒	☒	☒	☑	☒
	Prototype	☒	☒	☒	☒	☒ / ☒ / ☑
	Glass + FTO	☒	☒	☒	☒	☒ / ☒ / ☑
Deposition	Heating	☑	☑	☒ / ☑	☑	☑ / ☑ / ☒
	I_{target} (A)	1	1	1	1	1 / 1 / 0.8
	t_{dep} (min)	5 / 30	1 – 5	5	27 / 5	5 / 60 / 360
	O_2 flow (sccm)	7	0 – 15	7	0 – 15 / 7	7 / 7 / 6.5
Annealing	10^{-3} Pa, 500 °C	☑ / ☒	☑	☑	☒ / ☑	☒ / ☒ / ☑
	P_{amb}, 400 °C	☒ / ☑	☒	☒	☒	☒

2.3. Characterization Techniques

A variety of techniques were used to characterize the morphology, composition, optical, electrical, thermal and thermoelectric properties of the sputtered thin films.

2.3.1. Morphology, Surface and Interface Analysis

The surface and cross-sectional morphology, homogeneity, composition, cation segregation and crystallographic structure of the thin films was evaluated by X-ray diffraction (XRD), X-ray reflectometry (XRR), X-ray photoelectron spectroscopy (XPS), X-ray absorption spectroscopy (XAS), scanning electron microscopy (SEM), energy-dispersive X-ray spectroscopy (EDX), transmission electron microscopy (TEM), time-of-flight secondary ion mass spectrometry (TOF-SIMS) and atom probe tomography (APT) (**Figure 12**).

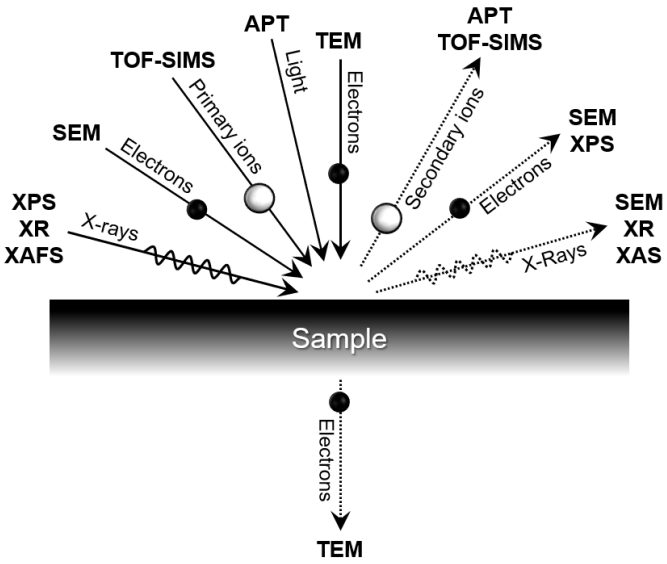

Figure 12. Schematic of the characterization techniques used for surface, interface and depth analysis and their respective types of incident *(solid arrows)* and outgoing *(dotted arrows)* radiation.

2.3.1.1. X-ray Diffraction (XRD) and Reflectometry (XRR)

XRD analysis was performed to investigate the crystallographic structure of the thin films. XRR analysis enabled the investigation of the chemical homogeneity, film thickness (for thin films with less than 50 nm of thickness), surface roughness and density.

The XRD and XRR measurements were done using a Bruker AXS D8 advanced Discovery diffractometer at the Materials Characterization Services of the University of Minho (SEMAT/UM), Portugal. The diffraction patterns were acquired in Grazing Incidence X-ray Diffraction (GIXRD), with incident angle of 1°, step of 0.02° and integration time of 1 s. CuKα radiation was used with a wavelength of 1.5406 Å. The software Fityk was used to analyse the XRD diffraction patterns. The weight fraction of rutile is obtained through the equation [93]

$$W_{\mathrm{R}} = \frac{A_{\mathrm{R}}}{A_{\mathrm{R}} + 0.884A_{\mathrm{A}}} \qquad \textbf{(13)}$$

where A_{R} and A_{A} are the integrated areas of the main rutile and anatase peaks, (101) and (110), for anatase and rutile, respectively.

The XRR patterns were analysed with the Bruker AXS Leptos software.

2.3.1.2. X-ray Photoelectron Spectroscopy (XPS)

XPS was used to evaluate the chemical composition, along with the valence state and binding energy of dopant ions, and as well as of the Ti and O ions. In XPS, soft X-rays (typically Al or Mg Kα radiation) excite and eject electrons from the inner shells or valence bands. The kinetic energy is then measured by a photoelectron spectrometer to obtain the binding energy of the ejected electrons [94,95].

The XPS experiments were performed using a Kratos Axis-Supra instrument equipped with monochromatic Al–Kα radiation (1486.6 eV), from the 3Bs Group (at the UM). Due to the non-conducting nature of the samples, it was necessary to use a co-axial electron neutralizer flood gun to minimize surface charging. Photoelectrons were collected from a take-off angle of 90° relative to the sample surface. The measurement was done in a Constant Analyser Energy mode (CAE) with a 160 eV pass energy and 15 mA of emission current for survey spectra and 40 eV pass energy for high resolution spectra, using emission currents of (15–20) mA. Charge referencing was done by setting the lower binding energy of the C1s hydrocarbon peak at 284.8 eV. The recorded experimental XPS spectra were fitted using the Unifit software.

2.3.1.3. X-ray Absorption Spectroscopy (XAS)

Temperature-dependent XAS was performed on TiO_2:Nb thin films to determine the coordination environment of the dopant ions (Nb) and their influence on the titanium oxide matrix. The X-ray absorption spectrum is typically divided in two regimes: the extended X-ray absorption fine-structure (EXAFS), used to determine the distances, coordination number, and neighbouring species, and X-ray absorption near-edge structure (XANES), used to determine the oxidation state and coordination chemistry.

Experiments were done in transmission and fluorescence modes at the P65 Applied XAS beamline [96] of the PETRA III storage ring at the Hamburg Synchrotron Radiation Laboratory and German electron synchrotron (HASYLAB/DESY), Germany. A set of powder samples (TiO_2, Nb_2O_5) was used for reference. The harmonic rejection was achieved by uncoated and Rh-coated silicon plane mirrors. Fixed exit Si(111) and Si(311) monochromators were used for the Ti and Nb K–edges, respectively. X-ray absorption spectra were collected using two ionization chambers in transmission mode, whereas passivated implanted planar silicon (PIPS) detector was used in fluorescence mode. The Oxford Instruments liquid helium flow cryostat was used to maintain the required sample temperature in the

range of 10 K to 300 K. For transmission measurements at the Ti K–edge, a stack of thin films deposited on Kapton was produced, with the number of layers giving the value of the absorption edge jump $\Delta\mu \approx 1$.

2.3.1.4. Scanning Electron Microscopy (SEM)

SEM was used to investigate the surface morphology and cross-section of the thin films, while EDX was used to study the surface composition. SEM is able to provide useful contrast imaging of the surface of a sample at nanometre lateral resolution, by electron absorption or emission [95].

The SEM measurements were performed with a FEI NOVA NanoSEM 200 at the SEMAT/UM. For cross-section imaging, the samples were cut with a diamond tip and fixed in the sample table with double-sided carbon tape.

2.3.1.5. Transmission Electron Microscopy (TEM)

TEM combined with EDX is an important tool not only to investigate the chemical composition of the TiO_2:Nb thin films, but also to determine the crystalline phase, domain sizes and respective crystallographic orientation, as well as dopant and host ion segregation to grain boundaries [95,97].

The experiments were conducted at the Advanced Electron Microscopy, Imaging & Spectroscopy (AEMIS) facility at the International Iberian Nanotechnology Laboratory (INL), Portugal. A planar view (parallel to the film-substrate interface) lamella was prepared by Focused Ion Beam (FIB) from a TiO_2:Nb thin film with approximately 200 nm of thickness deposited on a Si(111) substrate (**Figure 13**), using a Dual Beam FIB-SEM Helios NanoLab 450S equipped with a high resolution electron microscope (UHREM) field emission source (FEG)-SEM. Firstly, the region of interest (ROI) is covered with a protective layer of Pt (**Figure 13(b)**). The ion beam is then angled to erode trenches on either side of the ROI (**Figure 13(c)**), followed by a vertical cut at one of the edges, perpendicular to the initial trenches (**Figure 13(d)**). The cantilevered section is removed and attached to a carrier tip with Pt (**Figure 13(e)**). The last step involves thinning and polishing the lamella (**Figure 13(f)**) for analysis.

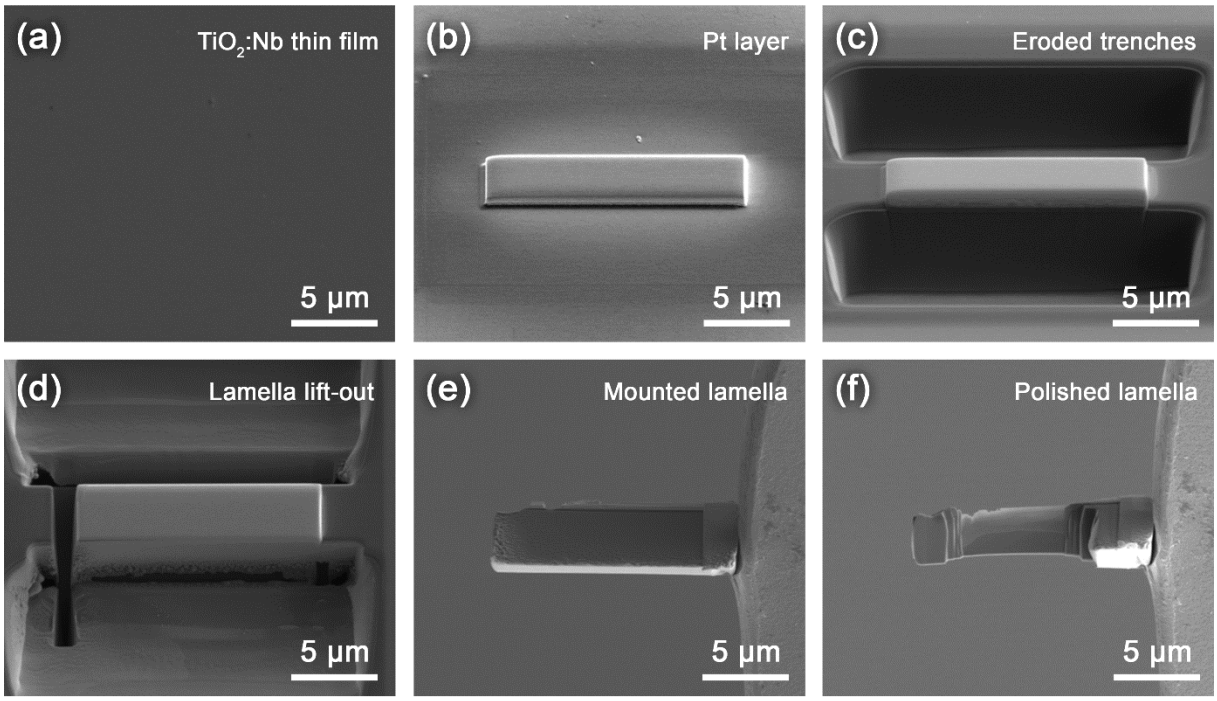

Figure 13. TEM sample preparation of TiO_2:Nb thin film **(a)** by FIB: deposition of a Pt protective layer **(b)**, sample erosion **(c)**, lamella lift-out **(d)**. Lamella polishing **(e,f)**.

High angle annular dark-field scanning transmission electron microscopy (HAADF-STEM), bright field scanning transmission electron microscopy (BF-STEM) and EDX were carried out using a FEI Titan G2 80–200 kV ChemiSTEM (Probe-Corrected) and a FEI Titan G3 Cubed Themis 60–300 kV (Double-Corrected) electron microscope, both equipped with a field emission gun (X-FEG), Cs probe corrector, and super X EDX detectors, operating at 200 kV.

2.3.1.6. Time-of-Flight Secondary Ion Mass Spectrometry (TOF-SIMS)

TOF-SIMS is a versatile technique and enables in-depth chemical identification to determine the bulk homogeneity of the films, surface and layer composition, as well as the composition of the atomic layers at the interface with the substrate [94,95,98,99].

TOF-SIMS analysis was performed at the Institute of Functional Interfaces at the KIT (IFG-KIT), Germany, on a TOF.SIMS 5 instrument (ION-TOF GmbH, Münster, Germany), schematised in **Figure 14**. This spectrometer (**Figure 14(a)**) is equipped with a Bi^+ cluster liquid metal ion gun (LMIG) as the primary ion source and a reflectron-type time-of-flight (TOF) analyser and operates at ultra-high vacuum (UHV) base pressure $< (5 \times 10^{-9})$ mbar. The LMIG contains a Bi reservoir that melts with increased

temperature and flows to the tip of a fine tungsten needle. A high-voltage extraction field is then applied at the tip of the needle (radius < 1 μm), resulting in primary ion emission. For high mass resolution the Bi^+ source was operated in high current bunched[2] (HCB) mode providing short primary ion pulses at 25 keV energy, a lateral resolution of approximately 4 μm, and a target current of 1.4 pA at 10 kHz repetition rate. The short pulse length of 0.8 ns allowed for high mass resolution.

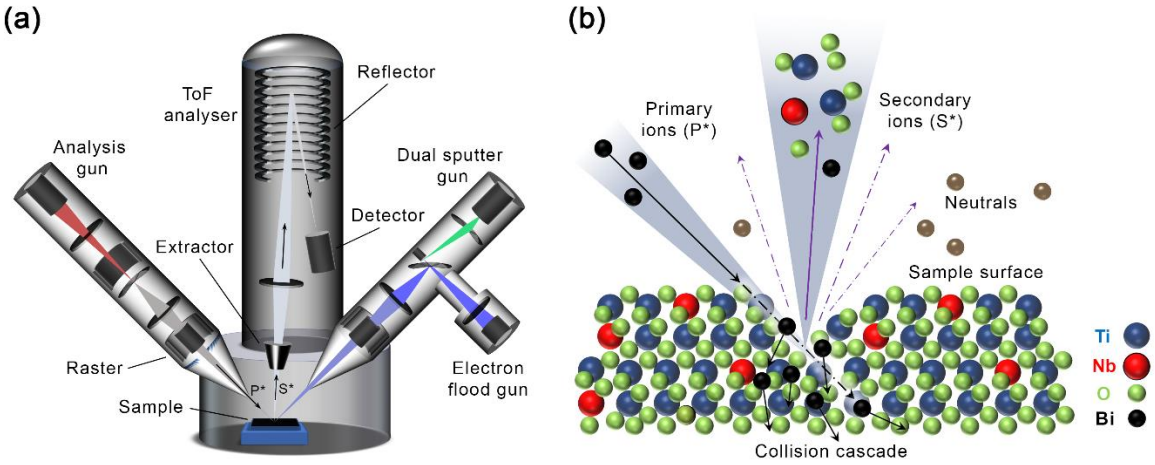

Figure 14. Schematic representation of a time-of-flight secondary ion mass spectrometer.

The primary ions bombard the surface of the sample, transferring energy to the target atoms by atomic collisions and creating a collision cascade (**Figure 14(b)**). When part of the energy is transferred back to surface it allows surface atoms to overcome surface binding energy. This process generates atomic and molecular secondary species, emitted with an angular distribution normal to the sample surface. Whilst most secondary particles emitted are neutrally charged, a small ratio comes off as either positive or negatively charged secondary ion, which are electrostatically accelerated by a high voltage potential and extracted into an analyser. Their mass to charge ratio[3] (m/z) is determined by measuring their TOF from the sample surface to the detector, also taking into account the kinetic energy and angular distributions, allowing to obtain composition, distribution and molecular information of the sample [94,95,99].

The static mode uses low primary ion dose and flux, and sputters only the top monolayer of the sample. The dynamic mode, employed in this work, uses an additional high flux beam that erodes the surface and yields elemental distribution over depth, making it a destructive technique. For depth profiling

[2] One of the three main primary ion beam guidance modes of operation in the TOF.SIMS 5 instrument. This mode enables high primary ion current with high mass resolution due to short primary ion pulses, but at a cost of lateral resolution.
[3] Different from the commonly used mass-to-charge ratio $\mathrm{m/Q}$, in $\mathrm{kg{\cdot}C^{-1}}$. A mass spectrometer acquires a mass spectrum, a histogram plot of ionic intensity (or counts) vs. mass-to-charge ratio (m/z, in Da) in a chemical sample.

a dual beam analysis was performed in fully interlaced mode, where the primary ion source is scanned over an area of (300 × 300) μm^2 (124 × 124 data points) and a sputter gun scans over a concentric field of view. For positive polarity profiles, O_2^+ erosion was applied, with 2 keV sputter energy, sputter range of (600 × 600) μm^2, target current of approximately 500 nA and at an incident angle of 45°. For negative polarity profiles, Cs^+ erosion at 2 keV, (500 × 500) μm^2 and target current of approximately 100 nA was used. The use of these ions affects the matrix of the sample surface, changing the yield of the secondary ion. O_2^+ enhances the ionization yield of the electropositive species, whereas Cs^+ enhances that of negatively charged ions.

Secondary ion intensities are plotted over sputter ion fluence as a measure for depth and can be calibrated if the thickness of the sample in known. Since the data acquisition is fast in respect of the observed erosion speeds, 25 data points were binned for plotting. Note however that this scale is not linear if different materials with different erosion rates / sputter yields are analysed.

2.3.1.7. Atom Probe Tomography (APT)

In order to quantify the cation segregation, as well as to study the morphology of the grain boundaries, APT was employed.

APT is currently the only technique able to map out the spatial distribution of atomic species in a three-dimensional (3D) image at near atomic scale, providing unique information about nanoscale structures and composition. APT enables the study of microscale and nanoscale features, like grain sizes[4], precipitates, chemical gradients and segregations on structural defects, related to the properties of materials [100–102].

A typical atom probe (schematized in **Figure 15**) requires a sample mount, a counter electrode with an aperture, and a detector, and can analyse target regions of interest with sample volumes usually around (100 x 100 x 100) nm^3. A high electric field of around 20 $V{\cdot}nm^{-1}$ is applied at the surface of a very sharp needle-shaped specimen by a standing positive voltage of V_{DC} = (3 to 15) kV and polarizes the surface atoms just below the point of atom evaporation. The evaporation of the surface atoms in initiated when a high frequency pulse (HF) is applied to the specimen, by either positive electrical pulses

[4] This is limited to grain sizes lower than ~ 1 µm, otherwise it is only possible to carry out the analysis within one grain. It is also dependent on sample morphology and measurement success, as it can be hard to distinguish orientations for highly textured materials or if the data is subpar.

(in the ns range, with a voltage of $V_{\mathrm{HF}} =$ (1 to 2) kV) or thermally induced pulses from laser irradiation[5] ($\leq$ ns) (**Figure 15(a)**), with subsequent ionization of the remaining surface atoms. Assuming the evaporation electric field ε is homogeneous across the surface of the sample and constant, it is given by the relation

$$\varepsilon = \frac{V}{k_{\mathrm{f}} r}, \tag{14}$$

where V is the total voltage (equal to $V_{\mathrm{DC}} + V_{\mathrm{HF}}$), k_{f} is the field reduction factor[6] and the tip apex is approximated to a sphere with a curvature radius $r <$ 100 nm [103]. The HF pulses are repeated periodically (typically 100 kHz to 200 kHz) and provide information regarding the sequence of evaporation events.

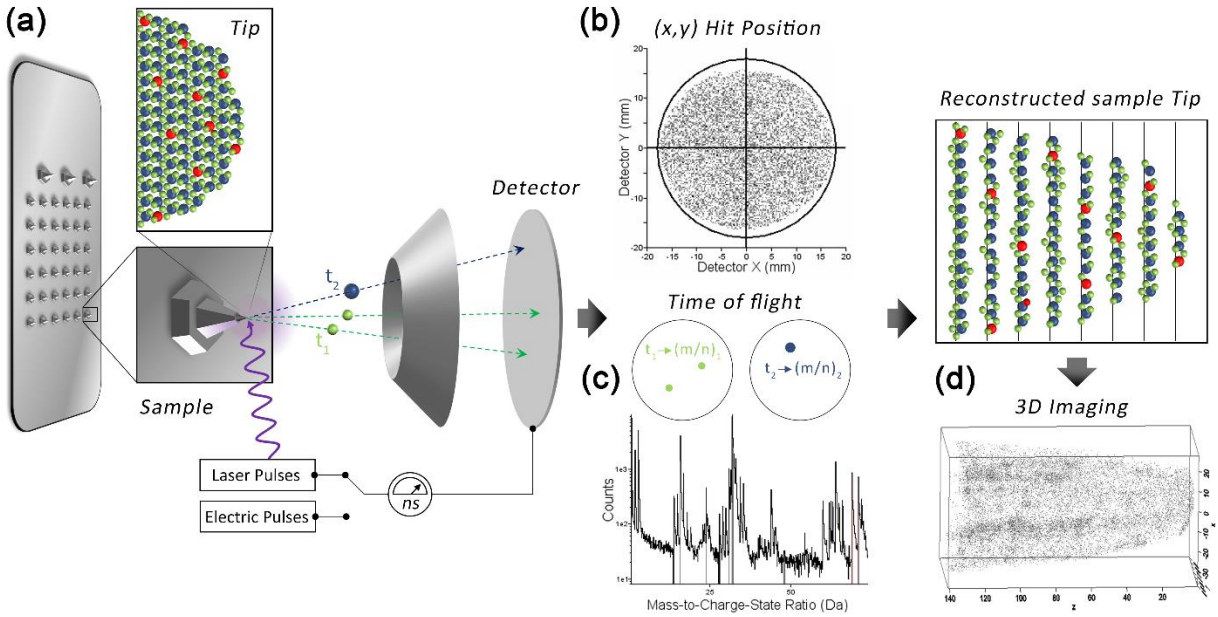

Figure 15. Schematic of the operation of a typical modern atom probe (based on the Local Electrode Atom Probe (LEAP). Atoms at the surface of a microtip are evaporated by field effect and are accelerated toward a detection system **(a)**, which determines (x,y) positions **(b)** and the chemical nature of each atom **(c)**, resulting in the mass spectrum of each element and 3D reconstruction of the sample **(d)**.

A position-sensitive counter electrode detector records the (x,y) hit position of individual ions in the sequence of evaporation events (**Figure 15(b)**). An evaporated ion first hits a microchannel plate (MCP) that converts it into an amplified flow of electrons. The electrons then travel through a delay line

[5] The formulation differs slightly in the case of thermally induced evaporation (laser mode), but further information can be found at [103].

[6] The field factor usually ranges from 3 to 8 and depends on the tip geometry and its electrostatic environment [103].

detector, creating electromagnetic pulses that are electronically processed to accurately pinpoint the original position of the ion in the sample [104].

The identity and z–position (depth into the specimen along its long axis) of an atom is determined by measuring the time (t_{TOF}) it takes the ion to travel the distance (L) from the specimen to the detector (typically 10 cm to 100 cm). During field evaporation, the potential energy of the surface atoms is converted into kinetic energy:

$$\mathrm{E_k} = \frac{1}{2} m v^2 \,, \tag{15}$$

where

$$v = \frac{L}{t_{\mathrm{TOF}}}, \tag{16}$$

where m is the mass and v the velocity of the resultant positive ions accelerated by the electric field [105]. This energy is proportional to the applied voltage and inversely proportional to the radius of curvature of the specimen tip.

The mass to charge ratio (m/z) of each evaporated ion is then obtained by

$$\frac{m}{z} = 2e \frac{V {t_{\mathrm{TOF}}}^2}{L^2}, \tag{17}$$

where z is the charge state of the ion, e is the electron charge and V is the total voltage applied to the sample [105].

A mass spectrum is built (**Figure 15(c)**) and a careful interpretation of various peaks permits the identification of chemical species. Using this information (TOF and lateral position), a reconstruction of the atomic positions in the specimen can be made, presented as two-dimensional or three-dimensional tomograms (**Figure 15(d)**). The data can be analysed in order to characterize both the solute ion distribution and solute partitioning to microstructural features [100–102].

The APT experiments were performed at the Karlsruhe Nano Micro Facility for Information-driven Material Structuring and Characterization (KNMFi) and Institute for Applied Materials – Materials Science and Engineering at the KIT (IAM-WK-KIT), Germany. APT tips can be prepared by either electropolishing[7] or FIB [104]. The process of tip preparation using FIB is typically done using the same lamellae lift-out technique performed for TEM samples (**Section 2.3.1.5**). A small wedge of material is carved out and

[7] Electropolishing is an electrochemical process that removes material from the surface of a needle-shaped sample and is used for conductive materials, such as metals and metallic alloys. The sample (anode) is sharpened by repeatedly moving it in and out of a wire loop (cathode) suspended in an electrolyte solution, while a DC or AC voltage is applied.

extracted from the sample, attached to a micromanipulator (using Pt) and mounted to a microtip (by attaching it with Pt and cutting a section loose from the micromanipulator), followed by milling. FIB can shape almost any material but is typically employed in highly resistive or semiconductor materials, thin films and site-specific features. The lift-out process is especially useful to study interfaces or features in a sample, but it is a time consuming and difficult process when dealing with thin films.

In the case of the samples prepared for this work, the thin films were deposited directly onto a specialized silicon coupon with prefabricated microtips from CAMECA® (**Figure 16(a)**) and sputtered with a protecting layer of either Ti or Ag. A detailed view of the microtip array tip configuration is illustrated in **Figure E 1**.

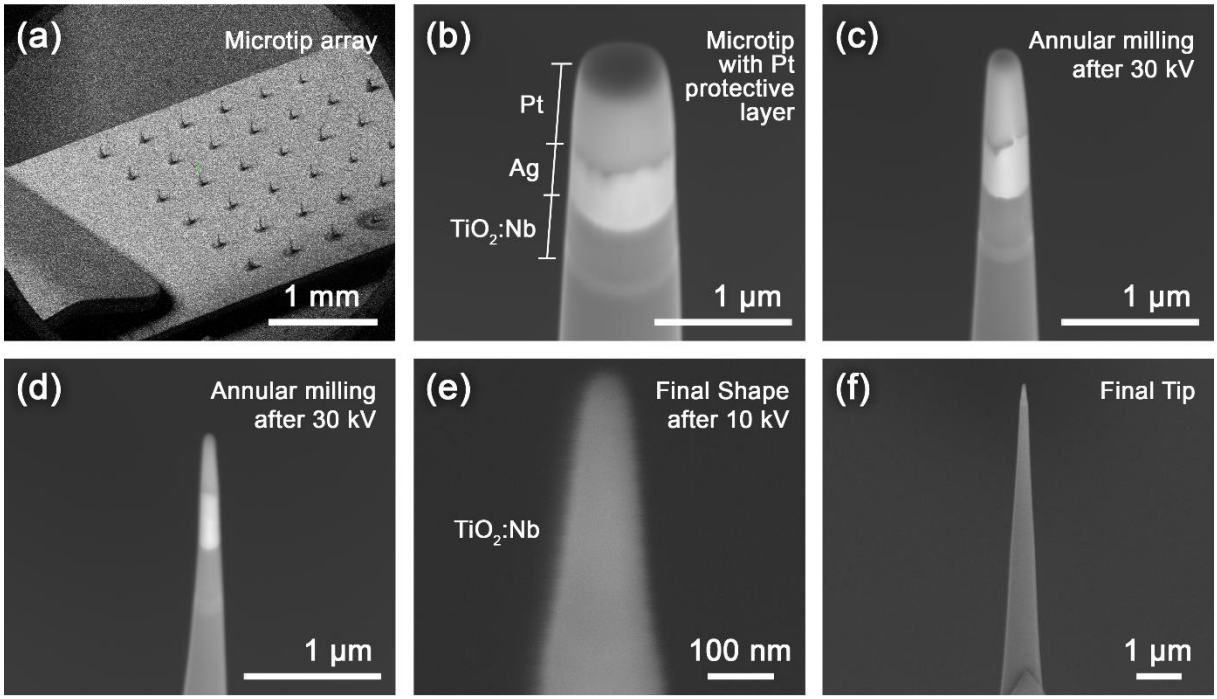

Figure 16. Si coupon with microtip array for APT analysis **(a)** and preparation of a microtip of TiO_2:Nb by FIB: deposition of a protective Pt layer **(b)**, annular milling with a 30 KV Ga-beam **(c,d)**, final milling step with a 10 KV Ga-beam and final tip shape **(e,f)**.

The tips were subsequently prepared for APT analysis using a Zeiss Auriga 60 Dual Beam FIB (**Figure 16**). A small layer of Pt was firstly deposited to protect the sample, followed by a multi-step milling process. The first annular milling stage uses a 30 kV Ga-beam, producing a cylinder around (1 to 2) µm in diameter (**Figure 16(b)**). The beam energy was progressively decreased to 10 kV together with the milling diameter (**Figure 16(c,d)**) to obtain a conical tip shape with an apex curvature radius $<$ 100 nm (**Figure 16(e,f)**).

The samples were then inserted into the UHV system (at a base pressure $< 10^{-9}$ Pa) and cooled to cryogenic temperatures (in the 20 K to 100 K range). The tips were measured in a local electrode atom probe (LEAP 4000X HR) in UV-laser mode (10 pJ to 30 pJ), with a pulse frequency of 100 kHz to 200 kHz, at a temperature of 40 K to 50 K and a detection rate of 0.2 % to 0.5 %. The data was reconstructed using the Ivas Ver. 3.6.14 software from CAMECA.

The initial geometric parameters, tip curvature radius r_0 and shank angle α_0 (half angle at the apex of the cone geometry), were obtained from the slope of the voltage curves or direct measurement by SEM imaging (**Figure 16(f)**). As the sample is progressively analysed, the change in the r of a sample is given by

$$r = r_0 + \frac{\sin \alpha_0}{1 - \sin \alpha_0} d \,. \qquad \textbf{(18)}$$

where d is the sample depth [103].

APT has its downsides, being a destructive technique, measurements cannot be repeated on the same sample tip. Difficulties can be encountered when simultaneous ions impact the detector, or when the spectral peaks (mass-to-charge ratio) of two different ions directly overlap. Furthermore, the field of view or the region of interest is quite limited and the analysed volume data quality is highly dependent on the tip shape (radius and shank angle), especially in pulsed laser experiments, where the sample is affected by the energy absorption and heat dissipation. Different atoms usually require different evaporation fields, which can introduce position-relative errors in a sample. It is difficult to relate the chemical information to the crystalline structure. The crystallographic directions of investigated phases and their local chemical composition are not just influenced by sample preparation, as trajectory aberrations of evaporated ions will introduce reconstruction artifacts, affecting their position and inter-distances and therefore shapes of microstructural features and overall tip [102,104].

Additionally, the sample tip inevitably blunts (radius increases) as layers are being field-evaporated, inducing a drop in the electric field and the detection rate. This leads to an increase of the standing voltage in order to maintain a constant electric field and to avoid fluctuations in the evaporation rate. This can introduce further strain in the sample, and when combined with highly resistive materials (as the material is harder to evaporate), can increase the probability of tip fracture for increased tip radii or at interfaces [103].

2.3.2. Optical Properties: Ultraviolet-Visible (UV-Vis) Spectrophotometry

The optical properties of the thin films were studied by Ultraviolet-Visible-near-Infrared (UV-Vis-NIR) spectrophotometry, which enabled the determination of transparency, thickness (in the case of transparent samples), optical band-gap energy and get an insight on the electrical properties.

The optical transmittance and reflectivity of the thin films deposited on glass substrates were analysed with Shimadzu UV-3600 Plus and Shimadzu UV-2501PC UV-Vis spectrophotometers at the CF-UM-UP, in the (250 to 2500) nm and (300 to 900) nm wavelength range, respectively. The samples were measured with a 2 nm slit and using the air as the baseline, for transmittance, and 20 nm slit and the calibration mirrors as the baseline, for reflectance, in a step of 1 nm.

The transmittance $\mathrm{T}(\lambda)$ and reflectance $\mathrm{R}(\lambda)$ spectra were fitted to a simulated model in the software SCOUT – Optical model, using four $\chi_{\mathrm{e}}(\lambda)$ models: the O'Leary-Johnson-Lm (OJL) model [106]; the Kim model [107]; the background dielectric constant model [108]; and the Extended Drude model [108].

The OJL model is used to describe the optical interband transitions, while the Drude model describes the susceptibility of the free charge carriers in semiconductors and metals. In the case of doped semiconductors, the free charge carriers respond to applied electric fields with frequencies in the infrared region. The Kim model is an extension of the simple harmonic oscillator model for vibrational modes. Similarly, the extended Drude model is used here instead of the classical Drude model due to the use of a frequency-dependent damping rate ($\Gamma_\tau(\omega)$), which makes sense when describing the scattering of free charge carriers by impurities in a semiconductor, given by the dielectric function:

$$\epsilon_\tau(\omega) = \epsilon_{\mathrm{optic}}\left(1 - \frac{\omega_{\mathrm{p}}^2}{\omega^2 + i\omega\Gamma_\tau}\right), \qquad \textbf{(19)}$$

where $\epsilon_{\mathrm{optic}}$ is the dielectric constant measured in the transparent spectral region below the interband absorption edge, Γ_τ characterizes the damping (inverse of the relaxation time τ), ω_{p} is the plasma frequency given by

$$\omega_{\mathrm{p}}^2 = \frac{n_{\mathrm{e}}e^2}{\epsilon_{\mathrm{optic}}\epsilon_0 m^*}, \qquad \textbf{(20)}$$

where m^* is the effective mass, ϵ_0 is the vacuum permittivity, n_{e} is the charge carrier density and e is the elementary electron charge [108].

The damping constant $\Gamma_\tau(\omega)$ smoothly changes between a low frequency bound ($\Gamma_{\tau,\mathrm{low}}$) and a high frequency bound ($\Gamma_{\tau,\mathrm{high}}$) [108], while the transition region is defined by the crossover frequency ($\Gamma_{\tau,\mathrm{crossover}}$) and the width parameter ($\Gamma_{\tau,\mathrm{width}}$) as

$$\Gamma_\tau(\omega) = \Gamma_{\tau,\mathrm{low}} + \frac{\Gamma_{\tau,\mathrm{high}} - \Gamma_{\tau,\mathrm{low}}}{\pi} \times \left[\tan^{-1}\left(\frac{\omega - \Gamma_{\tau,\mathrm{crossover}}}{\Gamma_{\tau,\mathrm{width}}}\right) + \frac{\pi}{2}\right]. \quad \textbf{(21)}$$

Assuming the optical measurements are equivalent to AC conductivity measurements of σ(ω) [108], the electrical conductivity can thus be estimated by

$$\sigma(\omega) = \frac{n_\mathrm{e} e^2 \sigma_0}{1 - i\omega\tau}, \quad \textbf{(22)}$$

where

$$\sigma_0 = \frac{n_\mathrm{e} e^2 \tau}{m^*}. \quad \textbf{(23)}$$

To obtain the transparency of the film layer, the transmittance was measured using the glass substrate as the baseline. The transmittance and specular reflectance (Rs) were averaged over 400 nm to 700 nm, equivalent to the visible wavelength range.

The optical band-gap energy (E_g) of the films was evaluated from Tauc plots of the absorption coefficient, α, against photon energy, $h\nu$, and extrapolating the linear fit of the plot to the photon energy axis, using the relationship

$$(\alpha h\nu)^{\frac{1}{n}} = \beta\left(h\nu - E_\mathrm{g}\right), \quad \textbf{(24)}$$

where for $n = 2$ for indirect permitted optical transitions, h is the Planck constant, ν is the phonon frequency and β is a constant of proportionality independent of ν [109]. E_g is then obtained as the intercept of the curve of $(\alpha h\nu)^{1/2}$ versus $h\nu$ in the high absorbance region. The absorption coefficient α can be determined from the relation [110]

$$\alpha = \frac{1}{d}\ln\left(\frac{1 - \mathrm{R}}{\mathrm{T}}\right), \quad \textbf{(25)}$$

where d is the film thickness, R is the reflectance and T is the transmittance.

It Is often the case that the measured optical band gap is higher than it would be expected. The Burstein-Moss effect describes the widening of the optical energy gap (by ΔE_g) in a doped semiconductor due to the accumulation of electrons (in the case of n-type) in the conduction band, expressed by

$$\Delta E_{\mathrm{g}} = \frac{\hbar^2}{2m^*}(3\pi^2 n_e)^{\frac{2}{3}}, \quad \textbf{(26)}$$

where $\hbar$ is the reduced Planck constant (equal to $h/2\pi$) [63].

2.3.3. Electrical Properties: Hall Effect

The electrical properties were evaluated through Hall effect measurements.

The samples were analysed using an Ecopia AMP55T HMS-5000 Hall Effect measuring system, equipped with a DC four-point probe apparatus in the Van der Pauw configuration, at the CF-UM-UP. The measurements were performed at room temperature under atmospheric pressure, with an applied magnetic field of approximately $B = 0.560$ T.

The Hall voltage (V_{H}) was determined, and the respective carrier concentration (n_{e}) and mobility (μ_{e}) were calculated with the equations

$$n_{\mathrm{e}} = \frac{|\mathbf{B}|I}{e|V_{\mathrm{H}}|d} \quad \textbf{(27)}$$

and

$$\mu_{\mathrm{e}} = \frac{1}{e\rho n_{\mathrm{e}}}, \quad \textbf{(28)}$$

where e is the electron charge, d is the film thickness, I is the injected current and ρ is the electrical resistivity. The results were averaged over ten measurements, performed for each sample deposited on Si substrates.

2.3.4. Thermal Properties: Frequency Domain Thermoreflectance (FDTR)

Frequency domain thermo-reflectance (FDTR) was used to investigate the thermal conductivity of the films, performed in a custom set-up at ICMAB, Spain.

FDTR is a non-destructive contactless optical method and uses two lasers to locally heat (pump, 405 nm) and probe (probe, 532 nm) the local temperature at the surface of a sample. In order to enhance the thermal sensitivity of the method, a 60 nm thick Au transducer was evaporated onto the surface of the specimens. The output power of the pump laser was modulated in the frequency range between 30

kHz and 20 MHz, which generates thermally induced oscillations of the reflectivity of the sample, leading to a modulation of the reflected power of the continuous wave probe laser. In this way, the phase lag between the heat wave generated by the pump laser and the harmonic response of the sample is sensed against the probe laser by using a lock-in amplifier. The frequency dependent phase lag is modelled numerically solving the parabolic heat equation for the described geometry. The model used to fit the phase lag curve describes the behaviour of a stack of layers composed by the Au transducer, the TiO_2:Nb film, the substrate, and an effective thermal boundary conductance that accounts for the two interfaces between the different layers [112,113].

One of the adjustable parameters obtained by least-squares fitting is the cross-plane thermal conductivity. In the present case, as the average coherent domain size is much smaller than the film thickness, we considered that the thermal conductivity of the films is isotropic, i.e., in-plane and out-of-plane components are similar, within experimental uncertainty.

2.3.5. Thermoelectric Properties: Seebeck Coefficient

The Seebeck coefficient was evaluated in two custom-made setups at the CF-UM-UP.

The first and primary equipment (**Figure 17**) is operated in low vacuum (1 Pa) using two Peltier devices (Quick-Ohm Küpper & Co. GmbH) for heating (HOT) and cooling (COLD) the edges of (25 × 75) mm^2 sample area. A water circuit operated by a chiller is responsible for cooling the base of the equipment. An electrical circuit measures the voltage V generated in the sample, in response to a thermal gradient across the film surface (in-plane).

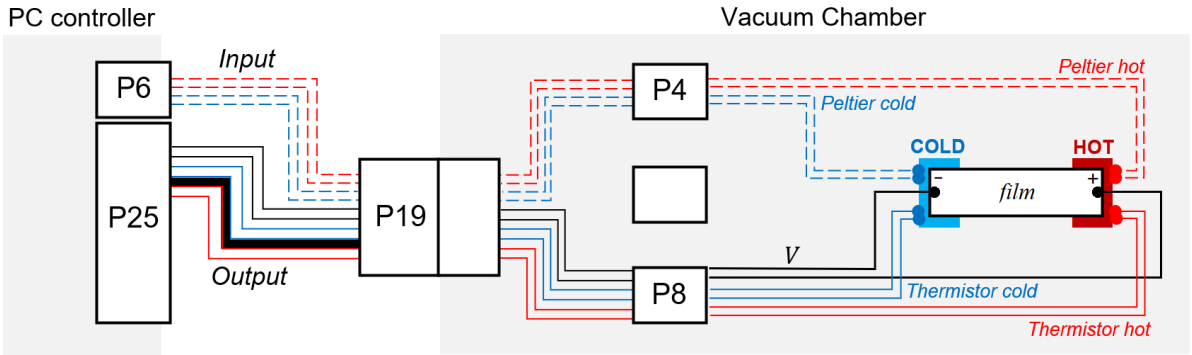

Figure 17. Schematic of the in-plane Seebeck coefficient measuring system at 1 Pa for an n-type thin film. P# indicates a pin connection. The power of the Peltier modules is individually adjusted, and the sample Voltage and thermistor temperatures are measured by the controller interface.

The heating stages and temperature stability is automated and controlled by custom-developed software and hardware. The COLD Peltier is maintained at a designated power P, while the P is progressively adjusted for the HOT Peltier, until achieving the desired temperature. The temperatures are measured by a pair of 10 kΩ NTC thermistors located between each edge of the sample and respective Peltier. The Seebeck coefficient (S, in μV·K^{-1}) can be estimated by equation **(2)**, with ΔT being the temperature difference between the edges of the plane of the film and V the respective measured potential difference [9,114]. The obtained V values were plotted as a function of ΔT and linearly fitted to determine the slope, and subsequently the Seebeck coefficient. The Seebeck coefficient was measured using different thermal gradients applied to the film deposited onto a glass slide.

A second setup (**Figure 18**) was developed to measure the thermal gradient across the depth of a sample and implemented in **Chapter 7**. This setup uses the same two Peltier as the in-plane equipment but positioned in a vertical stack facing the sample. The temperature is measured by a set of thermocouples in contact with the surfaces of the Peltier facing the sample and are manually controlled by two power supplies. A heat sink is attached to the backside of the COLD Peltier, as it enables produced thermal energy dissipation away from the sample. This is especially problematic at ambient pressure, where the Joule effect starts to affect the measurement once the temperature of the sample is overly high. The voltage is measured with a high-performance Agilent 34401A digital multimeter connected to flat copper contacts placed on the surface of the bottom Peltier (COLD) facing the sample. The contacts are arranged to specifically fit a specially designed (25 × 25 × 1.6) mm^3 sample (**Section 7.3.1.1**) with a bottom and top contact surrounding the film, fabricated on one side of a glass substrate.

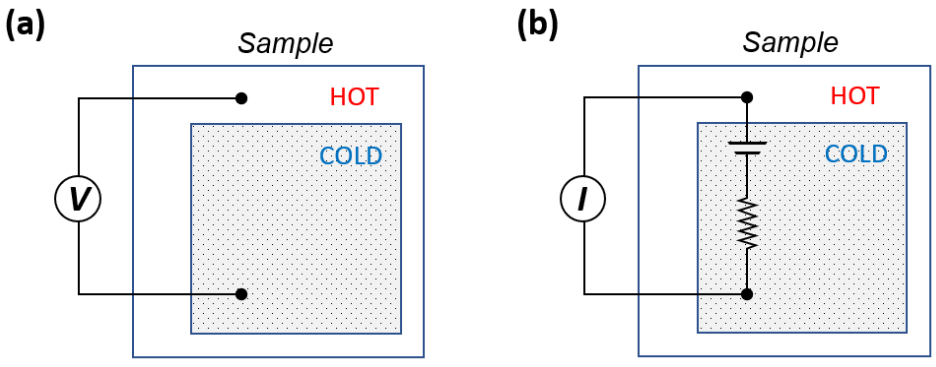

Figure 18. Schematic of the through-plane Seebeck coefficient measuring system at ambient pressure in voltage **(a)** and current **(b)** mode.

The electrical current (**Figure 18(b)**) can also be measured, instead of the voltage, by considering the thermoelectric sample as a power source in series with its internal resistance and setting

the multimeter in series with the sample, instead of in parallel. The power output of the device can then be obtained by the equation

$$P_{\text{out}} = SI\Delta T - I^2R\,, \tag{29}$$

where S is the Seebeck coefficient, I is the measured current, R is the electric resistance of the device and ΔT is the temperature difference [28].

2.3.6. Mechanical Properties

Scratch-testing and nano indentation provide the mechanical suitability of these thin films, in particular, adhesion strength of the film to glass and plastic substrates, hardness and stiffness of the coatings.

2.3.6.1. Scratch Test

The adhesion of a TiO_2:Nb thin film deposited on a glass substrate was evaluated by scratch tests, performed in a Revetest-Scratch Tester from CSM instruments, at the SEMAT/UM. A 200 μm tip radius diamond conical Rockwell C indenter with 90° angle (perpendicular to the sample surface) was used under progressively increasing load on a 5 mm scratch line. Two scratches were done, from 5 N to 50 N with a speed of 5 mm·min^{-1}, and from 5 N to 25 N with a speed of 2.5 mm·min^{-1}.

The scratch scars on coating surfaces were analysed with a Leica DM2500 optical microscope.

2.3.6.2. Nanoindentation

Nanoindentation is one of the most popular methods for determining the mechanical properties in thin films.

The hardness of a TiO_2:Nb thin film deposited on a Si substrate was determined from the loading and unloading curves carried out with a Berkovich-type NanoTester nanoindenter from Micro Materials, at the SEMAT/UM. 6 indentations with 50 μm lateral separation were performed. The indenter was operated in a loading rate of 0.5 mN·s^{-1} until a Maximum Load of 9.0 mN was reached, with 10 s of

dwelling time at the Maximum Load and unloading at a rate of 0.5 $mN{\cdot}s^{-1}$. Indentation depths of approximately 175 nm were required to keep them within the recommended value of approximately (10 to 20) % of the film's thickness.

These experiments enable a continuous monitoring of the load and depth of penetration experienced by the indenter during the indentation process and allow the estimation the hardness and the Young's modulus.

2.3.7. Data Analysis

Reverse Monte Carlo (RMC), X-ray absorption near-edge structure (XANES) and Density functional theory (DFT) calculations were used to study the properties of the deposited thin films.

2.3.7.1. Reverse Monte Carlo (RMC)

X-ray absorption spectra of Nb-doped TiO_2 thin film recorded at the Ti and Nb $K-$edges were analysed using the reverse Monte Carlo (RMC) method based on the evolutionary algorithm (EA), implemented in the EvAX code [115]. First, the extended X-ray absorption fine structures (EXAFS) $\chi(k)k^2$ were extracted using a conventional procedure [116]. Strong overlap of the outer coordination shells coupled with the presence of multiple-scattering contributions requires the use of the RMC approach. Further, simulation boxes (supercells) having different size ($4a \times 4b \times 2c$ for pure TiO_2, $5a \times 5b \times 2c$ for TiO_2:Nb) with periodic boundary conditions (PBC) were constructed based on anatase TiO_2 ($I4_1/amd$) crystallographic structure [117]. The size of the box was determined by the concentration of the dopant (Nb) element. RMC/EA calculations were simultaneously performed for 32 atomic configurations. At each iteration, the new atomic configuration was generated by randomly displacing all atoms in the simulation box with the maximally allowed shift of 0.4 Å to get the best possible agreement between the Morlet wavelet transforms (WTs) of the experimental and calculated EXAFS spectra at the Ti and Nb $K-$edges simultaneously. Note that for pure anatase TiO_2 only data for the Ti $K-$edge was used. The calculations were performed in the $k-$space range of (2.5 to 13) $Å^{-1}$ and in the $R-$space range of (0.8 to 4.5) Å. No significant improvement in the residual was observed after 5 000 iterations. The configuration-averaged EXAFS spectra were calculated by ab initio real-space multiple-scattering (MS) FEFF8.50L code [118,119], including the MS

effects up to 4^{th} order. The scattering potential and partial phase shifts were calculated only once within the muffin-tin (MT) approximation [118,119] for the cluster with the radius of 5.5 Å, centred at the absorbing Ti (Nb) atom and constructed based on crystallographic anatase TiO_2 structure [117]. Small variations of the cluster potential due to atom displacements during the RMC/EA simulations were neglected. The photoelectron inelastic losses were accounted for within the one-plasmon approximation using the complex exchange-correlation Hedin-Lundqvist potential [120]. The amplitude reduction factor[8] S_0^2 is included in the scattering amplitude [118,119], calculated by the FEFF code, and no additional correction of the EXAFS amplitude was performed.

2.3.7.2. X-ray Absorption Near-edge Structure (XANES)

XANES calculations were performed using ab initio real-space FDMNES code [121,122] implementing the finite difference method (FDM). The dipole and quadrupole transitions were taken into account, and the energy-dependent real Hedin-Lundqvist exchange-correlation potential was used [121,122]. The relativistic FDM calculations were performed with self-consistent potential. The calculated XANES spectra were broadened to account for the core-hole level widths ($\Gamma(K\text{–Ti}) = 0.94$ eV and $\Gamma(K\text{–Nb}) = 4.14$ eV) [123] and other multielectronic phenomena. The energy origin was set at the Fermi level E_F. The clusters of different size (radius) were constructed from the crystallographic anatase structure [117] centred at the absorbing Ti atom, which was substituted by Nb to simulated doping.

2.3.7.3. Density Functional Theory (DFT)

DFT calculations were performed using the Quantum ESPRESSO package [124,125]. The exchange-correlation functional was described through the generalized gradient approximation (GGA) and the Perdew–Burke–Ernzerhof (PBE), together with the optimized Vanderbilt pseudopotentials [126] provided through the SSSP package in its 1.2.1 version [127].

To account for the highly localized titanium $3d$–orbitals [128], the Hubbard correction setting $U = 5.7066$ eV was employed after the convergence test. For the structural optimization calculations, the

[8] The amplitude reduction factor has a characteristic dependence on atomic number and is usually an experimental parameter in EXAFS data analysis, [118,119].

plane-wave cutoff energy was set to 680 eV with a self-consistent field value of (1.6×10^{-7}) eV·atom^{-1}. At the same time, the convergence criterion of ionic minimization was achieved when all forces were smaller than (8.2×10^{-4}) eV·nm^{-1} and the total energy fluctuates less than (8.9×10^{-3}) eV·atom^{-1} in two consecutive self-consistent field steps, and all atoms were able to move without constraints. A $k-$point set of $4a \times 6b \times 5c$ and $5a \times 5b \times 5c$ was used to sample in the Brillouin zone, for the anatase and rutile phase, respectively.

The computation of the density of states (DOS) and projected density of states (PDOS) was performed using a $k-$point set of $8a \times 12b \times 10c$ and $10a \times 10b \times 10c$, for the anatase phase and rutile phase, respectively, with a cutoff energy of 816 eV for improved calculations. Structural visualization of the models was assisted by the VESTA ver. 3.5.8 [129] and XCrysden [130] codes.

The thermoelectric properties were calculated using Boltztrap2 code [131], which solves the linearized Boltzmann transport equation. Single-point energy calculations from Quantum ESPRESSO were used as input for the Boltztrap2 code to carry out the transport properties of doped TiO_2 configurations. BoltzTrap2 calculates the Onsager coefficients by solving the Boltzmann transport equation. All calculations were carried out at 300 K in a –0.2 Ha to 0.2 Ha energy interval.

CHAPTER III.

INFLUENCE OF NIOBIUM-DOPING

3. Influence of Niobium-doping

This chapter describes the Influence of Nb-doping on the local structure and thermoelectric properties of transparent TiO_2:Nb thin films and is based on the following publication:

> *J. M. Ribeiro, F. C. Correia, A. Kuzmin, I. Jonane, M. Konge, A. R. Goñie, J. S. Reparaz, A. Kalinko, E. Welter, C. J. Tavares, "Influence of Nb-doping on the local structure and thermoelectric properties of transparent TiO_2:Nb thin films", Journal of Alloys and Compounds. 838 (2020) 155561 (https://doi.org/10.1016/j.jallcom.2020.155561)* [73].

A focus is given on the effect of the Nb^{5+} integrating into the TiO_2 matrix. Nb-doped TiO_2 thin films were produced and investigated bearing in mind the material potential as a thermoelectric device. Thus, TiO_2:Nb thin films were deposited onto glass, Si and Kapton substrates, with thicknesses of 150 nm and 750 nm and using 6 sccm of reactive Oxygen flow. The thin films were comprehensively characterized by XRD, XPS, UV-Vis spectroscopy, FDTR, Temperature-dependent XAFS, Hall effect, and Seebeck coefficient measurement technique, which were experimentally determined as described in **Chapter 2**.

3.1. Experimental details

3.1.1. Sample Fabrication

TiO_2:Nb thin films with a thickness of 150 nm and 750 nm were deposited in an Ar/O_2 atmosphere at room temperature on Kapton® film (15 mm × 15 mm and 50 μm thick), glass slides (75 mm × 26 mm and 1 mm thick) and silicon substrates (15 mm × 15 mm and 0.5 mm thick) by reactive magnetron sputtering, from a pure Ti:Nb alloy target with 4 wt.% of Nb (99.99% purity, FHR). Before the depositions, a turbo molecular pump was used to achieve a base pressure of $\sim 10^{-4}$ Pa. The argon (working gas) and oxygen (reactive gas) flow rates were fixed at 40 sccm and 7.5 sccm, respectively, to attain optimised plasma conditions at a working pressure of 0.35 Pa. During the deposition of these films, the target-to-substrate distance was fixed at 100 mm, the cathode current density was set to 12.7 $mA{\cdot}cm^{-2}$, a substrate bias of –60 V was applied to the substrate holder, with a temperature of 175 °C for substrate

heating. These deposition conditions enable an effective ~ 2 at.% of Nb substitutional doping in the TiO_2 cell [72]. Subsequently to deposition, the as-deposited TiO_2:Nb films were annealed at 400 °C and 500 °C for 1 h.

3.1.2. Sample Characterization

A Bruker AXS D8 Discover system equipped with the copper anode X-ray tube (CuKα radiation) was used for XRD experiments. The diffraction patterns were collected in the range of $2\theta = 22°$ to 42° for as-deposited and annealed thin film samples to distinguish between anatase and rutile TiO_2 phases.

The XPS measurements were carried out using monochromatic Al–Kα radiation (1 486.6 eV) from a Kratos Axis-Supra instrument. Photoelectrons were collected from a take-off angle of 90° relative to the sample surface. The measurement was done in a Constant Analyser Energy mode (CAE) with a 160 eV pass energy and 15 mA of emission current for survey spectra and 40 eV pass energy for high-resolution spectra, using an emission current of 15 mA. Charge referencing was done by setting the lower binding energy of the C1s hydrocarbon peak at 248.8 eV; an electron flood gun was used to minimize surface charging.

Spectral transmittance and reflectance responses were measured with a Shimadzu UV-3600 Plus spectrophotometer, and the band-gap energy was calculated by plotting the squared absorbance versus the photon energy and extrapolating the linear fit of the plot to the photon energy axis [111].

The electrical properties were measured with an Ecopia AMP55T Hall Effect equipment equipped with a four-point probe in van der Pauw method.

The Seebeck coefficient was evaluated in custom-made equipment operated in a vacuum (1 Pa) using two Peltier devices (Quick-Ohm Küpper & Co. GmbH) for heating and cooling the edges of (26 × 75) mm sample area. The heating and cooling stability was controlled by custom-developed software and hardware.

The thermal conductivity of the TiO_2:Nb films was determined using FDTR [132], by determining the phase lag between the heat wave locally generated by a pump laser (405 nm), and the harmonic response of the sample as sensed by a probe laser (532 nm) using a lock-in amplifier. A 60 nm thick Au transducer was evaporated onto the surface of the specimens and the lasers were focused using an achromatic 30 mm focal distance lens to a spot size of ≈ 10 μm in diameter. The output power of the pump laser was modulated to a harmonic waveform in the frequency range between 30 kHz and 5 MHz.

The frequency dependent phase lag is numerically modelled solving the parabolic heat equation for the described geometry. The cross-plane thermal conductivity (κ) and the specific heat capacity (C_{p}) of the thin films, as well as the substrate-dependant effective thermal boundary conductance of the system were fitted using a least-squares routine.

Temperature-dependent XAS study of TiO_2:Nb thin films was performed to determine the coordination environment of the dopant ions (Nb) and their influence on titanium oxide matrix. Experiments were done in transmission and fluorescence modes at P65 Applied XAS beamline [96] of the PETRA III storage ring. A set of powder samples (TiO_2, Nb_2O_5) was used for reference. The harmonic rejection was achieved by uncoated and Rh-coated silicon plane mirrors. Fixed exit Si(111) and Si(311) monochromators were used for the Ti and Nb $K-$edges, respectively. X-ray absorption spectra were collected using two ionization chambers in transmission mode, whereas PIPS detector was used in fluorescence mode. The Oxford Instruments liquid helium flow cryostat was used to maintain the required sample temperature in the range of (10 to 300) K. For transmission measurements at the Ti $K-$edge, a stack of thin films deposited on Kapton was produced, with the number of layers giving the value of the absorption edge jump $\Delta\mu \approx 1$.

3.1.3. Data analysis

X-ray absorption spectra of Nb-doped TiO_2 thin film recorded at the Ti and Nb $K-$edges were analysed using the RMC method based on the EA, implemented in the EvAX code [115]. First, the EXAFS $\chi(k)k^2$ were extracted using a conventional procedure [116]. Strong overlap of the outer coordination shells coupled with the presence of multiple-scattering contributions requires the use of the RMC approach. Further, simulation boxes (supercells) having different size ($4a \times 4b \times 2c$ for pure TiO_2, $5a \times 5b \times 2c$ for TiO_2:Nb) with PBC were constructed based on anatase TiO_2 ($I4_1/amd$) crystallographic structure [117]. The size of the box was determined by the concentration of the dopant (Nb) element. RMC/EA calculations were simultaneously performed for 32 atomic configurations. At each iteration, the new atomic configuration was generated by randomly displacing all atoms in the simulation box with the maximally allowed shift of 0.4 Å to get the best possible agreement between the Morlet WTs of the experimental and calculated EXAFS spectra at the Ti and Nb $K-$edges simultaneously. Note that for pure anatase TiO_2 only data for the Ti $K-$edge was used. The calculations were performed in the $k-$space range from (2.5 to 13) $Å^{-1}$ and in the $R-$space range from (0.8 to 4.5) Å. No significant improvement in

the residual was observed after 5 000 iterations. The configuration-averaged EXAFS spectra were calculated by ab initio real-space multiple-scattering (MS) FEFF8.50L code [118,119], including the MS effects up to 4th order. The scattering potential and partial phase shifts were calculated only once within the muffin-tin (MT) approximation [118,119] for the cluster with the radius of 5.5 Å, centred at the absorbing Ti (Nb) atom and constructed based on crystallographic anatase TiO_2 structure [117]. Small variations of the cluster potential due to atom displacements during the RMC/EA simulations were neglected. The photoelectron inelastic losses were accounted for within the one-plasmon approximation using the complex exchange-correlation Hedin-Lundqvist potential [120]. The amplitude reduction factor S_0^2 is included in the scattering amplitude [118,119], calculated by the FEFF code, and no additional correction of the EXAFS amplitude was performed.

XANES calculations were performed using ab initio real-space FDMNES code [121,122] implementing the FDM. The dipole and quadrupole transitions were taken into account, and the energy-dependent real Hedin-Lundqvist exchange-correlation potential was used [121,122]. The relativistic FDM calculations were performed with self-consistent potential. The calculated XANES spectra were broadened to account for the core-hole level widths ($\Gamma(K\text{–Ti}) = 0.94$ eV and $\Gamma(K\text{–Nb}) = 4.14$ eV) [123] and other multielectronic phenomena. The energy origin was set at the Fermi level E_F. The clusters of different size (radius) were constructed from the crystallographic anatase structure [117] centred at the absorbing Ti atom, which was substituted by Nb to simulated doping.

3.2. Results and Discussion

XRD patterns of the as-deposited and thermally annealed TiO_2:Nb thin films deposited on Kapton substrates are shown in **Figure 19**. A single diffraction peak corresponding to a reflection from the (101) planes of anatase TiO_2 (I41/amd) is discerned at 25.4°, whereas for the thermally annealed film an additional diffraction peak is present at 27.3°, associated with a reflection from the (110) planes of rutile TiO_2 (P42/mnm). The broad background extended to lower diffraction angles is assigned to the Kapton substrate. The average crystallite size for anatase and rutile phases are 19 nm and 9 nm, respectively. It should be noted that, experimentally, EXAFS averages over all atoms located both in crystalline and amorphous structures, while XRD amplifies the crystalline domains.

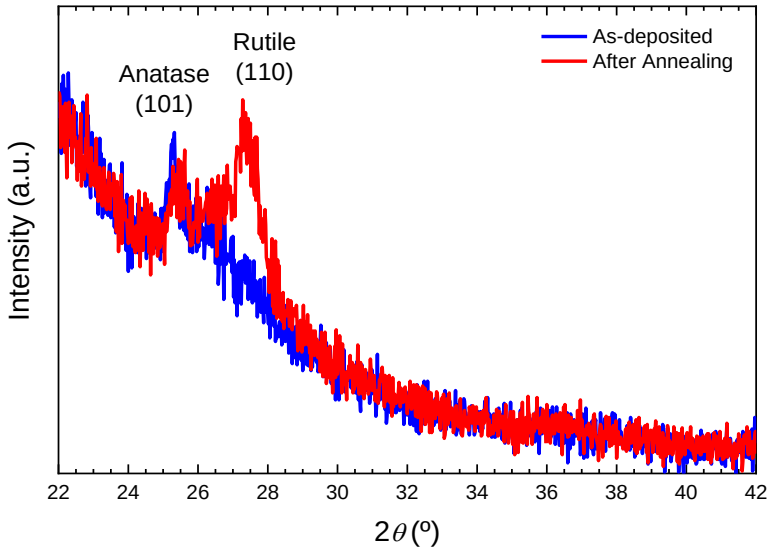

Figure 19. X-ray diffraction patterns of the as-deposited and annealed TiO_2:Nb thin films deposited on Kapton substrates.

To determine the chemical bonding state and film composition, XPS experiments were performed on a TiO_2:Nb thin film, as seen in **Figure 20**. The main peaks associated with the binding energies of 458.9 eV, 530.3 eV and 207.5 eV are ascribed to Ti $2p$, O $1s$ and Nb $3d$ orbitals [133–135], as listed in **Table 5**.

Table 5. XPS fitting parameters for as-deposited TiO_2:Nb thin film.

Peak	Position (eV)	FWHM (eV)	L–S (eV)	L–G	Area ratio	Concentration (at.%)
Ti $2p$ C1	458.9	1.2	5.7	0.3	2:1	28.7
Ti $2p$ C1	459.3	1.8	5.7	0.3	2:1	
O $1s$ C1	530.3	1.3	-	0.2	-	69.8
O $1s$ C2	532.1	1.3	-	0.2	-	
Nb $3d$	207.5	1.1	2.8	0.2	3:2	1.5

The spin-orbital (L–S) splitting is observed for both Ti $2p$ and Nb $3d$ core levels, being this splitting 5.7 eV and 2.8 eV, respectively, which is in agreement with the literature. It is also clear that the TiO_2 thin films have been efficiently doped with niobium, since peaks ascribed to binding energies of 207.5 eV are indexed to Nb $3d$ orbitals, while the L–S doublet separation (16 eV) registered in the survey spectra between 364 eV and 380 eV is attributed to Nb $3p$ orbitals of pentavalent Nb ions. From this analysis, it was obtained a level of Nb doping of 1.5 at.%. The Ti $2p$ core-level was fit with two components (C1 and C2) due to the asymmetry of the Ti $2p_{3/2}$ and $2p_{1/2}$ doublet peaks, which is not evident for undoped

TiO_2 (not shown). C1 is attributed to Ti–O bonding, as in undoped anatase TiO_2. This asymmetry, registered for the C2 component (6.6 % relative contribution), is attributed to the local order around the Ti^{4+} ions, resulting from Ti–O and Nb–O bonds. As for the O 1s core level, the fit includes two components, C1 and C2, with respective weights of 48.5 % and 51.5 %, being associated with Ti–O bonds and adsorbed oxygen species at the film surface, respectively. Silicon traces were found in the survey spectra due to the incidence of the beam spot on the sample border, where the Si substrate is exposed. Specific constraints were considered for all XPS fits [134], namely relative area ratio, full width at half maximum (FWHM) and Lorentzian-Gaussian relative profile in doublet peaks.

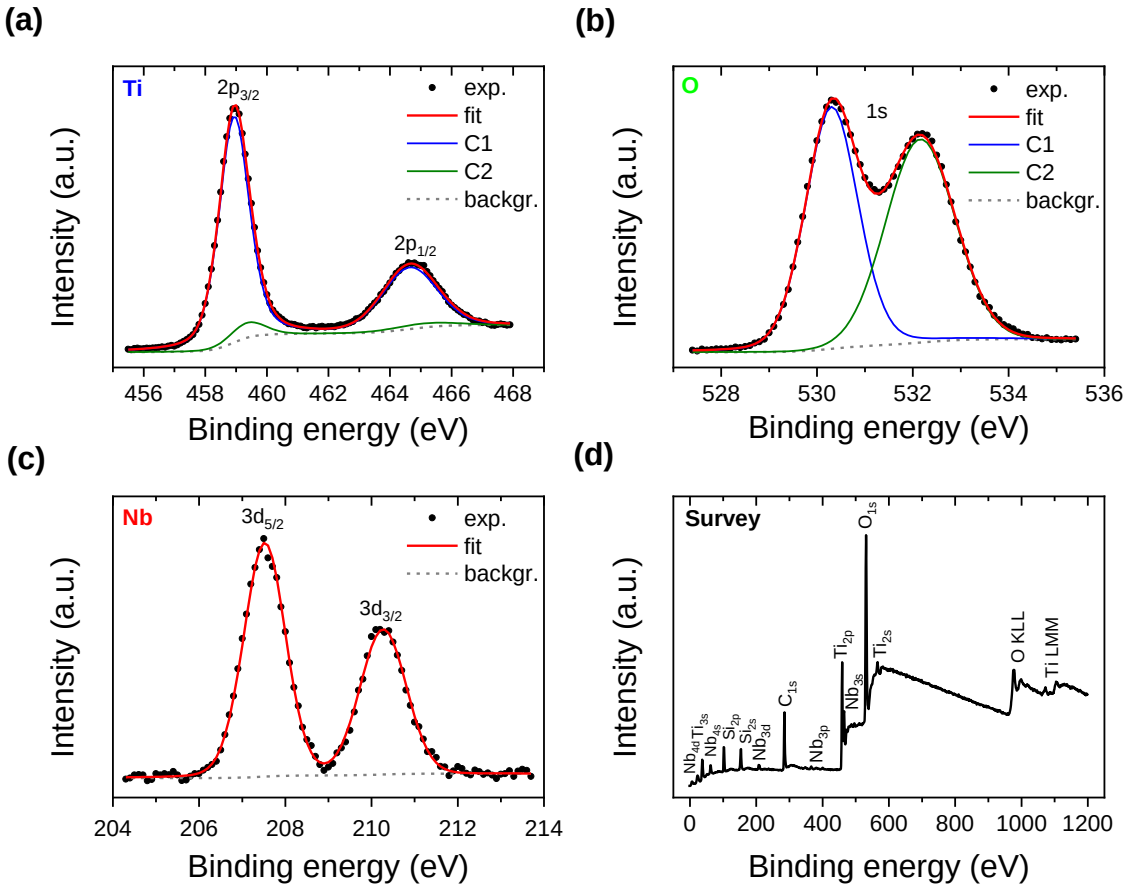

Figure 20. XPS experimental *(exp.)* spectra and respective fits *(fit)* for a TiO_2:Nb thin film where Ti 2p (fitted with 2 components, C1 and C2) **(a)**, O 1s (fitted with 2 components, C1 and C2) **(b)** and Nb 3d core levels **(c)**; in these plots the background *(backgr.)* is also shown. Survey spectrum **(d)**.

The local structure of as-prepared TiO_2:Nb thin film was studied by XAS. The experimental EXAFS spectra and their Fourier transforms (FTs) at the Ti and Nb K–edges for as-prepared TiO_2:Nb thin film and reference powders (TiO_2 and Nb_2O_5) are shown in **Figure 21**. A comparison of the EXAFS Ti K–edges in the film and two TiO_2 phases (rutile and anatase) unambiguously indicates the dominant

anatase phase in the film. Subsequently, by comparing signals at the Nb K–edge in the film and Nb_2O_5 powder with the signal at the Ti K–edge in anatase TiO_2 powder, it can be concluded that the local environment of Nb atoms in the film is close to that of Ti atoms in the anatase phase, but differ significantly from that in Nb_2O_5 powder. This suggests that the substitution of Ti by Nb ions occurs in the film without a strong influence on the TiO_2 matrix.

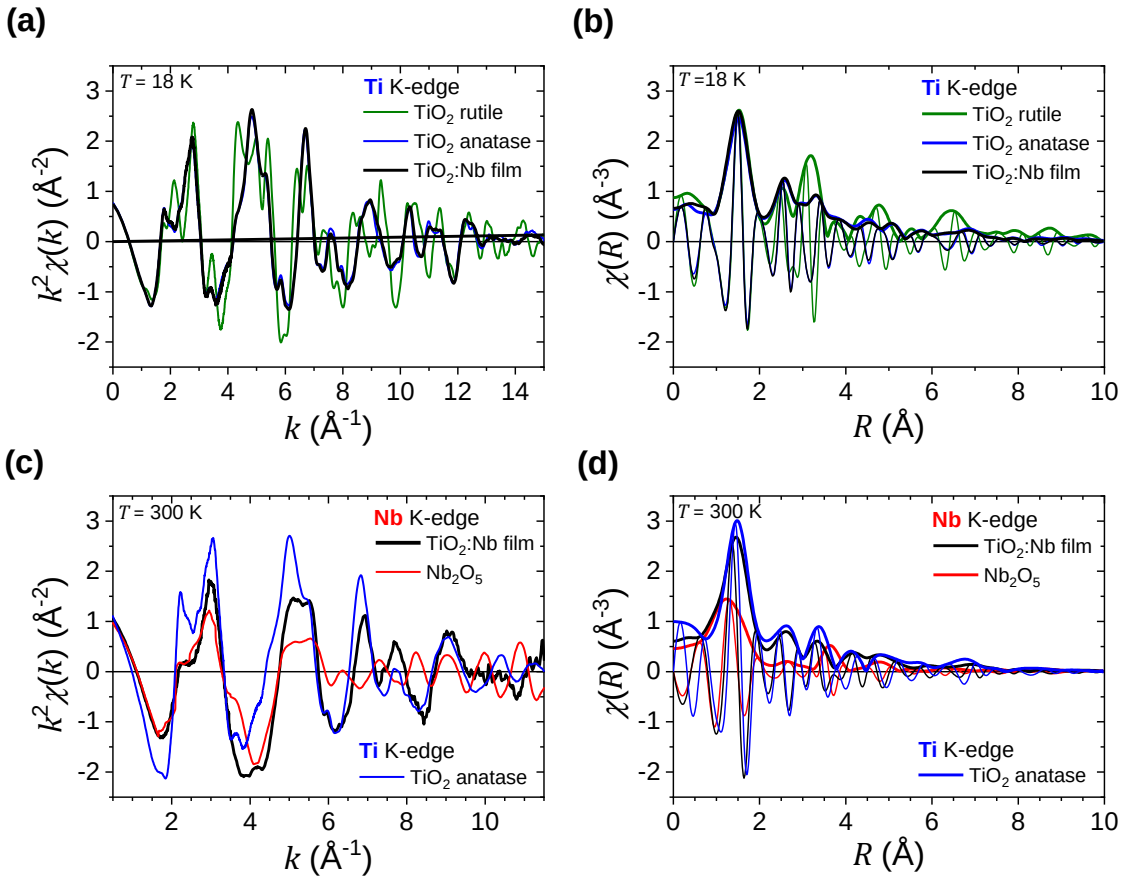

Figure 21. Ti K-edges EXAFS $\chi(k)k^2$ spectra **(a)** and their Fourier transforms (FTs) **(b)** at 18 K for rutile and anatase reference powders, and for as-prepared TiO_2:Nb thin film. Ti and Nb K–edges EXAFS $\chi(k)k^2$ spectra **(c)** and their FT **(d)** at 300 K for as-deposited TiO_2:Nb thin film (Nb K–edge) and two reference powders – anatase TiO_2 (Ti K–edge) and Nb_2O_5 (Nb K–edge).

Before performing the RMC analysis of EXAFS for the Nb-doped TiO_2 film, an approach was tested using reference anatase TiO_2 powder. **Figure 22** shows the experimental and calculated by RMC method Ti K–edge EXAFS spectra $\chi(k)k^2$ and their Fourier and Morlet WTs for anatase TiO_2 at two different temperatures (18 K and 300 K).

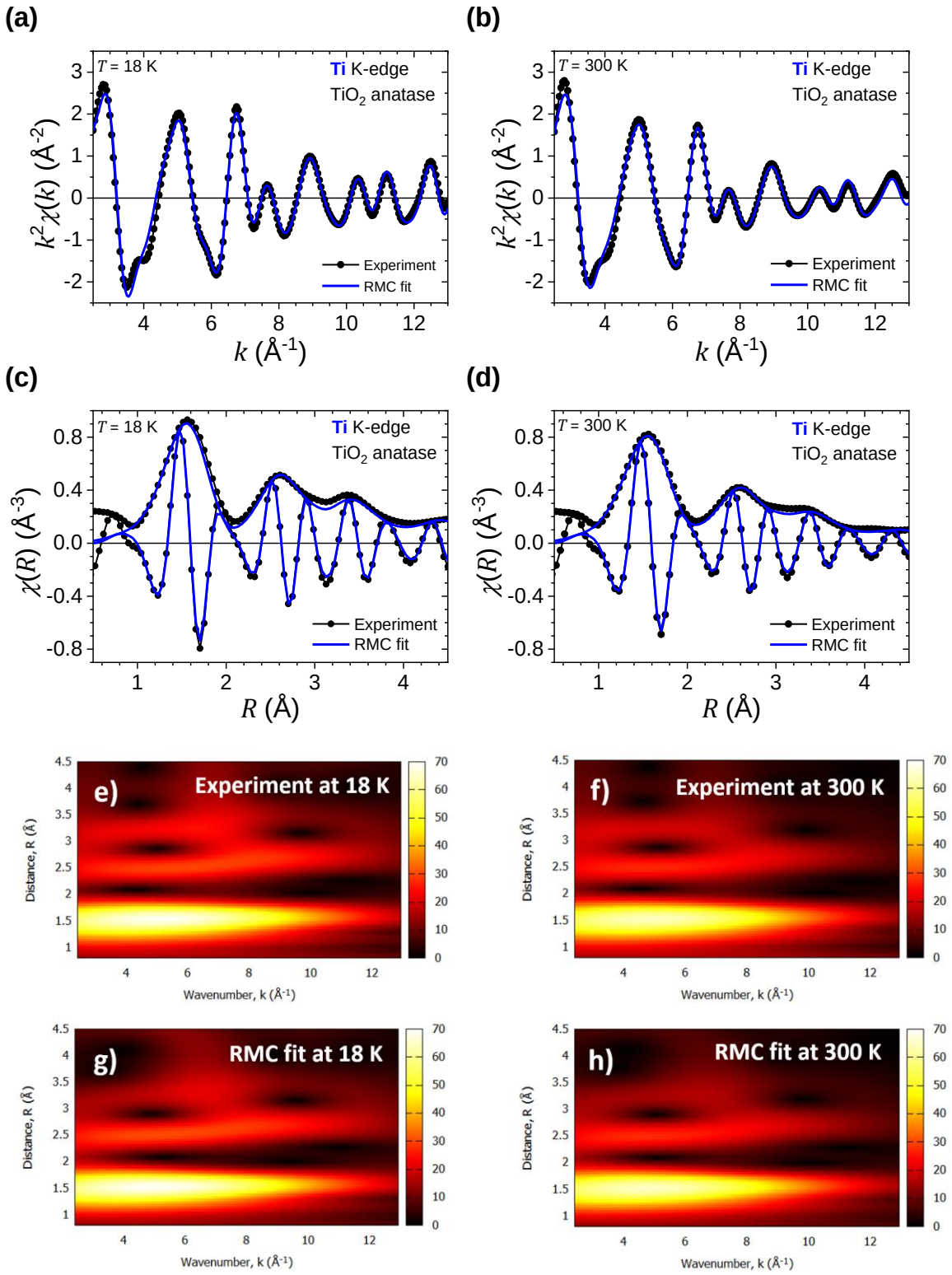

Figure 22. Experimental and calculated by RMC Ti K–edge EXAFS spectra $\chi(k)k^2$ **(a,b)** and their Fourier **(c,d)** and Morlet wavelet **(e,f,g,h)** transforms for anatase TiO_2 reference powder at 18 K and 300 K.

The strong interatomic bonding in the anatase phase is responsible for a rather weak temperature dependence of the Ti K–edge EXAFS. However, some EXAFS oscillation damping at high-k values occurs

upon temperature increase from 18 K to 300 K (**Figure 22(a,b)**) leading to the peak broadening in FTs (**Figure 22(c,d)**). The WTs of EXAFS reflect the same thermal disorder effect simultaneously in k and $R-$space. The WTs are dominated by the first shell contribution of six oxygen atoms (bright spots at $R =$ 1.5 Å), whereas titanium atoms of the outer shells are main responsible for the WT complex pattern at longer distances (**Figure 22(e,f)**). The RMC simulation box was a $4a \times 4b \times 2c$ supercell with anatase TiO_2 structure and PBC, including 128 Ti and 256 O atoms. Hence, the RMC fits reproduce well the temperature-dependence of the Ti $K-$edge EXAFS spectra and respective WT patterns for anatase TiO_2, so that the EXAFS analysis including the contributions from the coordination shells located as far as up to (4 to 5) Å can be reliably performed.

On a subsequent step, the RMC simulations were applied to the simultaneous analysis of the Ti and Nb $K-$edges EXAFS spectra of TiO_2:Nb thin film at 300 K. The obtained results are shown in **Figure 23**. The RMC simulation box was a larger 5a × 5b × 2c supercell with anatase TiO_2 structure comprising 10 % of Ti atoms substituted randomly by Nb atoms, resulting in a total of 180 Ti, 20 Nb and 400 O atoms in the supercell. As in the case of anatase TiO_2, the RMC simulation fits very well the experimental data of TiO_2:Nb thin film at both edges simultaneously and over a large (more than 4 Å) distance range in $R-$space. Note that in this case, the single structural model can describe well the environment around both Ti and Nb atoms taking into account the structure relaxation due to a difference in the Ti–O and Nb–O bonding. The similarity of the local atomic structure around Ti and Nb atoms in the TiO_2:Nb thin film is well reflected by close WT patterns (**Figure 23(e,f)**), which are well reproduced in the RMC simulations (**Figure 23(g,h)**). Similar RMC simulations (not shown), with 5 % of substituting Nb atoms and including 190 Ti, 10 Nb and 400 O atoms in the supercell, gave close agreement with the experimental data.

The atomic coordinates obtained in the RMC simulations of the TiO_2:Nb thin film with 5 % and 10 % of dopant Nb atoms at 300 K were used to calculate the radial distribution functions (RDFs) $G(R)$ for Nb–O, Nb–Ti, Ti–O and Ti–Ti atom pairs. They are shown in **Figure 24(a,b)** in comparison with the RDFs G(Ti–O) and G(Ti–Ti) for anatase TiO_2. To improve statistics, the RDFs were evaluated as an average over six independent RMC calculations. The two models with different percentage of Nb doping give close RDFs. Also, the RDFs G(Ti–O) and G(Ti–Ti) are rather close in the thin film and anatase suggesting that doping by niobium does not change significantly the local environment of Ti atoms.

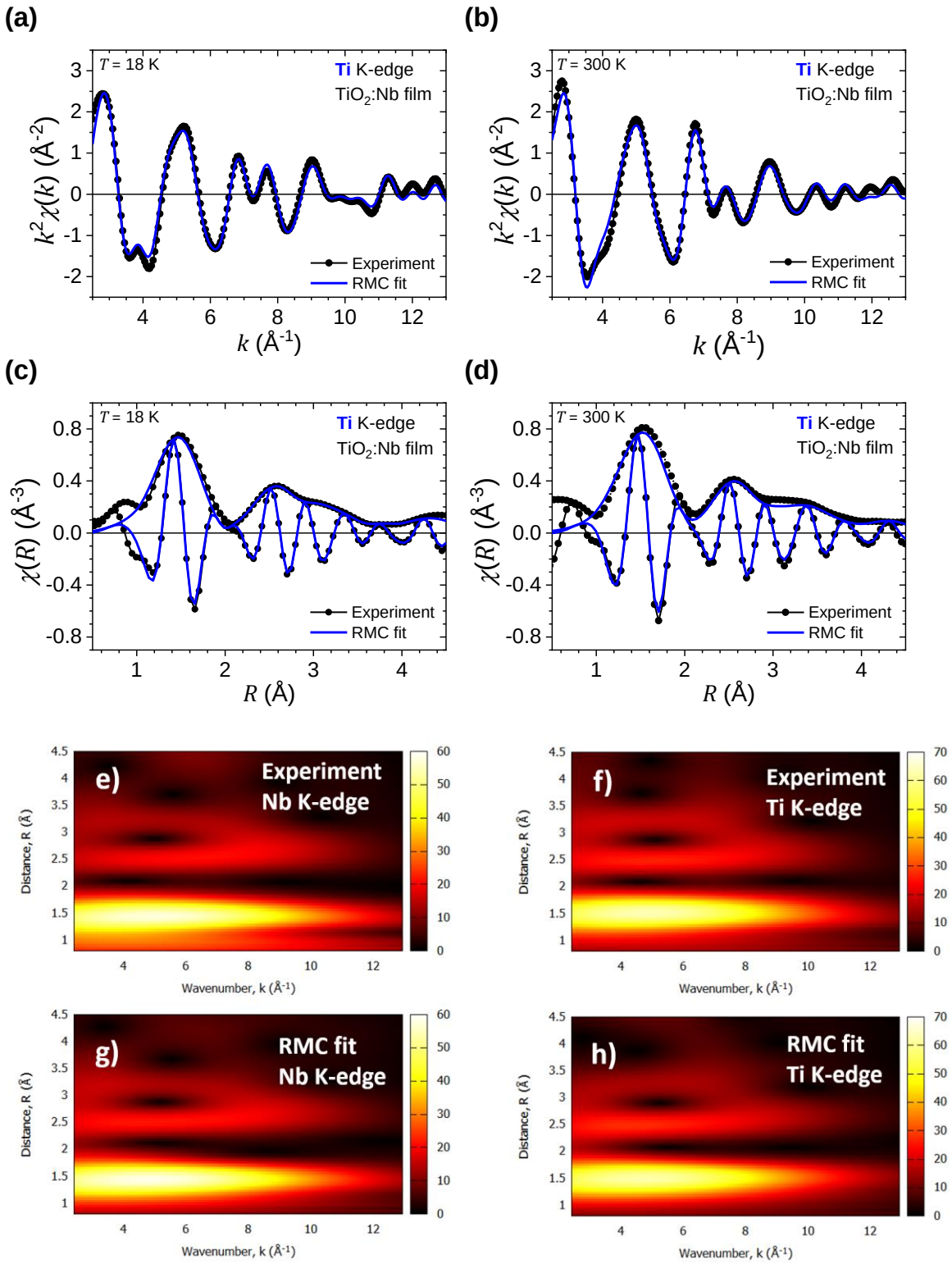

Figure 23. Experimental and calculated by RMC Ti and Nb K–edge EXAFS spectra $\chi(k)k^2$ **(a,b)** and their Fourier **(c,d)** and Morlet wavelet **(e,f,g,h)** transforms for TiO_2:Nb thin film at 300 K.

A comparison of the RDFs G(Nb–O) and G(Ti–O) in the thin film indicates that both Nb and Ti atoms are octahedrally coordinated by oxygen atoms. However, Nb environment relaxes leading to a larger splitting of the first coordination shell than that in the anatase structure. The first shell of Ti atoms

in anatase is split into two groups (3 + 3) of oxygen atoms located at 1.93 Å and 1.98 Å [117]. In our RMC calculations, the first shell of Ti atoms in both film and anatase does not split and is represented by a broad peak centred at ~ 1.95 Å. At the same time, the larger distortion of Nb environment leads to its first shell splitting into two groups (3 + 3) of oxygen atoms at ~ 1.88 Å and ~ 2.01 Å. Note that the second coordination shell of Nb (peak at 3 Å in **Figure 24(a,b)**) is also displaced slightly compared to that of Ti but to longer distances. The average values of the Nb–Ti and Ti–Ti distances are 3.11 Å and 3.04 Å, respectively. Thus, doping by Nb atoms modifies the local environment in the film; however, its average structure still resembles that of anatase (**Figure 24(c,d)**).

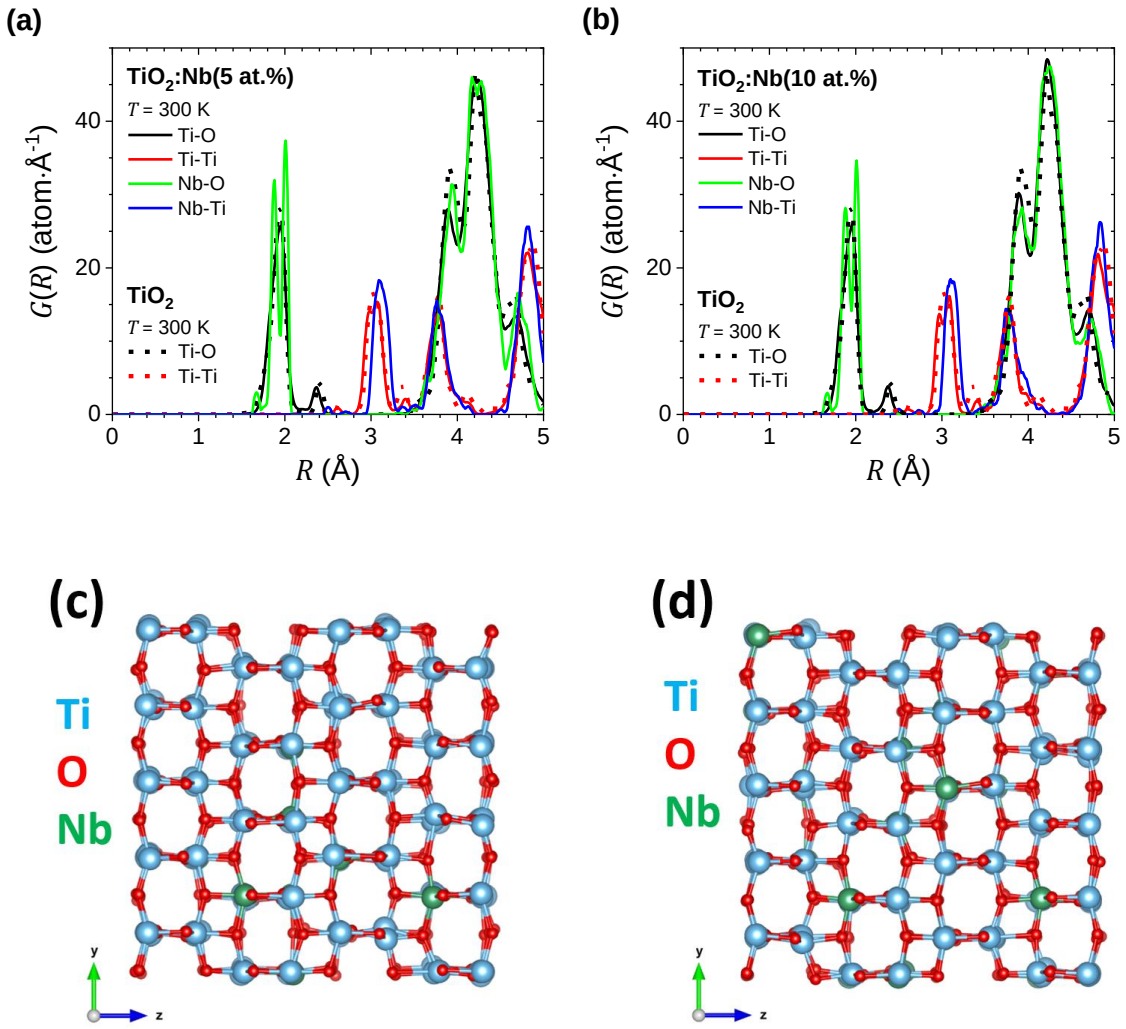

Figure 24. RDFs $G(R)$ calculated from the coordinates of atoms in a TiO_2 $5a \times 5b \times 2c$ supercell at 300 K, for 5 % **(a)** and 10 % **(b)** of dopant Nb atoms. Dashed (*black* and *red*) lines are for RDFs G(Ti–O) and G(Ti–Ti) in anatase TiO_2 at $T = 300$ K. Fragments of the RMC $5a \times 5b \times 2c$ supercells for 5 % **(c)** and 10 % **(d)** of Nb atoms.

The XANES spectra of TiO_2:Nb thin film measured at the Ti and Nb K–edges are presented in **Figure 25**. XANES spectra are better resolved at the Ti K–edge due to the smaller value of the core-

level width ($\Gamma(K\text{–Ti}) = 0.94$ eV *vs.* $\Gamma(K\text{–Nb}) = 4.14$ eV) [123]. This makes a difference mainly in the pre-edge region at (0 to 10) eV above the Fermi level. The main variance around 20 eV comes from the difference in the Ti(Nb) p-orbitals density of states (p-DOS, as seen later on). Note also that there is a slight difference in the fine structure above the two edges due to some modification of the local environment around Ti and Nb atoms caused by a difference in the Ti–O and Nb–O bonding. The Ti K–edge XANES spectra of the thin film and reference anatase TiO_2 powder are very similar, suggesting resemblances of their local environment in agreement with the results of our EXAFS analysis.

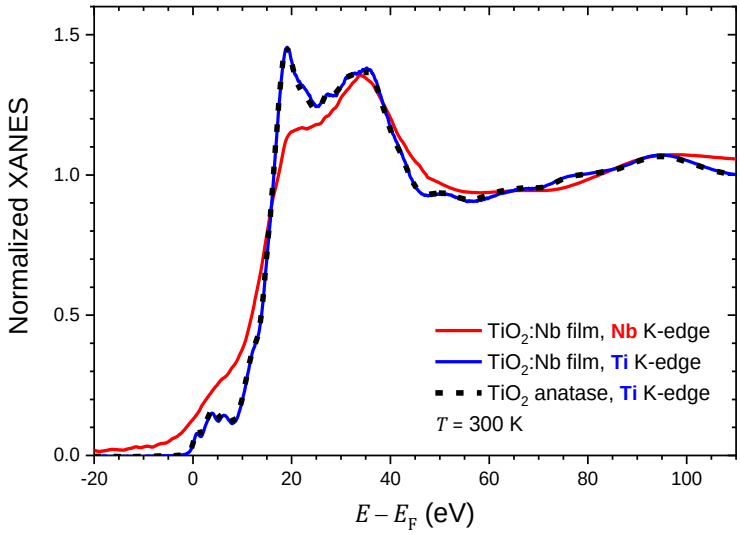

Figure 25. Experimental XANES spectra of TiO_2:Nb thin film at the Ti and Nb K–edges measured at 300 K. The Ti K–edge XANES spectrum *(dashed line)* of reference anatase TiO_2 powder is shown for comparison.

To understand the origin of the XANES features, theoretical simulation using ab initio FDMNES code [121,122] were performed using the finite difference method. This approach, while being more computationally time-consuming, gives better results in the case of the distorted environment, as in the case of both pure and Nb-doped TiO_2, than the Green function formalism with spherical muffin-tin potentials. Note also that the origin of XANES features above the absorption edge is due to the dipole-allowed transitions from $1s$(Ti/Nb) core state to unoccupied p-states, whereas three pre-edge peaks have mixed quadrupole-dipolar origin, involving d-metal states in the conduction band [136].

Experimental XANES spectra of TiO_2:Nb thin film at 300 K measured at the Ti and Nb K–edges are compared with those calculated by ab initio FDMNES code in **Figure 26**. A good agreement is observed for both Ti and Nb K–edges XANES for the cluster radius of 8.1 Å. However, main XANES features are reproduced already for the small cluster (4.0 Å) containing four coordination shells. It is

interesting to note that, despite similarities of the local structure around Nb and Ti atoms, their XANES spectra differ appreciably in the range of (15 to 40) eV above the edge, where the two main peaks have opposite amplitude. At the Ti K–edge, the peak at $\sim$ 20 eV is more intense than the peak at $\sim$ 35 eV, whereas, at the Nb K–edge, the situation is the opposite, i.e. the peak at $\sim$ 20 eV has a smaller amplitude than that at $\sim$ 35 eV. To understand the origin of this difference, a more detailed analysis was performed. First, the influence of the core-level width on the shape of XANES was studied.

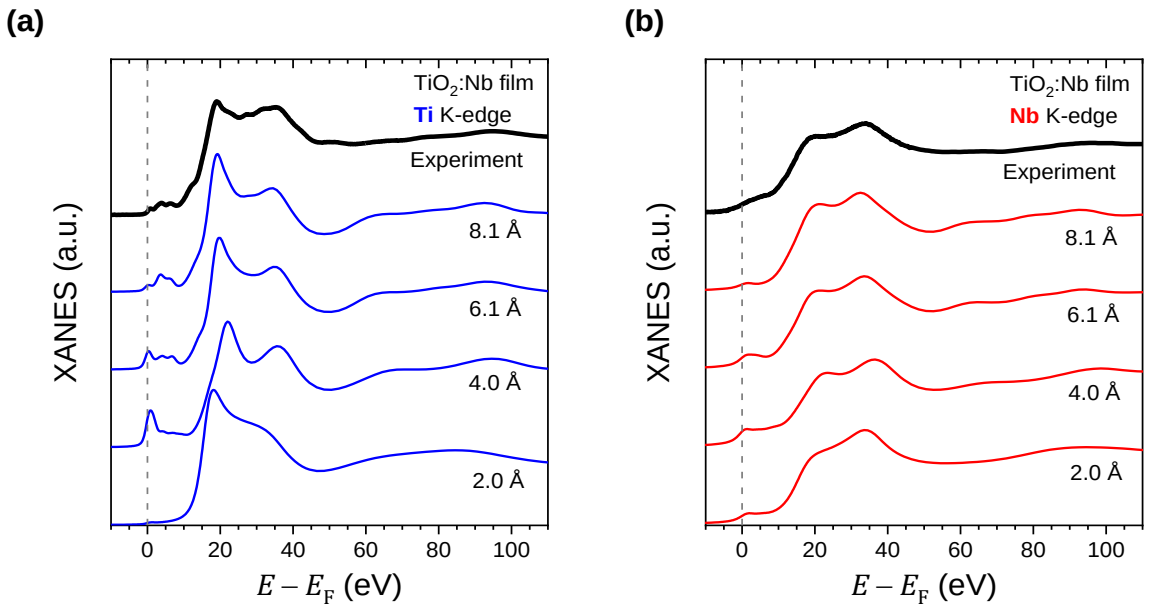

Figure 26. Experimental and calculated XANES spectra of TiO_2:Nb thin film measured at the Ti **(a)** and Nb **(b)** K-edges at 300 K. The calculations were performed for varying atomic cluster sizes. The spectra are vertically shifted for clarity.

The results of the Nb K–edge XANES simulations with the two core-level widths $\Gamma = 0.94$ eV and $\Gamma = 4.14$ eV [123] corresponding to the Ti and Nb K–edges, respectively, are shown in **Figure 27(a)**. The small pre-edge peak located just above the Fermi level is related to mixed Ti d-states and O p-states in the conduction band. As one can see, the reduction of the natural broadening influences the sharpness of all features but does not change their relative amplitudes. At the same time, the observed differences in the XANES at two absorption edges correlate well with the partial unoccupied DOS probed by $1s$ electron, i.e. p(Ti/Nb)-DOS, shown in **Figure 27(b)**. Also, in **Figure 27(b)** the opposite amplitude effect that is registered for the two main peaks at the Ti and Nb K–edges is more evident (highlighted by the blue oval shapes).

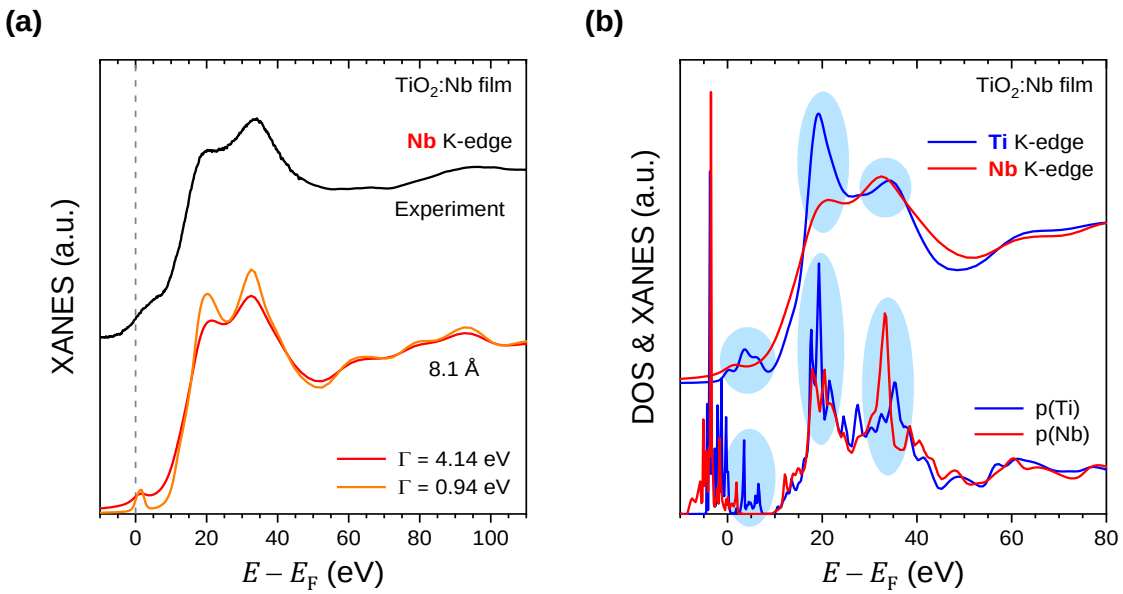

Figure 27. Experimental and calculated Nb K-edge XANES spectra of a TiO_2:Nb thin film. The calculations were performed for the cluster radius of 8.1 Å and two different core-level widths $\Gamma = 0.94$ eV and $\Gamma = 4.14$ eV **(a)**. A comparison of the calculated XANES spectra at the Ti and Nb K-edges (top) with p-DOS for Ti and Nb (bottom) **(b)**.

The measured thermal, thermoelectric, electrical and optical properties of the TiO_2:Nb film deposited on glass and Si substrates are presented in **Table 6**, and were experimentally determined as described in **Section 3.1**. A very high absolute Seebeck coefficient, $S = 155$ μV·K^{-1}, for n-type TiO_2 was achieved with Nb doping for the thinner film (150 nm). For the thicker film (750 nm), a 65 % lower value, $S = 101$ μV·K^{-1}, was obtained. These Seebeck coefficient values were determined from the slope of the ΔV vs. ΔT and the respective experimental errors are listed in **Table 6**.

Table 6. Thermoelectric, thermal, electrical and optical properties of TiO_2:Nb film for different thickness: Seebeck coefficient (S); thermoelectric power factor (PF) and figure of merit (ZT); thermal conductivity (κ); electrical conductivity (σ), carrier concentration (n_e) and mobility (μ_e); optical band-gap (E_g).

d (nm)	S (μV·K^{-1})	PF (mW·m^{-1}·K^{-2})	$ZT_{300\ K}$	κ (W·m^{-1}·K^{-1})	σ (10^2 Ω^{-1}·cm^{-1})	n_e (10^{19} cm^{-3})	μ_e (cm^2·V^{-1}·s^{-1})	E_g (eV)
150	−155 ± 2	0.5 ± 0.1	0.18 ± 0.05	1.3 ± 0.2	2.19 ± 0.02	8 ± 2	26 ± 10	3.27 ± 0.01
750	−101 ± 2	1.0 ± 0.1	0.13 ± 0.02	2.3 ± 0.3	9.92 ± 0.01	400 ± 200	2 ± 1	3.24 ± 0.01

In **Figure 28**, the Seebeck coefficient values were measured for both of these films at 5 K step values with a stabilization of 60 min per step, integration time of 40 min at that step, in order to thermally stabilize both ends of the sample. These S step values are a bit lower for the thicker film when compared to that obtained for the whole temperature gradient range (from the aforementioned slopes) due to a

small potential offset originated at the start of the experiment. This variation in S for both films is further elucidated later in the manuscript when discussing the electrical properties. It is noteworthy to mention that this magnitude of the Seebeck effect was registered within a relatively small thermal gradient of 50 K across the film surface (75 mm × 26 mm), for a 750 nm thick film. This thermal gradient is greater than expected and suitable for their use as thermal energy harvesters in touch displays or photovoltaic cells. The resulting power factor (PF) and figure of merit (ZT) were calculated using the equation **(8)** and **(7)**, respectively, where σ is the electrical conductivity, T is temperature and κ is the thermal conductivity of the TiO_2:Nb film. PF and ZT values at 300 K of 0.5 $mW{\cdot}m^{-1}{\cdot}K^{-2}$ and 0.18, respectively, were obtained for optimized (150 nm) TiO_2:Nb films, which excels what is commonly found in the literature for transparent thin films.

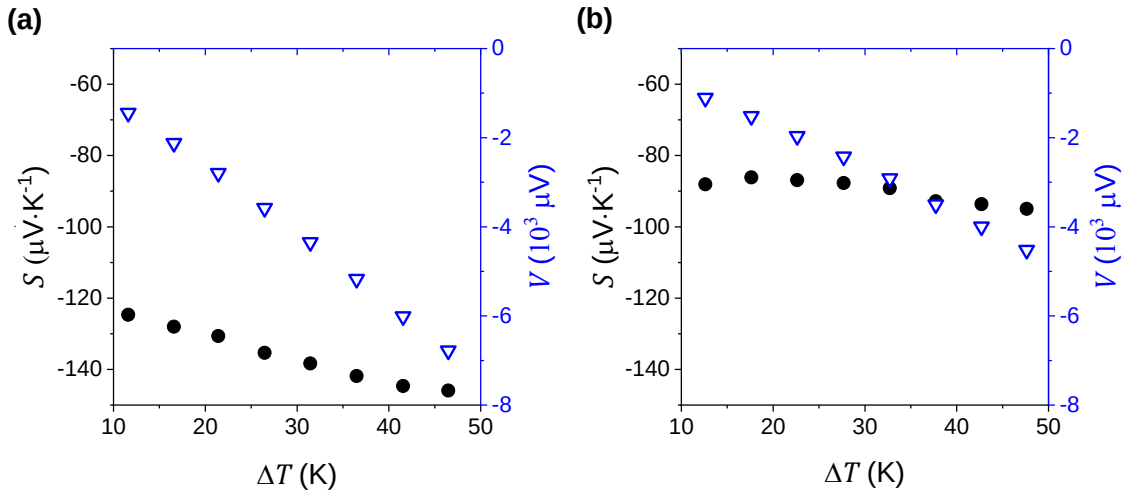

Figure 28. Evolution of the Seebeck coefficient *(black circles)* and potential difference *(blue triangles)* with a thermal gradient across the surface of a (75 × 26) mm, for 150 nm **(a)** and 750 nm thick **(b)** TiO_2:Nb film on a glass substrate.

The data in **Table 6** were recorded from a large collection of similar samples; hence, the registered uncertainty in some properties, such as thermal and electrical conductivities. The value of the thermal conductivity measured by FDTR at 300 K is 1.3 $W{\cdot}m^{-1}{\cdot}K^{-1}$ and 2.3 $W{\cdot}m^{-1}{\cdot}K^{-1}$, for 150 nm and 750 nm thick TiO_2:Nb films, respectively. The values of κ are quite low compared to what is known for undoped TiO_2 ((5 to 10) $W{\cdot}m^{-1}{\cdot}K^{-1}$) [137]. From the fit of the phase lag data in **Figure 29**, for both **(a)** 150 nm and **(b)** 750 nm TiO_2:Nb thick films, it was possible to calculate κ, with a maximum uncertainty of ± 0.3 $W{\cdot}m^{-1}{\cdot}K^{-1}$. Also, from these fits, values for C_p of 1200 $J{\cdot}kg^{-1}{\cdot}K^{-1}$ and 1050 $J{\cdot}kg^{-1}{\cdot}K^{-1}$ were obtained for 150 nm and 750 nm thick TiO_2:Nb films, respectively, which is in agreement with the variation in κ.

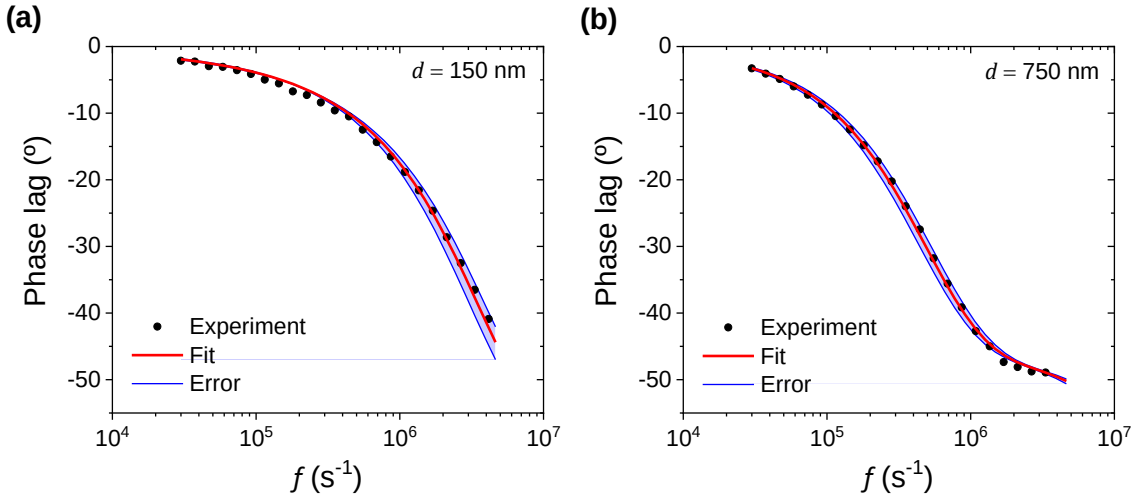

Figure 29. Frequency-dependent phase lag between the pump (405 nm) and probe (532 nm) lasers, for a 150 nm **(a)** and 750 nm thick **(b)** TiO_2:Nb thin film. The results from the fits are listed in Table 6. Error curves *(blue)* represents ± 0.2 $W{\cdot}m^{-1}{\cdot}K^{-1}$ and ± 0.3 $W{\cdot}m^{-1}{\cdot}K^{-1}$ uncertainty in κ for (a) and (b), respectively.

As comparison with the present results, Hong and co-workers (2013) [138] published ZT values lower than 0.01 for mesoporous TiO_2 sol-gel films, without disclosing thickness. In a similar deposition process, Xu and co-workers (2012) [139] prepared 320 nm thick TiO_2:Al films, with Al varying from (0 to 5) at.%, also presenting ZT values lower than 0.01. Kurita et al. (2006) [140] reported thermoelectric power factors in the range of 0.25 $mW{\cdot}m^{-1}{\cdot}K^{-2}$ at 900 K for heavily Nb-doped TiO_2 epitaxial films deposited at 800 K by pulse-laser deposition (PLD) with similar thickness, about 50 % of the value obtained in this work, albeit with similar S values, 145 $\mu V{\cdot}K^{-1}$. Moreover, the latter PF value was assessed at the triple of the temperature measured for the present TiO_2:Nb thin films, which are polycrystalline and were deposited below 450 K, in order to meet industrial applications. On the other hand, Ohta et al. (2005) [141] obtained a much higher PF and ZT values at 1000 K, ≈ 1.5 $mW{\cdot}m^{-1}{\cdot}K^{-2}$ and ≈ 0.3, respectively, for ~ 100 nm thick $SrTiO_3$ films deposited by PLD at ~ 1000 K, nonetheless with a much higher Nb content (40 at.%). No information in transmittance levels of the films is given for both literature references.

The average values at 300 K for electrical conductivity, n-type carrier concentration and mobility for TiO_2:Nb films are also displayed in **Table 6**. The thicker film has a higher electrical conductivity, 992 $\Omega^{-1}{\cdot}cm^{-1}$, when compared to the thinner one, 219 $\Omega^{-1}{\cdot}cm^{-1}$, as it would be expected. This explains why the Seebeck coefficient and thermal conductivity is higher in the thinner film, as mentioned in the last paragraph, since the number of impurities and defects (Nb^{5+} dopant ions, ionized oxygen vacancies) is lower, owing to the lower carrier concentration (~ 10^{20} cm^{-3}) and higher mobility (26 $cm^2{\cdot}V^{-1}{\cdot}s^{-1}$), when

compared to the thicker film, in **Table 6**. Moreover, for the thinner film, electron and phonon scattering is increased, due to decrease both in σ and κ, hence resulting a larger separation of charges between the hot and cold sides, and thus the increase in S. For the thicker film, the net result of cationic pentavalent doping of Nb in TiO_2 results in a substantial enhancement of transport properties due to charge unbalancing and oxygen vacancies creation [142], which concomitantly impacts on the increase in PF. Also, with the increase in impurities in TiO_2 for the thicker film, the mobility is reduced [143].

The TiO_2:Nb semiconductor band-gap (E_g) was derived from the measurement of optical transmittance and reflectance and subsequent calculation of the absorption coefficient (α), as presented in the Tauc plots in **Figure 30**.

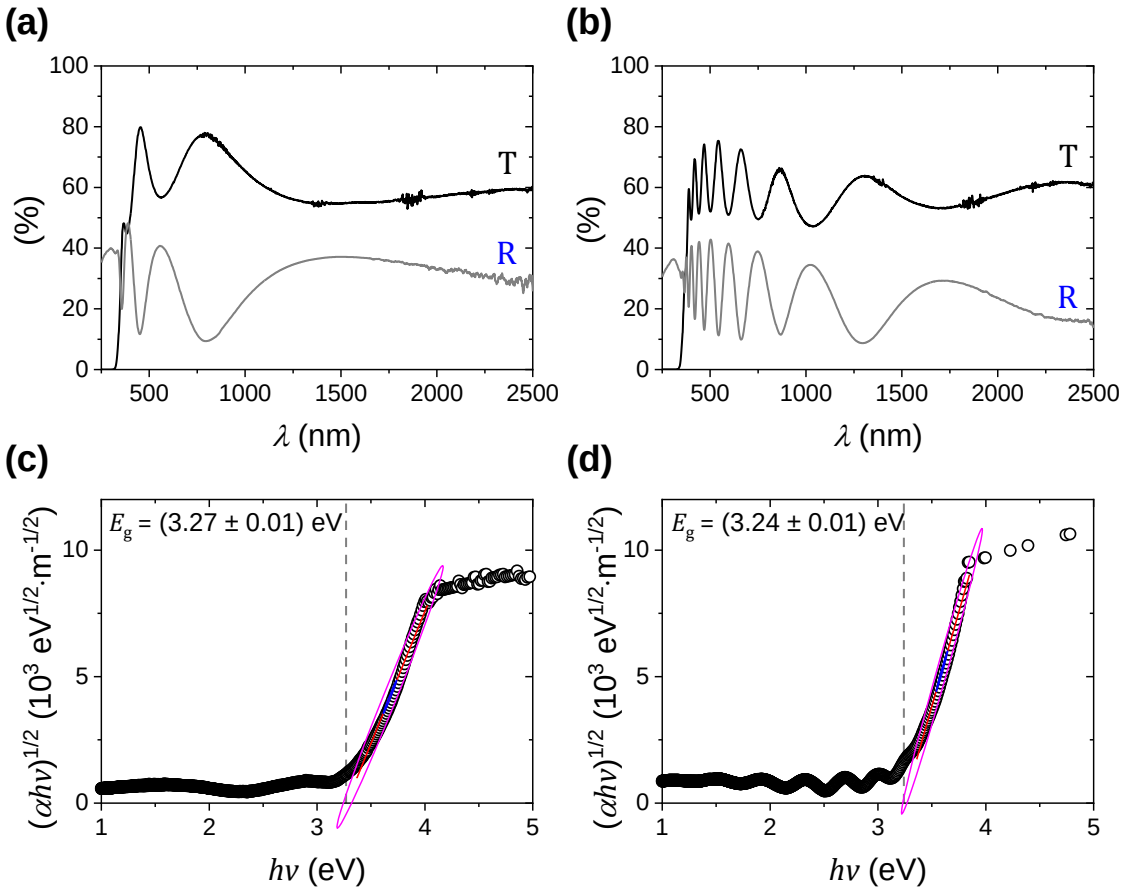

Figure 30. Transmittance (T) and Reflectance spectra of a 150 nm **(a)** and 750 nm thick **(b)** TiO_2:Nb thin film deposited on glass and respective determination of the optical band-gap **(c,d)**. The ellipses show the regions within 95 % confidence for the linear regressions.

From the intercept of the linear decay of α with the photon energy axis, values of $E_g = 3.27$ eV and $E_g = 3.24$ eV were determined for a 150 nm and 750 nm thick TiO_2:Nb film, respectively, which is slightly higher than that known for undoped TiO_2 (3.20 eV) [144]. The slight increase in E_g is attributed

to the Burstein-Moss effect [145] and can be explained through the Pauli Exclusion Principle, where a broadening of the band-gap is observed with increasing doping. This shift arises because the Fermi energy lies in the conduction band for heavy n-type doping (as is the case for TiO_2:Nb). The filled states, therefore, block thermal or optical excitation. Consequently, the measured band gap determined from the onset of interband absorption moves to higher energy (i.e. blue shift).

3.3. Partial Conclusions

Transparent n-type niobium-doped titanium dioxide thin films (TiO_2:Nb), with an optical band-gap of (3.21 to 3.24) eV, were successfully produced by reactive magnetron sputtering from a composite Ti:Nb target in an oxygen atmosphere. An amount of 1.5 at.% of Nb doping was estimated from XPS experiments. Optimized Nb-doped films exhibit pronounced thermoelectric properties with a very high absolute Seebeck coefficient of 155 $\mu V \cdot K^{-1}$ for a 150 nm thickness. The maximum PF and ZT values of 0.5 $mW \cdot m^{-1} \cdot K^{-2}$ and 0.18, respectively, were obtained for TiO_2:Nb films with a thermal conductivity of 1.3 $W \cdot m^{-1} \cdot K^{-1}$, which excels what is commonly found in the literature for transparent thin films.

Structural investigations by XRD and XAS at the Ti and Nb K–edges were performed to elucidate the role of Nb dopant on the film structure and properties. The as-deposited films possess anatase TiO_2 phase evidenced by XRD, however, the rutile phase is additionally formed upon film thermal annealing at 400 °C. Detailed information on the local structure of the thin films was obtained in terms of the RDFs determined from the simultaneous analysis of EXAFS data at two absorption edges using the RMC method. It was concluded that the local environment of the thin films is affected by Nb doping, however, their average local structure remains close to that of the anatase TiO_2 phase. This result is also supported by the analysis of XANES using ab initio simulations.

CHAPTER IV.

INFLUENCE OF THE OXYGEN FLOW

4. Influence of the Oxygen Flow

This chapter offers a comprehensibly study the of TiO_2:Nb thin films in order to optimize the production parameters to obtain transparent thin films with thermoelectric properties, and is based on the following publication:

> *J. M. Ribeiro, F. C. Correia, F. J. Rodrigues, J. S. Reparaz, A. R. Goñi, C. J. Tavares, "Transparent niobium-doped titanium dioxide thin films with high Seebeck coefficient for thermoelectric applications", Surface & Coatings Technology. 425 (2021) 127724 (https://doi.org/10.1016/j.surfcoat.2021.127724)* [146].

The TiO_2:Nb thin films presented so far showed great promise, but there is a need to tune their properties by optimizing the production parameters [72,73]. For this, several TiO_2:Nb thin films were deposited onto glass and Si substrates with thicknesses between approximately 100 nm and 300 nm. The reactive oxygen flow rate was varied in the range of (2.5 to 9.5) sccm. A post-deposition thermal annealing at 500 °C was performed to enhance the crystallinity of the films. The focus was put on the Oxygen flow during deposition and post-deposition annealing, due to their big influence on the electrical, optical and thermoelectrical properties of the thin films. The thin films were comprehensively characterized by SEM, XRD, XRR, XPS, UV-Vis spectroscopy, Hall effect, FDTR and Seebeck coefficient measurement technique, which were described in **Chapter 2**.

4.1. Experimental Details

4.1.1. Sample Fabrication

Thin films of TiO_2:Nb were produced by reactive DC magnetron sputtering. A target of Ti(96)Nb(4) wt.% (99.9 % of purity, FHR), with 10 cm of diameter, was used in planar configuration. The films were deposited on (76 × 26 × 1) mm^3 glass substrates (Normax Lda) and (10 × 10 × 0.5) mm^3 Si substrates, cut from P/B doped Si-wafer <100> (Siegert Wafers GmbH). To maximize the adhesion at the film/substrate interface, the substrates were cleaned with isopropyl alcohol (2-Propanol) and acetone in an ultrasonic bath, both for 15 min, removing contaminants on the surface of the substrates that may

arise during storage and handling [89,90]. The substrate-holders were mounted onto a rotating 6-position support controlled by a motor (used either in continuous rotation or to exchange samples over the magnetron). The chamber was evacuated with a primary rotary pump and a turbo molecular pump to achieve a base pressure of around 10^{-4} Pa. Target-substrate distance was kept at 6.5 cm and the substrate holder was heated up to 125 °C. Research grade Ar with 99.999 % purity was used as working gas to enable plasma formation and O_2 was used as reactive gas with flow rates in the range of (0 to 16) sccm. Prior to the deposition, 2 min of etching at 500 V was performed in an Ar atmosphere at a pressure of 1.8 Pa in continuous rotation at 18 rpm. This process removes oxides and impurities possibly accumulated and retained on the surface of the substrates and creates atomic defects in the substrate, enabling better nucleation of the film during deposition. Target current density, bias voltage and Ar flow were fixed at 12.7 $mA \cdot cm^{-2}$, –60 V and 40 sccm, respectively, for all depositions, depositing at a pressure of around 0.35 Pa.

A dummy deposition of 2 min for target cleaning (burn) was used in the first 68ositionn of the substrate holder. This was followed by the deposition of five samples in a single batch. The target current was turned off between depositions to enable a precise control of the next substrate holder position and deposition parameters. Experimental details concerning certain deposition variables were already optimized in previous works [72]. These deposition conditions enable an effective around 2 at.% of Nb substitutional doping in the TiO_2 cell [72,91]. Subsequently, the as-deposited TiO_2:Nb films were heat treated to enhance their microstructure and electrical properties [75,92], in a vacuum furnace at 10^{-3} Pa. The temperature was increased from room temperature to 500 °C in 90 min and maintained at 500 °C for 1 h, followed by a natural cooling stage to room temperature for 6 h.

The cathode potential hysteresis curve (**Figure 31**) was obtained by varying the reactive O_2 flow, ascending and descending, using the same processing conditions as previously described, with 5 min of stabilization time for each step. The metal mode is registered for oxygen flow rates below 3 sccm, while the oxide mode is achieved for oxygen flow rates above 8.5 sccm. The transition region seems to be between (6 and 8) sccm, which will be important in the discussion section.

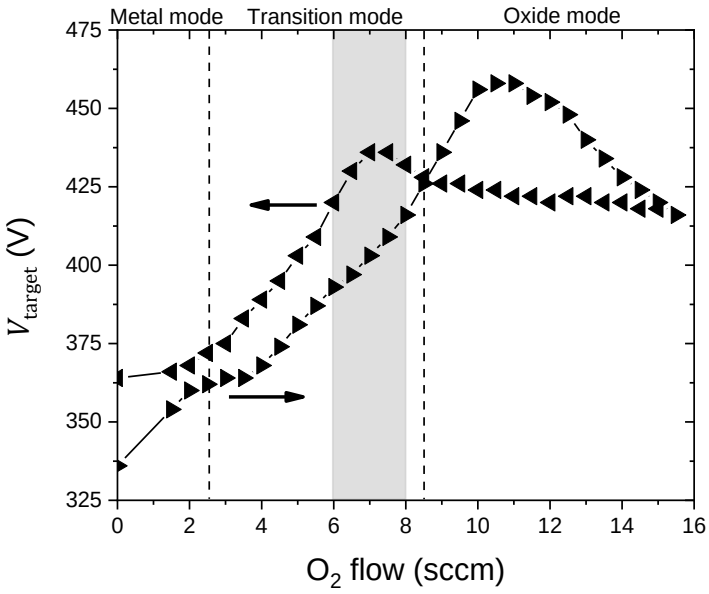

Figure 31. Cathode (target) potential vs. reactive oxygen flow hysteresis curve for the deposition of TiO_2:Nb thin films.

4.1.2. Sample Characterization

SEM was used to investigate the morphology and cross-section of the thin films, performed with a FEI NOVA NanoSEM 200. EDX was used to study the film composition. For cross-section imaging, the samples were cut with a diamond tip and fixed in the sample table with double-sided carbon tape.

XRD analysis was performed to investigate the crystallographic structure of the thin films, using a Bruker AXS D8 advanced Discovery diffractometer. The diffraction patterns were acquired in GIXRD, with incident angle of 1°, step of 0.02° and integration time of 1 s. CuKα radiation was used with a wavelength of 1.540 6 Å. The software Fityk was used to analyse the XRD patterns. The weight fraction of rutile is obtained through the Equation **(13)** [93], where A_R and A_A are the integrated areas of the main rutile and anatase peaks, (101) and (110), for anatase and rutile, respectively.

XRR analysis was also performed, and the patterns were analysed with the Bruker AXS Leptos software to investigate the chemical homogeneity, film thickness, surface roughness and density.

XPS was used to evaluate the film composition, along with the valence state and binding energy of dopant ions, and as well as of the Ti and O ions. The experiments were performed using a Kratos Axis-Supra instrument equipped with monochromatic Al–Kα radiation (1 486.6 eV). A co-axial electron neutralizer was used to minimize surface charging. Photoelectrons were collected from a take-off angle

of 90° relative to the sample surface. The measurement was done in a CAE mode with a 160 eV pass energy and 15 mA of emission current for survey spectra and 40 eV pass energy for high resolution spectra, using an emission current of 20 mA. Charge referencing was done by setting the lower binding energy of the C1s hydrocarbon peak at 284.8 eV. The Unifit Software was used to fit the recorded experimental XPS spectra.

The optical transmittance and reflectivity of the thin films were analysed with a Shimadzu UV-2501PC UV-Vis spectrophotometer in the (300 to 900) nm wavelength range. The transmittance was averaged from (400 to 700) nm, equivalent to the visible wavelength range. The optical band-gap energy (E_g) of the films was evaluated from Tauc plots of the absorption coefficient (α), determined using equations **(24)** and **(25)**, as the intercept of $(\alpha h\nu)^{1/2}$ versus photon energy ($h\nu$) in the high absorbance region.

The electrical conductivity of the thin films, was analysed using an Ecopia AMP55T HMS-5000 Hall Effect measuring system, equipped with a DC four-point probe apparatus in the Van der Pauw configuration. The measurements were performed at room temperature under atmospheric pressure, with an applied magnetic field of approximately 0.560 T.

The thermal properties of the thin films were determined using FDTR. A 60 nm thick Au transducer was evaporated onto the surface of the specimens. The output power of the pump laser (405 nm) was modulated in the frequency range between 30 kHz and 20 MHz, which generates thermally induced oscillations of the reflectivity of the sample, leading to a modulation of the reflected power of the continuous wave probe laser (532 nm). The frequency dependent phase lag between the heat wave generated by the pump laser and the harmonic response of the sample is sensed by the probe laser using a lock-in amplifier and modelled numerically solving the parabolic heat equation for the behaviour of a stack of layers (Au, TiO_2:Nb film and Si substrate) [112,113].

The Seebeck coefficient was evaluated in custom-made equipment operated in low vacuum (1 Pa) using two Peltier devices (Quick-Ohm Küpper & Co. GmbH) for heating and cooling the edges of (25 × 75) mm^2 sample area. An electrical circuit measures the Seebeck voltage generated in the sample, in response to a thermal gradient across the film surface. The Seebeck coefficient (S) was estimated with Equation **(2)**, with ΔT being the temperature difference between the edges of the plane of the film and ΔV the respective measured potential difference [9,114]. The Seebeck coefficient was measured using different thermal gradients applied to the film deposited onto a glass slide. The obtained ΔV values were plotted as a function of ΔT and linearly fitted to determine the slope, and subsequently the Seebeck coefficient.

4.2. Results and Discussion

From the observation of the film cross-sections (**Figure 32**), the film thickness decreases with increasing reactive oxygen flow rate, for a constant deposition time (5 min). It is apparent that the TiO_2:Nb thin films have homogeneous surfaces, without significant morphology variation with increasing oxygen flow rate during deposition. Although sputtering processes typically produce columnar structures with boundaries containing voids, this is not observed in the SEM micrographs in **Figure 32**. A columnar structure is not discerned due to the dense nature of the thin layers and the resulting film structure appears to be isotropic. Roughness values between (0.7 and 1.3) nm and density values between (3.2 and 4.4) $g \cdot cm^3$ were obtained from XRR fits (**Table B 1**).

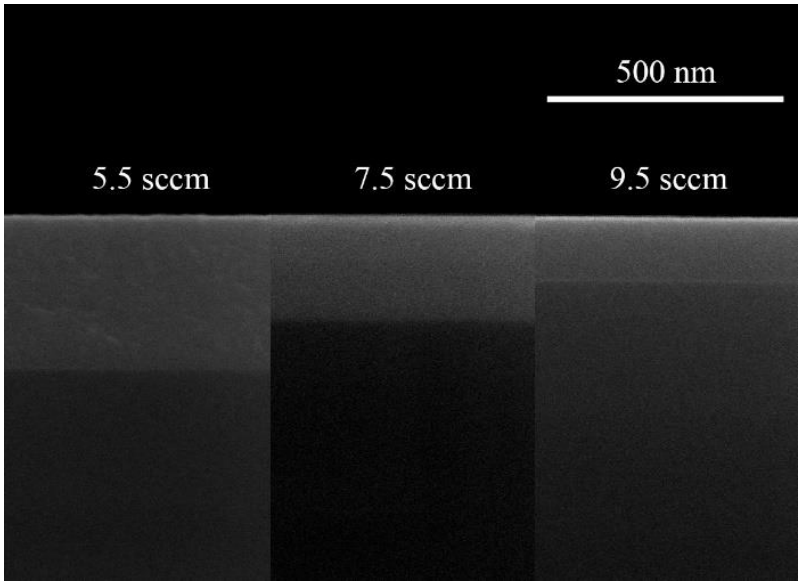

Figure 32. SEM cross-section micrographs from three TiO_2:Nb thin films deposited with reactive oxygen flow rates of 5.5 sccm, 7.5 sccm and 9.5 sccm, having thicknesses of 322 nm, 226 nm, 137 nm, respectively.

From EDX experiments (**Figure A 1**) it was possible to quantify O, Ti and Nb elemental composition, with 82.6 at.%, 16.6 at.% and 0.9 at.%, respectively. This is in agreement and within measurement error, with the Ti(96)Nb(4) wt.% (2.1 at.% of Nb) of the sputtering target used for the thin film deposition. The sputter yield of Nb and Ti is 0.474 and 0.394, respectively, for Ar^+ with an energy of 400 eV [147]. Since Nb is also closer in weight to Ar than Ti and has greater sputter yield than Ti, it is more easily pulverized. This Nb content is expected and desired as a threshold, since for a composition greater than 5 at.% the thin film loses substantial transparency.

XPS experiments were performed on TiO_2 (undoped) and TiO_2:Nb thin films to determine the chemical bonding state and film composition, as seen in **Figure 33** and **Figure C 2**, **Figure C 1** and **Figure C 3**.

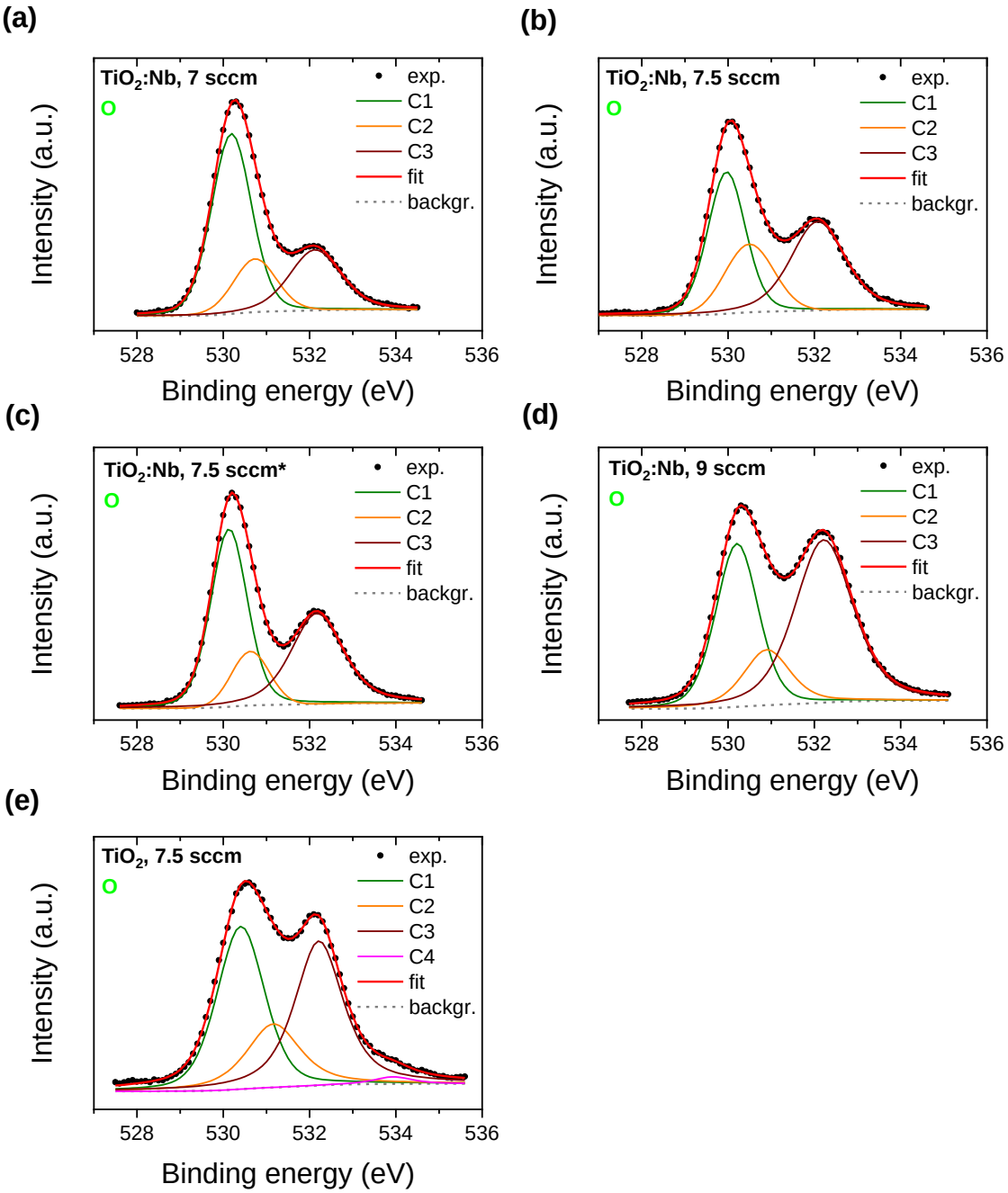

Figure 33. XPS spectra and respective fits for the O 1*s* core lines for as-deposited TiO_2:Nb thin film with a reactive oxygen flow rate of 7 sccm **(a)**, as-deposited TiO_2:Nb with 7.5 sccm **(b)**, TiO_2:Nb with 7.5 sccm after annealing (*) **(c)**, as-deposited TiO_2:Nb with 9 sccm **(d)** and as-deposited undoped TiO_2 with a reactive oxygen flow rate of 7.5 sccm.

The quantification of the elemental composition derived from the XPS fits for the Ti $2p$, O $1s$ and Nb $3d$ core levels [133–135] is presented in **Table 7**, whereas the respective fitting parameters are listed in **Table 8**, **Table 9** and **Table 10**, respectively. Specific constraints were considered for all XPS fits [134], namely relative area ratio, FWHM and Lorentzian-Gaussian relative profile in doublet peaks. Si traces were found in the survey spectra due to the incidence of the beam spot on the sample border, where the Si substrate is exposed.

Table 7. Composition of the as-deposited TiO_2:Nb and TiO_2 thin films as a function of reactive oxygen rate (in sccm) during deposition; * denotes a post-deposition thermal annealed sample at 500 °C in vacuum.

Sample	O_2 flow (sccm)	Ti (at.%)	O (at.%)	Nb (at.%)
TiO_2:Nb	7.0	38.4	60.4	1.2
TiO_2:Nb	7.5	38.0	60.9	1.1
TiO_2:Nb*	7.5	32.4	66.3	1.3
TiO_2:Nb	9.0	34.1	64.2	1.7
TiO_2	7.5	20.9	79.1	-

Table 8. Ti 2p core level XPS fitting parameters for the samples listed in Table 7.

Sample	Position (eV)	FWHM (eV)	L-S (eV)	Areas 3/2 / ½ (%)
TiO_2:Nb, 7 sccm	458.8	1.0	5.7	62/38
TiO_2:Nb, 7.5 sccm	458.7	1.0	5.7	69/31
TiO_2:Nb, 7.5 sccm*	458.9	1.0	5.7	61/39
TiO_2:Nb, 9.0 sccm	458.9	1.2	5.7	68/32
TiO_2, 7.5 sccm	458.8	1.2	5.7	66/34

Table 9. O 1s core level XPS fitting parameters for the samples listed in Table 7.

Sample	Position C1/C2 (eV)	FWHM C1/C2 (eV)	Areas C1/C2 (%)
TiO_2:Nb, 7 sccm	530.2/530.7	1.1/1.1	76/24
TiO_2:Nb, 7.5 sccm	530.0/530.5	1.0/1.3	63/37
TiO_2:Nb, 7.5 sccm*	530.1/530.3	1.0/1.0	70/30
TiO_2:Nb, 9.0 sccm	530.2/530.9	1.1/1.1	71/29
TiO_2, 7.5 sccm	530.4/531.2	1.3/1.1	40

Table 10. Nb 3d core level XPS fitting parameters for the samples listed in Table 7.

Sample	Position (eV)	FWHM (eV)	L–S (eV)	Areas 5/2 / 3/2 (%)
TiO_2:Nb, 7 sccm	207.3	1.0	2.8	60/40
TiO_2:Nb, 7.5 sccm	207.2	1.0	2.8	63/37
TiO_2:Nb, 7.5 sccm*	207.4	1.0	2.8	61/39
TiO_2:Nb, 9.0 sccm	207.5	1.1	2.8	60/40
TiO_2, 7.5 sccm	-	-	-	-

In respect to the Ti $2p$ and Nb $3d$ core level analysis, the spin-orbital (L–S) splitting is observed for both Ti $2p$ and Nb $3d$ core levels, being the widths 5.7 eV and 2.8 eV, respectively, as presented in **Table 8** and **Table 10**, which is in agreement with the literature [133,134]. The binding energies associated with Ti $2p$ (around 459 eV) and Nb $3d$ (around 207 eV) core lines are indicative of Ti–O and Nb–O bonds, respectively, and no traces of Ti–Ti and Nb–Nb metal bonds are present (**Figure C 2** and **Figure C 1**). These metal bonds should appear at around 454 eV for Ti and at around 202 eV for Nb, being absent in the survey spectra (**Figure C 3**). From this, it can de deduced that the TiO_2 thin films were efficiently doped with niobium, since peaks ascribed to binding energies of (207.2 to 207.5) eV are indexed to Nb $3d$ orbitals of pentavalent Nb ions [148]. Subsequently, from the fitting analysis, a lower level of Nb doping of (1.1 to 1.2) at.% is obtained for the films with lower oxygen inlet during deposition (7.0 sccm to 7.5 sccm), whereas for higher oxygen flow rates (9 sccm) the level of Nb doping increases to 1.7 at.% (see **Table 7** and **Figure 33**). The quantification of titanium is slightly influenced by the fact the Nb $3s$ core line binding energy (around 467 eV) is close to that of higher binding energy peak of the Ti $2p$ doublet (around 465 eV); albeit the former having much lower peak area. Hence, a careful approximation was taken into account for this partial overlap.

The concentration of Ti atoms varies between 38.0 at.% and 38.4 at.% for the lower limit of oxygen inlet, while decreasing substantially close to stoichiometry 34.1 at.% for the higher oxygen content during deposition, as expected since the O content in the film increases in this process from (60.4 to 60.9) at.% to 64.2 at.%, respectively. The post-deposition thermal annealing for the TiO_2:Nb film deposited with 7.5 sccm of oxygen flow rate (* in **Table 7**, **Table 8**, **Table 9** and **Table 10**) resulted in recrystallization with a close to stoichiometric TiO_2 (around 1:2) composition and 1.3 at.% of Nb. The expected area ratio between the Ti $2p$ doublet peaks is 2:1 ($2p_{3/2}$:$2p_{1/2}$), however a slight deviation occurs for films deposited with higher oxygen flow rate during deposition, as seen in **Table 8**. For the case of Nb $3d$, the

expected area ratio between the doublet peaks is 3:2 ($3d_{5/2}$:$3d_{3/2}$), which is approximately constant for all doped films.

As for the O $1s$ core level, the fit of the TiO_2:Nb films includes three components, C1, C2 and C3, being associated with Ti–O bonds (C1), defective oxygen (vacancies) and with Nb–O bonds (C2), and surface-adsorbed oxygen and hydroxides impurities (C3) [134,149]. Component C2 is increased with Nb concentration (**Figure 33** and **Table 9**) from the substitution of Ti^{4+} ions with Nb^{5+} in the anatase cell. Component C3 is substantially enhanced for undoped TiO_2 and TiO_2:Nb films deposited with higher amount of reactive oxygen inlet during sputtering. The area ratio between C1 and C2 is approximately 70:30 % for all Nb-doped TiO_2 films. In the case of the undoped TiO_2 film, component C1 is 40 % of the total area represented by the four components that were fit due to the asymmetry of the peaks, excessive oxygen in the film close to the surface and aforementioned adsorbed oxygen and hydroxide species on the film surface, towards which XPS is very sensitive. It is noteworthy to mention that the undoped TiO_2 thin film is over stoichiometric in oxygen (79.1 at.%).

The XRD in **Figure 34** indicate the influence of reactive oxygen flow rate during deposition in the crystalline phase of a series of deposited films after a post-deposition annealing. The patterns identify the main diffraction peaks from rutile (110), $2\theta = 27.4°$, and anatase (101), at $2\theta = 25.3°$, respectively referenced from the Joint Committee on Powder Diffraction Standard (JCPDS cards number 21-1272 and 21-1276, respectively). **Figure 35** shows XRD for TiO_2:Nb thin films measured as-deposited and after annealing, relating to thickness (deposition time), deposition temperature and the measured Seebeck coefficients (discussed in **Section 4.1.2**). Firstly, higher deposition temperatures and the post-deposition annealing at 500 °C clearly develops the crystallization of the anatase phase. This is supported by the literature, confirming that TiO_2 annealing at (400 to 500) °C results in the crystallization of anatase, while rutile can be obtained for annealing temperatures around 635 °C [150–152]. Secondly, no phase can be discerned for as-deposited films with deposition times below 3 min. This can be due to the low resolution for XRD analysis for very thin films or their amorphous nature. After annealing the anatase phase can be discerned. It is expected that up to a 5 at.% Nb-doping will develop anatase phase [72], albeit slightly strained. This is not always the case for the obtained TiO_2:Nb thin films, since for greater than 3 min of deposition time both anatase and rutile are discerned.

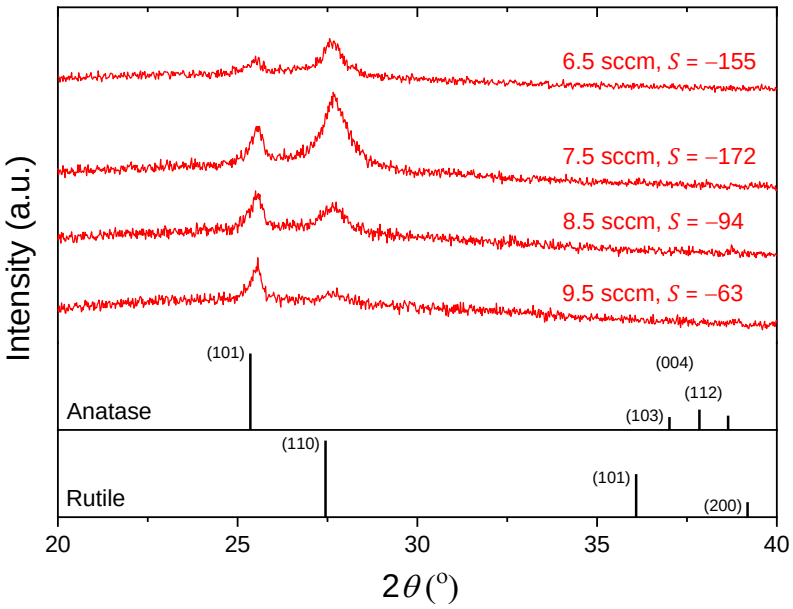

Figure 34. XRD for post-deposition annealed TiO_2:Nb thin films deposited with 6.5 sccm, 7.5 sccm, 8.5 sccm and 9.5 sccm of reactive oxygen flow rates, with corresponding Seebeck coefficient values (S, in $\mu V \cdot K^{-1}$). Lower portion shows XRD patterns for TiO_2 anatase JCPDS card 21-1272 and TiO_2 rutile JCPDS 21-1276 card.

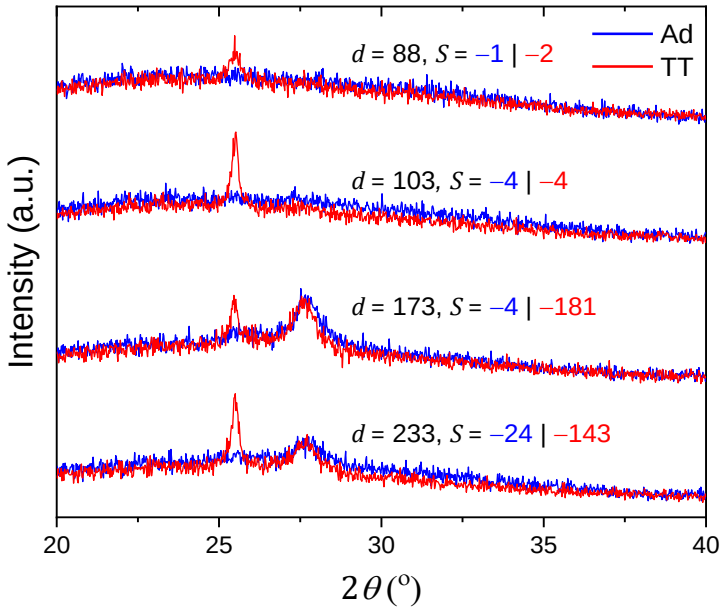

Figure 35. XRD for TiO_2:Nb thin films deposited with 7.5 sccm of reactive oxygen flow rates, as-deposited *(Ad, blue)* and after annealing *(TT, red)*.The corresponding film thickness (d, in nm) and the Seebeck coefficient (S, in $\mu V \cdot K^{-1}$) is indicated in the legend of each diffractogram.

There is an obvious relation between the Seebeck coefficient and the rutile phase, as seen in **Figure 36**, as the films with higher Seebeck coefficient also have a higher fraction of rutile phase. Lower

oxygen flow rates develop preferentially the rutile phase, while higher oxygen flow rate enhance crystallization of anatase phase. Both anatase phase and rutile phases are a tetragonal structure but differ from the arrangement of oxygen ions and have indirect band-gaps, although there is also a direct forbidden transition near 3 eV in rutile. Here the valance band corresponds to the O $2p$ orbitals and the conduction band arises from Ti $3d$ orbitals. Due to a crystal field of six oxygen atoms, the Ti $3d$ states split into two components, making the field not exactly octahedral. This small oxygen deficiency is considered as an impurity and provides n-type doping.

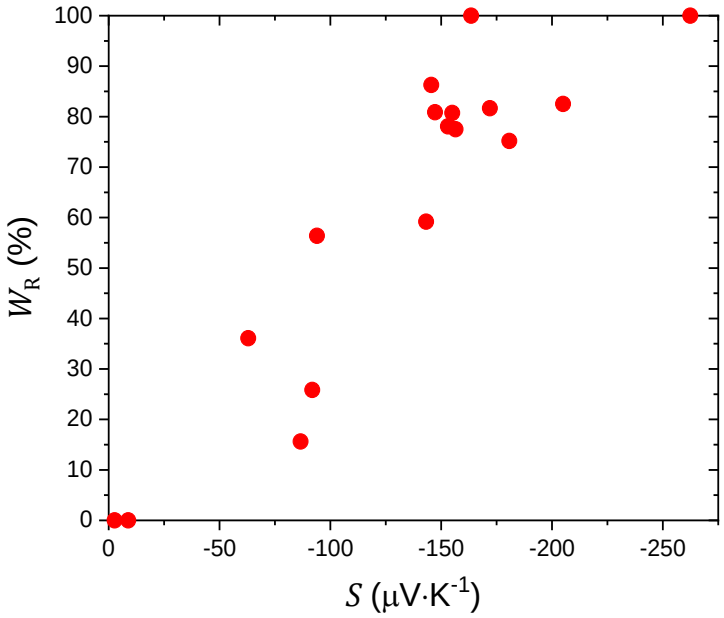

Figure 36. Weight fraction of rutile calculated from equation (13) as a function of the measured Seebeck coefficient for TiO_2:Nb thin films measured after annealing.

The transmittance of the TiO_2:Nb thin films was measured using the glass substrate as the baseline. The specular reflectance of the thin films was measured using the calibration mirrors as the baseline. The optical transmittance and specular reflectance spectra are presented in **Figure D 1**. **Figure 37** shows the evolution of the transmittance and reflectance averaged from 400 nm to 700 nm of the TiO_2:Nb thin films deposited for 5 min as a function of the oxygen flow rate used during deposition. Thicknesses range from (150 to 300) nm, depending on the oxygen flow rate during deposition. Thin films produced with oxygen below 5.5 sccm were completely opaque, whereas those produced over 7 sccm of oxygen flow rate have transmittance values over 60 %, with a maximum transmittance of 86 %. Similar to the reactive oxygen hysteresis curve back in **Figure 31** (**Section 4.1.1**), (6 to 7) sccm of reactive oxygen flow rate during sputtering seems to be the threshold of transition between metal (Ti) and

oxide (TiO_2). The average transmittance and reflectance were not significantly affected by the thermal annealing, so only the as-deposited thin film $\overline{T}_{\mathrm{vis}}$ and $\overline{Rs}_{\mathrm{vis}}$ results are shown.

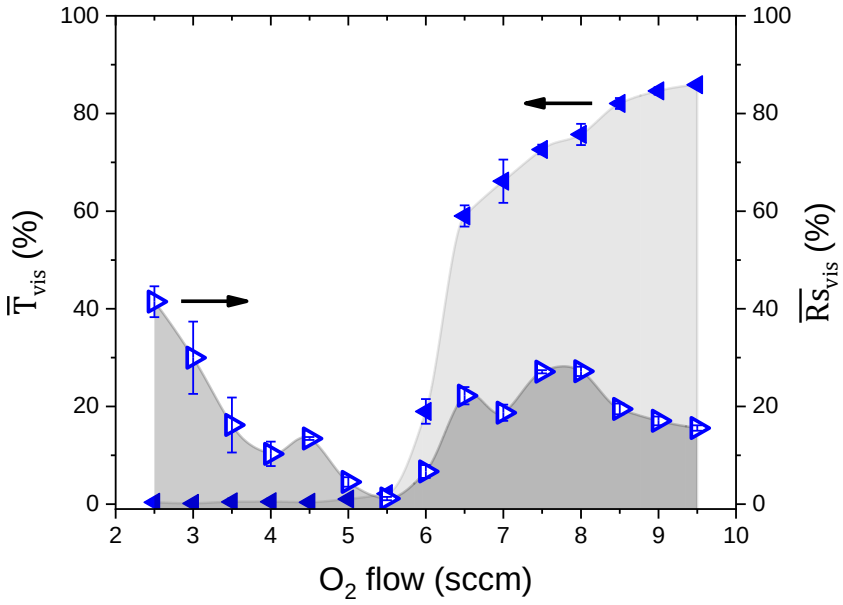

Figure 37. Transmittance *(full triangles)* and specular reflectance *(open triangles)* of the as-deposited TiO_2:Nb thin films, averaged from 400 sccm to 700 nm, as a function of the reactive oxygen flow rate during deposition.

Figure 38 shows the as-deposited transmittance (T) and specular reflectance (Rs) spectra and respective Tauc plot for a TiO_2:Nb thin film deposited with a reactive oxygen flow rate of 7.5 sccm, yielding an average transmittance of (72 ± 1) %, an average reflectance of (27.1 ± 0.3) % and an energy band-gap of (3.345 ± 0.002) eV. Below the absorption edge the average transmittance and reflectance remain constant and the observed signal oscillations are originated by the multiple internal reflections of the light in the film, which is an effect of the film thickness. Reflectance signal is low because the plasma frequency is in the far infrared.

Band-gap energies derived from Tauc plots are plotted in **Figure 39**, where the E_g energy increases with the increase in reactive oxygen flow rate used during deposition.

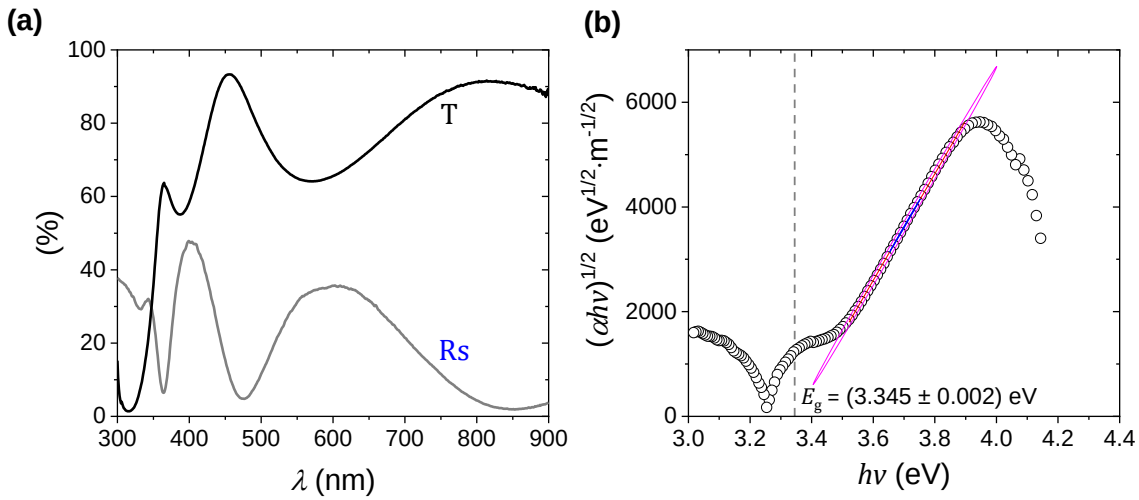

Figure 38. Transmittance and specular reflectance spectra **(a)** and Tauc plot **(b)** for an as-deposited TiO_2:Nb thin film deposited for 5 min with 7.5 sccm of oxygen flow rate.

The band-gap energy increases after post-deposition annealing for all of the studied TiO_2:Nb thin films, with a higher increase for films with lower oxygen flow used during deposition. The as-deposited values vary from (3.04 ± 0.01) to (3.42 ± 0.01) eV, corresponding to as-deposited TiO_2:Nb thin films with 6.0 sccm and 9.5 sccm oxygen flow rates during deposition, respectively, increasing to (3.20 ± 0.01) eV and (3.422 ± 0.002) eV, respectively, after annealing. This increase is explained by the filling of the electronic states in the conduction band by electron accumulation, which impacts on the increase of the photon energy that is required for the inter-band transitions from the valence band to the higher energy vacant states in the conduction band. Typically, the increase of the band-gap in TCOs is justified by the Burstein-Moss effect [145,153]. For n-type materials, doping increases the number of electrons which populate the conduction band lower levels, resulting in the apparent band-gap widening. Since there are more available electrons in metallic films than for oxide films, the band-gap increases. However, when observing **Figure 39** the same cannot be concluded since the resistivity is lower for films with lower band-gap. This variation can be attributed instead to a structural effect due to the phase transition from rutile to anatase, when increasing the oxygen flow. Anatase (3.2 eV) has a higher band-gap than that of rutile (3.0 eV), which further justifies the increase of the band-gap both for higher reactive oxygen flow during deposition and after annealing. The highest band-gap energy of (3.45 ± 0.01) eV, measured after annealing, was obtained for a TiO_2:Nb thin film deposited with 9 sccm of reactive oxygen flow rate.

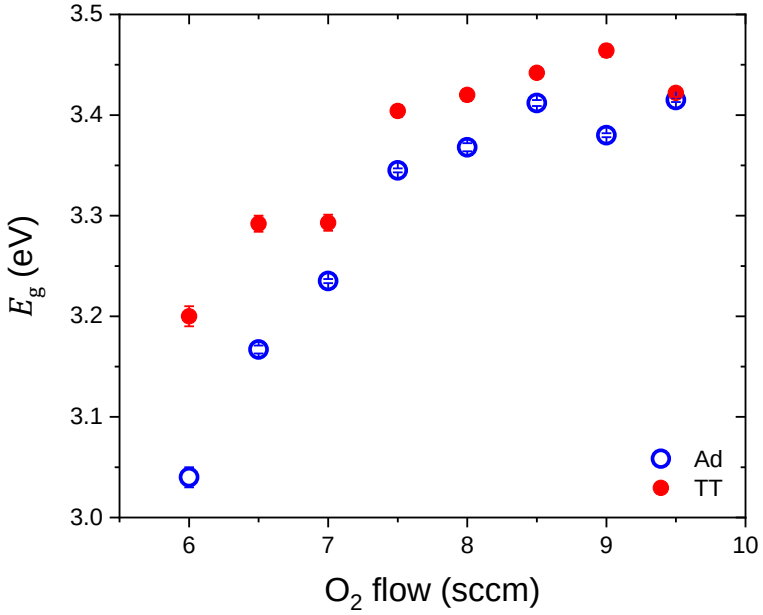

Figure 39. Band-gap energies for TiO_2:Nb thin films as a function of the reactive oxygen flow rate used during deposition, as-deposited *(Ad, blue)* and after annealing *(TT, red)*.

The average electrical resistivity as a function of the oxygen flow rate used during deposition is registered in **Figure 40**. As expected, the films demonstrate an increase in electrical resistivity due to the increase in the reactive oxygen content during deposition. The electrical resistivity increases almost two orders of magnitude above 6 sccm. Oxygen flow rates between 6 sccm and 8 sccm produce electrical resistivities around 10^{-1} Ω·cm. The thermal annealing decreases the electrical resistivity for films deposited with reactive oxygen flow rates greater than 6 sccm, achieving a minimum resistivity of around (5×10^{-2}) Ω·cm in the (6 to 8) sccm range. From hysteresis curve presented in **Figure 31** (**Section 4.1.1**), for a reactive oxygen flow rate during deposition above 8 sccm the films are in the oxide mode. Hence, a higher electrical resistivity is expected. While below 5.5 sccm, the films are deposited in metal mode, being opaque with a high electrical conductivity (**Figure 37**). These changes in electrical conductivity are also in agreement with the XRD results in **Figure 34**, where higher reactive oxygen flow rates during deposition enhances the crystallization of the anatase phase. Although the anatase phase has a higher band-gap than rutile, a staggered energy band alignment between the two phases explains why anatase is able to promote free electrons in the conduction band in the presence of oxygen vacancies [154,155]. Finally, it is obvious that the annealing process, which also favours the development of anatase phase, is crucial for lowering the electrical resistivity (to the 10^{-2} Ω·cm order of magnitude).

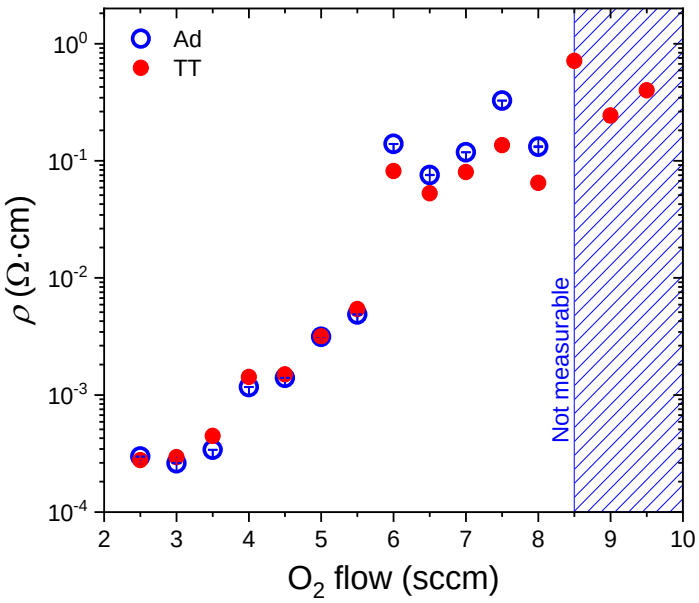

Figure 40. Electrical resistivity of TiO_2:Nb thin films as a function of oxygen flow rate during deposition, measured as-deposited *(Ad, blue)* and after thermal annealing at 500 °C *(TT, red)*. The *blue striped zone* refers to very resistive as-deposited films, unable to be measured.

The thermal conductivity (κ) was obtained through FDTR experiments and the results can be seen in **Figure 41** and **Figure 42**, being plotted in relation to film thickness and oxygen flow rate during deposition. Firstly, thin films were produced with deposition times between 4 min and 15 min (oxygen flow rate fixed at 7.5 sccm). Secondly, the reactive oxygen flow rate was varied between 4.5 sccm and 8 sccm (deposition time fixed at 5 min). From the FDTR results it is concluded that the TiO_2:Nb films have a thermal conductivity below 2 $W{\cdot}m^{-1}{\cdot}K^{-1}$ for film thickness smaller than 500 nm. The thermal conductivity appears to increase with both film thickness and the oxygen flow rate during deposition. For oxygen flow rate values between (6.5 and 7.5) sccm, the thermal conductivity is very low, in the range of (1.3 to 1.7) $W{\cdot}m^{-1}{\cdot}K^{-1}$, which excels what is commonly found in the literature for transparent thin films. In order to calculate the figure of merit for thin films deposited with oxygen flow rates outside the measured values (below 4.5 sccm and above 8 sccm), the thermal conductivity values were extrapolated from two linear fits in **Figure 42**: for oxygen flow rates below 6.5 sccm the thermal conductivity decreases from (1.5 to 0.8) $W{\cdot}m^{-1}{\cdot}K^{-1}$ with decreasing oxygen flow rates due to the presence of structural defects owing to oxygen deficiency; for oxygen flow rates above 6.5 sccm a constant thermal conductivity value of (1.52 ± 0.05) $W{\cdot}m^{-1}{\cdot}K^{-1}$ is expected. For polycrystalline films, the thermal conductivity should be independent of thickness, because the phonon scattering is mainly dominated by grain boundary scattering. When considering low thicknesses, though, additional scattering from surface roughness might

set in, further reducing the thermal conductivity (**Figure 41**). There was no significant change in the thermal conductivity of the thin films measured as-deposited and after annealing, hence only the as-deposited results are shown.

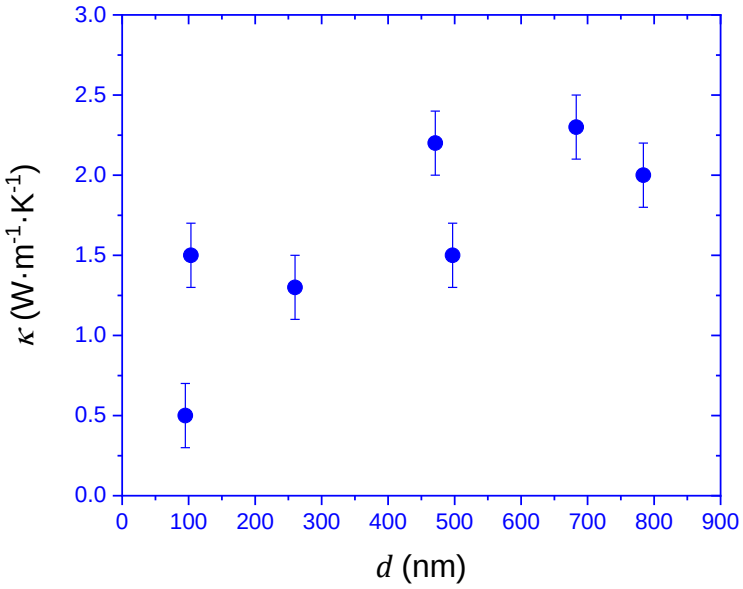

Figure 41. Thermal conductivity of TiO_2:Nb thin films measured as-deposited by FDTR as a function of film thickness. Oxygen flow rate during deposition was set to 7.5 sccm.

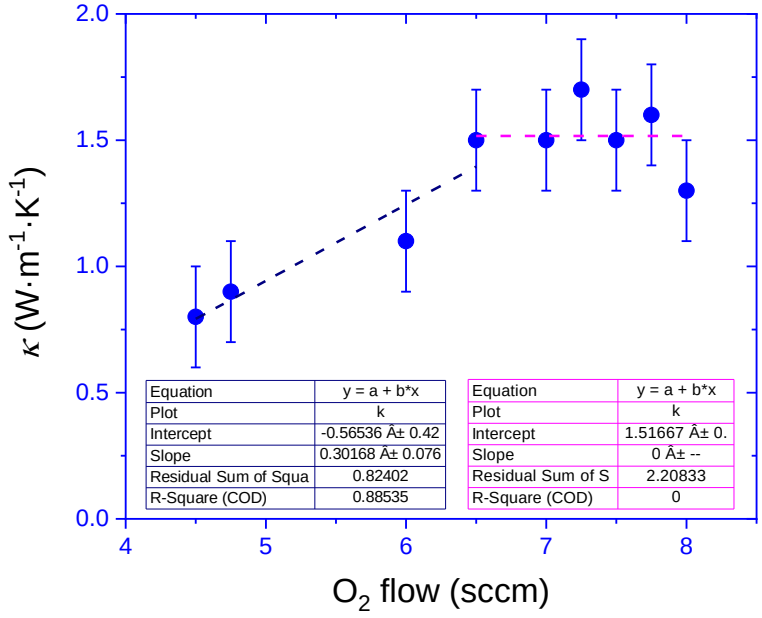

Figure 42. Thermal conductivity of TiO_2:Nb thin films measured as-deposited by FDTR as a function of reactive oxygen flow rate during deposition. The data was fitted with two linear fits: for oxygen flow rates below 6.5 sccm *(navy dashed line)*; for oxygen flow rates above 6.5 sccm *(magenta dashed line)*.

Figure 43 shows the Seebeck coefficient of TiO_2:Nb thin films for both as-deposited and after annealing states, plotted in relation to the oxygen flow rate during deposition. A negative potential was measured for all films, indicating n-type nature of TiO_2. From the results presented in **Figure 41**, the absolute Seebeck coefficient increases concomitantly with oxygen flow rate, reaching a maximum of (223 ± 1) $\mu V \cdot K^{-1}$ at 7 sccm and decreasing substantially thereafter. The observed trend relates with the reactive oxygen hysteresis curve (**Figure 31** in **Section 4.1.1**), since films deposited in metal mode are very electrically and thermally conductive, which inhibits the separation of charge carriers. On the other hand, for films deposited above the aforementioned oxygen flow rate threshold (7 sccm) the excessive oxygen in the film structure renders transforms the material into an electrical insulator and decreases the thermoelectric property. The annealing process increased the Seebeck coefficient of thin films deposited with 6 sccm and over 7.5 sccm of oxygen flow rate, while decreased this property for thin films deposited with 6.5 sccm and 7 sccm of oxygen flow rate.

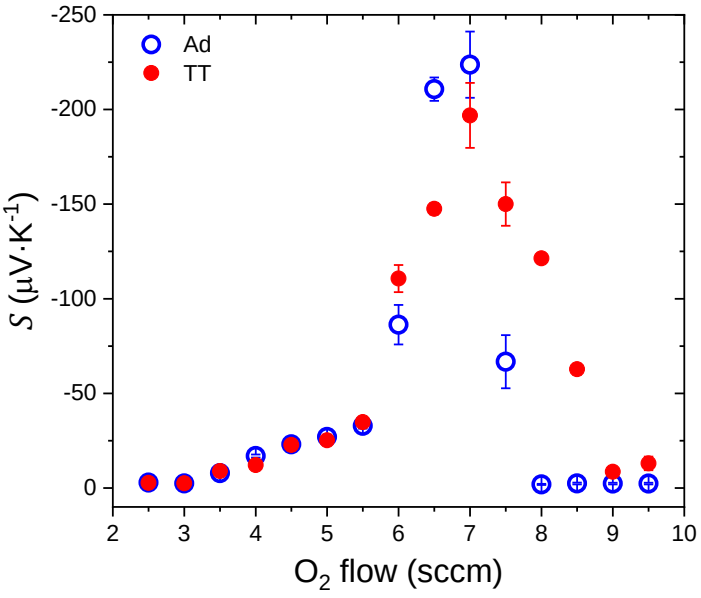

Figure 43. Seebeck coefficient for TiO_2:Nb thin films as a function of the reactive oxygen flow rate during deposition, measured as-deposited *(Ad, blue)* and after annealing *(TT, red)*.

From the results in **Figure 44**, the Seebeck coefficient increases with film thickness (for oxygen flow rate set at 7.5 sccm), with absolute values greater than 100 $\mu V \cdot K^{-1}$ for thicknesses over 200 nm. The post-deposition thermal annealing improves the thermoelectric property for films with as-deposited absolute Seebeck coefficients lower than 150 $\mu V \cdot K^{-1}$ (**Figure 43** and **Figure 44**). However, when the as-deposited thin films already exhibit an absolute Seebeck coefficient larger than 150 $\mu V \cdot K^{-1}$, the annealing process is useless. This correlates with the XRD results previously presented in **Figure 35**

and **Figure 36**, where a higher Seebeck coefficient is ascribed to the rutile phase, while the anatase phase, favoured by the annealing process, relates to higher electrical conductivity.

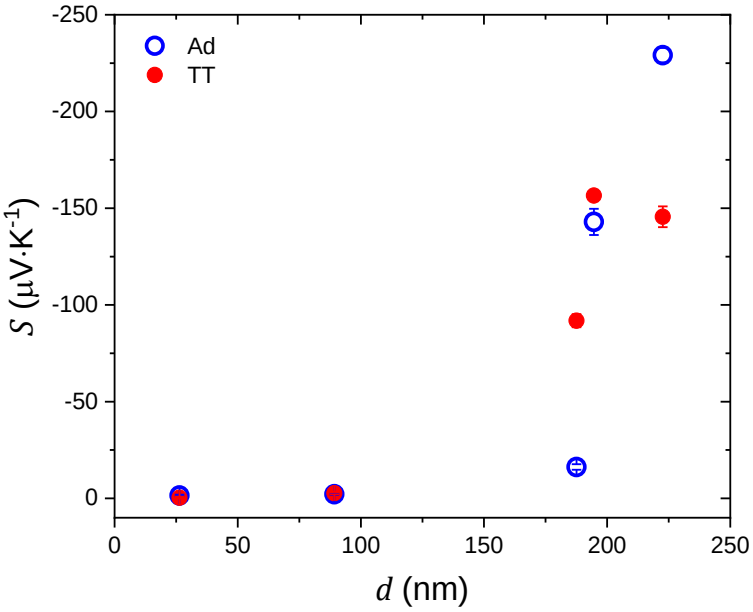

Figure 44. Seebeck coefficient of TiO_2:Nb thin films as a function of the film thickness. Oxygen flow rate was set at 7.5 sccm, measured as-deposited *(Ad, blue)* and after annealing *(TT, red)*.

The thermoelectric power factor and figure of merit at 300 K were calculated using equations **(7)** and **(8)** and plotted in relation to the oxygen flow rate during deposition (**Figure 45** and **Figure 46**). **Table 11** presents a summary of the most relevant results and **Figure 47** shows the figure of merit values for as-deposited films plotted against films after annealing. As expected from the deposition hysteresis curve (**Figure 31** in **Section 4.1.1**), PF and ZT reach a maximum in the range of (6.5 to 7.0) sccm. Although the thin film produced with 4.5 sccm of oxygen flow rate has one of the highest PF ((38 ± 9) μW·m^{-1}·K^{-2} as-deposited and (35 ± 8) μW·m^{-1}·K^{-2} after annealing) and ZT (0.044 ± 0.007 as deposited and 0.013 ± 0.007 after annealing), its average transmittance is very low, so it is not considered an appropriate film for the intended purpose, which is transparent thermoelectric films. The thin film produced with 7 sccm of oxygen flow rate improved its PF after annealing, from (42 ± 7) μW·m^{-1}·K^{-2} to (48 ± 9) μW·m^{-1}·K^{-2}, achieving a ZT of 0.009 ± 0.002 after annealing. The film produced with 6.5 sccm of oxygen flow rate wielded the largest PF and ZT measured for an as-deposited film, (59 ± 4) μW·m^{-1}·K^{-2} and 0.013 ± 0.002, respectively, but decreased slightly the PF after annealing to (41 ± 3) μW·m^{-1}·K^{-2}.

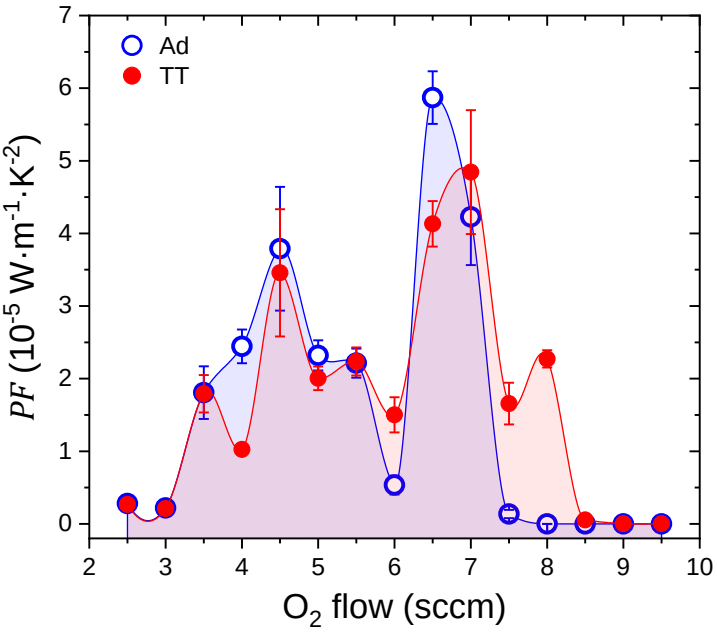

Figure 45. Thermoelectric power factor for TiO_2:Nb thin films as a function of the reactive oxygen flow rate during deposition, calculated as-deposited *(Ad, blue)* and after annealing *(TT, red)*.

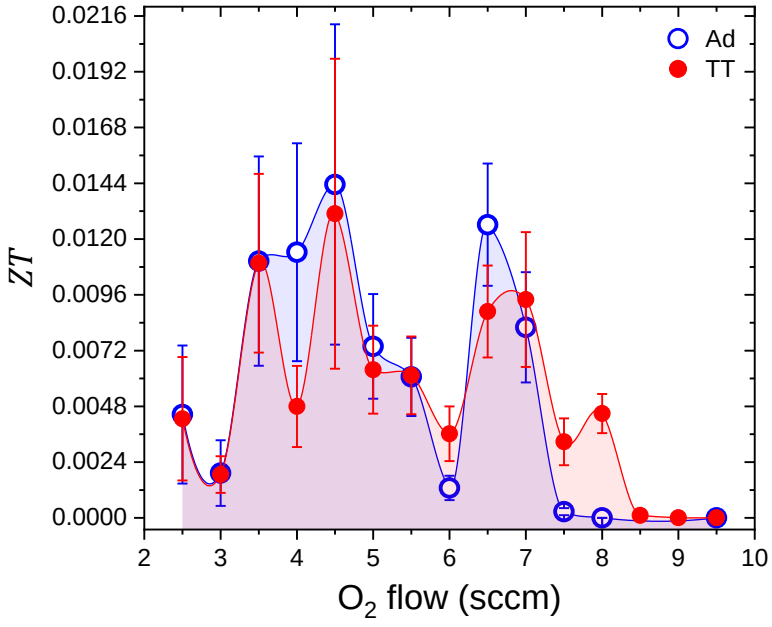

Figure 46. Thermoelectric figure of merit at 300 K for TiO_2:Nb thin films as a function of the reactive oxygen flow rate during deposition, calculated as-deposited *(Ad, blue)* and after annealing *(TT, red)*.

Table 11. Summary of results for Transmittance ($\bar{T}_{vis}$) averaged in the (400 to 700) nm range, Band-Gap Energy (E_g), Seebeck coefficient (S), electrical conductivity (σ), thermal conductivity (κ) and calculated Power Factor (PF)

and Figure of Merit (ZT) at 300 K of TiO_2:Nb thin films deposited with different reactive oxygen flow rates, measured as-deposited (Ad) and after annealing at 500 °C (TT).

O_2 flow (sccm)		**$\overline{T}_{vis}$ (%)**	**E_g (eV)**	**S (μV·K^{-1})**	**σ (Ω^{-1}·cm^{-1})**	**κ (W·m^{-1}·K^{-1})**	**PF (μW·m^{-1}·K^{-2})**	**$ZT_{300\ K}$ (10^{-2})**
2.5	**(Ad)**	0	-	-2.9 ± 0.2	3359 ± 1	0.2 ± 0.1	2.8 ± 0.4	0.4 ± 0.3
	(TT)	-	-	-2.73 ± 0.09	3604 ± 88	-	2.7 ± 0.2	0.4 ± 0.3
3	**(Ad)**	0	-	-2.4 ± 0.5	3823 ± 1	0.3 ± 0.1	2 ± 1	0.2 ± 0.1
	(TT)	-	-	-2.5 ± 0.1	3394 ± 84	-	2.1 ± 0.3	0.19 ± 0.08
3.5	**(Ad)**	0	-	-7.8 ± 0.8	2938 ± 4	0.5 ± 0.1	18 ± 4	1.1 ± 0.5
	(TT)	-	-	-9.0 ± 0.6	2236 ± 31	-	18 ± 3	1.1 ± 0.4
4	**(Ad)**	0	-	-16.9 ± 0.8	856.49 ± 0.07	0.6 ± 0.2	24 ± 2	1.1 ± 0.5
	(TT)	-	-	-12.1 ± 0.2	702 ± 14	-	10.3 ± 0.5	0.5 ± 0.2
4.5	**(Ad)**	0	-	-23 ± 3	712.40 ± 0.04	0.8 ± 0.2	38 ± 9	1.4 ± 0.7
	(TT)	-	-	-23 ± 3	668 ± 4	-	35 ± 8	1.3 ± 0.7
5	**(Ad)**	1	-	-27 ± 1	318.89 ± 0.04	0.9 ± 0.2	23 ± 2	0.7 ± 0.2
	(TT)	-	-	-25 ± 1	316 ± 1	-	20 ± 2	0.6 ± 0.2
5.5	**(Ad)**	2	-	-33 ± 1	205.17 ± 0.07	1.1 ± 0.2	22 ± 2	0.6 ± 0.2
	(TT)	-	-	-35 ± 1	185 ± 4	-	22 ± 2	0.6 ± 0.2
6	**(Ad)**	19	3.04 ± 0.01	-86 ± 10	7.176 ± 0.006	1.2 ± 0.2	5 ± 1	0.13 ± 0.05
	(TT)	-	3.20 ± 0.01	-111 ± 7	12.3 ± 0.4	-	15 ± 2	0.4 ± 0.1
6.5	**(Ad)**	59	3.167± 0.004	-211 ± 6	13.22 ± 0.04	1.4 ± 0.2	59 ± 4	1.3 ± 0.3
	(TT)	-	3.292 ± 0.008	-148 ± 3	19.0 ± 0.7	-	41 ± 3	0.9 ± 0.2
7	**(Ad)**	66	3.235 ± 0.002	-224 ± 18	8.450 ± 0.002	1.5 ± 0.2	42 ± 7	0.8 ± 0.2
	(TT)	-	3.293 ± 0.008	-197 ± 17	12.49 ± 0.02	-	48 ± 9	0.9 ± 0.3
7.5	**(Ad)**	73	3.345 ± 0.002	-67 ± 14	3.057 ± 0.001	1.5 ± 0.2	1.4 ± 0.6	0.03 ± 0.01
	(TT)	-	3.404 ± 0.006	-150 ± 11	7.4 ± 0.1	-	17 ± 3	0.3 ± 0.1
8	**(Ad)**	76	3.368 ± 0.004	-1.9 ± 0.3	7.57 ± 0.07	1.5 ± 0.2	$(3.8 \pm 0.9) \times 10^{-3}$	$(6 \pm 3) \times 10^{-5}$
	(TT)	-	3.420 ± 0.006	-121 ± 2	15.4 ± 0.2	-	23 ± 1	0.45 ± 0.08
8.5	**(Ad)**	82	3.412 ± 0.003	-2.4 ± 0.5	-	1.5 ± 0.2	-	-
	(TT)	-	3.442 ± 0.004	-63 ± 3	1.4 ± 0.1	-	0.55 ± 0.08	0.011 ± 0.003
9	**(Ad)**	85	3.38 ± 0.002	-2.3 ± 0.4	-	1.5 ± 0.2	-	-
	(TT)	-	3.464 ± 0.006	-9 ± 2	4.2 ± 0.5	-	0.03 ± 0.02	$(6 \pm 4) \times 10^{-4}$
9.5	**(Ad)**	86	3.415 ± 0.002	-2.4 ± 0.4	0.03 ± 0.03	1.5 ± 0.2	$(2 \pm 1) \times 10^{-5}$	$(3 \pm 6) \times 10^{-7}$
	(TT)	-	3.422 ± 0.004	-13 ± 4	2.501 ± 0.002	-	0.04 ± 0.02	$(8 \pm 6) \times 10^{-4}$

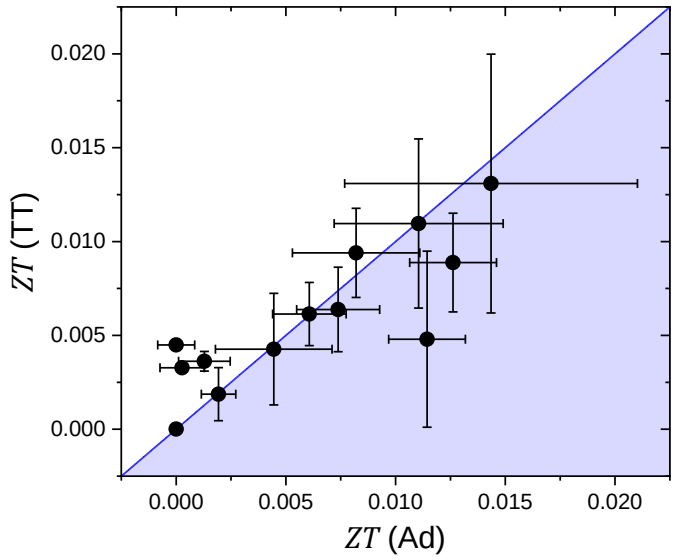

Figure 47. Figure of Merit values from **Figure 46** plotted as as-deposited *(Ad)* versus after annealing *(TT)* for TiO_2:Nb thin films. *Blue line* plots $y = x$ and *blue zone* refers to the as-deposited tendency of the data.

Overall, the post-deposition annealing does not seem to change the average transmittance and reflectance in the considered visible range (400 nm to 700 nm) of the as-deposited thin films. It does, however, increase the band-gap for all of the studied TiO_2:Nb thin films, independently of the oxygen flow rate during deposition. This post-deposition treatment also improves the electrical conductivity of the thin films deposited with oxygen flow rates above 5.5 sccm, and the thermoelectric property for films with as-deposited Seebeck coefficients lower than 150 $\mu V \cdot K^{-1}$. The main factor of the observed variation between the as-deposited and after annealing films is attributed to the structural change in crystalline phase from rutile to anatase.

4.3. Partial Conclusions

Transparent n-type niobium-doped titanium dioxide thin films (TiO_2:Nb) thin films were produced by reactive DC magnetron sputtering in high vacuum from a composite Ti:Nb(2.1 at.%) target in an oxygen and argon atmosphere. This study enabled a good correlation between the optical properties, morphology, structure and composition, electric, thermal and thermoelectric properties of the produced films. The thin TiO_2:Nb films show homogeneous surfaces, with roughness of (0.7 to 1.3) nm and densities of (3.2 to 4.4) $g \cdot cm^{-3}$. Lower level of Nb doping of (1.1 to 1.2) at.% is obtained for films with intermediate oxygen

inlet during deposition (7.0 sccm to 7.5 sccm), whereas for higher oxygen flow rates (9 sccm) the level of Nb doping increases to 1.7 at.%. The post-deposition thermal annealing on the TiO_2:Nb film deposited with 7.5 sccm of oxygen flow resulted in recrystallization with a close to stoichiometric TiO_2 (around 1:2) composition and 1.3 at.% of Nb doping. The amount of Nb in the TiO_2 unit cell is in the range of (1 to 2) at.%, based on the total composition of the material. With this quantity of Nb, it is possible to have optimized performance, in particular for being optically transparent, electrically conductive, poor thermal conductor and thus achieving a high thermoelectric power.

The as-deposited films develop both anatase and rutile TiO_2 phases, evidenced by XRD. A larger fraction of rutile phase is correlated to larger Seebeck coefficient values. The post-deposition annealing increases the band-gap of the TiO_2:Nb thin films due to the crystallization of the anatase phase. Furthermore, this treatment increases the electrical conductivity for films deposited with reactive oxygen flow rates above 5.5 sccm. It also improves the thermoelectric property for as-deposited films with absolute Seebeck coefficients lower than 150 $\mu V \cdot K^{-1}$. The thermoelectric power factor of the films deposited with 6 sccm, 7 sccm, 7.5 sccm and 8 sccm of oxygen flow was clearly improved after annealing.

An optimized process parameter window was defined for reactive oxygen flow rates in the range of (6.5 to 7.5) sccm. TiO_2:Nb films with (120 to 300) nm thickness have an average optical transmittance in the visible range of 73 %, maximum electrical resistivity of 0.05 $\Omega \cdot cm$, thermal conductivity below 1.7 $W \cdot m^{-1} \cdot K^{-1}$, maximum absolute Seebeck coefficient of 223 $\mu V \cdot K^{-1}$, a maximum thermoelectric power factor of 60 $\mu W \cdot m^{-1} \cdot K^{-2}$, and a maximum thermoelectric figure of merit of around 0.014.

Although transparency is required for applications such as touch-screen displays or in photovoltaic cell electrodes, it is a trade-off for the electrical conductivity and should be carefully weighted depending on the desired application.

CHAPTER V.

INFLUENCE OF THE DEPOSITION TEMPERATURE

5. Influence of the Deposition Temperature

This chapter describes the Influence of the deposition temperature and post-deposition annealing on the local structure and thermoelectric properties of transparent TiO_2:Nb thin films, obtained from the following publication:

> *J. M. Ribeiro, O. A. López-Galán, A. Welle, T. Boll and C. J. Tavares, "Effect of the Deposition temperature and annealing on the optical and thermoelectric properties of niobium-doped titanium dioxide thin films", to-be submitted in 2024.*

It has been previously reported that higher Ti target temperature allows for the deposition of stoichiometric TiO_2 films in reactive mode at high sputtering rates, which should stabilise the transition between the elemental and the reactive sputtering modes [156].

Several TiO_2:Nb thin films were deposited onto glass and Si substrates with thicknesses ranging between 191 nm and 221 nm, using 7 sccm of reactive Oxygen flow. The deposition temperature was varied in the range of (30 to 240) °C. A post-deposition thermal annealing at 500 °C was performed to enhance the crystallinity of the films. The thin films were comprehensively characterized by XRD, TOF-SIMS, DFT, UV-Vis spectroscopy, Hall effect and Seebeck coefficient measurements, which were described in **Chapter 2**.

5.1. Experimental Details

5.1.1. Sample Fabrication

Thin films of TiO_2:Nb were produced by reactive DC magnetron sputtering at the CF-UM-UP. A target of Ti(96)Nb(4) wt.% (99.9 % of purity, FHR), with 10 cm of diameter, was used in planar configuration. The films were deposited on (76 × 26 × 1) mm^3 glass substrates (Normax Lda) and (10 × 10 × 0.5) mm^3 Si substrates, cut from P/B doped Si-wafer <100> (Siegert Wafers GmbH). The substrates were cleaned with isopropyl alcohol (2-Propanol) and acetone in an ultrasonic bath, both for 15 min. The substrate-holders were mounted onto a rotating 6-position support controlled by a motor (used either in continuous rotation or to exchange samples over the magnetron). Target-substrate distance was kept at 6.5 cm. The

chamber was evacuated to achieve a base pressure of around 10^{-4} Pa and the substrate holder was heated up to 125 °C. Research grade Ar with 99.999 % purity was used as working gas to enable plasma formation and O_2 was used as reactive gas with a flow rate of 7 sccm. Prior to the deposition, 2 min of etching at 500 V was performed in an Ar atmosphere at a pressure of 1.8 Pa in continuous rotation at 18 rpm. A dummy deposition of 2 min for target cleaning (burn) was used in the first position of the substrate holder. Target current density, bias voltage and Ar flow were fixed at 12.7 mA·cm^{-2}, –60 V and 40 sccm, respectively, for all depositions, depositing at a pressure of around 0.23 Pa for 5 min. This was followed by the deposition of five samples in a single batch (labelled from A to E in **Figure 48**). The target current was turned off between depositions to enable a precise control of the next substrate holder position and deposition parameters.

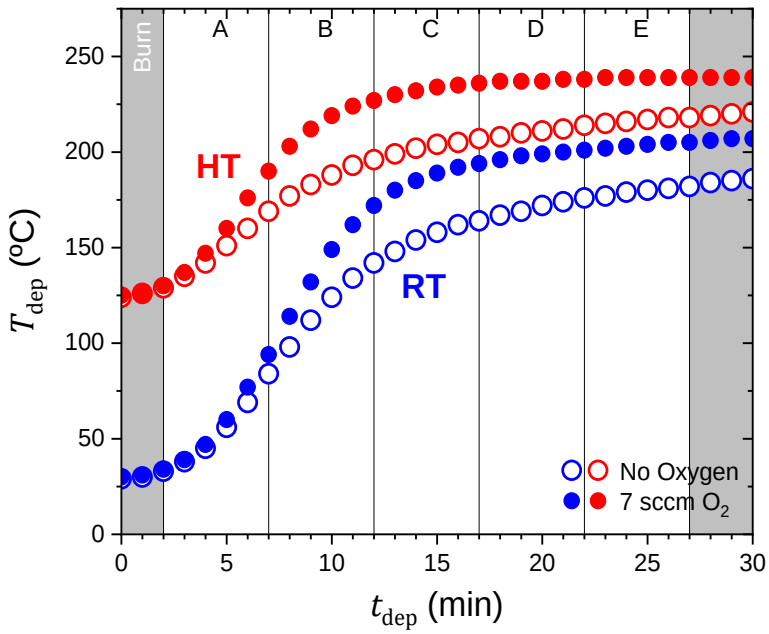

Figure 48. Temperature of the deposition chamber as a function of deposition time for samples deposited with *(HT, red)* and without *(RT, blue*) substrate heating. *Open circles* represent depositions with no Oxygen inside the chamber.

The deposition temperature (**Figure 48**) was measured with a thermistor located near the substrate position within the chamber. The plasma deposition process heats up the chamber even when it has not been pre-heated, decreasing the temperature difference between heated and non-heated samples the further the deposition progresses through the samples. It is important to keep in mind that, for each deposited sample, the substrate holder is rotated, and the substrate is changed, hence, the first few atomic layers are deposited onto a cooler substrate then before and will then proceed to be heated

further by the plasma. With heating, chamber temperature appears to stabilize after 15 min of deposition (start of sample D), while chamber temperature only stabilizes after 27 min of deposition (end of sample E) without heating.

The cathode potential hysteresis curve (**Figure 49**) was obtained by varying the reactive O_2 flow, ascending and descending, using the same processing conditions as previously described, with 5 min of stabilization time for each step. The metal mode is registered for oxygen flow rates below 3 sccm, resulting in electrically and thermally conductive thin films. There is an increase in target Voltage and a shift of the hysteresis curve to the right when substrate heating is used, although the start and end Voltage (at 0 sccm of O_2 flow) is the same, independently of temperature. The oxide mode is achieved for O_2 flow rates above 8.5 sccm and 7.5 sccm with and without heating, respectively. Thin films deposited above this threshold flow results in an excess of oxygen in the film structure, rendering the material into an electrical insulator and decreasing the thermoelectric property. The transition region seems to be between 6 sccm and 7.5 sccm without substrate heating, and 6 sccm and 8 sccm with substrate heating.

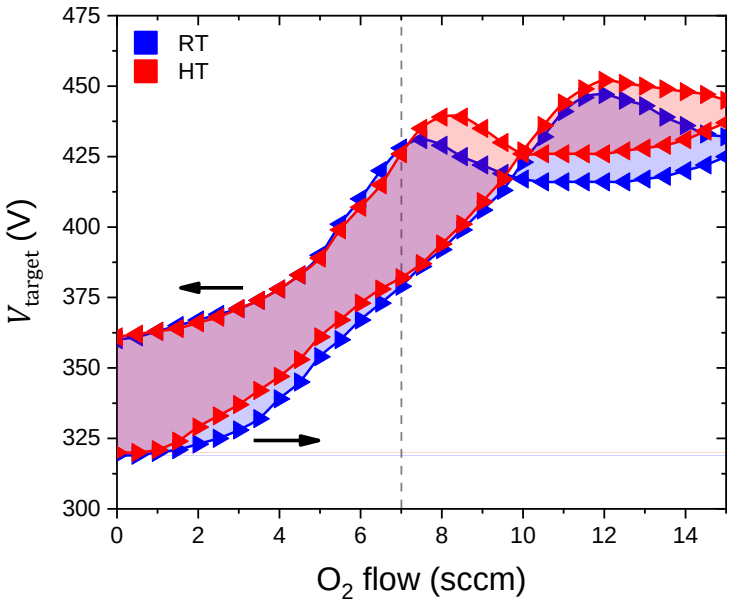

Figure 49. Cathode potential vs. reactive oxygen flow rate hysteresis curve for the deposition of TiO_2:Nb thin films with *(HT, red)* and without *(RT, blue*) substrate heating. *Crossed black line* refers to the chosen O_2 flow for the present study.

Subsequently, the as-deposited TiO_2:Nb films were heat treated to enhance their microstructure and electrical properties [75,92], in a vacuum furnace at 10^{-3} Pa. The temperature was increased from room temperature to 500 °C in 90 min and maintained at 500 °C for 1 h, followed by a natural cooling stage to room temperature for 6 h.

5.1.2. Sample Characterization

XRD analysis was performed thin films deposited on glass substrates, using a Bruker AXS D8 advanced Discovery diffractometer. The diffraction patterns were acquired in GIXRD, with incident angle of 1°, step of 0.02° and integration time of 1 s. CuKα radiation was used with a wavelength of 1.540 6 Å. The software Fityk was used to analyse the XRD diffraction patterns. The weight fraction of rutile is obtained through equation **(8)** [93].

The optical transmittance and specular reflectance of the thin films deposited on glass substrates were analysed with a Shimadzu UV-2501PC UV-Vis spectrophotometer in the (300 to 900) nm wavelength range. The samples were measured using the air and the calibration mirrors as the baseline, for transmittance and specular reflectance, respectively. The transmittance (T) and specular reflectance (Rs) spectra were fitted to a simulated model in the software SCOUT, using three $\chi_e(\lambda)$ models: the O'Leary-Johnson-Lm model; the Extended Drude model; and the background dielectric constant model. To obtain the transparency of the film layer, the transmittance was measured using the glass substrate as the'baseline. T and Rs were averaged from 400 nm to 700 nm, equivalent to the visible wavelength range. The optical band-gap energy (E_g) of the films was evaluated from Tauc plots of the absorption coefficient, α, against photon energy, $h\nu$, and extrapolating the linear fit of the plot to the photon energy axis, using equations **(24)** and **(25)**.

TOF-SIMS was performed on thin films deposited on Si substrates, on a TOF.SIMS5 spectrometer (ION-TOF GmbH) equipped with a Bi cluster primary ion source and a non-linear TOF analyser, at the IFG-KIT. Under UHV base pressure $< 5 \times 10^{-9}$ mbar, the primary ion source was operated in HCB mode providing short Bi^+ primary ion pulses of 0.8 ns / 25 keV, a lateral resolution of approximately 4 μm, and a target current of 1.4 pA at 10 kHz repetition rate. For depth profiling a dual beam analysis was performed in interlaced mode, with the primary ion source scanned over an area of (300 × 300) μm^2 (128 × 128 data points) and the sputter gun scanned over a concentric field of view. For positive polarity profiles an O_2^+ beam was applied to erode the sample, with 2 keV sputter energy, at 45° incident angle, a scan range of (600 × 600) μm^2 and a target current of approximately 500 nA. For negative polarity profiles a Cs^+ beam eroded the sample, with 2 keV sputter energy, a scan range of (500 × 500) μm^2 and target current of approximately 100 nA. Since the data acquisition is fast in respect of the observed erosion speeds, 25 data points were binned for plotting. Secondary ion intensities are plotted over depth, using total thickness obtained through the SCOUT simulations obtained by UV-Vis measurements. Note

however that this scale is not linear if different materials with different erosion rates / sputter yields are analysed.

The electrical conductivity of the thin films deposited on Si substrates was analysed using an Ecopia AMP55T HMS-5000 Hall effect measuring system, equipped with a DC four-point probe apparatus in the Van der Pauw configuration. The measurements were performed at room temperature under atmospheric pressure, with an applied magnetic field of approximately 0.560 T. The results are an average of 10 measurements for each sample.

The in-plane Seebeck coefficient was evaluated for thin films deposited on glass substrates in a custom-made equipment operated in low vacuum (1 Pa). A temperature difference is applied between the edges of a 75 mm long sample by two Peltier devices (Quick-Ohm Küpper & Co. GmbH) for heating and cooling. A two-probe contact geometry measures the voltage generated in the sample, in response to a thermal gradient across the film surface. For each sample, the applied thermal gradients varied between 30 °C and 55 °C with a step of 5 °C, with 10 min of thermal stabilization to obtain a good and coherent value. The Seebeck coefficient (S, in $\mu V \cdot K^{-1}$) was estimated by plotting the obtained ΔV values as a function of ΔT and linearly fitting to determine the slope. The thermoelectrical potential is generally determined by a measure of its dimensionless figure of merit (ZT) [13], which equates the relation between the electronic transport and thermal transport in a material (equation **(7)**). However, due to the lack of thermal conductivity measurements, the thermoelectric power factor (PF) (equation **(8)**), is alternatively used:

DFT calculations were performed using the Quantum ESPRESSO package [124,125]. The exchange-correlation functional was described through the GGA and the PBE, together with the optimized Vanderbilt pseudopotentials [126] provided through the SSSP package in its 1.2.1 version [127]. To account for the highly localized titanium $3d$–orbitals [128], the Hubbard correction setting $U = 5.7066$ eV is employ after the convergence test. For the structural optimization calculations, the plane-wave cutoff energy was set to 680 eV with a self-consistent field value of (1.6×10^{-7}) $eV \cdot atom^{-1}$. At the same time, the convergence criterion of ionic minimization was achieved when all forces were smaller than (8.2×10^{-4}) $eV \cdot nm^{-1}$ and the total energy fluctuates less than (8.9×10^{-3}) $eV \cdot atom^{-1}$ in two consecutive self-consistent field steps, and all atoms were able to move without constraints. A k–point set of $4a \times 6b \times 5c$ and $5a \times 5b \times 5c$ was used to sample in the Brillouin zone, for the anatase and rutile phase, respectively. The computation of DOS and PDOS was performed using a k–point set of $8a \times 12b \times 10c$ and $10a \times 10b \times 10c$, for the anatase phase and rutile phase, respectively, with a cutoff energy of 816 eV for improved calculations. Structural visualization of the models was assisted by the VESTA ver. 3.5.8

[129] and Xcrysden [130] codes. The thermoelectric properties were calculated using Boltztrap2 code [131], which solves the linearized Boltzmann transport equation. Single-point energy calculations from Quantum ESPRESSO were used as input for the Boltztrap2 code to carry out the transport properties of doped-TiO_2 configurations. BoltzTrap2 calculates the Onsager coefficients by solving the Boltzmann transport equation. All calculations were carried out at 300 K in a –0.2 Ha to 0.2 Ha energy interval.

5.2. Results and Discussion

The TiO_2:Nb thin films produced while varying the deposition temperature are shown in **Table 12**. The thickness was obtained from SCOUT simulations fitted to the transmittance and reflectance spectra. Samples deposited with substrate heating showed an overall higher deposition rate, when compared to samples deposited without heating, with the exception of sample B, which showed the same thickness in both cases.

Table 12. Summary of samples A, B, C, D and E, deposited with and without substrate heating.

Sample	Deposition order	$\Delta T_{\mathbf{dep(i-f)}}$ (°C)	Substrate Heating	d (nm)
RT_A	1	31 – 77	No Heating	195
RT_B	2	77 – 162	No Heating	215
RT_C	3	162 – 192	No Heating	195
RT_D	4	192 – 200	No Heating	203
RT_E	5	200 – 205	No Heating	191
HT_A	1	126 – 176	Heating	208
HT_B	2	176 – 224	Heating	214
HT_C	3	224 – 235	Heating	221
HT_D	4	235 – 238	Heating	220
HT_E	5	238 – 239	Heating	221

Figure 50 shows the TOF-SIMS depth profiles of Nb-related signals for the TiO_2:Nb thin films. At first glance, the deposition temperature and annealing does not seem to change the total nor depth composition of the TiO_2:Nb thin films but taking a closer look at the Nb-related signals near the interface with the substrate (first nanometres of deposition) revealed some interesting details. Nb-related signals show an increase closer to the interface with the substrate, indicating a higher Nb doping content in the beginning of the film's growth (at the first 40 nm to 50 nm of deposition).

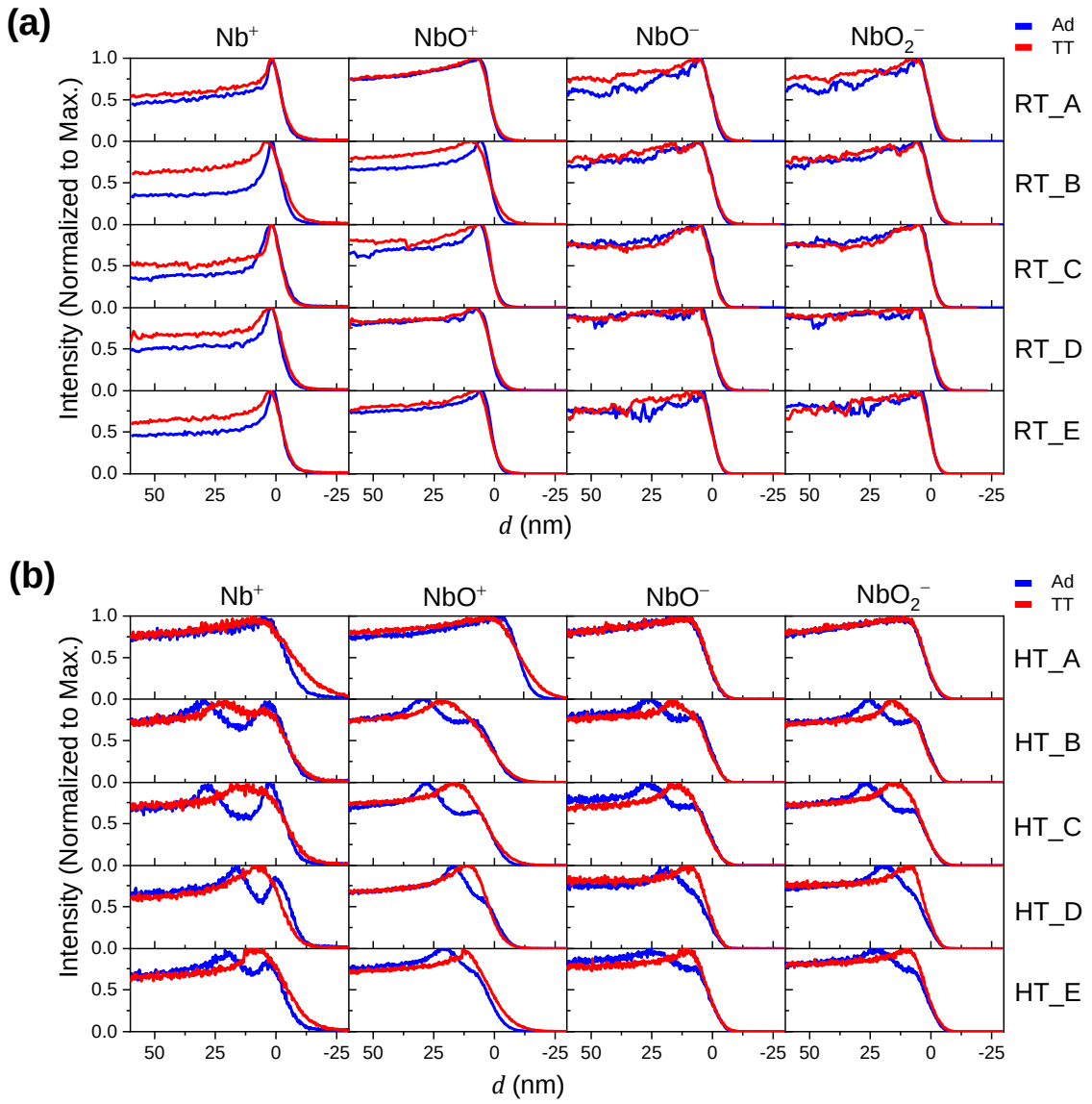

Figure 50. TOF-SIMS depth profiles of Nb^+, NbO^+ (positive polarity), NbO^- and NbO_2^- (negative polarity) normalized to maximum signal intensities in TiO_2:Nb thin films deposited without substrate heating *(RT)* **(a)** and with substrate heating *(HT)* **(b)**, measured as-deposited *(Ad, blue)* and after annealing at 500 °C *(TT, red)*. The interface with the Si substrate and beginning of film growth is indicated at $d = 0$ nm.

There is good agreement between the NbO^+, NbO^- and NbO_2^- signals in all the samples. The difference in the Nb^+ and NbO-related signals closer to the substrate between the samples measured as-deposited shows a change of Nb content and stoichiometry closer to the substrate. All signals in both analyses are analogous for sample HT_A, with a maximum at the first (5 to 10) nm of deposition. Sample HT_B and sample HT_C show a secondary maximum closer to the interface with the substrate (first 5 nm to 10 nm of deposition), sample HT_E has a smaller secondary maximum and sample HT_D sows only a slight bump, which is not seen in sample HT_A. Nb^+ signals don't quite match with the NbO-related signals, as it shows an even higher Nb^+ signal at the interface with the substrate, at the same

secondary maximum as with NbO^+, NbO^- and NbO_2^- on samples HT_B, HT_C, HT_D and HT_E. Hence, the increase in target temperature after the deposition of sample HT_A increases the heterogeneity of Nb in the first 50 nm of sample HT_B. As the chamber temperature further increases, the highest Nb content shifts closer to the interface with the substrate. The sputter yield of Nb (0.474) is higher to that of Ti (0.394), for Ar^+ with an energy of 400 eV [147]. Since Nb is also closer in weight to Ar than Ti, it is more easily pulverized. For samples measured after annealing there is a clear increase of Nb content at the interface with the substrate, showing only one maximum in all Nb and NbO-related, with the exception of samples HT_B(TT) and HT_C(TT) but, where there is either a small secondary maximum or a slight bump in the signals. In these cases, the highest Nb content is registered after (20 to 30) nm of deposition. Nonetheless, the annealing homogenizes the Nb signals in the first 50 nm of deposition.

A relative content of Nb was determined by dynamic TOF-SIMS (in positive polarity) by calibrating Nb^+ and NbO^+ signals on the $^{46}Ti^+$ and $^{46}TiO^+$ peak area signals, respectively, over the total depth of the samples. The Nb to Ti signal ratios (normalized to maximum) presented in **Figure 51** are lower for as deposited samples B and C, while both RT_A and HT_A show a comparatively higher Nb signal. After annealing, increased Nb and NbO signal comparative ratios were observed for samples with higher deposition temperature, although sample HT_A still maintained higher ratios in comparison to HT_B. Of course, it is impossible to evaluate the bulk Nb content inside the samples with relative composition rations, especially when not considering oxygen content and impurities. Nonetheless, but it is clear the substrate temperature during deposition does not influence the incorporation of Nb in a linear way.

The optical transmittance and specular reflectance of the TiO_2:Nb thin films deposited for 5 min are presented in **Figure D 2**. **Figure 52** shows the transmittance and specular reflectance averaged from 400 nm to 700 nm as a function of the deposition temperature. The average transmittance varies between 67 % and 76 % and the specular reflectance ranges between 16 % and 29 %. The thin films deposited without substrate heating show higher as-deposited average transmittance and lower specular reflectance, with sample RT_A(Ad) (deposited at (51 ± 15) °C) and RT_C(TT) (deposited at (184 ± 7) °C) having the highest transparency in the visible range at 76 %. Even so, the average transmittance is not significantly affected by the thermal annealing (**Figure 52(a)**), but the average specular reflectance decreases for all samples after annealing (**Figure 52(b)**), specially for the samples deposited with substrate heating, getting as low as 16 %.

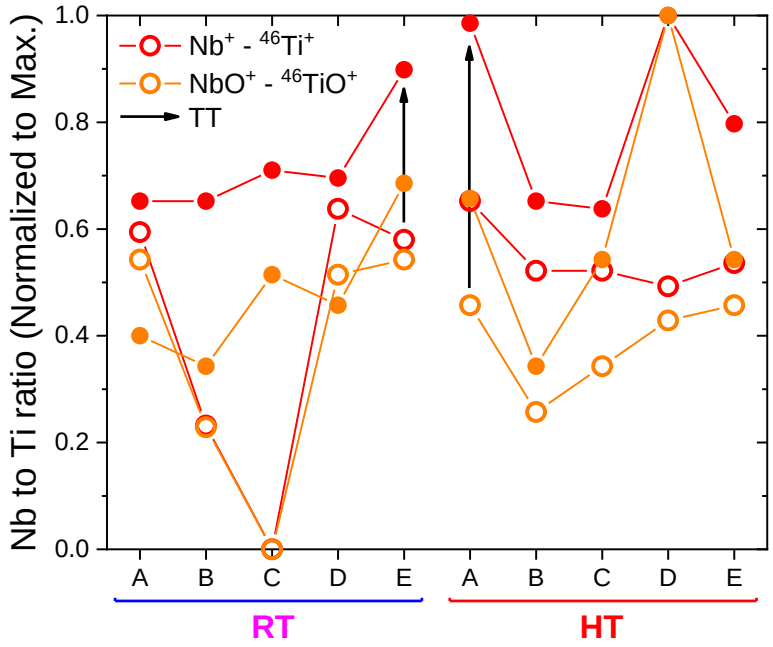

Figure 51. Relative ratio of $Nb^+$and NbO^+ signals calibrated on the $^{46}Ti^+$ and $^{46}TiO^+$ peak area signals, respectively, normalized to maximum signal intensities in TiO_2:Nb thin films deposited without substrate heating *(RT)* and with substrate heating *(HT)*, measured as-deposited *(Ad, open circles)* and after annealing at 500 °C *(TT, closed circles)*, obtained by TOF-SIMS in positive polarity with Oxygen beam erosion.

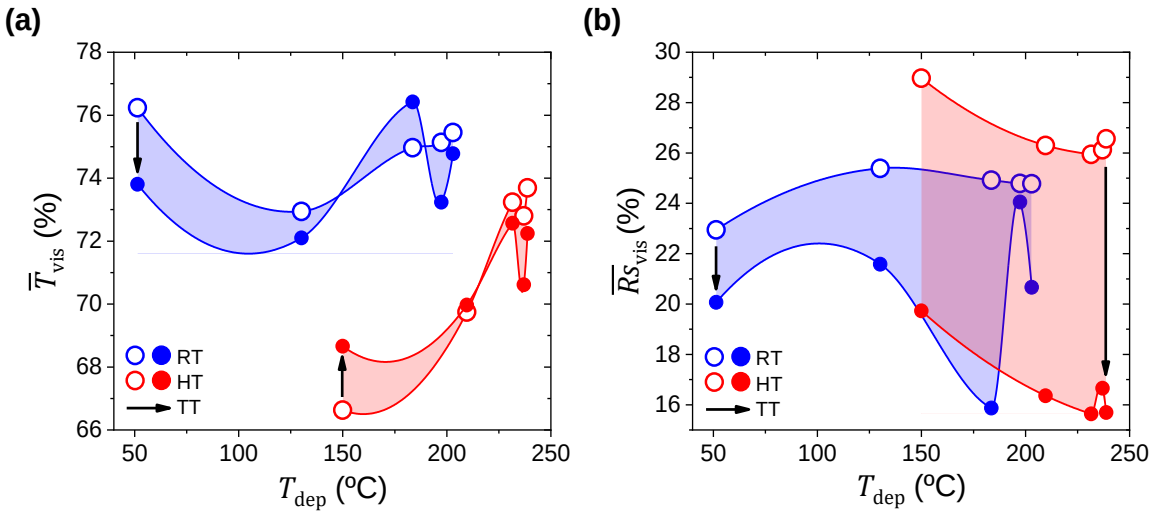

Figure 52. Average Transmittance (400 nm to 700 nm) **(a)** and average Specular Reflectance (400 nm to 700 nm) **(b)** of TiO_2:Nb thin films in relation to the chamber temperature during deposition, for films deposited with substrate heating *(HT, red)* and without substrate heating *(RT, blue)*, measured as-deposited *(Ad, open circles)* and after annealing at 500 °C *(TT, closed circles)*.

Band-gap energies derived from Tauc plots are plotted in **Figure 53(a)**. Samples deposited with and without substrate heating show a similar behaviour, however, sample HT_E has the highest band-gap energy at (3.36 ± 0.01) eV as-deposited. Sample RT_A has the highest band-gap energy after

annealing, increasing from (3.340 ± 0.005) eV to (3.406 ± 0.006) eV. The band-gap energy increased after thermal annealing, with the exception of sample HT_B, which has the lowest band-gap energy, decreasing from (3.310 ± 0.008) eV to (3.227 ± 0.003) eV. This sample is interesting, as it is one of the few that did not re-crystallize with a higher fraction of anatase phase after annealing at 500 °C, becoming prevalently rutile instead (**Figure 53(b)**). The increase in band-gap energy in the thin films after annealing is attributed to a structural effect due to the phase transition from rutile to anatase, as typical anatase (3.2 eV) has a higher band-gap energy than that of rutile (3.0 eV).

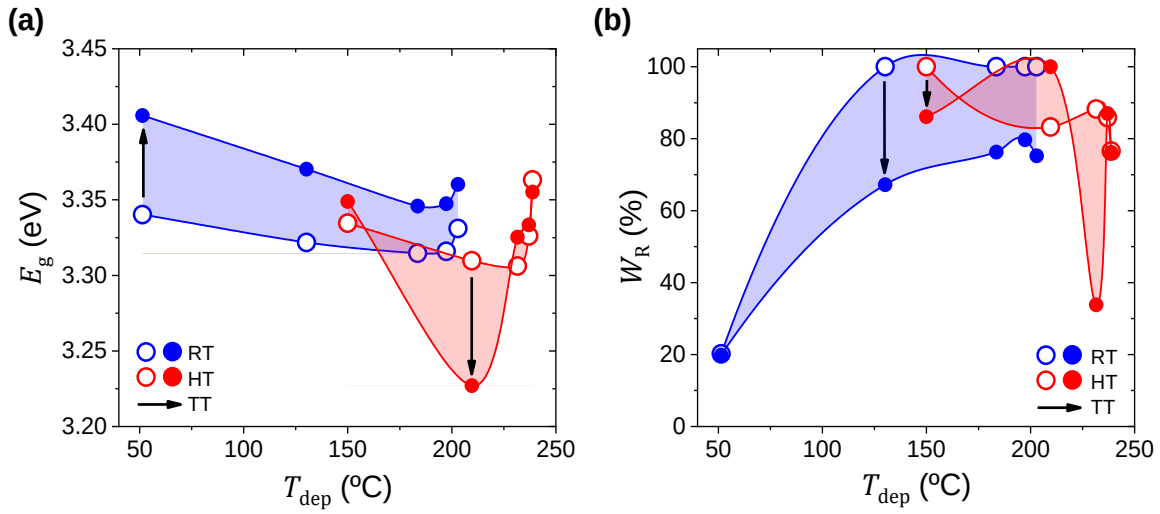

Figure 53. Band-gap Energy **(a)** and rutile phase content **(b)** of TiO_2:Nb thin films in relation to the chamber temperature during deposition, for films deposited with substrate heating *(HT, red)* and without substrate heating *(Ad, blue)*, measured as-deposited *(Ad, open circles)* and after annealing at 500 °C *(TT, closed circles)*.

The X-ray diffractograms in **Figure 54** indicate the influence of the deposition temperature and the post-deposition annealing in the crystalline phase of the TiO_2:Nb thin films. The patterns identify the main diffraction peak from rutile (110), $2\theta = 27.4°$, and anatase (101), at $2\theta = 25.3°$, respectively referenced from the Joint Committee on Powder Diffraction Standard (JCPDS cards number 21-1272 and 21-1276, respectively). It is expected that up to a 5 at.% Nb-doping will develop anatase phase [72], albeit slightly strained. This is not always the case for the obtained TiO_2:Nb thin films. Lower deposition temperatures clearly develop the crystallization of the rutile phase, with the exception of the as-deposited sample RT_A, where no phase can be discerned. The annealing process helps develop the anatase phase. This is especially true for the first sample deposited without substrate heating (RT_A) which seemed amorphous as-deposited and became predominantly anatase after annealing. This is supported by the literature, which emphasizes that the crystallization of anatase can be obtained by annealing TiO_2 at (400 to 500) °C, and at around 635 °C for the rutile phase [150–152]. The thin films with substrate heating

showed an overall higher rutile crystallization, especially on the first depositions. Sample HT_A, deposited with substrate heating, presented only rutile as-deposited and developed a mixture of anatase and rutile after annealing. Higher deposition temperature develops a mix of rutile and anatase phase, with subsequently lower content of rutile with deposition progression and increase in temperature. When comparing the heated and non-heated samples, the last deposited sets of deposited thin films showed quite similar results. HT_B is an interesting sample, as it maintained its predominantly rutile phase after annealing. Usually, rutile is only obtained by high temperature post-deposition annealing TiO_2 films [60,150–152].

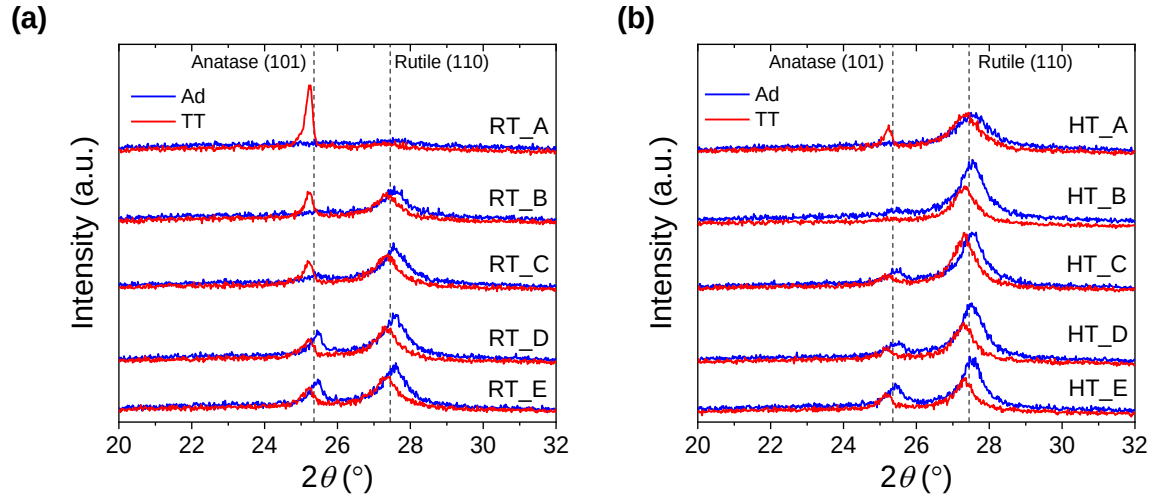

Figure 54. Grazing Incidence X-ray diffractograms of TiO_2:Nb thin films deposited without substrate heating *(RT)* **(a)** and with substrate heating *(HT)* **(b)**, measured as-deposited *(Ad, blue)* and after annealing at 500 °C *(TT, red)*. *Dashed black lines* refer to the XRD patterns for TiO_2 anatase JCPDS card 21-1272 and TiO_2 rutile JCPDS 21-1276 card.

The lattice parameters of the unit cells after the structural optimization are in excellent agreement with previous reports [157] and the experimental lattice constants [158], denoting that the DFT methodology used is reliable for modelling TiO_2 supercells (**Table 13**). The lattice constants of the unit cells (U_c) were then expanded in the x, y, and z direction to $3a \times 2b \times 1c$ and $2a \times 2b \times 3c$, for TiO_2 anatase and rutile, respectively, to create a supercell model (S_c), containing 48 O atoms and 24 Ti atoms in each supercell. In agreement with the experimental results, the substitution of one Ti atom by one Nb atom led to a total Nb concentration at each of the supercell models of 1.4 at.% (**Figure 55**). The resulting lattice parameters from anatase and rutile supercells in the undoped and doped conditions show that, after Nb-doping, the anatase must expand its lattice by about 1.18 % and its total volume by 3.15 %, while the rutile phase can accommodate the substitutional Nb dopant without expansion of the lattice.

Table 13. Resulting lattice parameters for the anatase and rutile unit cells (U_c) and supercells (S_c) models.

	Anatase			Rutile		
	U_c	S_c (3 × 2 × 1)		U_c	S_c (2 × 2 × 3)	
	TiO_2	TiO_2	TiO_2:Nb	TiO_2	TiO_2	TiO_2:Nb
a (Å)	3.798	11.395	11.529	4.643	9.285	9.285
b (Å)	3.798	7.596	7.686	4.643	9.285	9.285
c (Å)	9.700	9.700	9.774	2.963	8.890	8.890
V_c (Å^3)	139.932	839.594	866.067	63.873	766.472	766.472
α	90°	90°	90°	90°	90°	90°
β	90°	90°	90°	90°	90°	90°
γ	90°	90°	90°	90°	90°	90°

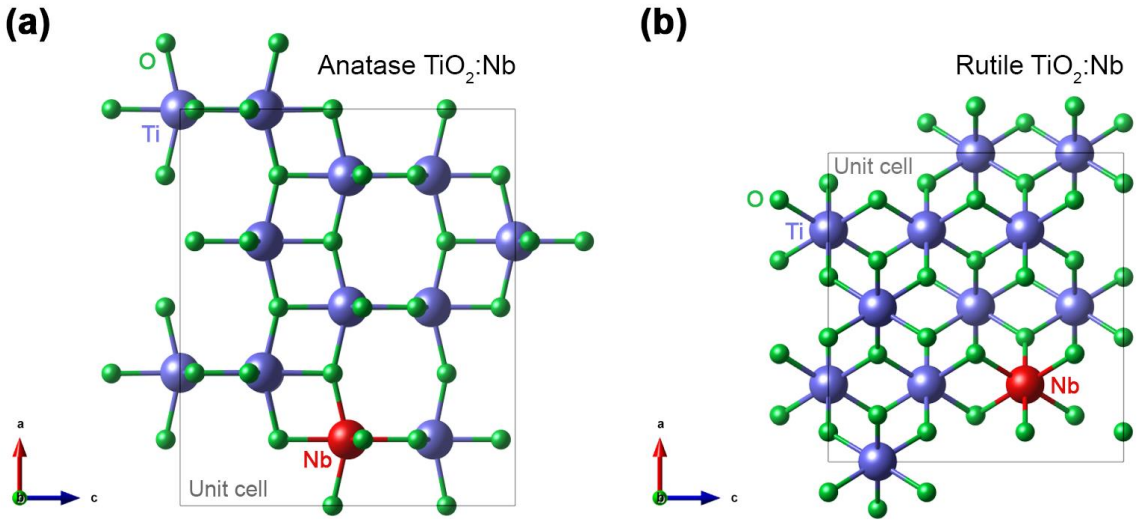

Figure 55. Structural model of TiO_2:Nb anatase ($3a \times 2b \times 1c$) **(a)** and rutile ($2a \times 2b \times 3c$) **(b)** supercells for 1.4 % Nb atoms visualised by VESTA.

From partial density of states, the valence band is mainly located in the O part, while the conduction band is mainly at the Ti part, in both the anatase and rutile phases (**Figure 56**). When doping TiO_2 with Nb (**Figure 56**), the Fermi level shifts from the valence to the conduction band, showing a typical n-type metallic behaviour. This is also evidenced by the band structures presented in **Figure 57**. For undoped TiO_2 the band-gap energy is at 3.1 eV for anatase and 2.6 eV for rutile, which agrees with the literature. For the TiO_2:Nb, the band-gap energy decreases for both, anatase to 2.9 eV and rutile to 2.3 eV, which contradicts the higher values obtained in **Figure 53(a)**. This difference is explained by the Burstein-Moss effect [145,153]. Doping n-type materials increases the number of electrons that fill the lower electronic states of the conduction band. This increases the photon energy required for the

inter-band transitions from the valence band to the higher energy vacant states in the conduction band, resulting in the apparent widening of the optical band-gap energy.

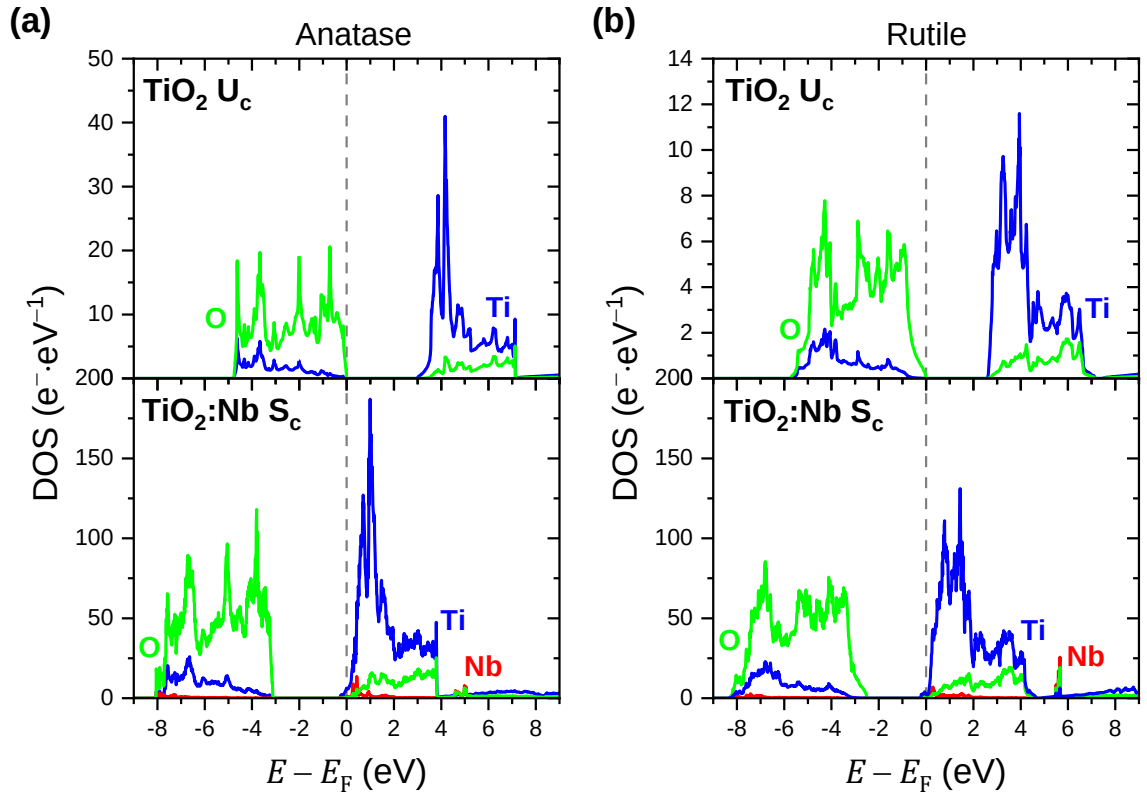

Figure 56. Projected density of states for Nb *(red)*, Ti *(blue)* and O *(green)* for anatase **(a)** and rutile **(b)** unit cells (U_c) of undoped TiO_2 (Top) and supercells (S_c) of doped TiO_2:Nb. The Fermi level is located at 0 eV.

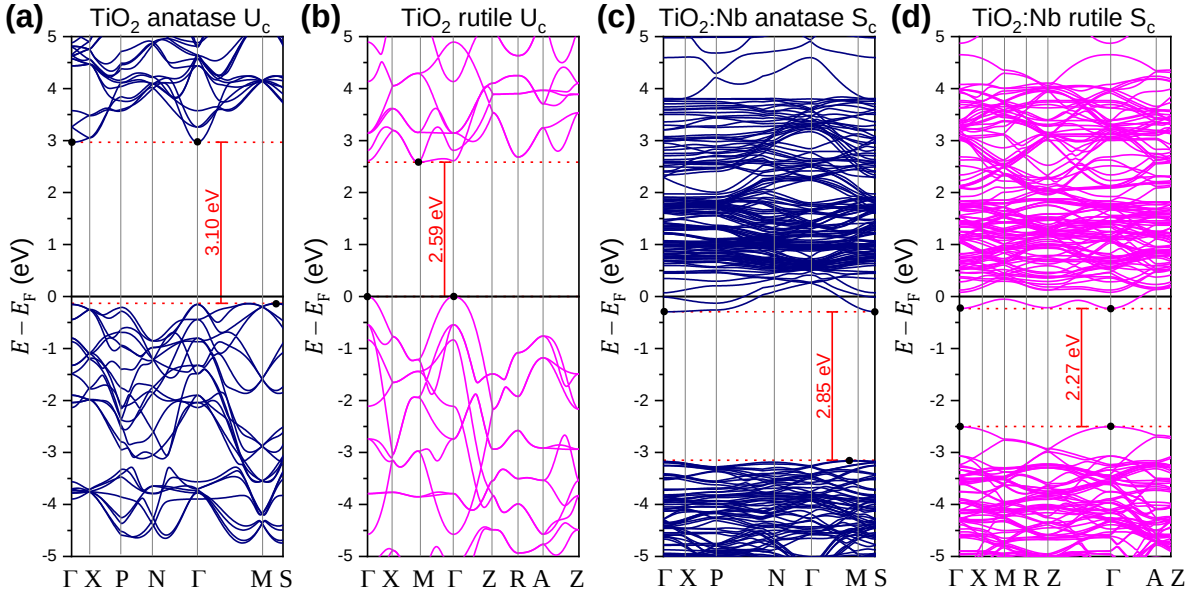

Figure 57. Band structures for undoped anatase **(a)** and rutile **(b)** TiO_2 unit cells and doped anatase **(c)** and rutile **(d)** TiO_2:Nb supercells. The Fermi level is located at 0 eV and band-gap energy in indicated in *red*.

The comparison between the undoped and doped conditions reveals an interaction concerning the Nb d-orbital and the Ti d-orbital, in what is suggested to be a hybridization process (**Figure 56**). For the doped conditions, the valence band and conduction band continue to be dominated by the O and the Ti orbitals, respectively. Furthermore, the density of Nb states is higher at positive energies (above the Fermi level), suggesting it is contributing primarily to the conduction band.

The PDOS for each element was plotted to resolve the induvial contribution of each orbital to the total DOS and are presented in **Figure 58**.

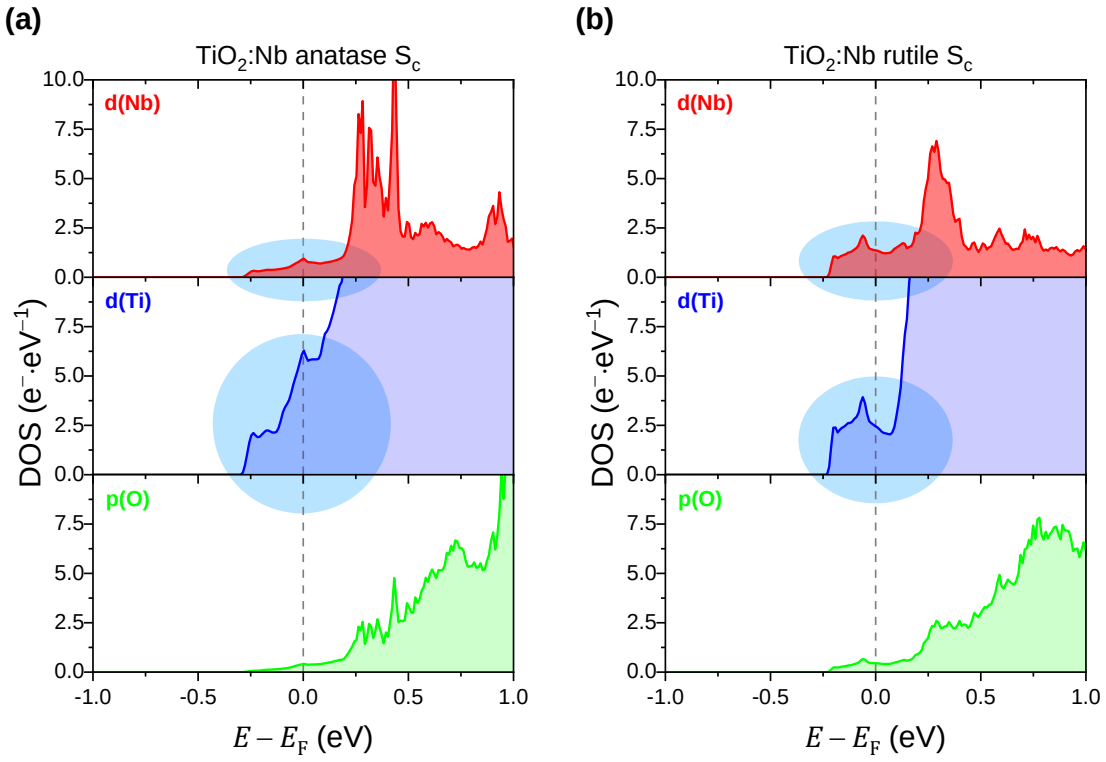

Figure 58. Projected density of states per element, Nb *(red)*, Ti *(blue)*, and O *(green)*, per orbital for doped anatase **(a)** and rutile **(b)** TiO_2:Nb supercells. The Fermi level is located at 0 eV. The remaining contributions of the orbitals from Nb, Ti, and O remain negligible around the Fermi level (not plotted). The *dark yellow circles* point to the contribution arising from the interaction between the Ti and Nb d-orbitals around the Fermi level.

The orbitals contributing the most to the valence band are the O $2p$-orbitals. For the conduction band, it is mainly composed of Ti $3d$-orbitals, specifically t_{2g} and e_g symmetry orbitals, as specified for metal in octahedral coordination with crystal field splitting [159,160]. The O s-orbitals (not plotted in **Figure 58**) do not significantly contribute to either the valence or conduction band. The same occurs for both the Ti s-orbitals and p-orbitals and the Nb s-orbitals and p-orbitals. The Ti contribution just at the Fermi level shows an increment at the doped condition with Nb, supporting the previous statement of a hybridization process between the d-orbitals from the metals. This hybridization is occurring between the

Ti $3d_{xy}$-orbitals and the Nb $4d$-orbitals, with the same symmetry, in the positive side of the Fermi level. Moreover, the additional Nb electrons located at the $4d$-orbital are most probably spreading, thus displacing the initial position of the conduction band to higher energy levels.

Figure 59(a) shows the Seebeck coefficient of TiO_2:Nb thin films measured as-deposited and after annealing at 500 °C, plotted in relation to the deposition temperature. A negative potential was measured for all films, relating to the n-type nature of TiO_2. The average electrical resistivity as a function of the deposition temperature is registered in **Figure 59(b)**.

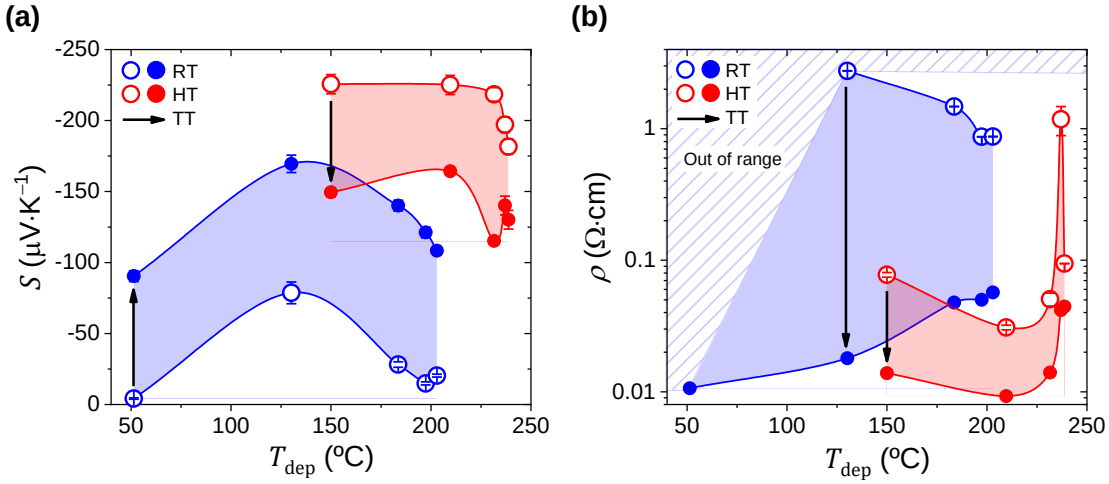

Figure 59. Seebeck Coefficient **(a)** and electrical resistivity **(b)** of TiO_2:Nb thin films in relation to the chamber temperature during deposition, for films deposited with substrate heating *(HT, red)* and without substrate heating *(RT, blue)*, measured as-deposited *(Ad, open circles)* and after annealing at 500 °C *(TT, closed circles)*. The *blue striped zone* refers to as-deposited thin films with extremely high electrically resistivity and are unable to be measured.

Samples deposited with substrate heating show a higher absolute Seebeck coefficient (between 182 $\mu V \cdot K^{-1}$ and 226 $\mu V \cdot K^{-1}$) and lower electrical resistivity (between 0.03 Ω·cm and 0.09 Ω·cm) compared to samples deposited without heating (Seebeck coefficient between 4 $\mu V \cdot K^{-1}$ and 79 $\mu V \cdot K^{-1}$ and electrical resistivity between 0.87 Ω·cm and 2.76 Ω·cm). The exception to this is sample HT_D, which has a low electrical resistivity of (1.2 ± 0.3) Ω·cm. Samples HT_A and HT_B show the highest absolute Seebeck coefficients at (226 ± 7) $\mu V \cdot K^{-1}$ and (225 ± 7) $\mu V \cdot K^{-1}$. After annealing the thin films at 500 °C, the thin films show a quite similar range of values, both for Seebeck coefficient and electrical resistivity. On the one hand, the electrical resistivity decreases for all samples, to as low as (9.270 ± 0.009) × 10^{-3} Ω·cm for sample HT_B. Sample RT_A was unable to be measured as-deposited, due to high resistivity. However, after annealing, the electrical resistivity decreases beyond two orders of magnitude to (1.06 ± 0.02) × 10^{-2} Ω·cm. On the other hand, the Seebeck coefficient increases for

samples deposited without heating (to the range of (90 to 169) $\mu V \cdot K^{-1}$) but decreases in samples deposited with heating (to the range of (115 to 164) $\mu V \cdot K^{-1}$). A similar result was observed in a previous study [146], where the post-deposition annealing improved the thermoelectric property for TiO_2:Nb films with as-deposited absolute Seebeck coefficients lower than 150 $\mu V \cdot K^{-1}$, but it actually decreased when the thin films already exhibit high as-deposited absolute Seebeck coefficients.

This correlates with the XRD results previously presented in **Figure 36**, where a higher Seebeck coefficient is ascribed to the rutile phase, while the anatase phase, favoured by the annealing process, relates to higher electrical conductivity.

The thermoelectric, electrical and thermal properties calculated by DFT (**Figure 60**) show very interesting differences between the behaviour of anatase and rutile for Nb-doped and undoped TiO_2, although a direct quantitative comparison cannot be made, due to the different number of atoms in the unit cells and supercells. Compared to the unit cells of undoped TiO_2, the projected properties for the supercells of TiO_2:Nb show a shift of Fermi Level to the right (more pronounced for the anatase phase), meaning an overlap of the Fermi level with the conduction band, with electrons as the majority carriers.

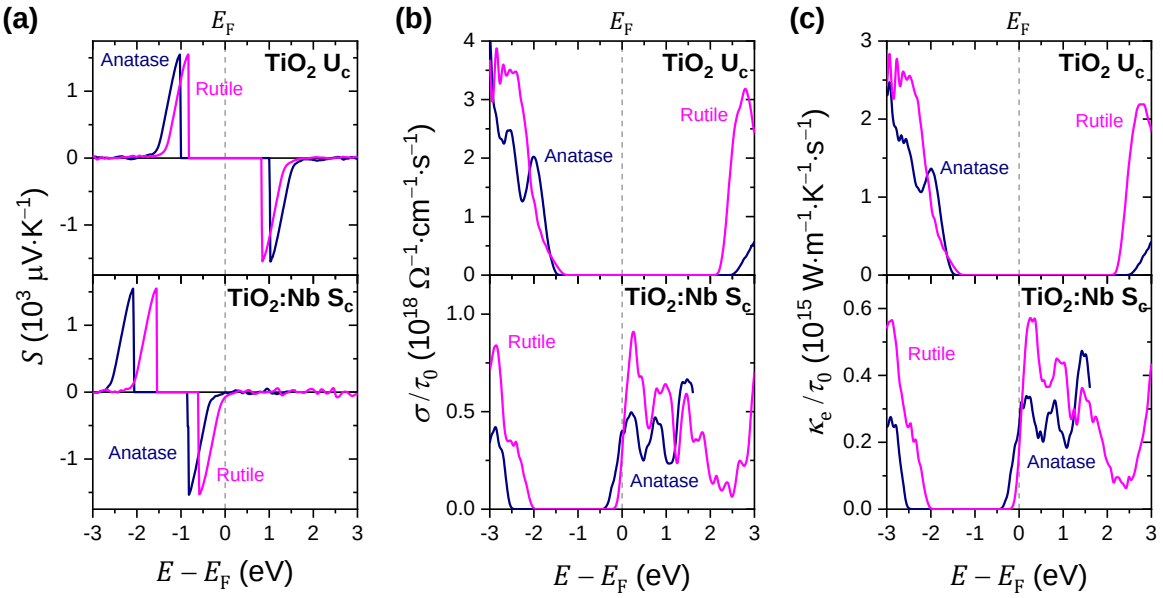

Figure 60. Projected Seebeck coefficient **(a)**, electrical conductivity dependent of τ_0 **(b)** and electronic component of the thermal conductivity dependent of τ_0 **(c)** for the unit cells (U_c) of undoped anatase and rutile TiO_2 (top) and supercells (S_c) of anatase and rutile TiO_2:Nb (bottom). The anatase phase is indicated in *navy*, the rutile phase is indicated in *magenta* and the Fermi level is located at 0 eV.

For the unit cell of TiO_2, there is both a positive and a negative Seebeck coefficient (S) (**Figure 60(a)**) located at negative and positive energies, respectively. Due to its lower band-gap energy, rutile's density of states overlap the Fermi level at higher Seebeck coefficient values, with a significantly higher

density at positive energy levels, when compared to anatase, agreeing with the experimental results attributing increased thermoelectric properties to the rutile phase. This agrees with the n-type conductivity (and therefore negative Seebeck) associated with Nb-doping for both phases of TiO_2. TiO_2:Nb anatase presents a broader electrical conductivity (σ) peak around the Fermi level, while rutile intersects the E_F at lower intensities (**Figure 60(b)**), explaining its lower contribution to the electrical conductivity, compared to anatase. It is also no surprise that the electronic component of the thermal conductivity (κ_e) (**Figure 60(c)**) closely follows the behaviour of the electrical conductivity. Although not calculated, it would have been interesting to see the respective phononic component due to its significantly higher contribution to the thermal conductivity than the electronic component, as the low number of free electrons in a semiconductor make phonons the main carriers of thermal energy. Measurements presented in **Chapter 4** attribute higher thermal conductivity to the anatase phase.

Figure 61 shows the charge carriers mobility and concentration obtained by Hall effect measurements of TiO_2:Nb thin films measured as-deposited and after annealing at 500 °C, plotted in relation to the deposition temperature. Overall, the films showed higher mobility after annealing, possibly caused by reduced phonon scattering, with the exception of sample RT_C, which decreased its μ_e around 2 $cm^2 \cdot V^{-1} s \cdot^{-1}$. An overall increase in carrier concentration was also observed after annealing but sample HT_E decreased its n_e by one order of magnitude. These results showed good relation to the optical model calculations obtained with SCOUT (not shown). Sample HT_B measured a $\mu_e \approx 2$ $cm^2 \cdot V^{-1} s \cdot^{-1}$ as-deposited and $\mu_e \approx 3.1$ $cm^2 \cdot V^{-1} s \cdot^{-1}$ after annealing and maintained a $n_e \approx 2 \times 10^{20}$ cm^{-3}.

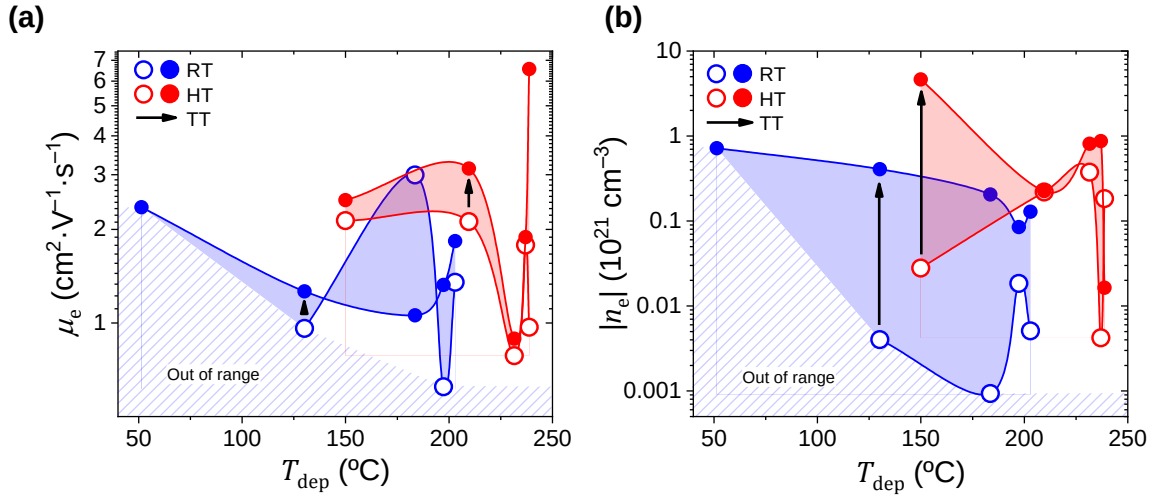

Figure 61. Charge carriers mobility **(a)** and concentration **(b)** of TiO_2:Nb thin films in relation to the chamber temperature during deposition, for films deposited with substrate heating *(HT, red)* and without substrate heating *(RT, blue)*, measured as-deposited *(Ad, open circles)* and after annealing at 500 °C *(TT, closed circles)*. The *blue striped zone* refers to as-deposited thin films with extremely high electrically resistivity and are unable to be measured.

The thermoelectric Power Factor for TiO_2:Nb thin films measured as-deposited and after annealing at 500 °C, was calculated using equation **(8)** and plotted in relation to the deposition temperature (**Figure 62**). Samples measured as-deposited without substrate heating showed an overall lower PF (varying from (0.025 ± 0.004) μW·m^{-1}·K^{-2} to (0.22 ± 0.04) μW·m^{-1}·K^{-2}), when compared to samples deposited with substrate heating (varying from (4 ± 1) μW·m^{-1}·K^{-2} to (160 ± 20) μW·m^{-1}·K^{-2}). The samples deposited at higher temperatures are an exception to this, as samples HT_D and HT_E showed lower PF than the first three deposited thin films with substrate heating. After annealing at 500 °C, the PF increases in all samples, peaking at a maximum of (160 ± 10) μW·m^{-1}·K^{-2} for sample RT_B (deposited at (130 ± 24) °C) and (291 ± 9) μW·m^{-1}·K^{-2} for sample HT_B (deposited at (210 ± 12) °C).

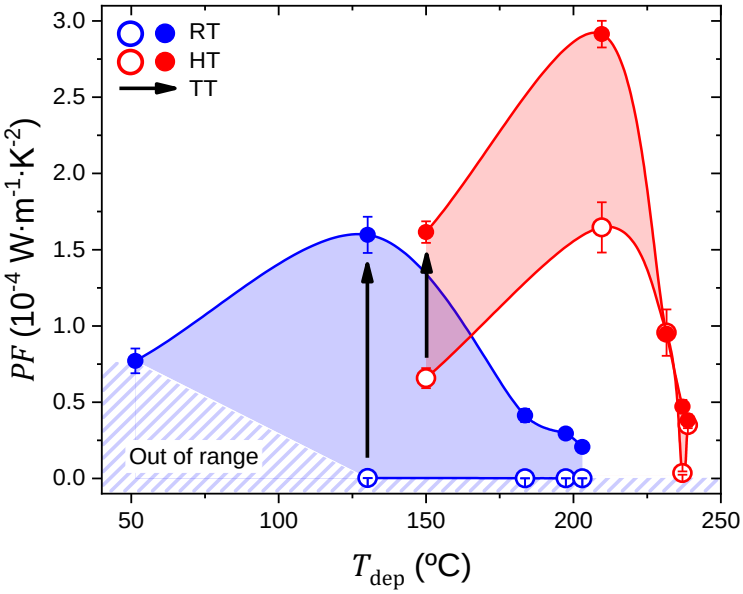

Figure 62. Calculated Power Factor of TiO_2:Nb thin films in relation to the chamber temperature during deposition, for films deposited with substrate heating *(HT, red)* and without substrate heating *(RT, blue)*, measured as-deposited *(Ad, open circles)* and after annealing at 500 °C *(TT, closed circles)*. The *blue striped zone* refers to as-deposited thin films with extremely high electrically resistivity and are unable to be measured.

Regarding the DFT calculations for the Power factor and electronic Figure of Merit (Z_eT) of supercells of TiO_2:Nb (**Figure 63**), it is no surprize that rutile demonstrates considerably higher values than anatase around the intersection with the Fermi level. Considering the relaxation time dependency of σ and κ_e, by taking a constant $\tau_0 = 8.47 \times 10^{-19}$ s for anatase and $\tau_0 = 8.47 \times 10^{-18}$ s for rutile (based on Hall effect measurements), for carrier concentrations of $n_e = 1 \times 10^{21}$ cm^{-3} and $n_e = 1 \times 10^{22}$ cm^{-3}, respectively, yields a PF = (0.02 ± 0.01) μW·m^{-1}·K^{-2} and a $Z_eT = 0.003 \pm 0.001$ for anatase, and a PF = (0.14 ± 0.01) μW·m^{-1}·K^{-2} and a $Z_eT = 0.28 \pm 0.05$ for rutile, at ± 0.01 eV around

the Fermi level. Although it is difficult to use DFT to accurately calculate PF and ZT values, it still offers a valuable qualitative comparison between both anatase and rutile, and the values obtained experimentally.

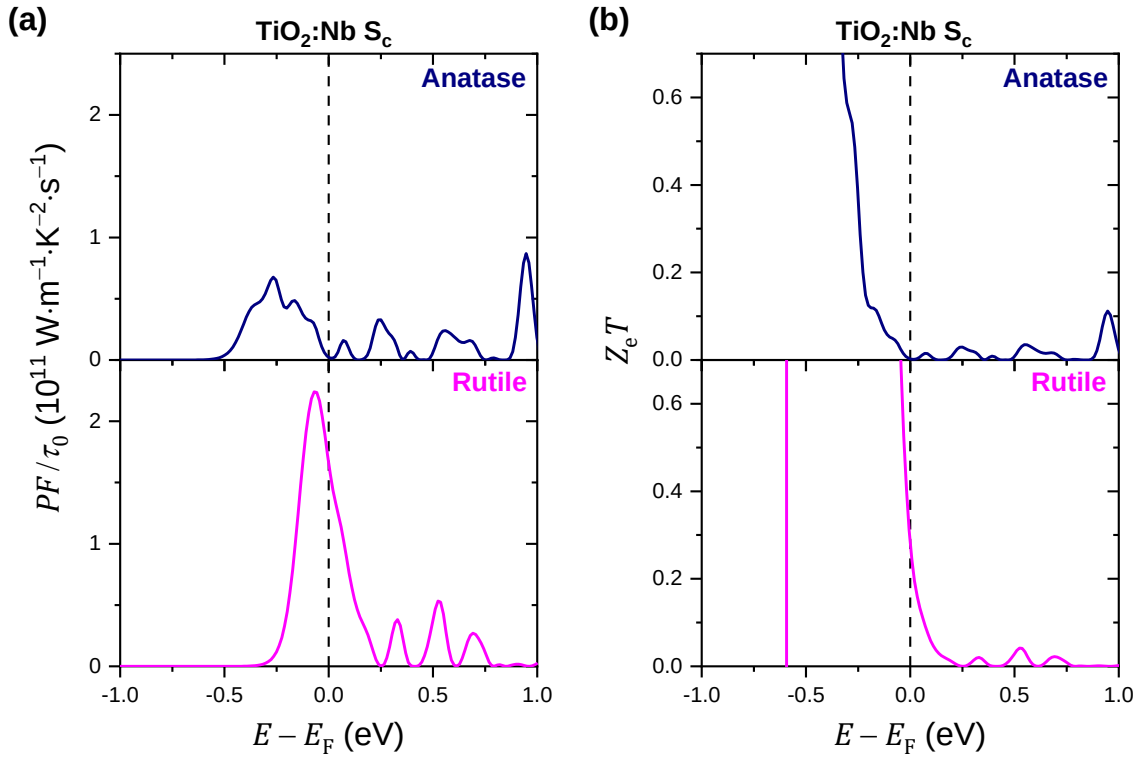

Figure 63. Projected thermoelectric Power Factor dependent of τ_0 **(a)** and electronic Figure of Merit at 300 K **(b)** for the supercells of anatase *(top)* and rutile *(bottom)* TiO_2:Nb. The anatase phase is indicated in *navy*, the rutile phase is indicated in *magenta* and the Fermi level is located at 0 eV.

Table 14 presents the results for all of the samples, measured as-deposited and after annealing at 500 °C. It is obvious that samples RT_B(TT), HT_A(TT), HT_B(TT) and HT_C(Ad) showed the best thermoelectric properties, with PF values above 100 $\mu W \cdot m^{-1} \cdot K^{-2}$, transparency above 65 %, absolute Seebeck coefficient values above 150 $\mu V \cdot K^{-1}$ and electrical resistivity below 0.05 $\Omega \cdot cm$. Similar to what was found in a previous study, the trade-off of a decreased Seebeck coefficient after the annealing, is compensated by a decrease in the electrical resistivity [146].

Sample HT_B(TT) exhibited the highest electrical conductivity at (107.9 ± 0.1) $\Omega^{-1} \cdot cm^{-1}$ and an absolute Seebeck coefficient of (164 ± 2) $\mu V \cdot K^{-1}$. This resulted in the best thermoelectric Power Factor at (291 ± 9) $\mu W \cdot m^{-1} \cdot K^{-2}$ and an estimated Figure of Merit of 0.06 ± 0.01 at 300 K, while maintaining an average transparency of 70 % in the visible range.

Table 14. Summary of results for Transmittance ($\overline{T}_{vis}$) averaged in the (400 to 700) nm range, Band-Gap Energy (E_g), fraction of Rutile phase (W_R), Seebeck coefficient (S), electrical conductivity (σ) and calculated Power Factor (PF) of TiO_2:Nb thin films deposited with (HT) and without (RT) substrate heating, measured as-deposited (Ad) and after annealing at 500 °C (TT), with different deposition temperatures (T_{dep}). The Figure of Merit (ZT) at 300 K was estimated by considering $\kappa = (1.5 \pm 0.1)$ W·m^{-1}·K^{-1} [146].

Sample ($\overline{T}_{dep}$ (°C))		$\overline{T}_{vis}$ (%)	E_g (eV)	W_R (%)	S (μV·K^{-1})	σ (Ω^{-1}·cm^{-1})	PF (μW·m^{-1}·K^{-2})	$ZT_{300\,K}$ (10^{-2})
RT_A (51 ± 15)	**(Ad)**	76	3.340 ± 0.005	20	-4.2 ± 0.4	–	–	–
	(TT)	74	3.406 ± 0.006	20	-90 ± 4	94.3 ± 2.0	77 ± 8	1.5 ± 0.4
RT_B (130 ± 24)	**(Ad)**	73	3.322 ± 0.005	100	-79 ± 8	0.3629 ± 0.0002	0.22 ± 0.04	0.004 ± 0.001
	(TT)	72	3.370 ± 0.007	67	-169 ± 6	55.6 ± 0.2	160 ± 10	3.2 ± 0.7
RT_C (184 ± 7)	**(Ad)**	75	3.315 ± 0.006	100	-28 ± 2	0.678 ± 0.001	0.054 ± 0.008	0.0011 ± 0.0003
	(TT)	76	3.346 ± 0.008	76	-140 ± 4	21 ± 1	41 ± 4	0.82 ± 0.2
RT_D (197 ± 2)	**(Ad)**	75	3.316 ± 0.006	100	-15 ± 1	1.1491 ± 0.0001	0.025 ± 0.004	0.0005 ± 0.0001
	(TT)	73	3.347 ± 0.009	80	-121 ± 4	20.0 ± 0.3	29 ± 2	0.6 ± 0.1
RT_E (203 ± 1)	**(Ad)**	75	3.331 ± 0.007	100	-20 ± 1	1.146 ± 0.004	0.048 ± 0.005	0.0009 ± 0.0002
	(TT)	75	3.360 ± 0.009	75	-108 ± 3	17.6 ± 0.2	21 ± 1	0.41 ± 0.08
HT_A (150 ± 16)	**(Ad)**	67	3.335 ± 0.008	100	-226 ± 7	12.9 ± 0.5	66 ± 7	1.4 ± 0.3
	(TT)	69	3.349 ± 0.009	86	-149 ± 3	72.35 ± 003	162 ± 7	3.5 ± 0.7
HT_B (210 ± 12)	**(Ad)**	70	3.310 ± 0.008	83	-225 ± 7	33 ± 1	160 ± 20	3.5 ± 0.9
	(TT)	70	3.227 ± 0.003	100	-164 ± 2	107.9 ± 0.1	291 ± 9	6 ± 1
HT_C (232 ± 3)	**(Ad)**	73	3.31 ± 0.01	88	-218 ± 5	20 ± 2	100 ± 20	2.1 ± 0.6
	(TT)	73	3.325 ± 0.003	34	-115 ± 2	71.52 ± 0.09	95 ± 4	2.0 ± 0.4
HT_D (237 ± 1)	**(Ad)**	73	3.326 ± 0.009	86	-197 ± 6	0.9 ± 0.2	4 ± 1	0.07 ± 0.03
	(TT)	71	3.333 ± 0.008	87	-140 ± 7	23.956 ± 0.006	47 ± 4	1.0 ± 0.2
HT_E (239 ± 1)	**(Ad)**	74	3.36 ± 0.01	77	-182 ± 5	10.594 ± 0.006	35 ± 2	0.7 ± 0.2
	(TT)	72	3.355 ± 0.009	76	-130 ± 7	22.497 ± 0.006	38 ± 4	0.8 ± 0.2

5.3. Partial Conclusions

Optically transparent Nb-doped TiO_2 thin films with enhanced thermoelectric properties were successfully deposited by reactive DC magnetron sputtering in high vacuum and thoroughly characterized. A difference in the Nb and NbO-related signals in TOF-SIMS between the as-deposited samples shows a change of Nb content and stoichiometry closer to the substrate. A higher heterogeneity of Nb near the interface to the

substrate was observed for higher deposition temperatures, while it is homogenised after annealing at 500 °C. This indicates the importance of the deposition temperature and annealing in the incorporation of Nb into the thin films.

The optimization of the deposition temperature results in thin films with thickness of approximately 200 nm and average optical transmittance in the visible range between 67 % and 76 % and specular reflectance between 16 % and 29 %. Lower substrate temperatures resulted in higher average transmittance, lower specular reflectance and higher band-gap energy. The average transmittance is not significantly affected by the thermal annealing, but the average specular reflectance decreases for all samples. The band-gap energy increased for most cases after thermal annealing, as the thin films re-crystallize with a higher fraction of anatase phase, also evidenced by XRD. The thin films with substrate heating showed an overall higher rutile crystallization. Higher deposition temperature develops a mix of rutile and anatase phase, with subsequently lower content of rutile with deposition progression and increase in temperature. The annealing process helps develop the anatase phase. A higher absolute Seebeck coefficient and lower electrical resistivity were observed for higher deposition temperatures. After annealing the electrical resistivity decreased for all samples, however the Seebeck coefficient only increased for samples deposited without heating, which correlates with past results.

DFT simulations showed a shift of the Fermi level from the valence to the conduction band when doping TiO_2 with Nb, showing an n-type behaviour. The comparison between undoped TiO_2 and TiO_2:Nb reveals an interaction between the Nb 4d-orbital and the Ti 3d-orbital, suggesting a hybridization process. The density of Nb located at the right of the Fermi level suggests its primary contribution to the conduction band, while the additional Nb electrons located at the 4d-orbital displace the conduction band to higher energy levels, more pronounced in the rutile phase. The thermoelectric, electrical and thermal properties calculated by DFT showed a similar behaviour to the obtained experimental results. Owing to its lower band-gap energy, rutile overlaps the Fermi level at higher Seebeck coefficient values than anatase. Anatase presents a broader electrical conductivity peak around the Fermi level, while rutile shows higher values to the right of the Fermi level. A similar behaviour was observed for the electronic component of the thermal conductivity.

The TiO_2:Nb with the best properties was deposited at a temperature between 176 °C and 224 °C, yielding a transparency of 70 %, an n-type electrical resistivity of $(3.1 \pm 0.1) \times 10^{-2}$ Ω·cm and an absolute Seebeck coefficient of (225 ± 7) μV·K^{-1}, resulting in a thermoelectric Power Factor of (160 ± 20) μW·m^{-1}·K^{-2} and an estimated Figure of Merit of 0.035 ± 0.009. After annealing, the same thin film decreased its electrical resistivity to $(0.9270 \pm 0.0009) \times 10^{-2}$ Ω·cm but also decreased its absolute

Seebeck coefficient to (164 ± 2) $\mu V \cdot K^{-1}$, resulting in a maximum thermoelectric Power Factor of (291 ± 9) $\mu W \cdot m^{-1} \cdot K^{-2}$ and an estimated Figure of Merit of 0.06 ± 0.01, while maintaining its transparency. These results are related to the anatase/rutile mixed phase with the prevalence of the rutile phase and correlate with the XRD results and DFT simulations, where the rutile phase enhances the thermoelectric properties, while the anatase phase relates to higher electrical conductivity.

CHAPTER VI.

MORPHOLOGY, MICROSTRUCTURE AND GRAIN BOUNDARY CHARACTERIZATION

6. Morphology, Microstructure and Grain Boundary Characterization

This chapter describes the effect of the stoichiometry in TiO_2:Nb/Ti:Nb thin films on the thermoelectric properties and is based on the following publication:

> *J. M. Ribeiro, A. Welle, T. Boll and C. J. Tavares, "Study of niobium-doped titanium and titanium dioxide thin films by TOF-SIMS, APT and TEM", to-be submitted in 2024.*

Firstly, two 700 nm-thick samples were produced by reactive magnetron sputtering, with varying levels of Oxygen flow, controlled during the reactive sputtering deposition process. This is a follow-up on the study done in **Chapter 4**, which highlighted the importance of the Oxygen content (controlled by the O_2 flow during reactive sputtering), resulting in a small threshold of high Seebeck Coefficient. Secondly, a 220 nm-thick sample was re-produced and thermally annealed from the optimized conditions in **Chapter 5**. The homogeneity of the TiO_2:Nb thin films and segregation of ions into intersections and grain boundaries was analysed by APT, TOF-SIMS and TEM, which were described in **Chapter 2**.

6.1. Experimental Details

6.1.1. Sample Fabrication

Thin films of TiO_2:Nb were produced by reactive DC magnetron sputtering at the CF-UM-UP. A target of Ti(96)Nb(4) wt.% (99.9 % of purity, FHR), with 10 cm of diameter, was used in planar configuration. The films were deposited on (10 × 10 × 0.5) mm^3 Si substrates, cut from P/B doped Si-wafer <100> (Siegert Wafers GmbH) and a specialized silicon coupon with prefabricated microtips from CAMECA. The Si substrates were cleaned with isopropyl alcohol (2-Propanol) and acetone in an ultrasonic bath, both for 15 min. The substrate-holders were mounted onto a rotating 3-position support controlled by a motor (used either in continuous rotation or to exchange samples over the magnetron) and target-substrate distance was kept at 6.5 cm. The chamber was evacuated with a primary rotary pump and a turbo molecular pump to achieve a base pressure of around 10^{-4} Pa and heated up to 125 °C. Research grade

Ar with 99.999 % purity was used as working gas to enable plasma formation and O_2 was used as reactive gas. Prior to the deposition, 2 min of etching at 500 V was performed in an Ar atmosphere at a pressure of 1.8 Pa in continuous rotation at 18 rpm. Target current density, bias voltage and Ar flow were fixed at 12.7 mA·cm^{-2}, –60 V and 40 sccm, respectively, for all depositions, depositing at a pressure of around 0.22 Pa and temperature range of (150 to 239) °C. A dummy deposition of 2 min for target cleaning (burn) was used in the first position of the substrate holder. This was followed by the deposition of two samples (sample A and sample B) for a total time of 18 minutes each. The deposition time and reactive oxygen flow were varied during a continuous deposition for both samples (**Table 15**). The target current was turned off between samples to enable a precise control of the next substrate holder position and deposition parameters. Sample A and sample B were then coated with a protective layer of Ti, deposited using a pure Ti target (99.8 % of purity, FHR), with 10 cm of diameter, in the same configuration as above. Target current density, bias voltage and Ar flow were fixed at 12.7 mA·cm^{-2}, –60 V and 40 sccm, respectively, for 4 min at a pressure of around 0.21 Pa.

Table 15. Deposition conditions for sample A, sample B and sample C. The different deposition times were used to compensate for the lower deposition rate for higher Oxygen flows.

Sample	Layer (deposition order)	t_{dep} (min)	I_{target} (A)	$\Delta V_{target(i-f)}$ (V)	O_2 flow (sccm)
A	1	1	1	351 – 351	0
	2	1	1	353 – 353	1
	3	1	1	353 – 353	2
	4	1	1	354 – 354	3
	5	1.5	1	356 – 363	4
	6	1.5	1	366 – 379	5
	7	1.5	1	381 – 383	6
	8	1.5	1	386 – 388	7
	9	2	1	394 – 406	8
	10	2	1	413 – 428	9
	11	2	1	435 – 448	10
	12	2	1	452 – 455	11
	13 (Ti)	4	1	321 – 317	0
B	1	2	1	458 – 454	11
	2	2	1	453 – 453	10
	3	2	1	451 – 449	9
	4	2	1	444 – 439	8
	5	1.5	1	430 – 425	7
	6	1.5	1	417 – 409	6
	7	1.5	1	403 – 395	5
	8	1.5	1	391 – 388	4
	9	1	1	384 – 380	3
	10	1	1	377 – 374	2
	11	1	1	372 – 370	1
	12	1	1	369 – 365	0
	13 (Ti)	4	1	318 – 320	0
C	1	6	1	403	7

Considering the results obtained in **Chapter 4** and **Chapter 5**, the best-performing TiO_2:Nb thin film was reproduced (sample C), also in **Table 15**, using the same setup as for sample A and sample B, described above. A burn deposition of 7 min was used in a clean substrate holder both for target cleaning and to increase the substrate temperature to around 180 °C. Target current density, bias voltage, O_2 flow and Ar flow were fixed at 12.7 mA·cm^{-2}, –60 V, 7 sccm and 40 sccm, respectively, depositing at a pressure of around 0.22 Pa for 5 min.

Subsequently, sample C was heat treated in a vacuum furnace at 10^{-3} Pa. The temperature was increased from room temperature to 500 °C in 90 min and maintained at 500 °C for 1 h, followed by a natural cooling stage to room temperature for 6 h.

6.1.2. Sample Characterization

SEM was used to investigate the morphology and cross-section of the thin films, performed with a FEI NOVA NanoSEM 200. For cross-section imaging, the samples were cut with a diamond tip and fixed in the sample table with double-sided carbon tape.

TOF-SIMS was performed on thin films deposited on Si substrates, on a TOF.SIMS5 spectrometer (ION-TOF GmbH) equipped with a Bi cluster primary ion source and a non-linear TOF analyser, at the IFG-KIT. UHV base pressure was < 5 × 10^{-9} mbar. The primary ion source was operated in HCB mode providing short Bi^+ primary ion pulses 0.8 ns / 25 keV energy, a lateral resolution of approximately 4 μm, and a target current of 1.4 pA. For depth profiling a dual beam analysis was performed in interlaced mode: the primary ion source was scanned over an area of (300 × 300) μm^2 (128 × 128 data points) and a sputter gun scanned over a concentric field of view. For positive polarity profiles a O_2^+ beam was applied to erode the sample, with 2 keV sputter energy, at 45° incident angle, a scan range of (600 × 600) μm^2 and a target current of approximately 500 nA. For negative polarity profiles a Cs^+ beam eroded the sample, with 2 keV sputter energy, a scan range of (500 × 500) μm^2 and target current of approximately 100 nA. Since the data acquisition is fast in respect of the observed erosion speeds, 25 data points were binned for plotting. Secondary ion intensities are plotted over depth, using total thickness obtained through cross-section SEM images. Note however that this scale is not linear if different materials with different erosion rates / sputter yields are analysed.

APT experiments were performed at the IAM-KIT. The samples were deposited onto a specialized Si coupon with prefabricated microtips from CAMECA. To protect the thin film in sample C, a protective

layer of Ag was deposited by DC magnetron sputtering using a pure Ag target (99.99 % of purity, FHR), with 10 cm of diameter, in planar mode. Target current density, bias voltage and Ar flow were fixed at 7.6 mA·cm^{-2} (corresponding to 374 V), –60 V and 40 sccm, respectively, depositing for 90 sec at a pressure of around 0.23 Pa. The tips were prepared using a Zeiss Auriga 60 Dual Beam FIB, in order to obtain a sharp tip with an apex diameter of around 60 nm, and subsequently measured in a LEAP 4000X HR in UV-laser mode (10 pJ to 30 pJ), with a pulse frequency of 100 kHz to 200 kHz, at a temperature of 40 K to 50 K and a detection rate of 0.2 % to 0.5 %. The data was reconstructed using the software Ivas 3.6.14 and AP Suite from CAMECA.

STEM combined with EDX was conducted on a thin film deposited on a Si substrate. A planar view (parallel to the film-substrate interface) lamella was prepared by FIB from sample C deposited on a Si(111) substrate, using a Dual Beam FIB-SEM Helios NanoLab 450S equipped with a UHREM FEG-SEM, operating with a Ga gun. HAADF-STEM, BF-STEM and EDX were carried out using a FEI Titan G2 80–200 kV ChemiSTEM (Probe-Corrected) and a FEI Titan G3 Cubed Themis 60–300 kV (Double-Corrected) electron microscope, both equipped with a X-FEG, Cs probe corrector, and super X EDX detectors, operating at 200 kV. The experiments were conducted at the AEMIS facility (INL).

6.2. Results and Discussion

The cross-sections of samples A and B were analysed with SEM (**Figure 64**), where the total thickness was determined.

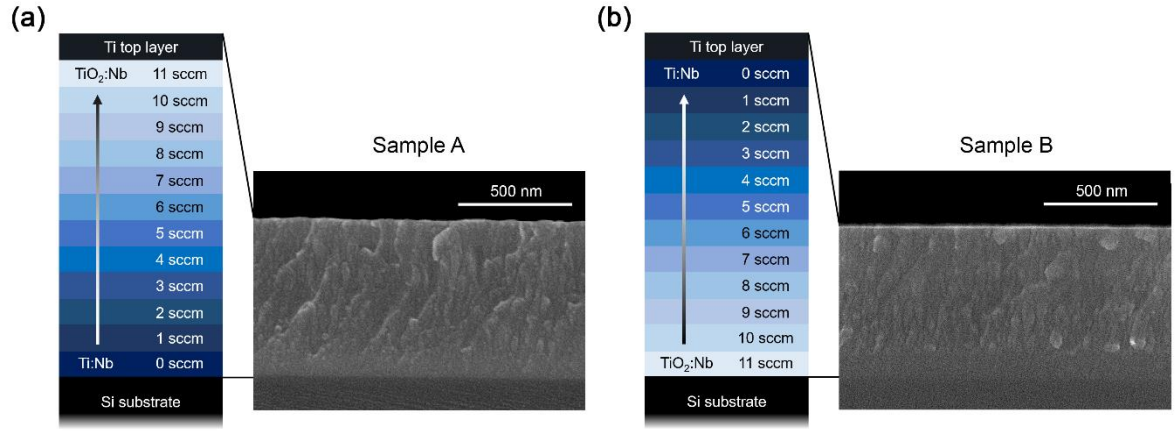

Figure 64. Representation and respective SEM cross-section of Sample A: Ti:Nb → TiO_2:Nb (11 sccm O_2) + Ti **(a)** and Sample B: TiO_2:Nb (11 sccm O_2) → Ti:Nb + Ti **(b)**, both measuring 700 nm of thickness.

There is no evident difference between sample A and sample B and no clear distinction of layers within the films, everything appears continuous, apart from the first ~ 100 nm of the film growth, which is a normal result of sputtering.

The TOF-SIMS depth profiles (**Figure 65**) show a clear distinction of layers within the samples, including the topmost Ti layer, and the negative and positive polarity analysis complement each other quite well. Sample A was easier to analyse, as it shows the 12 layers more clearly. Only 9 layers were able to be discerned on sample B, since the interfaces were less obvious and pronounced. There is a higher Nb content near the interface with the substrate (first nm of growth). The Oxygen clearly increases for higher Oxygen flows, but so does the Nb content within the film. The same is not discerned from the Ti and TiO signals. Interestingly, for the positive polarity, the Nb and NbO signals follow the same trend when the Oxygen content is higher, splitting halfway through the sample, for lower Oxygen flows. The NbO signal decreases with lower Oxygen content, but the Nb signal does not, even increasing for Oxygen flows close to 0 sccm. This trend is also seen for the negative polarity, but for NbO and NbO_2 signals, indicating a change in the stoichiometry of the samples relating to the Oxygen content.

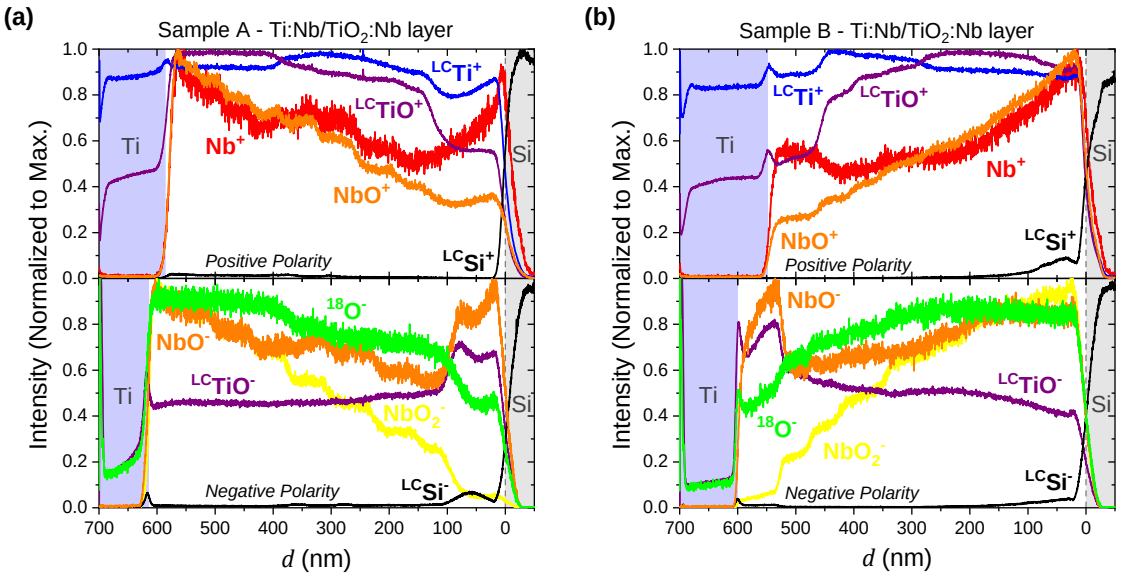

Figure 65. TOF-SIMS depth profile of Sample A **(a)** and Sample B **(b)**, in positive polarity (sample erosion with Oxygen) – $^{LC}Ti^+$ (linear combination of $^{50}Ti^+$, $^{46}Ti^+$,$^{47}Ti^+$ and $^{49}Ti^+$), $^{LC}TiO^+$ (linear combination of $^{50}TiO^+$, $^{46}TiO^+$,$^{47}TiO^+$ and $^{49}TiO^+$), Nb^+, NbO^+ and $^{LC}Si^+$ (linear combination of $^{30}Si^+$ and $^{29}Si^+$) – and negative polarity (sample erosion with Cesium) – $^{18}O^-$, $^{LC}TiO^-$ (linear combination of $^{50}TiO^-$, $^{46}TiO^-$ and $^{49}TiO^-$), NbO^-, NbO_2^- and $^{LC}Si^-$ (linear combination of $^{30}Si^-$ and $^{29}Si^-$) – normalized to maximum signal intensities with 4 point binning in the x-axis. Note that both depth profiles from each sample were not recorded at the same spot.

A relative content of Nb was determined by dynamic TOF-SIMS (in positive polarity) by calibrating Nb^+, NbO^+ and NbO_2^+ signals on the $^{46}Ti^+$, $^{46}TiO^+$ and $^{46}TiO_2^+$ peak area signals, respectively, over

the depth of sample A. **Figure 66** shows the Nb to Ti signal ratios (normalized to maximum) plotted versus the oxygen flow, showing a proportional linear behaviour for the three signals, which confirms that the use of reactive O_2 during sputtering favours the implantation of Nb into the TiO_2 films.

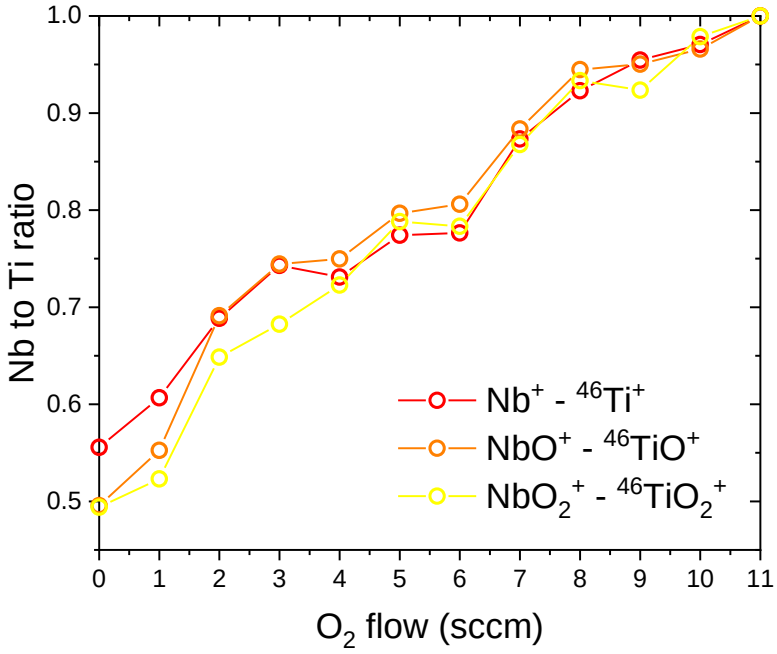

Figure 66. Relative ratio of Nb^+, NbO^+ and NbO_2^+ signals calibrated on the $^{46}Ti^+$, $^{46}TiO^+$ and $^{46}TiO2^+$ peak area signals, respectively, plotted against the reactive oxygen flow during sputter deposition over the depth of sample A, obtained by TOF-SIMS in positive polarity with Oxygen beam erosion.

Regarding the APT analyses, which can be found in their entirety as supplementary information in **APPENDIX E – APT Analysis**, some challenges were encountered during the tip measurements. One of the most common problems during APT analyses is sample tip fracture, which occurs due to high mechanical stress.

The initially prepared tips for sample A fractured at the interface of the topmost Ti layer and the 12^{th} layer of TiO_2:Nb (with 11 sccm of O_2 flow). This was due to the high electrical resistivity of the TiO_2:Nb layer, compared to that of undoped Ti. As described in **section 2.3.1.7**, the electric field during an APT measurement increases with the voltage applied to the sample, and the voltage is proportional to the tip apex radius, as the tip is eroded and dulled and becomes harder to evaporate ions. This is problematic when analysing materials with different electrical resistivities. In the case of Sample A, when at the interface of the Ti layer to the more resistive TiO_2:Nb layer, the system needs to increase the voltage accordingly to be able to evaporate the atoms, increasing the probability of tip fracture. To counter this, new tips were prepared with FIB by milling further into the sample, which enables the analysis of the first

deposited layers. The best APT analysis enabled the distinction of 4 layers (**Figure 67(a)**) and the Si substrate underneath. Sample B was successful in analysing the top layers of the material, due to their higher electrical conductivity. The tip with the most success displayed a total of 5 apparent layers of varying Ti and O content (**Figure 67(b)**) before the tip fractured. The same approach of milling further into the sample was mostly unsuccessful for Sample B, as it reaches layers with increased electrical resistivity and makes it difficult to evaporate the atoms, increasing the voltage and eventually causing a tip fracture.

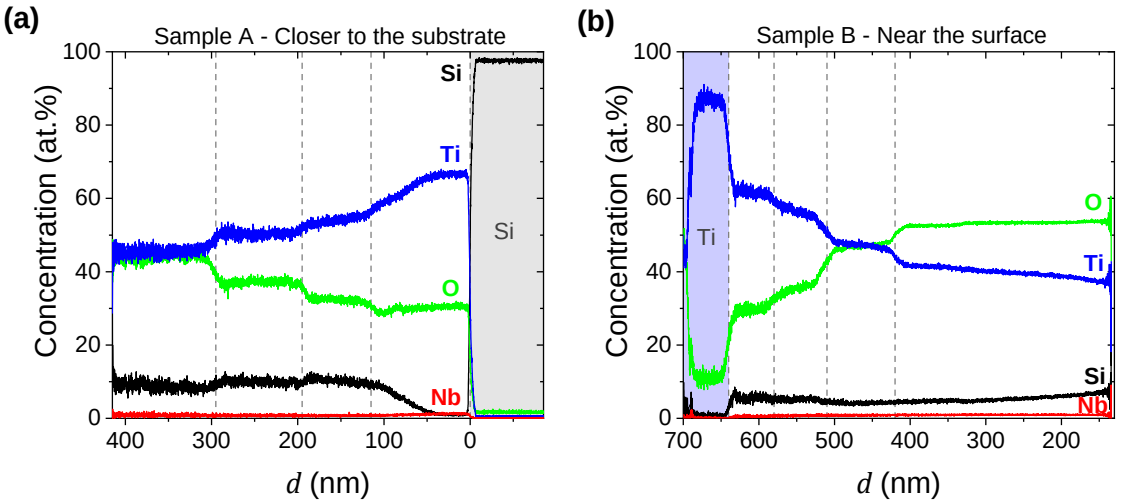

Figure 67. 1D concentration profile in the *z*-axis (parallel to the film growth) for sample A **(a)**, analysed closer to the substrate, and sample B **(b)** obtained by APT.

For sample A, the total Nb atomic content seems to increase with lower O content inside the Ti:Nb/TiO_2:Nb layers, except for the first deposited layer, where the Nb content drastically decreases. As for Sample B, The Nb content is quite low but slightly increases with higher O content. These trends somewhat match with what was observed with TOF-SIMS.

Figure 68 presents side views of atomic Ti and O concentration, rendered in volume, for sample A and sample B, while **Figure 69** shows a rendered volume of atomic Ti concentration and density, for sample A and sample B. In both samples, there is not only an evident change in not just atomic Ti concentration, but also density, in the *z*-axis. Sample A shows a progressive increase in atomic Ti concentration with increased O_2 flow (**Figure 69(a)**). When O_2 flow is increased, Ti density decreases and seems to have a higher distribution when no oxygen is added into the chamber (**Figure 69(b)**). In sample B, the Ti concentration gets progressively higher as the O_2 flow rate decreased but allows a more evident difference of the different layers, while showing homogeneity inside each layer (**Figure 69(c)**). Ti density on the other hand, although following the same trend as the concentration, shows an increase

at the interface between layers, meaning a change in the deposition of Ti atoms right after the O_2 flow was adjusted each time (**Figure 69(d)**).

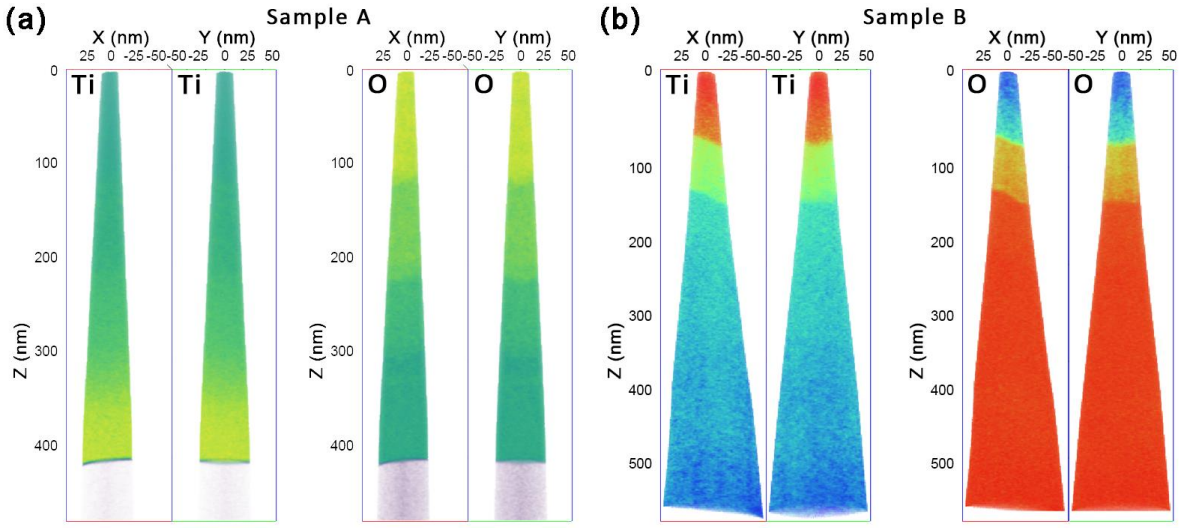

Figure 68. Volume render of atomic Ti and O concentrations for tip M10* of sample A **(a)**, analysed closer to the substrate, and M9 of sample B **(b)**. Sample count threshold at 0 %, with confidence sigma of 0. Opacity is at half value and a darker colour value relates to a higher atomic concentration value.

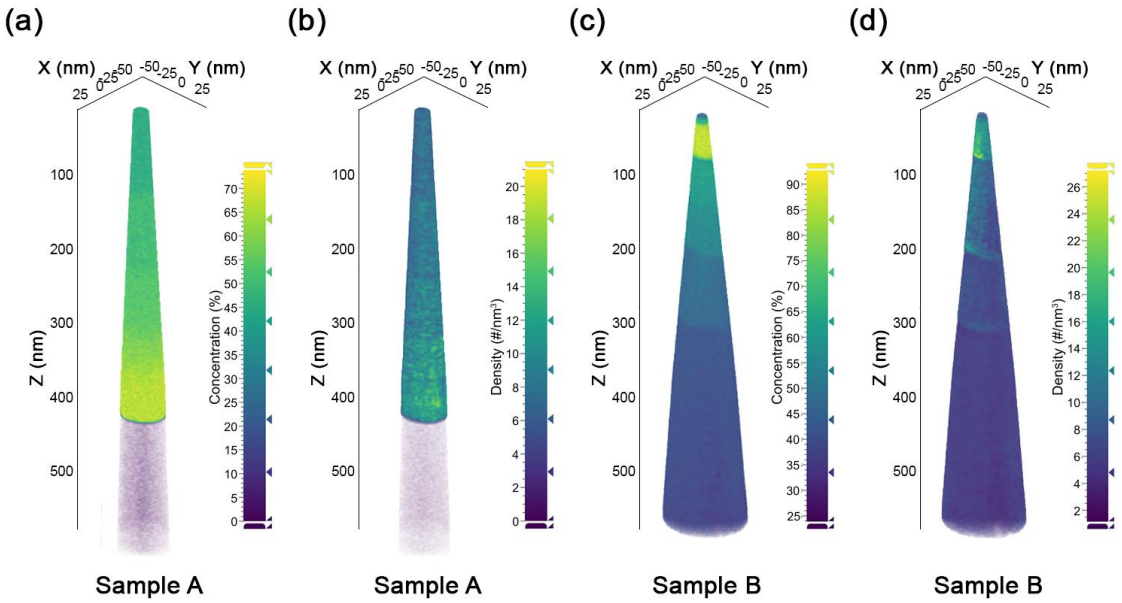

Figure 69. Volume render of atomic Ti concentration **(a)** and density **(b)** for tip M10* of Sample A, analysed closer to the substrate, and atomic Ti concentration **(c)** and density **(d)** for tip M4 of Sample B. Sample count threshold at 0 %, with confidence sigma of 0. Opacity is at half value and a darker colour value relates to a higher atomic concentration/density value.

Even so, sample A is useful in analysing the first deposited layers (closer to the substrate), while sample B is useful in analysing the topmost set of layers, both complementing each other well and showing good agreement with the TOF-SIMS results.

Considering the results obtained in **Chapter 4** and **Chapter 5**, the best-performing TiO_2:Nb thin film (sample C) was reproduced and analysed as-deposited (Ad) and after annealing at 500 °C (TT). **Figure 70** shows the TOF-SIMS depth profile of Sample C, measured as-deposited and after annealing at 500 °C. 220 nm of thickness.

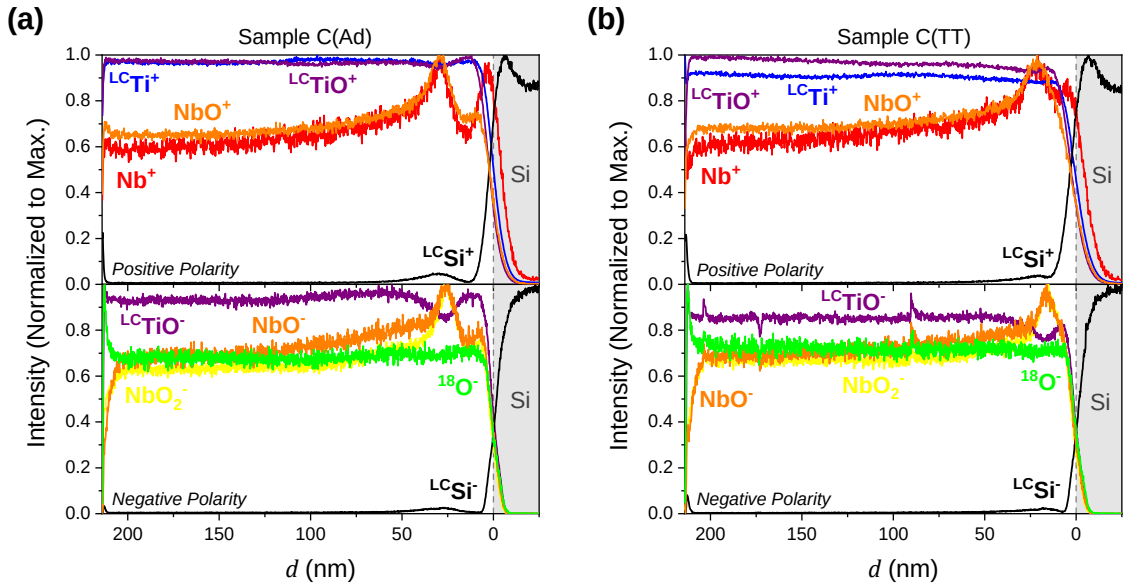

Figure 70. TOF-SIMS depth profile of a TiO_2:Nb thin film (Sample HT_B) measured as-deposited (Ad) **(a)** and after annealing at 500 °C (TT) **(b)**, in positive polarity – $^{LC}Ti^+$ (linear combination of $^{50}Ti^+$, $^{46}Ti^+$,$^{47}Ti^+$ and $^{49}Ti^+$), $^{LC}TiO^+$ (linear combination of $^{50}TiO^+$, $^{46}TiO^+$,$^{47}TiO^+$ and $^{49}TiO^+$), Nb^+, NbO^+ and $^{LC}Si^+$ (linear combination of $^{30}Si^+$ and $^{29}Si^+$) – and negative polarity – $^{18}O^-$, $^{LC}TiO^-$ (linear combination of $^{50}TiO^-$, $^{46}TiO^-$ and $^{49}TiO^-$), NbO^-, NbO_2^- and $^{LC}Si^-$ (linear combination of $^{30}Si^-$ and $^{29}Si^-$) – normalized to maximum signal intensities with 4 point binning in the x-axis.

APT measurements of the thinnest TiO_2:Nb film (sample C) were very successful in assessing the in-depth composition and show good agreement with TOF-SIMS. **Figure 71** displays the 1D concentration profile in the z-axis assessed over a (10 × 10) nm cylinder at the centre of the sample tip. The annealing does chance the overall composition of Sample C, as the signals are more homogeneous throughout the film's depth. Si and Nb contents in sample C(Ad) are higher closer to the interface with the substrate, contrary to Ti and O, as evidenced by the decomposed atomic signals.

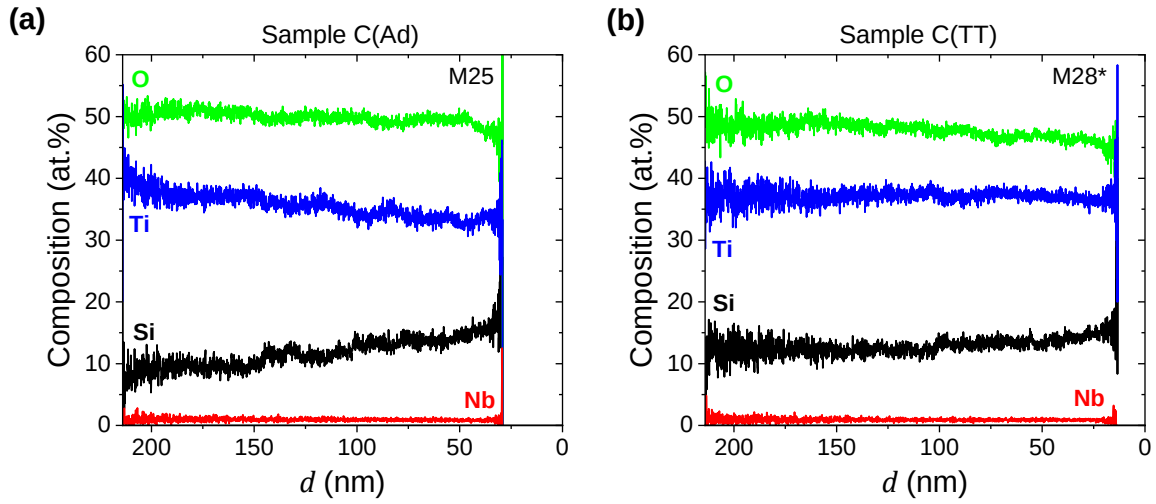

Figure 71. 1D concentration profile in the *z*-axis (parallel to the film growth) of two tips of a TiO_2:Nb thin film (Sample C), M25 measured as-deposited *(Ad)* **(a)** and M28* measured after annealing at 500 °C *(TT)* **(b)**, obtained by APT.

The atomic concentrations of Sample C obtained by APT and TEM-EDS show good agreement with previous results obtained by SEM-EDX and XPS (**Table 16**). Over the various APT tip and TEM zone measurements, the atomic content does not significantly change, even after the annealing process. TEM-EDS shows an average Ti/O content of (40/53 ± 6) %, with (1.4 ± 0.3) of Nb content for sample C(TT).

Table 16. Relative atomic Ti, O and Nb composition of a TiO_2:Nb thin film (Sample C) as-deposited (Ad) and after annealing at 500 °C (TT), obtained by APT (APPENDIX E – APT Analysis), SEM-EDX (APPENDIX A – SEM-EDX Analysis), STEM-EDX (APPENDIX F – HAADF-STEM Analysis) and XPS (Section 3.2).

Method		Ti (at.%)	O (at.%)	Nb (at.%)
APT	Ad	44.4	54.7	0.9
	TT	47.9	51.2	0.9
SEM-EDX	Ad	28.1	70.8	0.7
STEM-EDX	TT	42.2	56.3	1.5
XPS	Ad	38.0	60.9	1.1
	TT	32.4	66.3	1.3

Another challenge, affecting both APT and TOF-SIMS, is the overlaps of peaks in the mass spectra during data reconstruction, between elements at different charge states, such as O^+ and Ti^{3+} at around m/z =16 Da in the mass spectrum. In most cases, overlaps can be distinguished based on the presence of other peaks or isotopes, but elements can field evaporate in conjunction with H, C or O, producing a

complex mass spectrum that makes it difficult to interpret and identify single atoms. Additionally, surface migration can occur due to collision cascade, inherently influencing the subsequent analysis layers.

Observing the APT 3D reconstructed ion maps in **Figure 72**, everything inside the film appears homogeneous, with no distinguishable difference between as-deposited and after annealing measurements. Grain boundaries are not easily discerned, due to the small grain size of the TiO_2:Nb thin films.

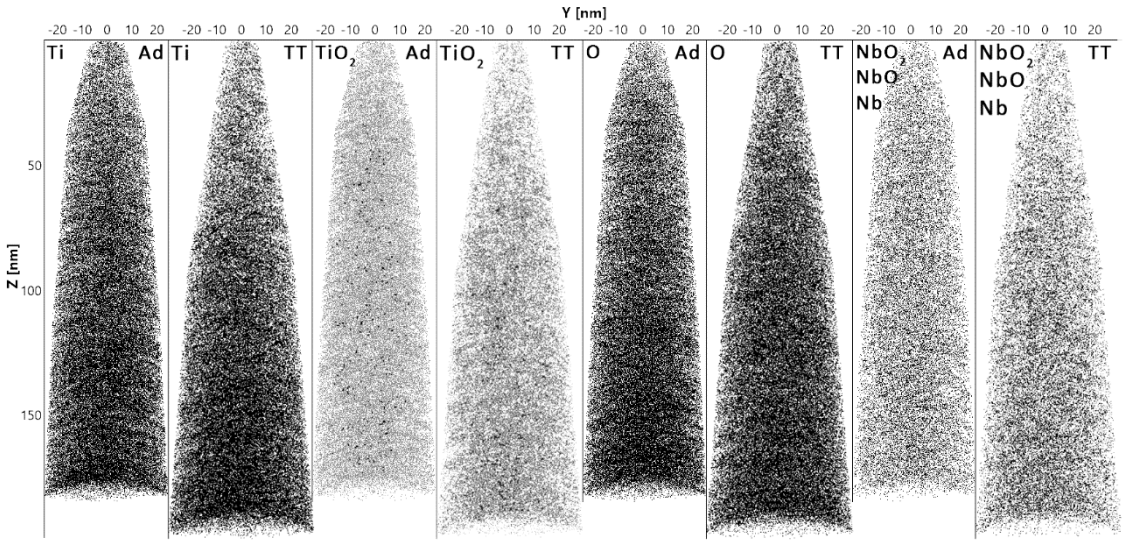

Figure 72. APT profile viewed ionic maps of Ti, TiO_2, O and a combination of Nb, NbO and NbO_2 signals of the 3D reconstruction of a TiO_2:Nb thin film (Sample C), tip M25 measured as-deposited *(Ad)* and M28* measured after annealing at 500 °C *(TT)*.

Figure 73 presents side views of tip M25 for sample C(Ad) and M28* for sample C(TT), with decomposed atomic concentration iso-surfaces of Nb and Ti, making it apparent that there is, in fact, compositional differences. On the one hand, Nb still appears homogeneously distributed, although with some apparent preferential zones within the samples. On the other hand, the top of both tips shows preferential higher Ti content, with some segregation along *z*-oriented lines, showing an indication of column-shaped grain. The 36 % Ti iso-surfaces were spread out over a larger tip volume after annealing, similar to what was observed in the 1D concentration profiles. This does not necessarily indicate a change in Ti atomic content and could be due to analysis in a different tip depth point, as the sample milling through FIB is not able to be accurately controlled for very thin layers.

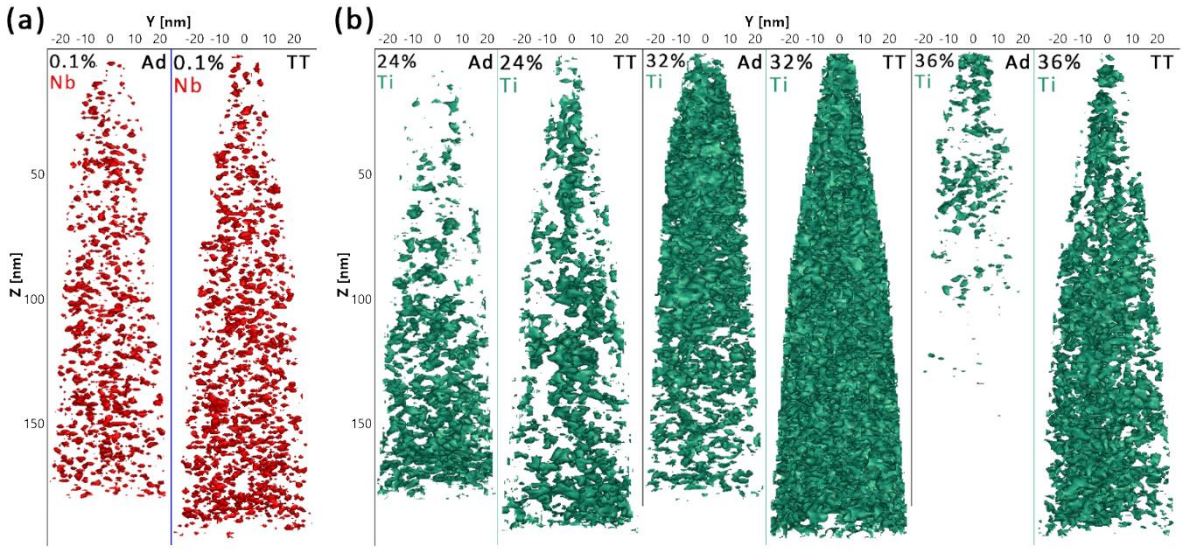

Figure 73. APT profile views of the 3D reconstruction of a TiO_2:Nb thin film (Sample C), tip M25 measured as-deposited *(Ad)* and M28* measured after annealing at 500 °C *(TT)*, with decomposed atomic concentration iso-surfaces of Nb at 0.1 % **(a)** and Ti at 24 %, 32 % and 36 **(b)**. Sample count threshold at 1 % for Nb and 5 % for Ti, with confidence sigma of 1.

Figure 74 presents a top viewed slice in the *z*-axis of tip M27 for sample C(Ad), with three different decomposed atomic concentration iso-surfaces of Ti, Si, O and Nb.

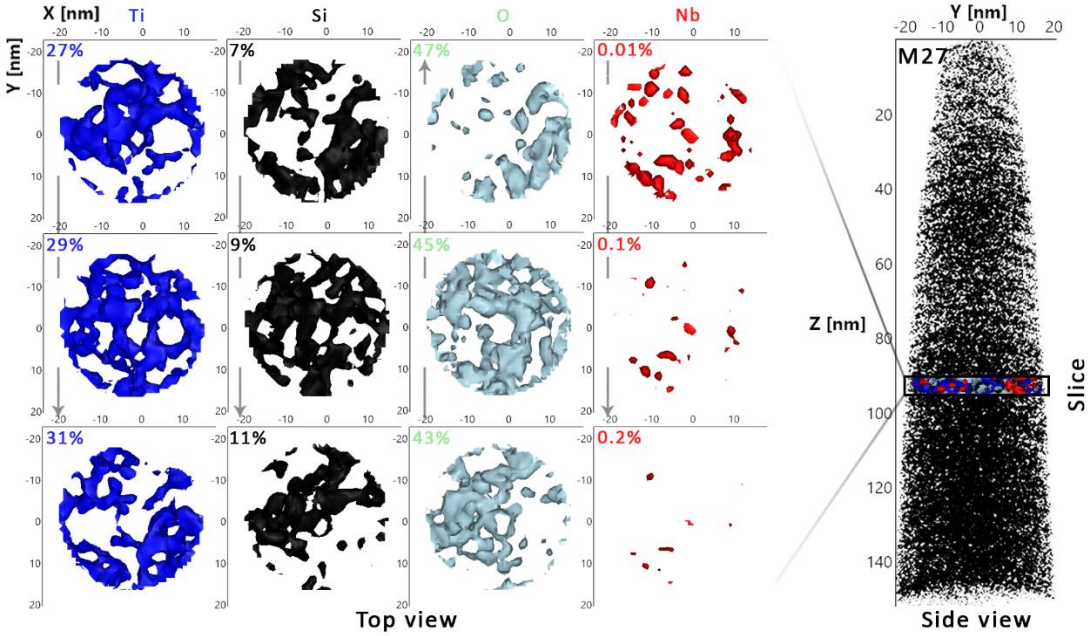

Figure 74. APT sliced top view of the 3D reconstruction of tip M27 (5113) of a TiO_2:Nb thin film (Sample C(Ad)), decomposed atomic Ti (*blue*, at 27 %, 29 % and 31 %), Si (*black*, at 7 %, 8 % and 11 %), O (*green*, at 47 %, 45 % and 43 %) and Nb (*red*, at 0.01 %, 0.1 % and 0.2 %) concentration iso-surfaces. Sample count threshold at 1 % for Si and Nb and 5 % for Ti and O, with confidence sigma of 1.

The iso-surfaces of atomic Ti concentration show a clear heterogeneous distribution within the sample. At around 30 at.%, the Ti is somewhat homogeneous throughout the film, with higher and lower regions having higher and lower concentration of Ti ions, respectively. The atomic Si concentration iso-surfaces also show zones with distinct stoichiometry within the sample, somewhat inversely matching with the Ti surfaces. As for atomic Nb, there is no clear distinction of region-dominated content as was observed with Ti and Si. However, the Nb ions are not completely homogeneously distributed and appear to be clustering, as evidenced by decreasing iso-surface areas for higher Nb concentrations, culminating in preferential spots within the sample. At higher concentrations the Nb iso-surfaces are mainly located at sample regions with higher Ti and lower Si concentrations. Nearest neighbour distributions (not included) do not indicate Nb clustering is any of the measurements.

HAADF-TEM was conducted on sample C(TT) to get further insight on grains and grain boundary morphology. An overall view of the sample is shown in **Figure F 1**. **Figure 75** and **Figure 76** present the compositional TEM-EDX mapping of Ti, Nb and O signals for ROI#1 and ROI#53, respectively. The TEM-EDX results for ROI#2, ROI#3, ROI#36, ROI#49 and ROI#240 are given in **APPENDIX F – HAADF-STEM Analysis**.

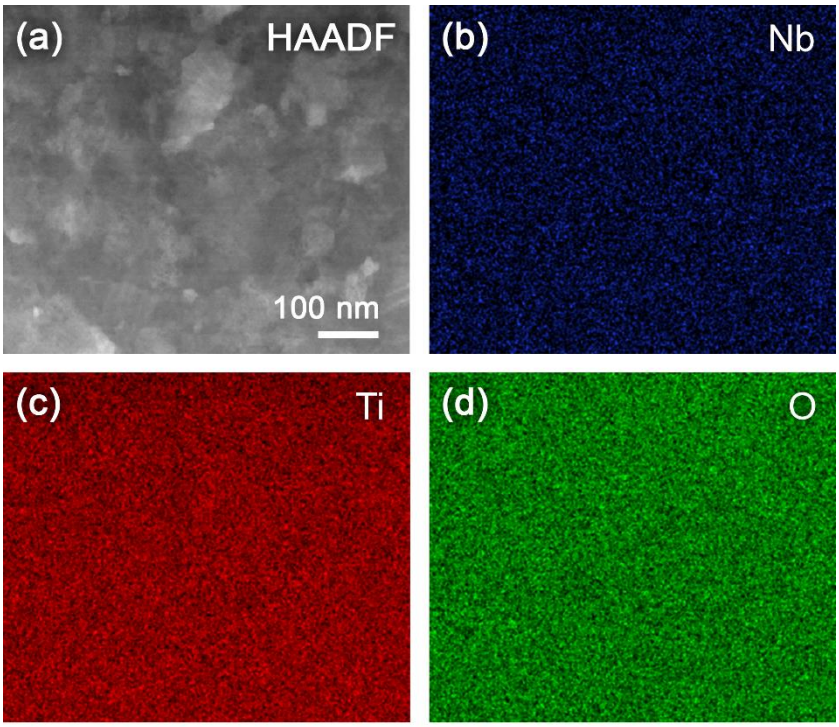

Figure 75. HAADF-STEM (ROI#1) **(a)** and respective Nb **(b)**, Ti **(c)** and O **(d)** EDX maps of a TiO_2:Nb thin film after thermal annealing at 500 °C (Sample C(TT)).

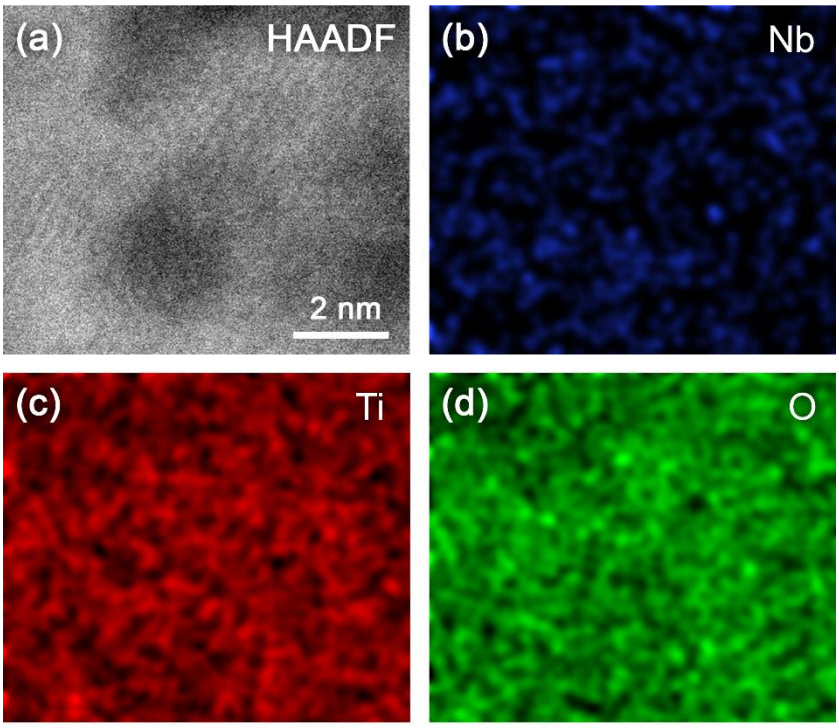

Figure 76. HAADF-STEM (ROI#53) **(a)** and respective Nb **(b)**, Ti **(c)** and O **(d)** EDX maps of a TiO_2:Nb thin film after thermal annealing at 500 °C (Sample C(TT)).

It is possible to detect Ti and O and the presence of Nb through the TEM-EDX and no segregation is observed in **Figure 75**, which correlates with what was observed in **Chapter 3**. In the smaller analysis area in **Figure 76**, however, Nb is clearly concentrating in preferential zones within the crystalline grains, which agrees with the APT findings. Ti and O signals are also somewhat heterogeneous within the grains, but no concentration differentiation can be discerned at grain boundaries. Hence, although Nb is not completely homogeneously distributed, it is not segregating to the grain boundaries and is fully integrated into the TiO_2 matrix.

It is also possible to discern various crystalline grains with distinct plain orientations, with sizes around (5 to 6) nm. In most cases, such as ROI#53 in **Figure 77**, the interplanar distance d_{hkl} of a crystal can be measured directly. In order to obtain phase and crystal orientation information, the interplanar distance was measured from the fast Fourier transform (FFT) in a chosen zone. The Micrograph for an analysed zone in Sample C(TT) (ROI#230) in **Figure 78**, and respective FFT for a chosen region, shows rutile (110) with interplanar distance $d = 3.30$ Å.

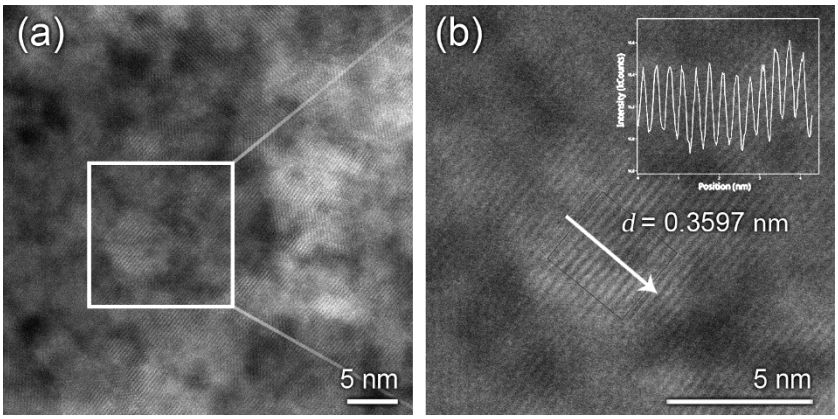

Figure 77. HAADF-STEM (ROI#53) of a TiO_2:Nb thin film (Sample C(TT)) **(a)** and zoomed-in amplification **(b)** represented by the white square on the main micrograph in (a). A direct measurement of the interplane distance (d) in indicated by the white arrow and intensity vs. position plot in (b).

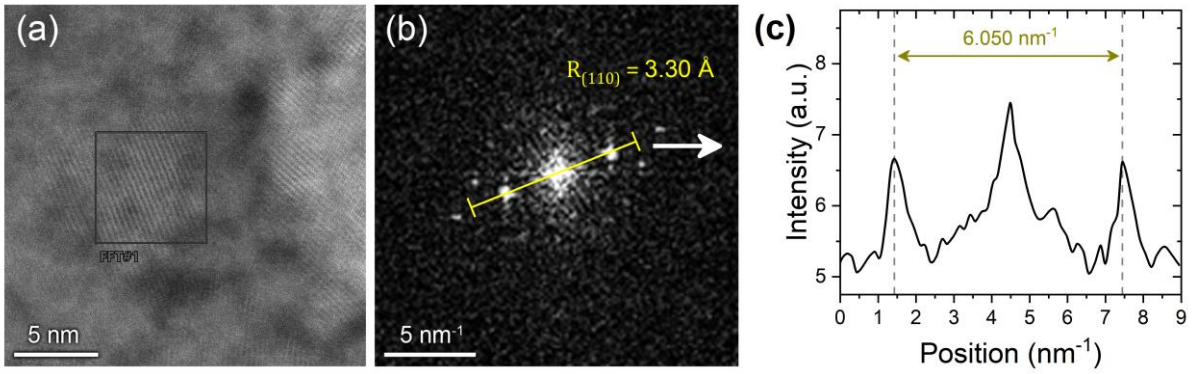

Figure 78. HAADF-STEM (ROI#230) along [110] **(a)**, FFT **(b)** and Intensity Profiles **(c)** for an analysis zone in a TiO_2:Nb thin film (Sample C(TT)). The FFT is represented by the coloured square on the main micrographs in (a) and yellow line in (b) represents plane orientation positions plotted in (c).

Through the STEM analysis of various regions in sample C(TT), a contribution of both anatase and rutile phases was found, with rutile being the most prevalent throughout the measurements, per average interplanar distances of $d_{\mathrm{R}(011)} = (2.52 \pm 0.04)$ Å, $d_{\mathrm{R}(110)} = (3.29 \pm 0.07)$ Å and $d_{\mathrm{R}(120)} = (2.03 \pm 0.04)$ Å.

Figure 79(a) exhibits a STEM micrograph for ROI#22, with FFTs of four smaller analysis zones. The smaller analysis regions Z_b (**Figure 79(b)**) and Z_d (**Figure 79(d)**) show rutile (110) and Z_c (**Figure 79(c)**) presents both rutile (110) and (011). Z_e (**Figure 79(e)**) also shows rutile (011) but it also presents anatase planes oriented along (004) with $d_{\mathrm{A}(004)} = 2.35$ Å. ROI#27 (**Figure 80(a)**) is a magnification of the top-right region of ROI#22. Analysis region Z_b (**Figure 80(b)**) presents planes oriented along rutile (110) and (121). Z_d (**Figure 80(d)**), a smaller analysis region contained in Z_b, shows both anatase (011) planes, with $d_{\mathrm{A}(011)} = 3.45$ Å, and rutile (120) and (220), with interplanar

distances of 2.04 Å and 1.59 Å, respectively. Z_e (**Figure 80(e)**) shows and rutile (110), (120) and (121) ($d_{R(121)} = 1.67$ Å).

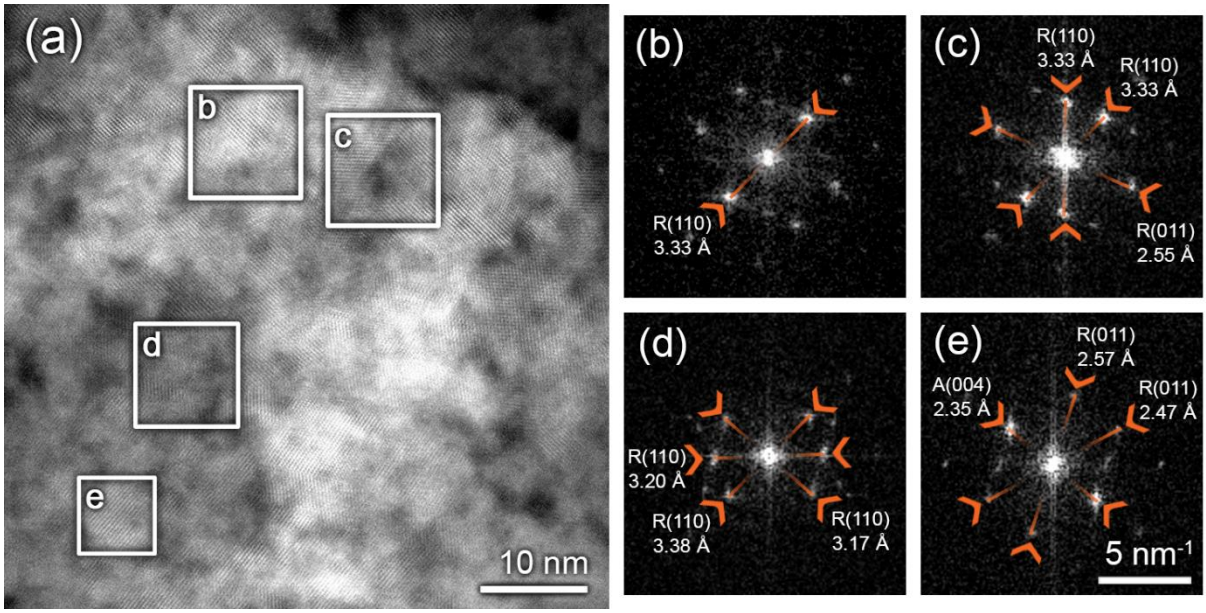

Figure 79. HAADF-STEM (ROI#22) **(a)** and FFTs **(b,c,d,e)** for four analysis zones in a TiO_2:Nb thin film (Sample C(TT)). The FFTs are represented by the white squares correspondingly identified on the main micrographs in (a). Plain orientation positions are indicated in orange. Analysis zone Z_e (e) is located around ROI#53.

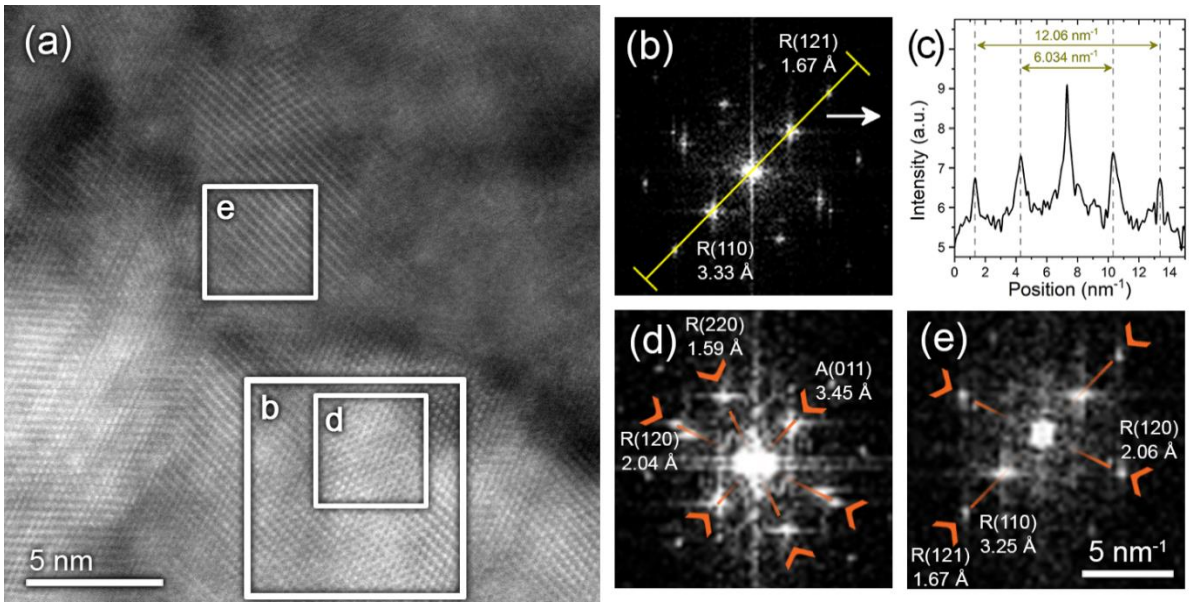

Figure 80. HAADF-STEM (ROI#27) **(a)**, FFTs **(b,d,e)** and intensity profile **(c)** for three analysis zones in a TiO_2:Nb thin film (Sample C(TT)). The FFTs are represented by the white squares correspondingly identified on the main micrographs in (a). Plain orientation positions are indicated in orange and yellow line in (b) represents plane orientation positions plotted in (c).

In a separate region, ROI#756 (**Figure 81(a)**) indicates smaller polycrystalline grains of around (2 to 3) nm, with crystals oriented in different between the anatase (115), (002) and (112) planes (**Figure 81(b)**), with interplanar distances of $d_{A(115)} = 1.38$ Å, $d_{A(002)} = 1.92$ Å to $d_{A(112)} = 2.26$ Å. ROI#747 (**Figure 82(a)**) exhibits similarly-sized grains, but with only rutile (120) and (031) planes (**Figure 82(b)**), with respective interplanar distances of 1.98 and 1.38 Å.

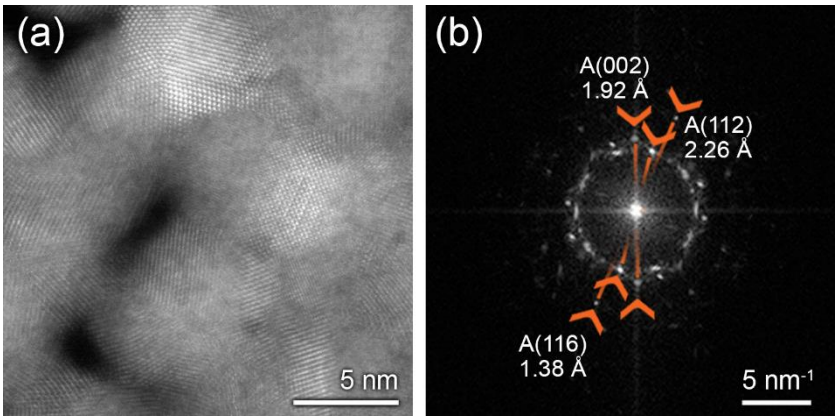

Figure 81. HAADF-STEM (ROI#756) **(a)** and FFT **(b)** in a TiO_2:Nb thin film (Sample C(TT)). Plain orientation positions are indicated in orange.

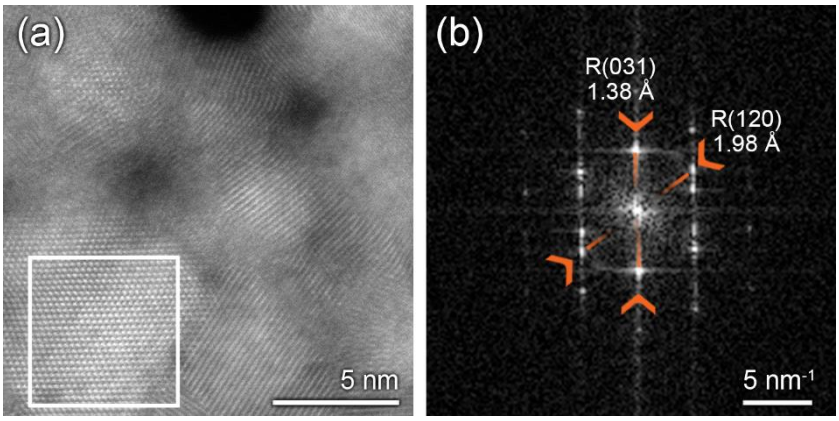

Figure 82. HAADF-STEM (ROI#747) **(a)** and FFT for an analysis zone **(b)** in a TiO_2:Nb thin film (Sample C(TT)). The FFT is represented by the white square on the main micrographs in (a). Plain orientation positions are indicated in orange.

The crystalline planes observed in the HAADF-STEM micrographs indicate a synergistic interaction between phases and agree with the main A(101) and R(110) planes observed in the GIXRD patterns previously presented in **Chapter 5**, with rutile being the most predominantly found. It's interesting that anatase along [112] was detected, relating to a rarely observed twinning.

As expected from APT observations, sample C(TT) possesses small grains around 5 nm, non-observable through previous SEM cross-sections.

6.3. Partial Conclusions

Thin films of Ti:Nb and TiO_2:Nb were successfully deposited by reactive DC magnetron sputtering, creating a stack of layers by varying the O_2 flow rate during deposition. The samples were covered with a protective layer of Ti. SEM cross profiles measured a thickness of approximately 700 nm and was not able to discern any obvious morphological different inside the films.

TOF-SIMS measurements were able to distinguish between the different layers where the O_2 was varied, with sample A (depositing from 0 sccm to 11 sccm of O_2 flow) being easier to measure. Nb content is higher near the interface with the substrate (first nm of growth). The Oxygen clearly increases for higher Oxygen flows, but so does the Nb content within the film. The same is not discerned from the Ti and TiO signals. Interestingly, for the positive polarity, the Nb and NbO signals follow the same trend when the Oxygen content is higher, splitting halfway through the sample, for lower Oxygen flows. The NbO signal decreases with lower Oxygen content, but the Nb signal does not, even increasing for Oxygen flows close to 0 sccm. This trend is also seen for the negative polarity, but for NbO and NbO_2 signals, indicating a change in the stoichiometry of the samples relating to the Oxygen content.

Although no grain boundaries were observed, APT measurements allowed to study the atomic concentration and homogeneity of the samples. For sample A, the total Nb atomic content seems to increase with lower O content inside the Ti:Nb/TiO_2:Nb layers, except for the first deposited layer, where the Nb content drastically decreases. As for Sample B, The Nb content is quite low but slightly increases with higher O content. These trends somewhat match with what was observed with TOF-SIMS.

Both APT and TEM detected Nb in the TiO_2:Nb thin film, with some Nb heterogeneity but no apparent segregation to grain boundaries, indicating Nb is fully integrated into the TiO_2 matrix.

The annealed TiO_2:Nb thin film analysed in TEM showed polycrystalline grains with different plane orientations, from both anatase and rutile, with the latter being the most predominant.

CHAPTER VII.

APPLICATION IN A THERMOELECTRIC PROTOTYPE

7. Application in a Thermoelectric Prototype

This chapter describes the application of the developed TiO_2:Nb thin film as a functional thermoelectric layer. This is the ultimate objective of this work. Firstly, the mechanical properties of the TiO_2:Nb thin films were studied. Secondly, the thin film was implemented into a thermoelectric prototype, while discussing its progression. Lastly, the final device was produced and tested. The production parameters were slightly tuned for the developed device.

7.1. Introduction

Most thermoelectric modules are design to work in conjunction with two materials, n-type and p-type semiconductors. To design a functional prototype featuring a single n-type thermoelectric thin films, a few possibilities were considered:

The first idea was to insert the thermoelectric thin film is a perovskite solar cell. Although the efficiency of a photovoltaic modules is measured at room temperature, the weather and time of day offer great variability. Days with high radiation incidence can heat the panel, typically reaching temperatures ranging between 20 °C to 40 °C higher than those of the environment, making the actual efficiency of the cell usually less than expected. Also, a 15 °C increase in the temperature of an electronic component decreases its lifetime to 25 % [161]. Implementing a transparent thermoelectric device into the cell will make use of the naturally created thermal gradient and not only generate energy, but also help cool down the device, increasing its overall efficiency. Due to the transparent nature of the thermoelectric layer, it could be implemented on the top side of the cell, taking advantage of the thermal gradient inherently generated by the cell, while enabling the transmission of the solar light across the cell. None the less, because this process generates a thermal gradient perpendicular to the surface of the film and its thinness, the thermal gradient between the top and bottom surfaces of the thermoelectric thin film would be quite low, generating a very minute voltage and losing its effectiveness. Hence, there is a need to develop an approach in order to successfully implement a thin film in a way to usefully generate thermoelectric power.

Another option would be a thin film in a touch screen or wearable device. In most smartphones, touch screens consume about 5 % of the cell phone battery, by the use of capacitive sensors that detect every touch by changing the local capacitance at a point on a grid located on the screen. By implementing a thermoelectric grid, the total energy consumption will be lower. Similarly, in smaller wearable devices with screens, a thermoelectric module system can be implemented, using the wearer's own body heat and the device's cooling system to lower the device's energy consumption. Typical power consumption of such small devices is approximately (10 to 150) mW [24].

These would be good ideas, in theory, but a typical thermoelectric generation efficiency is about 5% given current thermoelectric technology [162], so it could be difficult to justify implementing it in most devices where the thermal gradient is not significant. Given this, another possibility is to use the thermoelectric thin film as a sensor, instead of a generator, by sensing the thermal gradient between two in-plane positions of the film. This way, it would be possible to detect the position of a human finger by touch and its inherent temperature difference to the device.

7.2. Study of the Mechanical Properties

Before attempting to sputter the TiO_2:Nb thin films onto a prototype, the mechanical properties of two TiO_2:Nb samples were assessed to test their suitability as stable and durable coatings.

7.2.1. Experimental Details

7.2.1.1. Sample Fabrication

Thin films of TiO_2:Nb were produced by reactive DC magnetron sputtering at the CF-UM-UP. A target of Ti(96)Nb(4) wt.% (99.9 % of purity, FHR), with 10 cm of diameter, was used in planar configuration. The films were deposited on (76 × 26 × 1) mm^3 glass substrates (Normax Lda) and (10 × 10 × 0.5) mm^3 Si substrates, cut from P/B doped Si-wafer <100> (Siegert Wafers GmbH). The substrates were cleaned with 2-Propanol alcohol and acetone in an ultrasonic bath, both for 15 min. The substrate-holders were mounted onto a rotating support fixed at 6.5 cm from the target. The chamber was evacuated to a base pressure of around 10^{-4} Pa and the substrate holder was heated to 125 °C. Prior to the deposition, 2

min of etching at 500 V was performed in an Ar atmosphere at a pressure of 1.8 Pa in continuous rotation at 18 rpm, followed by a fixed dummy deposition of 2 min for target cleaning (burn). Target current density, bias voltage, O_2 flow and Ar flow were fixed at 12.7 mA·cm^{-2}, –60 V, 7 sccm and 40 sccm, respectively, depositing at a pressure of around 0.35 Pa for 5 min and 60 min, for Sample A and B, respectively.

7.2.1.2. Sample Characterization

The morphology of the films was investigated by SEM, performed with a FEI NOVA NanoSEM 200 at SEMAT/UM. For cross-section imaging, the samples were cut with a diamond tip and fixed in the sample table with double-sided carbon tape.

The optical transmittance and specular reflectance were analysed with a Shimadzu UV-2501PC UV-Vis spectrophotometer (CF-UM-UP) in the (300 to 900) nm wavelength range, using air and a mirror as the baseline, respectively.

The adhesion of a TiO_2:Nb thin film on a glass substrate was evaluated by scratch tests, performed by Revetest-Scratch Tester (CSM instruments) at SEMAT/UM, with a 200 μm tip radius diamond conical Rockwell C indenter with 90° angle (perpendicular to the sample surface) under progressively increasing load on a 5 mm scratch line. Two scratches were done, from 5 N to 50 N with a speed of 5 mm·min^{-1}, and from 5 N to 25 N with a speed of 2.5 mm·min^{-1}. The scratch scars on coating surfaces were analysed with a Leica DM2500 optical microscope.

The hardness (H_V) and Young's modulus (δ) of a TiO_2:Nb thin film on a Si substrate was determined by nanoindentation measurements carried out with a Berkovich-type NanoTester nanoindenter (Micro Materials) at SEMAT/UM. 6 indentations with 50 μm lateral separation were performed. The indenter was operated in a loading rate of 0.5 mN·s^{-1} until a Maximum Load of 9.0 mN was reached, with 10 s of dwelling time at the Maximum Load, and unloaded at a rate of 0.5 mN·s^{-1}. Indentation depths of approximately 175 nm were required to keep them within the recommended value of approximately (10 to 20) % of the film's thickness.

7.2.2. Results and Discussion

The SEM cross section of Samples A and B are shown in **Figure 83**. Sample B displays larger grains and increased roughness, with a clear vertical columnar structure, while this cannot be discerned in sample A, which shows a homogeneous surface and cross section. This is an expected consequence of the sputtering process, where the first layers of deposited material will present a denser nature. The transmittance (T) and specular reflectance (Rs) of sample A and sample B are presented in **Figure 84**. The increased number of bands in the spectra and overall lower transmittance of sample B relate to its higher thickness.

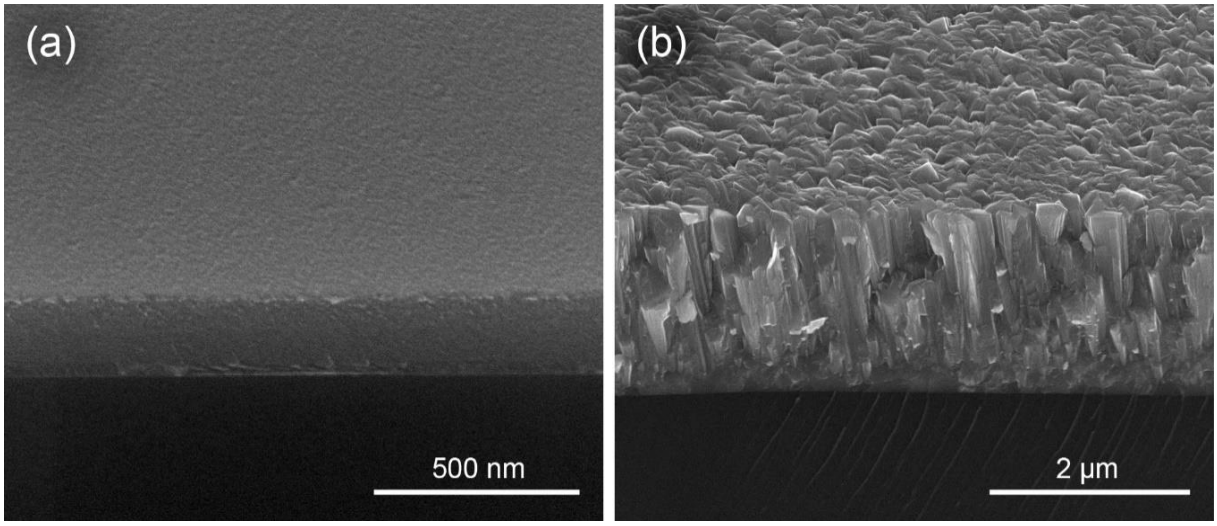

Figure 83. SEM cross section of two TiO_2:Nb films. Sample A measured 251 nm of thickness **(a)** and Sample B measured 1.73 µm of thickness **(b)**.

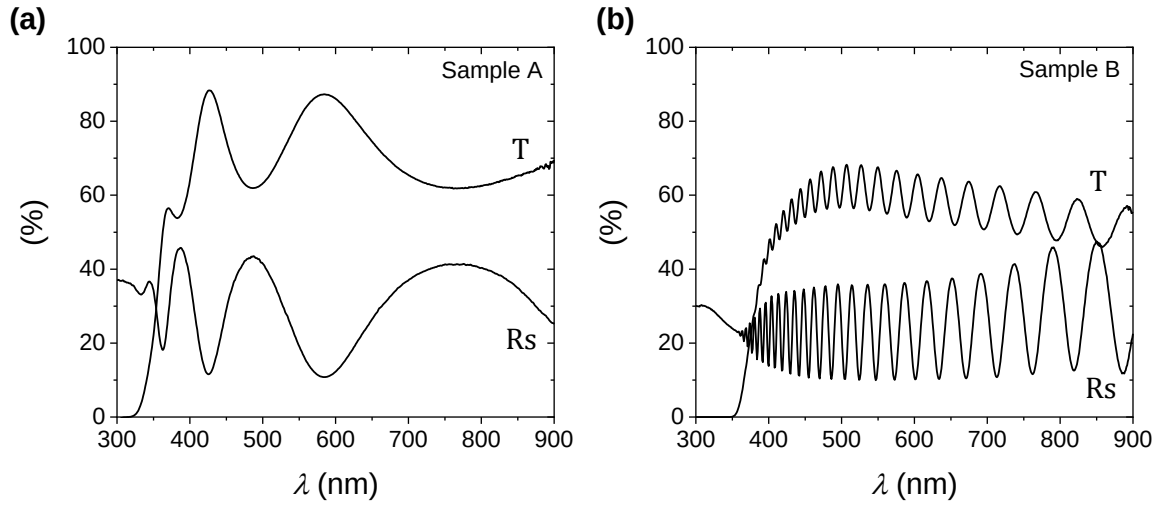

Figure 84. Transmittance and specular reflectance spectra for sample A (tdep=5 min) **(a)** and sample B **(b)**.

The Tangential Force and Acoustic Emission signals measured by Scratch Testing and corresponding critical loads (Lc) for are presented in **Figure 85**. The adhesion tests revealed average critical loads of $Lc1 = (9.1 \pm 0.8)$ N and $Lc2 = (15.7 \pm 0.3)$ N, for Sample A. $Lc1$ refers to a cohesive failure of the coating, due to cracking without substrate exposure. $Lc2$ refers to an adhesive failure, due to cracking and/or delamination, with exposure of a relevant area of the substrate.

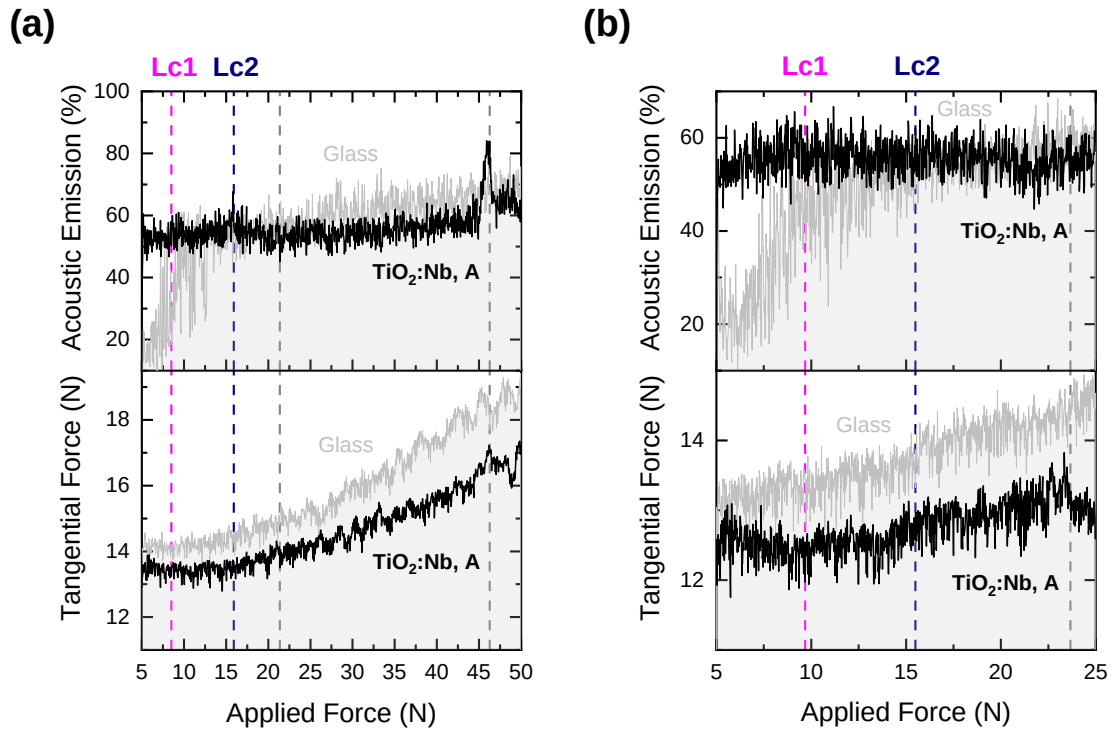

Figure 85. Tangential Force and Acoustic Emission in response to the tangential Force applied to a TiO_2:Nb thin film (sample A), measured with a Load between 5 N and 50 N and a scratch speed of 5.0 mm·min^{-1} **(a)** and a Load between 5 N and 25 N and a scratch speed of 2.5 mm·min^{-1} **(b)**. *Light grey* stands for a plain glass substrate, Lc1 and Lc2 are represented by dashed *magenta* and *navy* lines, while *grey dashed* lines represent the fracture points of the glass substrate.

The scratch channels (**Figure 86**) show hertzian cracking in the film at low loads (Lc1), while the cracking is more intense and is coupled with a loss of adhesion at higher loads (Lc2), causing optical interference effects when viewed with the microscope. The glass is also severely damaged at higher loads.

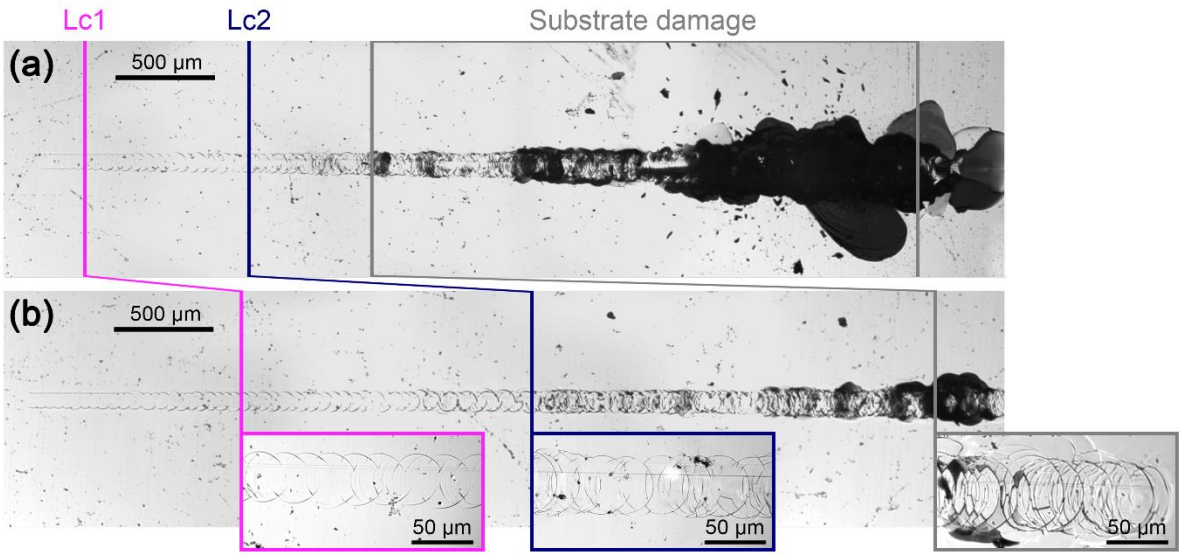

Figure 86. Scratch channels on a TiO_2:Nb thin film (sample A), with a Load between 5 N and 50 N and a scratch speed of 5.0 mm·min^{-1} **(a)** and a Load between 5 N and 25 N and a scratch speed of 2.5 mm·min^{-1} **(b)**. Lc1 and Lc2 are represented in *magenta* and *navy* lines, while *grey* lines represent the fracture points of the glass substrate.

Figure 87 shows the applied Load in relation to the indentation depth relating to the nanoindentation stress measurements for sample B. Similar results were observed for all 6 intents, with an average nano hardness of (18 ± 4) GPa and a Young's modulus of (188 ± 42) GPa, considerably higher than that of bulk TiO_2 at ~ 10 GPa [59]. The 5th indent reached a maximum load only at 207 nm, relating to its low nano hardness, achieving the lowest δ value of 138 GPa. Indent number 2 presents the lowest H_V and highest δ at 14 GPa and 260 GPa, respectively. These variations are related to signal noise, with the system acquiring values for H_V and δ determination at the maximum measured depth, although the measurement curves show close similarities. The exception to this is indent 3, presenting the highest H_V value of 26 GPa, where a maximum load was clearly reached at a lower film depth (167 nm).

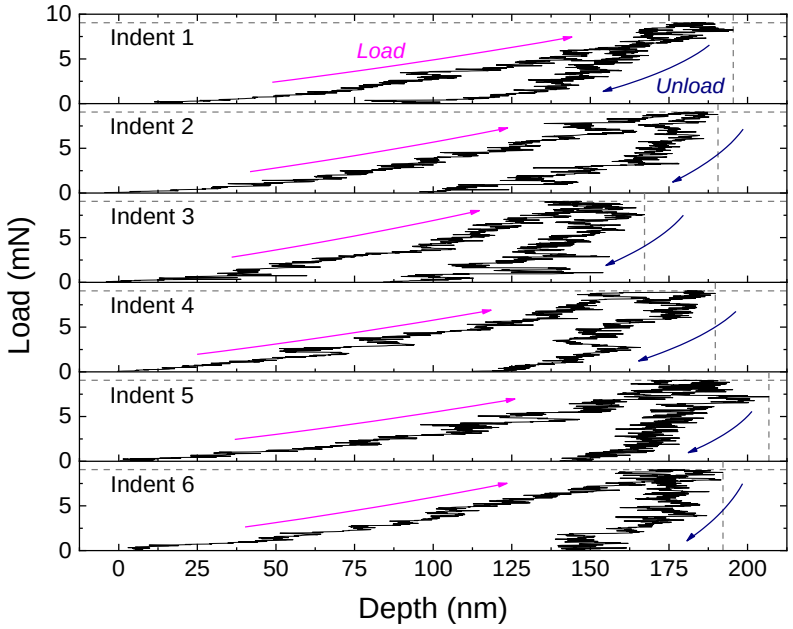

Figure 87. Applied Load vs. indentation depth for different nanoindentations on a TiO_2:Nb thin film (sample B) with 9.0 mN of maximum applied Load. *Magenta* and *navy* arrows refer to the load and unload stages of measurement, while the *grey dashed lines* refer to the maximum values read by the system. H_V is the nano hardness and δ is the Young's modulus.

The measurements carried out on the TiO_2:Nb films presented a challenge, particularly regarding the nano indentation. An account has also to be taken on the thickness, phase and substrate, which inherently influence the nanostructure and mechanical properties. The hardness and Young's modulus for TiO_2-based coatings highly depend on its nanostructure, ranging from ~ (0.1 to 14.3) GPa and ~ (17 to 176) GPa in the literature [163–165], asserting the obtained experimental results as promising. Overall, although limited, these results still provide useful insight on their mechanical properties.

Although not tested, the flexibility of a TiO_2:Nb layer was noticed in **Chapter 3** when sputtering over Kapton substrates. The layers did not peel, even after the Kapton was rolled and stretched. The film also proved very difficult to remove from the steel shield plates and covers (some also flexible) during the cleaning of the sputtering vacuum chamber, only peeling at very high thicknesses of accumulated layers, suggesting a durable and stable coating.

7.3. Design of a Transparent Thermoelectric Prototype

The most useful use case for the developed transparent thermoelectric would be to harvest heat perpendicular to its surface, when there is a thermal gradient between surfaces, enabling its deposition

in a plethora of devices, such as windows and displays. However, to effectively measure the Seebeck coefficient there must be a voltage measured across an appropriately sized sample. The first strategy meant using the available Seebeck coefficient measuring system, which works with glass-slide-sized samples with (76 × 26 × 1) mm^3. To have an efficient comparison, three types of samples were designed (**Figure 88**). The first sample (**Figure 88(a)**) consists of a single TiO_2:Nb thin film, similar to other samples produced throughout this work, where a thermal gradient is generated parallel to the film's surface. In a similar way, the second sample (**Figure 88(b)**) consists of 4 squared sections of sputtered TiO_2:Nb thin film, connected by contact lines of Ag paint. The third sample (**Figure 88(c)**) maintains the position of the edge voltage points but aims to measure the voltage generated by a thermal gradient applied perpendicularly to the film's surface. Transparent thin film contacts of AZO stand on top and bottom of the 4 TiO_2:Nb squared sections, establishing the electric connection, following the length of the glass slide. This last method design enables a stacking of the TiO_2:Nb thin film sections, with increased voltage when compared to a single continuous layer, but in order to significantly increase the thermoelectric power, nanofabrication techniques must be employed.

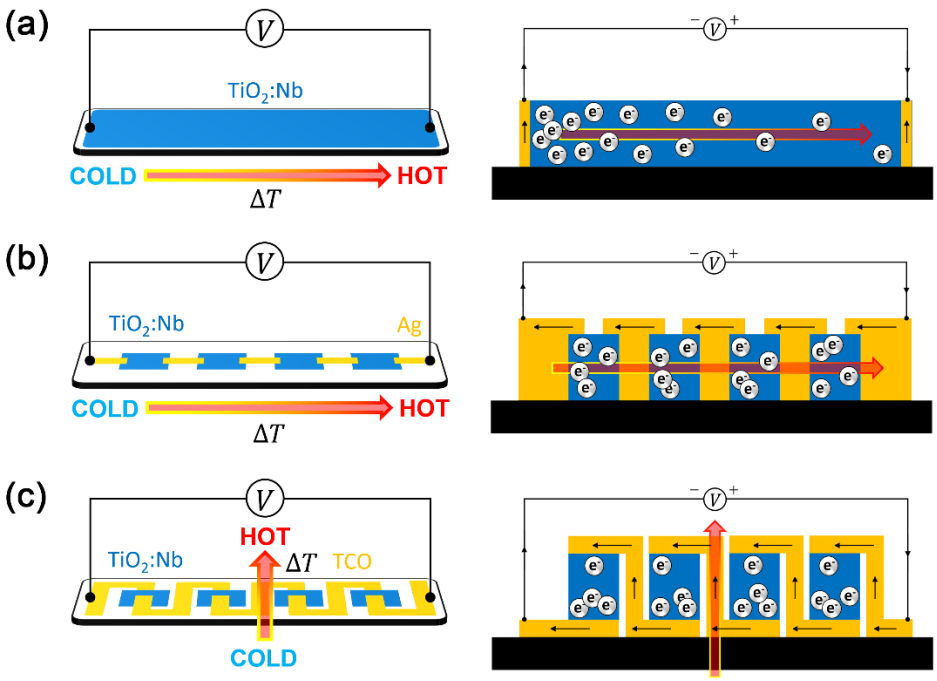

Figure 88. Schematic of three TiO_2:Nb-based thermoelectric prototype designs: a single TiO_2:Nb thin film (thermal gradient generated parallel to the film's surface) **(a)**, a 4-sectional TiO_2:Nb thin film horizontally connected by Ag painted contact (thermal gradient generated parallel to the film's surface) **(b)** and a 4-sectional TiO_2:Nb thin film connected by a bottom TCO contact layer (sputtered before) and an intercepting top layer (sputtered after the thermoelectric layer) (thermal gradient applied perpendicularly to the film's surface) **(c)**. TiO_2:Nb is represented in *blue*, electrical contacts in *orange* and substrate in *black*.

A subsequent fourth and final prototype was developed as a collaboration, resulting in the following Master dissertation:

Bruno Gonçalo Neiva Fernandes, "Thermoelectric transparent micro-arrays for thermal energy harvesting", University of Minho (2023) (https://hdl.handle.net/1822/85237) [166].

This work involved the production of transparent thermoelectric pillars of TiO_2:Nb for thermal energy harvesting, developed in a collaboration with *Bruno Fernandes'* Master's dissertation work [166]. The final device (schematized in **Figure 89**) consists of a glass substrate, a bottom continuous layer of fluorine-doped tin oxide (FTO) (serving as the bottom electrode), an array of equally spaced TiO_2:Nb micropillars vertically positioned in a parallel arrangement (serving as the thermoelectric layer), electrical and thermally insulated by silicon dioxide (SiO_2), and a topmost continuous layer of aluminium-doped zinc oxide (AZO) (serving as the top electrode).

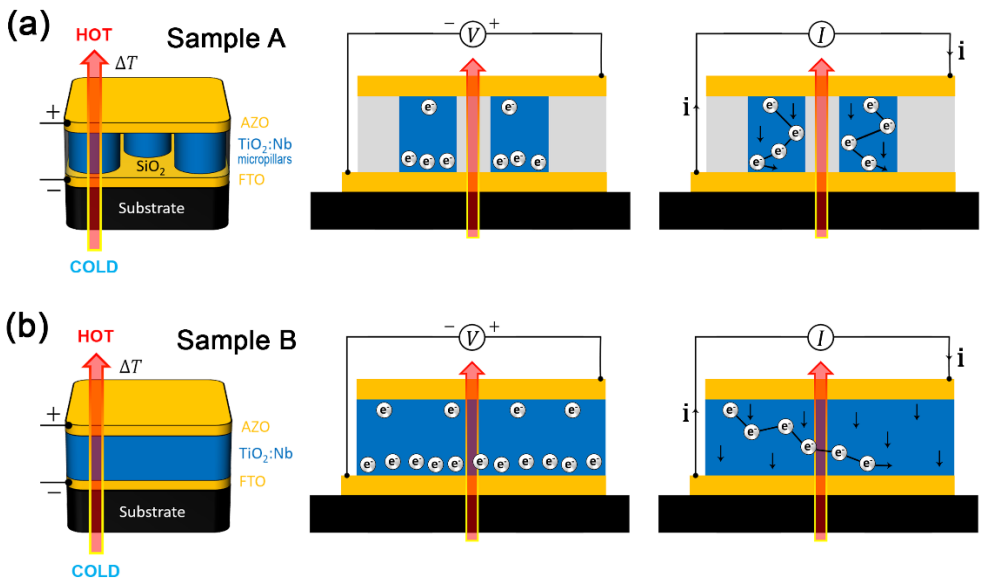

Figure 89. Schematic representation a thermal gradient applied perpendicularly to two thermoelectric prototypes, consisting of bottom (FTO) and top (AZO) electrode layers and thermoelectric layers of TiO_2:Nb. The parallel arrangement of the TiO_2:Nb micropillars (electrical and thermally insulated by SiO_2) in sample A **(a)** yields increased total generated electric current compared to a continuous TiO_2:Nb layer in Sample B **(b)**, although sample B generates a higher voltage. TiO_2:Nb is represented in *blue*, AZO/FTO electrical contacts in *orange* and substrate in *black*. Middle figures represented in electrochemical equilibrium (electrons accumulated near the coldest regions). *Black arrows* in right-hand figures indicate the flow of electric current.

The hypothesis is that the contribution of electric current produced by each of the parallel pillars of TiO_2:Nb film, will result in increased total generated power. As discussed in **Section 1.2**, when a thermal gradient is applied perpendicular to a continuous TiO_2:Nb layer (sample B in **Figure 89(b)**), the increase in charge mobility at the hot edge will result in the accumulation of electrons away from the heat

source, creating a given electrical potential between the top and bottom surfaces. A smaller area will mean fewer charges accumulated at a surface, resulting in lower generated potential.

However, when acting as a power generator in series, a continuous layer offers greater dispersion of electrons, caused by internal collisions. Similar to the motion of a gas confined to a volume, the greater the volume, the higher the probability of gas dispersing in all directions. The increased probability of an electron colliding with another charge decreases the probability of it migrating from one surface to the other. In this sense, an increased surface area will hinder the flow of electrons crossing over the depth of the material, decreasing the electric current produced. A smaller confined volume (such as a pillar in sample A, **Figure 89(a)**) should hence lead to an increase in the charge carrier mobility, increasing the charge flux over the depth of the layer due to fewer collisions. The electric current generated in each sectional pillar gets added up and increases the total current generated by the sample when compared to a single continuous film.

7.3.1. Experimental Details

7.3.1.1. Sample Fabrication

To conduct comparative tests for the efficiency of the pillars, two (2.5 × 2.5) cm^2 devices were manufactured, Sample A and Sample B (illustrated in **Figure 90**), with an outer area of (1.8 × 1.8) cm^2 of thermoelectric material. Sample A (**Figure 90(a)**) was produced with a micro-array of 16 629 micro-fabricate thermoelectric pillars, consisting of 1 μm-thick pillars of TiO_2:Nb arranged in a hexagonal pattern with 50 μm of radius and 150 μm of distance between the centre point of the pillars. Sample B (**Figure 90(b)**) was produced without pillars, but with a continuous film of TiO_2:Nb. The top (AZO) and bottom (FTO) contacts remain the same for both samples, as does the substrate.

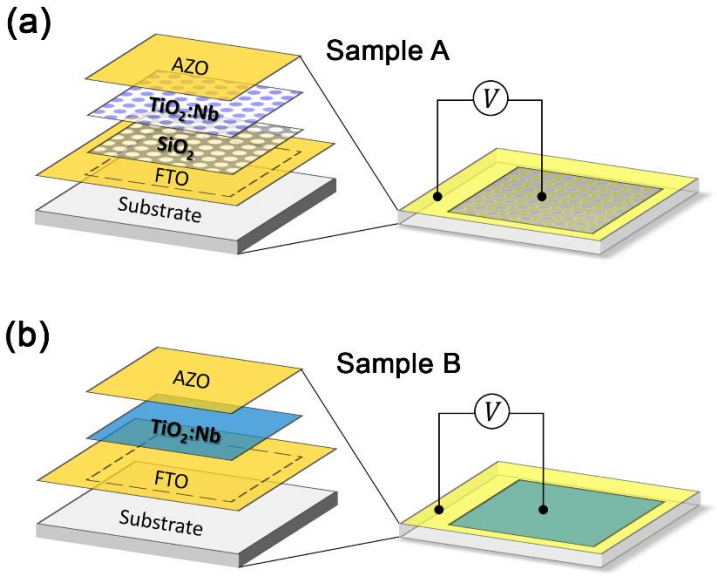

Figure 90. Schematic representation of Sample A **(a)** with micro-array of 16 629 TiO_2:Nb pillars and sample B **(b)** with a continuous TiO_2:Nb layer.

The samples were prepared using 1.6 mm thick FTO-coated soda-lime glass (SLG) substrates (TOC16-15) fabricated by Solaronix (Switzerland). FTO serves as the bottom electrode (anode), with a resistance of 15 $\Omega \cdot \square^{-1}$, while maintaining sample transparency. A layer of SiO_2 was deposited by Plasma Enhanced Chemical Vapour Deposition (PECVD), serving as an insulating material between the pillars. The samples were then coated with a positive photoresist (AZP4110) [167] by spin-coating using a Suss Microtec Gamma Cluster equipment. The micro-pillar array was imprinted using a Direct Laser-Write (DWL) 2000 from Heidelberg Instruments, followed by the removal of the exposed photoresist using the same Suss Microtec Gamma Cluster, with a AZ400K 1:4 developer [168]. Reactive Ion Etching (RIE) was used to etch SiO_2 that was left uncovered by the photoresist, creating the pillar wells.

The thermoelectric TiO_2:Nb film was deposited by reactive DC magnetron sputtering at the CF-UM-UP with a target of Ti(96)Nb(4) wt.% (99.9 % of purity, FHR), with 10 cm of diameter, in planar configuration. The substrate-holder was mounted onto a rotating support kept at 6.5 cm from the target. The chamber was evacuated to a base pressure of around 10^{-4} Pa and the bias voltage, O_2 flow and Ar flow were fixed at, –60 V, 6.5 sccm and 40 sccm, respectively, depositing at a pressure of around 0.22 Pa and temperature range of (25 to 70) °C.

The chosen conditions for the TiO_2:Nb layer differ slightly to those thoroughly studied throughout this work. The use of the photoresist, which is needed for pillar fabrication, was found to be very sensitive to temperature and high current, causing some problems during sputtering. This led to the use of a pulsed

power supply with a lower applied current, no heating applied to the substrate, no etching and no target cleaning during each deposition. These changes inevitably change the deposited thin film, so its resulting properties cannot be directly compared with the previously obtained results.

Compared to a continuous DC power supply, a pulsed power supply decreases the impact of atomic collisions during sputtering, allowing for reduced sample stress. The bipolar pulsed power supply reproduces a pulse with a frequency of a 150 kHz (**Figure 91(a)**), alternating between 70 V and -292 V (for 1 A of applied target current), and works similarly to an applied bias, where either electrons or argon ions are attracted toward the magnetron. The hysteresis curve shown in **Figure 91(b)**, exhibits the metal-oxide transition zone around (3.5 and 6.5) sccm, which is quite lower than the threshold previously observed. Considering the absence of substrate heating, an O_2 flow of 6.5 sccm was chosen to ensure the optical transparency of the device, although compromising the thermoelectric potential.

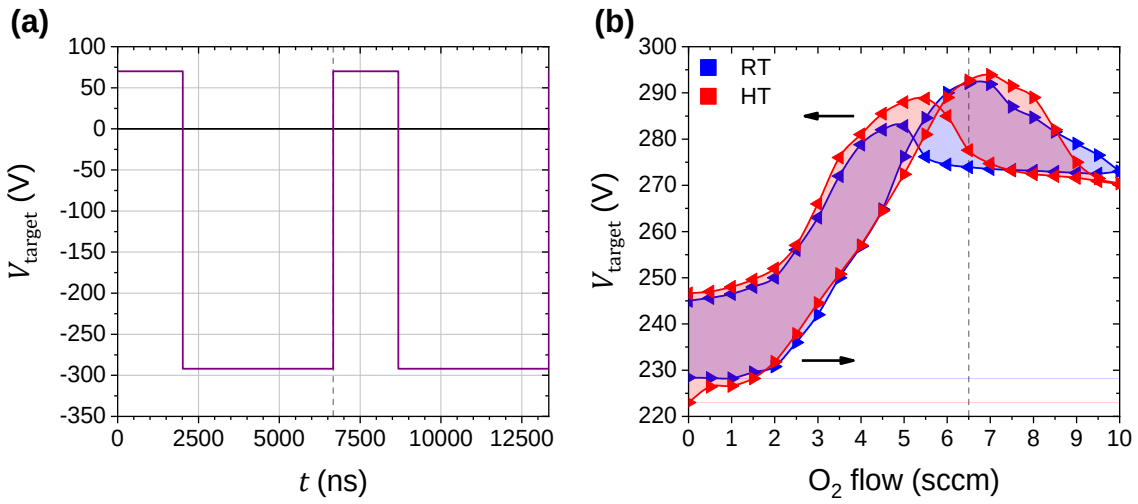

Figure 91. Two pulse representation *(navy)* **(a)** and cathode potential vs. reactive oxygen flow rate hysteresis curve for the deposition of TiO_2:Nb thin films with *(HT, in red)* and without *(RT, in blue)* substrate heating (*dashed grey line* refers to the chosen O_2 flow for the present study of 6.5 sccm) **(b)** of a pulsed power supply using an applied target current of 1 A.

To further ensure the stability of the photoresist, an applied target current of 0.8 A (current density of 10.2 $mA \cdot cm^{-2}$), corresponding to approximately 266 V, was used. Due to the reduction in deposition rate, the deposition time, 6 h, also had to be adjusted.

To remove both the photoresist and the excess TiO_2:Nb material sitting on top of the photoresist, the Lift-Off technique was used with a Piranha solution (75 % of H_2SO_4 and 25 % of H_2O_2).

Finally, the entire devices were covered with an AZO layer to create the top electrode (cathode). Thin films of ZnO and doped with Al (~ 3 at.%) were produced by DC magnetron sputtering at the CF-UM-

UP. A target of ZnO(98)Al_2O_3(2) wt.% (99.95 % of purity, FHR), with 10 cm of diameter, was used in confocal geometry. The substrates were mounted to a rotating single-sample holder at the centre point of the magnetrons with target-substrate distances kept at 6.5 cm. The vacuum chamber was evacuated to a base pressure of 10^{-4} Pa. The film was deposited for 5 min, with a target current density of 5.1 mA·cm^{-2} (corresponding to approximately 338 V), substrate bias of –60 V, temperature of 55 °C and Ar flow of 50 sccm, corresponding to a working pressure of 0.35 Pa.

Subsequently, sample A was heat treated in a vacuum furnace at 10^{-3} Pa. The temperature was increased from room temperature to 500 °C in 90 min and maintained at 500 °C for 60 min, followed by a natural cooling stage to room temperature for 6 h.

7.3.1.2. Sample Characterization

The morphology and cross-section were investigated by SEM, performed with a FEI NOVA NanoSEM 200 (SEMAT/UM). For cross-section imaging, the samples were cut with a diamond tip and fixed in the sample table with double-sided carbon tape.

The optical transmittance was measured with a Shimadzu UV-2501PC UV-Vis spectrophotometer (CF-UM-UP) in the (300 to 900) nm wavelength range, using the air as the baseline.

A custom Seebeck measuring system was developed at the CF-UM-UP to measure the electric potential (V) and current (I) between the top and bottom layer of a sample in response to a temperature difference (ΔT) applied perpendicular to its surface (discussed in **section 2.3.5**).

The electrical conductivity (σ) was obtained through the electrical resistivity (ρ) and is given by

$$\sigma = \frac{d}{RA} \tag{30}$$

where A is the total surface area of the pillars, d the thickness (length of the pillars) and R is the electrical resistance of the device obtained from the Ohm's law, $V = RI$, by a linear fit of I and V measured in function of the ΔT.

7.3.2. Results and Discussion

The cross section of Sample A and Sample B can be seen in **Figure 92**. Both samples show stacks of homogeneous FTO, SiO_2, TiO_2:Nb and AZO layers, with thicknesses of about (366 ± 30) nm, (947 ± 21) nm, (982 ± 21) nm and (163 ± 62) nm, respectively. A columnar structure is discerned for both FTO and TiO_2:Nb. Sample A (**Figure 92(a)**) presents a relatively homogeneous surface, with the microfabricated pillars are clearly distributed throughout. An inherent accumulation of material during the non-conformal sputtering process originates a bump at the edge of the pillars (designated ears), as seen at the TiO_2:Nb/SiO_2 interface, but a there is still a clear distinction between the TiO_2:Nb-filled well and the SiO_2 layer, both covered by AZO.

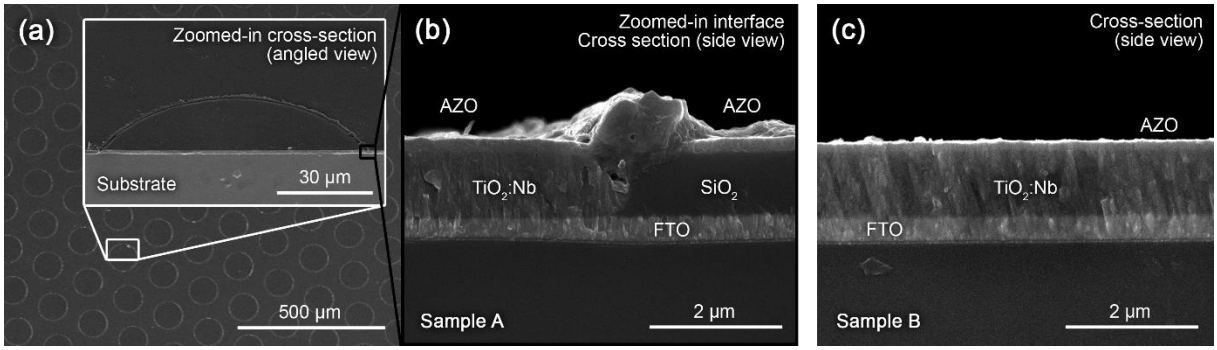

Figure 92. Top-view SEM of Sample A and zoomed-in angled view *(white square)* of a cross section of a TiO_2:Nb micropillar **(a)**, zoomed-in angled view *(black square)* at the interface between the TiO_2:Nb micropillar and the SiO_2 layer **(b)**, and cross section side view of Sample B **(c)**.

Figure 93 illustrates the transmittance spectra for Sample A and Sample B in the (300 to 900) nm range. The transmittance was also measured for two control samples, an FTO/SiO_2/AZO stack with empty microfabricated pillars (without TiO_2:Nb), and a continuous FTO/SiO_2/AZO stack. The presence of the micropillars in the SiO_2 layer is enough to decrease transmittance from (87 ± 2) % to (83 ± 2) %. Compared with (68 ± 5) % for Sample B, Sample A showed the highest average transmittance in the visible range (400 nm to 700 nm) at (73 ± 5) %, which is explained by the thermoelectric material dispersed with SiO_2. SiO_2 presents higher transmittance compared to TiO_2:Nb and, occupying a larger area (about 60 % of the device area) than the pillars, increases the overall transparency of the device. After the thermal annealing at 500 °C, the average transmittance of Sample A decreased to (69 ± 4) %. Both spectra for sample A show a similar behaviour but appears to have shifted slightly towards lower wavelengths after annealing, with an overall lower transmittance except in the range of 350 nm to 375 nm.

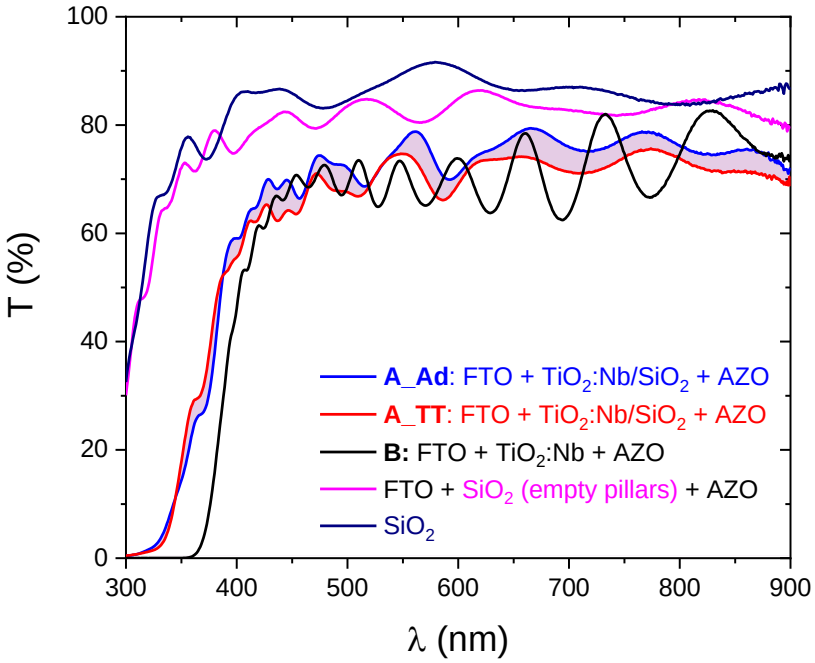

Figure 93. Transmittance spectra for Sample A, measured as-deposited *(Ad)* and after annealing at 500 °C *(TT)*, Sample B, a control sample with empty wells and a control sample of SiO_2.

Regarding the thermoelectric tests, **Figure 94** presents the electric potential as a function of the temperature gradient across the depth of the samples and measured electric current. The measured electric potential and current for an applied temperature difference of 5.5 °C and calculated efficiency (equation **(12)**) for Sample A (Ad and TT) and Sample B, are presented in **Table 17**.

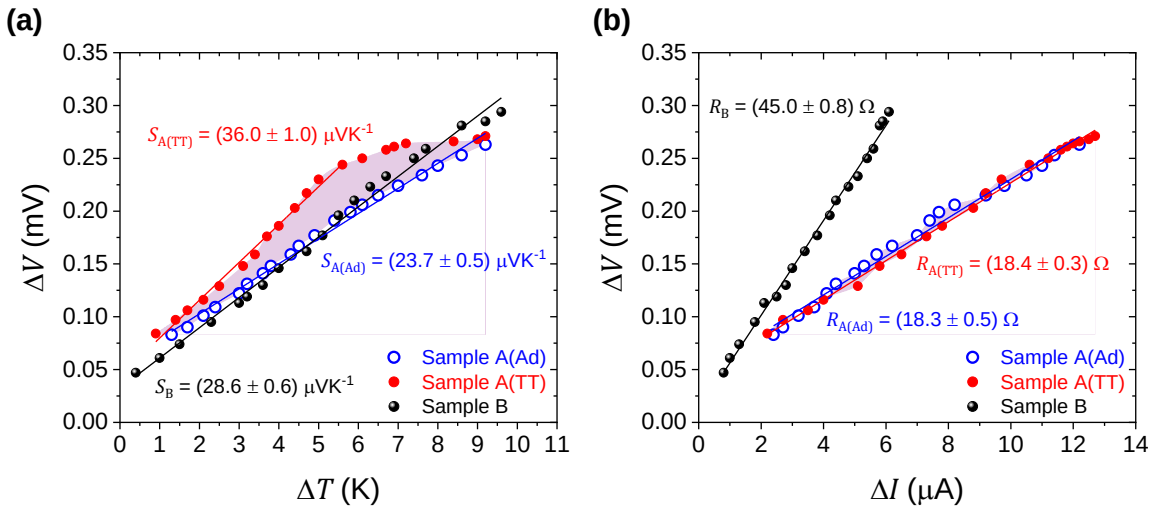

Figure 94. Electric potential plotted against temperature gradient **(a)** and electric current **(b)** for Sample A, measured as-deposited *(Ad)* and after annealing at 500 °C *(TT)*, and Sample B. Seebeck coefficient and electric resistance were obtained by the slope of the linear fit for each sample, for (a) and (b), respectively.

Table 17. Summary of measured electric potential (V), electric current (I) and efficiency (η) for Sample A, measured as-deposited (Ad) and after annealing at 500 °C (TT) and Sample B, for an applied temperature difference (ΔT) of 5.5 °C.

Sample	V (mV)	I (μA)	ΔT (°C)	η (%)
A(Ad)	0.191	0.2	5.5	2.14×10^{-13}
A(TT)	0.244	9.7	5.5	4.83×10^{-13}
B	0.196	3.8	5.5	4.99×10^{-14}

Sample B generated the highest voltage, for a $\Delta T = (9.3 \pm 0.1)$ K, at (0.285 ± 0.003) mV, but the lowest electric current at (6 ± 1) μA. Sample A produced about 118 % additional electric current than sample B for similar ΔTs, which is notable considering that sample A has 59 % less effective volume of thermoelectric material than the sample with a continuous TiO_2:Nb layer. After annealing at 500 °C Sample A showed a slight further increase in both generated voltage (~ 25 %) and current (~ 20 %), until reaching a $\Delta T \sim 6.0$ K, where it appears to saturate. For this reason, the Seebeck coefficient for sample A(TT) is the result of a linear fit for $0 < \Delta T < 6$.

Table 18 presents the optical, electric and thermoelectric results for sample A, as-deposited and after annealing at 500 °C, and sample B. The Figure of Merit (ZT) was estimated at 300 K and with a thermal conductivity of (1.5 ± 0.1) $W \cdot m^{-1} \cdot K^{-1}$ for all samples, previously obtained in **Chapter 4** [146]. On the one hand, the greater total surface area of TiO_2:Nb in sample B facilitates the flow of electrons and increases the generated electrical potential between both ends of the sample. This correlates with the higher Seebeck coefficient of (28.6 ± 0.6) $\mu V \cdot K^{-1}$, compared to (23.7 ± 0.5) $\mu V \cdot K^{-1}$ measured for sample A. On the other hand, a continuous layer implies a greater scattering of electrons, due to internal collisions, which relates to its higher resistance of (45.0 ± 0.8) Ω, whereas a smaller area (such as when confined to a pillar) contributes to fewer collisions and increases the mobility of charge carriers over the depth of the film. Because the measured current is the sum of the contributions of each pillar, this agrees with sample A having a higher electrical conductivity of (0.041 ± 0.001) $\Omega^{-1} \cdot cm^{-1}$, compared to (0.0066 ± 0.0001) $\Omega^{-1} \cdot cm^{-1}$ for sample B.

The resulting higher thermoelectric power factor of (0.23 ± 0.02) $pW \cdot m^{-1} \cdot K^{-2}$ and ZT of (4.7 ± 0.6) $\times 10^{-11}$ of sample A, compared to (0.054 ± 0.003) $pW \cdot m^{-1} \cdot K^{-2}$ and (1.1 ± 0.1) $\times 10^{-11}$ for sample B, proves the effectiveness of the pillars in increasing current production.

Table 18. Summary of results for Transmittance ($\overline{T}_{vis}$), averaged in the (400 to 700) nm range, electrical Conductivity (σ), Seebeck coefficient (S) and calculated Power Factor (PF) of the thermoelectric devices. Sample A was measured as-deposited (Ad) and after annealing at 500 °C (TT). To estimate the Figure of Merit (ZT) at 300 K, a thermal conductivity value of (1.5 ± 0.1) W·m^{-1}·K^{-1} was considered [146].

Sample	$\overline{T}_{vis}$ (%)	σ (Ω^{-1}·cm^{-1})	S (μV·K^{-1})	PF (pW·m^{-1}·K^{-2})	$ZT_{300\,K}$ (10^{-11})
A(Ad)	73 ± 5	0.041 ± 0.001	23.7 ± 0.5	0.23 ± 0.02	4.7 ± 0.6
A(TT)	69 ± 4	0.0411 ± 0.007	36 ± 1	0.53 ± 0.04	10 ± 1
B	68 ± 5	0.0066 ± 0.0001	28.6 ± 0.6	0.054 ± 0.003	1.1 ± 0.1

Although the transmittance for Sample A decreased to (69 ± 4) % and the electrical conductivity did not significantly change after annealing, the Seebeck coefficient increased to (36 ± 1) μV·K^{-1}, leading to a higher thermoelectric power factor of (0.53 ± 0.04) pW·m^{-1}·K^{-2} and Figure of Merit of (10 ± 1) × 10^{-11}. These agree with what was previously reported on the significance of annealing to increase the Seebeck coefficient.

While these results show promise, the obtained PF and ZT values still seem subpar to the in-plane thermoelectric power previously measured. Although the fabrication process needed to be adapted and there is most certainly a difference between the through-plane and in-plane thermal properties, the main significant factor can be attributed to the huge difference in the considered depth (or length) of the samples. On the one hand, because σ is depth-dependent (equation **(30)**), it is harder for electric charges to travel over a longer distance, i.e. a longer or thicker layer, which explains the lower resistance. But S is in the same order of magnitude as previous results (∼ 29 μV·K^{-1}), compared to ∼ (101 to 155) μV·K^{-1} from **Chapter 3**, ∼ (0 to 223) μV·K^{-1} from **Chapter 4** and ∼ (4 to 226) μV·K^{-1} from **Chapter 5**, making the significantly lower generated thermoelectric power counter intuitive if the material, room temperature and applied temperature difference are the same.

On the other hand, it also makes sense that a thin enough layer is not able to easily maintain a high temperature difference, quickly reaching thermal equilibrium instead. It is possible that at some point, as the temperature difference between the HOT and COLD Peltier in increased, the sample conducts and dissipated thermal energy back to the system and environment faster than what the COLD Peltier can mitigate. This increases the average temperature of the whole measurement and sample system, inherently increasing the generated thermoelectric power, without changing the ΔT between the surface edges of the sample, and limiting the voltage and electric current generation.

7.4. Partial Conclusions

Firstly, the mechanical properties of the TiO_2:Nb films were successfully evaluated, confirming their suitability as stable and durable coatings. The adhesion tests revealed average critical loads of $Lc1 =$ (9.1 ± 0.8) N and $Lc2 =$ (15.7 ± 0.3) N, for a TiO_2:Nb thin film with 251 nm of thickness. An average hardness value of (18 ± 4) GPa and corresponding Young's modulus of (196 ± 45) GPa was obtained for a TiO_2:Nb thin film with 1.73 μm of thickness.

Secondly, the design, fabrication and characterization of a thermoelectric transparent device containing a TiO_2:Nb film for thermal energy harvesting was successfully achieved. The (2.5 × 2.5) cm^2 device was fabricated using an assortment of techniques, resulting in 1 μm thick layer of SiO_2 with an array of 50 μm radius 16 629 micro-fabricated pillars of TiO_2:Nb, occupying an area of (1.8 × 1.8) cm^2. The thermoelectric TiO_2:Nb and the top electrode AZO were deposited by DC magnetron sputtering. To accurately access the influence of the pillars (Sample A), sample B was produced with continuous layers of FTO/TiO_2:Nb/AZO (without SiO_2 and pillars) using the same conditions.

Sample A showed a higher optical transmittance averaged between 400 nm and 700 nm of (73 ± 5) %, when compared to (68 ± 5) % for Sample B, due to the presence SiO_2, which exhibits higher transmittance than TiO_2:Nb, although it slightly decreased to (69 ± 4) % after annealing at 500 °C.

On the one hand, sample B generated the highest voltage of (0.285 ± 0.003) mV at $\Delta T =$ (9.3 ± 0.1) K and measured a higher Seebeck coefficient of (28.6 ± 0.6) $\mu V \cdot K^{-1}$, compared to (23.7 ± 0.5) $\mu V \cdot K^{-1}$ for sample A. On the other hand, it produced about 54 % less electric current overall than sample A, even though the effective surface area of thermoelectric TiO_2:Nb in sample B is 41 % greater than the total area of the pillars in sample A. Sample A also presented higher electrical conductivity of (0.041 ± 0.001) $\Omega^{-1} \cdot cm^{-1}$, compared to (6.6 ± 0.1) × 10^{-5} $\Omega^{-1} \cdot m^{-1}$ for sample B.

This results in a higher thermoelectric power factor and ZT at 300 K attributed to the pillars of (0.23 ± 0.02) $pW \cdot m^{-1} \cdot K^{-2}$ and (4.7 ± 0.6) × 10^{-11}, respectively, proving their effectiveness.

The mobility of charge carriers influences the generated electrical potential between the edges of a sample, so while an increased surface area facilitates the flow of electrons, it also increases scattering. Contrariwise, the smaller area increases the mobility of charge carriers over the depth of the film due to the lower probability of charge collisions. The electric current generated for each pillar also adds up, increasing the total current generated by the device.

Both the generated voltage and current further increased ~ 25 % and 20 %, respectively, with the annealing process, although a saturation regime is reached for ΔT above ~ 6.0 K. The increase in the Seebeck coefficient to (36 ± 1) $\mu V \cdot K^{-1}$ was enough to increase the thermoelectric power factor to (0.53 ± 0.04) $pW \cdot m^{-1} \cdot K^{-2}$ and ZT at 300 K to (10 ± 1) × 10^{-11}, presenting an interesting starting point for this transparent thermoelectric device.

The device was constrained by the use of the photoresist during its fabrication, which limited the deposition temperature of the TiO_2:Nb material (absence of substrate heating). The need of the pulsed power supply meant a lack of optimized deposition parameters that will need to be studied in the future. Likewise, the effect of the annealing on the heterostructured device was not properly studied, as it can alter the properties of the layers apart from TiO_2:Nb and even facilitate diffusion.

Even so, the overall results show much promise and indicate that the pillars do, in fact, increase the current generated through the device, but there is still a lot more to be done.

CHAPTER VIII.

FINAL REMARKS AND FUTURE WORK

8. Final Remarks and Future Work

Transparent n-type niobium-doped titanium dioxide thin films (TiO_2:Nb) were successfully produced by reactive magnetron sputtering from a composite Ti:Nb target in an oxygen atmosphere.

An amount of 1.5 at.% Nb doping was estimated from XPS experiments, with an optical band-gap of (3.21 to 3.24) eV. Optimized Nb-doped films exhibit pronounced thermoelectric properties with a very high absolute Seebeck coefficient of 155 $\mu V \cdot K^{-1}$ for a 150 nm thickness. The maximum power factor and figure of merit values of 0.5 $mW \cdot m^{-1} \cdot K^{-2}$ and 0.18, respectively, were obtained for TiO_2:Nb films with a thermal conductivity of 1.3 $W \cdot m^{-1} \cdot K^{-1}$, which excels what is commonly found in the literature for transparent thin films. Structural investigations by XRD and XAFS at the Ti and Nb K-edges were performed to elucidate the role of Nb dopant on the film structure and properties. The as-deposited films possess anatase TiO_2 phase evidenced by XRD, however, the rutile phase is additionally formed upon film thermal annealing at 400 °C. Detailed information on the local structure of the thin films was obtained in terms of the radial distribution functions determined from the simultaneous analysis of EXAFS data at two absorption edges using the RMC method. It was concluded that the local environment of the thin films is affected by Nb doping, however, their average local structure remains close to that of the anatase TiO_2 phase. This result is also supported by the analysis of XANES using ab initio simulations.

The second study enabled a good correlation between the optical properties, morphology, structure and composition, electric, thermal and thermoelectric properties of the produced films. The thin TiO_2:Nb films show homogeneous surfaces, with roughness of (0.7 to 1.3) nm and densities of (3.2 to 4.4) $g \cdot cm^{-3}$. Lower level of Nb doping of (1.1 to 1.2) at.% is obtained for films with intermediate oxygen inlet during deposition (7.0 sccm to 7.5 sccm), whereas for higher oxygen flow rates (9 sccm) the level of Nb doping increases to 1.7 at.%. The post-deposition thermal annealing on the TiO_2:Nb film deposited with 7.5 sccm of oxygen flow resulted in recrystallization with a close to stoichiometric TiO_2 (around 1:2) composition and 1.3 at.% of Nb doping. The amount of Nb in the TiO_2 unit cell is in the range of (1 to 2) at.%, based on the total composition of the material. With this quantity of Nb, it is possible to have optimized performance for being optically transparent, electrically conductive, poor thermal conductor and thus achieving a high thermoelectric power. The as-deposited films develop both anatase and rutile TiO_2 phases, evidenced by XRD. A larger fraction of rutile phase is correlated to larger Seebeck coefficient

values. The post-deposition annealing increases the band-gap of the TiO_2:Nb thin films due to the crystallization of the anatase phase. Furthermore, this treatment increases the electrical conductivity for films deposited with reactive oxygen flow rates above 5.5 sccm. It also improves the thermoelectric property for as-deposited films with absolute Seebeck coefficients lower than 150 $\mu V \cdot K^{-1}$. The thermoelectric power factor of the films deposited with 6 sccm, 7 sccm, 7.5 sccm and 8 sccm of oxygen flow was clearly improved after annealing. An optimized process parameter window was defined for reactive oxygen flow rates in the range of (6.5 to 7.5) sccm. TiO_2:Nb films with (120 to 300) nm thickness have an average optical transmittance in the visible range of 73 %, maximum electrical resistivity 0.05 $\Omega \cdot cm$, thermal conductivity below 1.7 $W \cdot m^{-1} \cdot K^{-1}$, maximum absolute Seebeck coefficient of 223 $\mu V \cdot K^{-1}$, a maximum thermoelectric power factor of 60 $\mu W \cdot K^{-2} \cdot m^{-1}$, and a maximum thermoelectric figure of merit of around 0.014. Although transparency is required for applications such as touch-screen displays or in photovoltaic cell electrodes, it is a trade-off for the electrical conductivity and should be carefully weighted depending on the desired application.

The thermoelectric properties of the Nb-doped TiO_2 thin films were further enhanced by optimizing the deposition temperature, resulting in thin films with thickness of approximately 200 nm and average optical transmittance in the visible range between 67 % and 76 %. The TiO_2:Nb with the best properties was deposited at a temperature between 176 °C and 224 °C, yielding a transparency of 70 %, an n-type electrical resistivity of $(3.1 \pm 0.1) \times 10^{-2}$ $\Omega \cdot cm$ and an absolute Seebeck coefficient of (225 ± 7) $\mu V \cdot K^{-1}$, resulting in a thermoelectric Power Factor of (160 ± 20) $\mu W \cdot m^{-1} \cdot K^{-2}$ and an estimated Figure of Merit of 0.035 ± 0.009. After annealing, the same thin film decreased its electrical resistivity to $(0.9270 \pm 0.0009) \times 10^{-2}$ $\Omega \cdot cm$ but also decreased its absolute Seebeck coefficient to (164 ± 2) $\mu V \cdot K^{-1}$, resulting in a maximum thermoelectric Power Factor of (291 ± 9) $\mu W \cdot m^{-1} \cdot K^{-2}$ and an estimated Figure of Merit of 0.06 ± 0.01, while maintaining its transparency.

Stacked layers of Ti:Nb and TiO_2:Nb thin films were successfully sputtered by continuously varying the O_2 flow rate during deposition and covered with a protective layer of Ti. SEM cross profiles measured a thickness of approximately 700 nm and was not able to discern any obvious morphological different inside the films. TOF-SIMS was able to distinguish between the different layers. Nb content is higher near the interface with the substrate (first nm of growth). The O and Nb content within the film increase for higher Oxygen flows. The same was not discerned from the Ti and TiO signals. In positive polarity, the Nb and NbO signals follow the same trend when the Oxygen content is higher, splitting halfway through the sample, for lower Oxygen flows. The NbO signal decreases with lower Oxygen content, but the Nb signal does not, even increasing for Oxygen flows close to 0 sccm. This trend is also seen for the negative

polarity, but for NbO and NbO_2 signals, indicating a change in the stoichiometry of the samples relating to the Oxygen content. Although no grain boundaries were observed, APT allowed to study the atomic concentration and homogeneity of the samples. For sample A, the total Nb atomic content seems to increase with lower O content inside the Ti:Nb/TiO_2:Nb layers, except for the first deposited layer, where the Nb content drastically decreases. As for Sample B, The Nb content is quite low but slightly increases with higher O content. These trends somewhat match with what was observed with TOF-SIMS.

TOF-SIMS, APT and DFT were used to understand the role of Nb doping, and the effect of the deposition temperature and post-deposition annealing in the properties of the thin films. Nb shows some preferential zones but is still homogeneously distributed and fully integrated into the TiO_2 matrix. The annealing process does not seem to significantly change the Nb atomic content. Grain boundaries were not initially discerned due to the small grain size of the TiO_2:Nb thin films, but thanks to the presence of a Si contamination, and its segregation to grain boundaries, it was possible to observe vertically-oriented grains of TiO_2:Nb. It is also proposed that the mix of the anatase and rutile phases lead to the formation of grains with different Ti-O stoichiometry.

Some work was done to search for the source of the Si contamination, with little to no results. Unfortunately, Si is almost anywhere, used as a substrate, present in primary vacuum pump oil, in the sandpaper used in the cleaning of the vacuum chamber and its components. It is also possible that it is simply present inside the chamber from the result of past depositions using a Si-based target and its incorporation in the TiO_2 samples can be enhanced during sputtering in reactive mode. It is also very interesting that, under normal conditions, rutile is very difficult to obtain at such low deposition temperatures, so it is speculated that the unwanted Si addition during the deposition process can facilitate the formation of the combined anatase/rutile crystalline grains. Nonetheless, more studies need to be conducted in order the asses the real effect of the Si on the TiO_2:Nb matrix.

Finally, the design, fabrication and characterization of a thermoelectric transparent device containing a TiO_2:Nb film for thermal energy harvesting was successfully achieved. The mechanical properties of the TiO_2:Nb films were successfully evaluated, confirming their suitability as stable and durable coatings. The adhesion tests revealed average critical loads of $\mathrm{Lc1} =$ (9.1 ± 0.8) N and $\mathrm{Lc2} =$ (15.7± 0.3) N, for a TiO_2:Nb thin film with 251 nm of thickness. An average hardness value of (18 ± 4) GPa and corresponding Young's modulus of (196 ± 45) GPa was obtained for a TiO_2:Nb thin film with 1.73 μm of thickness.

A final (2.5 × 2.5) cm^2 device was fabricated using an assortment of techniques, resulting in an array of 16 629 micro-fabricated pillars (1 μm in height and 50 μm in radius, separated by 150 μm of

SiO_2) of TiO_2:Nb, occupying an internal area of (1.8 × 1.8) cm^2. The thermoelectric TiO_2:Nb and the top electrode AZO were deposited by DC magnetron sputtering. Due to the combination of TiO_2:Nb pillars and SiO_2, the device showed a higher optical transmittance averaged between 400 nm and 700 nm of (73 ± 5) %, when compared to (69 ± 5) % of a continuous layer stack of FTO, TiO_2:Nb and AZO, also produced using the same conditions. While the greater total surface area of the continuous TiO_2:Nb layer aids the flow of electrons and contributes to a higher generated voltage, the small area of a pillar contributes to fewer collisions and increases the mobility of charge carriers over the depth of the film. Hence, adding the contributions of each pillar increases the total generated electric current in 118 %. This results in a 1 order of magnitude higher thermoelectric power factor and figure of merit, proving the effectiveness of the micropillars.

The device saw a further increase in both the generated electric voltage ~ 25 % and current ~ 20 % with the annealing at 500 °C, though a saturation regime is reached for ΔT above ~ 6.0 K. Although the average transmittance decreased to (69 ± 4) % and the electrical conductivity did not significantly change, the increase in the Seebeck coefficient from (23.7 ± 0.5) $\mu V \cdot K^{-1}$ to (36 ± 1) $\mu V \cdot K^{-1}$ was enough to increase the thermoelectric power factor to (0.53 ± 0.04) $pW \cdot m^{-1} \cdot K^{-2}$ and figure of merit at 300 K to (10 ± 1) × 10^{-11}. These are promising results, indicating the increase in the current generated through the device by the micro-fabricated pillars, but there is still much to be done.

The significantly lower thermoelectric power compared to the in-plane in-vacuum measurements from previous results can mainly be attributed to the difficulty to apply a useful temperature difference in such a thin sample, limited by the equipment. The in-plane Seebeck coefficient would need to be measured in vacuum to mitigate thermal irradiation to the environment and the temperature probes adapted to be in direct contact with only the surfaces of the sample. The use of a photoresist during fabrication also limited the deposition temperature of the TiO_2:Nb material, leading to the use of a pulsed power supply lacking optimized deposition parameters. This opens the door to future studies, such as varying the deposition and annealing conditions on the heterostructured device.

A summary of best results is presented in **Table 19**. There is of course a need to design new ways to implement these types of thermoelectric coatings in useful ways. The use of microfabricated patterns, such as the developed micro-pillar array, are a step forward but also provide challenges due to the complex combination of manufacturing processes. Sputtering has always had limitations, especially in coating big surfaces, but it's ease of use and versatility asserts its place as a technique still relevant today. It is hard to ignore how much was accomplished with a small, rudimentary system.

Table 19. Summary of results for Transmittance ($\overline{T}_{vis}$), averaged in the (400 to 700) nm range, electrical Conductivity (σ), Seebeck coefficient (S) and calculated Power Factor (PF) and Figure of Merit (ZT) at 300 K of the best samples from each chapter, measured as-deposited (Ad) and after annealing at 500 °C (TT).

Chapter	Sample	$\overline{T}_{vis}$ (%)	σ ($\Omega^{-1}\cdot cm^{-1}$)	S ($\mu V\cdot K^{-1}$)	PF ($W\cdot m^{-1}\cdot K^{-2}$)	$ZT_{300\,K}$
III	$d \sim$ **150 nm (TT)**	88	219	-155	0.5×10^{-3}	0.18
III	$d \sim$ **750 nm (TT)**	70	992	-101	1.0×10^{-3}	0.13
IV	O_2 **flow ~ 7 sccm (Ad)**	66	8	-224	42×10^{-6}	0.008
IV	O_2 **flow ~ 7 sccm (TT)**	71	12	-197	48×10^{-6}	0.009
V	$T_{dep} \sim$ **210 °C (Ad)**	70	33	-225	160×10^{-6}	0.035
V	$T_{dep} \sim$ **210 °C (TT)**	70	107	-164	291×10^{-6}	0.06
VII	**Micropillar device (Ad)**	73	0.04	-24	0.23×10^{-9}	4.7×10^{-11}
VII	**Micropillar device (TT)**	69	0.04	-36	0.53×10^{-9}	10×10^{-11}

During the course of this work several other studies (not included) were initialized but left unfinished due to either time constraints, logistics, absence of funding, lack of the necessary conditions or just due to the COVID-19 pandemic, which severely impacted this work. These include:

- Grain boundary and phase characterization using Kelvin probe force microscopy (KFM) at the INL, which was halted by the COVID-19 pandemic.
- Further thermal conductivity studies of the TiO_2:Nb thin films, namely with varying deposition conditions. Unfortunately, the measurements were limited due to the equipment at the ICMAB, which has since become unavailable.
- Testing these TiO_2:Nb in Field ion microscopy (FIM) at the KIT, to get further insight on the grain boundaries complementary to APT and TEM. The thin films (25 nm) would have to be deposited onto specialized Al and W tips, fixed onto to a Cu tube and pre-sharpened by electropolishing. Unfortunately, several difficulties interrupted the depositions and analyses.
- Thermal annealing with H_2 hot filament and at higher temperatures, which was limited due to the use of glass substrates and the available equipment. Some initial tests showed increased electrical conductivity, but the impossibility to measure the Seebeck coefficient and study the optical properties severely restrained further pursuit.
- Deposition using a combination of two targets in confocal disposition in reactive mode. This configuration enables a very fine tuning of the Nb doping, with either a combination of pure Ti and Nb targets, or their use in conjunction with pre-doped Ti:Nb targets. Early results were not promising, as the deposition parameters were tricky to adjust and would take further effort to

optimize. The lack of a pure Nb target limits this, and the use of Nb pellets was found to not be the best option in terms of deposition homogeneity, as evidenced by another study involving the deposition of ZnO:Sb thin films using Sb pellets on a pure ZnO target [169].

- Testing the TiO_2:Nb thin films as coatings in the photocatalytic degradation of pollutants, which is currently being somewhat tested as part of a Master dissertation work.
- Development of a Seebeck coefficient measuring system with incorporated Nd magnets, to study the magnetic contribution. Several improvements to the base system were done and base prototypes that can be improved upon and integrated were designed and 3d printed.

REFERENCES

[1] U.S Department of Energy Information Administration, (EIA), International Energy Outlook 2023, (2023) 1–70. https://www.eia.gov/outlooks/ieo/pdf/IEO2023_Narrative.pdf.

[2] Lawrence Livermore National Laboratory, U.S. Energy Flow Chart 2022, (2023). https://flowcharts.llnl.gov/commodities/energy.

[3] S. Brückner, S. Liu, L. Miró, M. Radspieler, L.F. Cabeza, E. Lävemann, Industrial waste heat recovery technologies : An economic analysis of heat transformation technologies, Appl. Energy 151 (2015) 157–167. https://doi.org/10.1016/j.apenergy.2015.01.147.

[4] K. Zeb, S.M. Ali, B. Khan, C.A. Mehmood, N. Tareen, W. Din, U. Farid, A. Haider, A survey on waste heat recovery: Electric power generation and potential prospects within Pakistan, Renew. Sustain. Energy Rev. 75 (2016) 1142–1155. https://doi.org/10.1016/j.rser.2016.11.096.

[5] K. Matsubara, Development of a high efficient thermoelectric stack for a waste exhaust heat recovery of vehicles, in: Twenty-First Int. Conf. Thermoelectr. 2002. Proc. ICT '02., IEEE, 2002: pp. 418–423. https://doi.org/10.1109/ICT.2002.1190350.

[6] J. Yang, T. Caillat, Thermoelectric materials for space and automotive power generation, MRS Bull. 31 (2006) 224–229. https://doi.org/10.1557/mrs2006.49.

[7] J.R. Sootsman, D.Y. Chung, M.G. Kanatzidis, New and old concepts in thermoelectric materials, Angew. Chemie Int. Ed. 48 (2009) 8616–8639. https://doi.org/10.1002/anie.200900598.

[8] Alphabet Energy Inc (California US), Thermoelectrics History Timeline, (n.d.). https://web.archive.org/web/20140804040940/http://www.alphabetenergy.com/thermoelectrics-timeline/.

[9] D. Beretta, N. Neophytou, J.M. Hodges, M.G. Kanatzidis, D. Narducci, M. Martin-Gonzalez, M. Beekman, B. Balke, G. Cerretti, W. Tremel, A. Zevalkink, A.I. Hofmann, C. Müller, B. Dörling, M. Campoy-Quiles, M. Caironi, Thermoelectrics: From history, a window to the future, Mater. Sci. Eng. R Reports 138 (2019) 210–255. https://doi.org/10.1016/j.mser.2018.09.001.

[10] T.J. Seebeck, Ueber die magnetische Polarisation der Metalle und Erze durch Temperatur-Differenz, Ann. Phys. 82 (1826) 133–160. https://doi.org/10.1002/andp.18260820202.

[11] A. Volta, Le opere di Alessandro Volta: Edizione nazionale sotto gli auspici della Reale Accademia dei Lincei i del Reale Istituto lombardo di scienze e lettere, Hoepli, 1918. https://books.google.pt/books?id=2mJYAAAAYAAJ.

[12] T.M. Tritt, M. a. Subramanian, Thermoelectric Materials, Phenomena, and Applications: A Bird's Eye View, MRS Bull. 31 (2006) 188–198. https://doi.org/10.1557/mrs2006.44.

[13] A.F. Ioffe, L.S. Stil'bans, E.K. Iordanishvili, T.S. Stavitskaya, A. Gelbtuch, G. Vineyard, Semiconductor Thermoelements and Thermoelectric Cooling, Phys. Today 12 (1959) 42–42. https://doi.org/10.1063/1.3060810.

[14] M. Hamid Elsheikh, D.A. Shnawah, M.F.M. Sabri, S.B.M. Said, M. Haji Hassan, M.B. Ali Bashir, M. Mohamad, A review on thermoelectric renewable energy: Principle parameters that affect their performance, Renew. Sustain. Energy Rev. 30 (2014) 337–355. https://doi.org/10.1016/j.rser.2013.10.027.

[15] D. Champier, Thermoelectric generators: A review of applications, Energy Convers. Manag. 140 (2017) 167–181. https://doi.org/10.1016/j.enconman.2017.02.070.

[16] G.J. Snyder, T.S. Ursell, Thermoelectric efficiency and compatibility, Phys. Rev. Lett. 91 (2003) 148301/1-148301/4. https://doi.org/10.1103/PhysRevLett.91.148301.

[17] M. Telkes, The Efficiency of Thermoelectric Generators. I., J. Appl. Phys. 18 (1947) 1116–1127. https://doi.org/10.1063/1.1697593.

[18] H.J. Goldsmid, R.W. Douglas, The use of semiconductors in thermoelectric refrigeration, Br. J. Appl. Phys. 5 (1954) 386–390. https://doi.org/10.1088/0508-3443/5/11/303.

[19] B.C. Blanke, J.H. Birden, K.C. Jordan, E.L. Murphy, Nuclear Battery-Thermocouple Type Summary Report, 1960. https://doi.org/10.2172/4807049.

[20] D. Beretta, M. Massetti, G. Lanzani, M. Caironi, Thermoelectric characterization of flexible micro-thermoelectric generators, Rev. Sci. Instrum. 88 (2017). https://doi.org/10.1063/1.4973417.

[21] H. Bottner, J. Nurnus, A. Schubert, F. Volkert, New high density micro structured thermogenerators for stand alone sensor systems wafer with different Micropelt designs, in: 26th Int. Conf. Thermoelectr., IEEE, 2007: pp. 306–309. https://doi.org/10.1109/ICT.2007.4569484.

[22] N.P. Klochko, D.O. Zhadan, K.S. Klepikova, S.I. Petrushenko, V.R. Kopach, G.S. Khrypunov, V.M. Lyubov, S.V. Dukarov, A.L. Khrypunova, Semi-transparent copper iodide thin films on flexible substrates as p-type thermolegs for a wearable thermoelectric generator, Thin Solid Films 683 (2019) 34–41. https://doi.org/10.1016/j.tsf.2019.05.025.

[23] N.P. Klochko, K.S. Klepikova, V.R. Kopach, I.I. Tyukhov, V.V. Starikov, D.S. Sofronov, I.V. Khrypunova, D.O. Zhadan, S.I. Petrushenko, S.V. Dukarov, V.M. Lyubov, M.V. Kirichenko, A.L. Khrypunova, Development of semi-transparent ZnO/FTO solar thermoelectric nanogenerator for

energy efficient glazing, Sol. Energy 184 (2019) 230–239. https://doi.org/10.1016/j.solener.2019.04.002.

[24] C. Yang, D. Souchay, M. Kneiß, M. Bogner, H.M. Wei, M. Lorenz, O. Oeckler, G. Benstetter, Y.Q. Fu, M. Grundmann, Transparent flexible thermoelectric material based on non-toxic earth-abundant p-type copper iodide thin film, Nat. Commun. 8 (2017) 4–10. https://doi.org/10.1038/ncomms16076.

[25] K.S. Karimov, N. Fatima, T.A. Qasuria, K.J. Siddiqui, M.M. Bashir, H.F. Alharbi, N.H. Alharth, Y.S. Al-Harthi, N. Amin, M. Akhtaruzzaman, Innovative semitransparent photo-thermoelectric cells based on bismuth antimony telluride alloy, J. Alloys Compd. 816 (2020) 152593. https://doi.org/10.1016/j.jallcom.2019.152593.

[26] I.T. Taneli Juntunen, Tomi Koskinen, Large area transparent thin film thermoelectric devices for smart window and flexible applications, 2020. http://cordis.europa.eu/project/rcn/194300_en.html.

[27] N. Wang, L. Han, H. He, N.H. Park, K. Koumoto, A novel high-performance photovoltaic-thermoelectric hybrid device, Energy Environ. Sci. 4 (2011) 3676–3679. https://doi.org/10.1039/c1ee01646f.

[28] J. Coroa, B.M. Morais Faustino, A. Marques, C. Bianchi, T. Koskinen, T. Juntunen, I. Tittonen, I. Ferreira, Highly transparent copper iodide thin film thermoelectric generator on a flexible substrate, RSC Adv. 9 (2019) 35384–35391. https://doi.org/10.1039/c9ra07309d.

[29] G.-M. Chen, L.-Y. Ma, I.-Y. Huang, T.-E. Wu, Development of a novel transparent micro-thermoelectric generator for solar energy conversion, in: 6th IEEE Int. Conf. Nano/Micro Eng. Mol. Syst., 2011: pp. 976–979. https://doi.org/10.1109/NEMS.2011.6017518.

[30] A. Boyer, E. Ciss, M. Ii, E. Bataillon, M.C. France, Properties of thin film thermoelectric materials: application to sensors using the Seebeck effect, Mater. Sci. Eng. B13 (1992) 103–111. https://doi.org/10.1016/0921-5107(92)90149-4.

[31] R. Venkatasubramanian, E. Siivola, T. Colpitts, B. O'Quinn, Thin-film thermoelectric devices with high room-temperature figures of merit, Nature 413 (2001) 597–602. https://doi.org/10.1038/35098012.

[32] K. Uchida, S. Takahashi, K. Harii, J. Ieda, W. Koshibae, K. Ando, S. Maekawa, E. Saitoh, Observation of the spin Seebeck effect, Nature 455 (2008) 778–781. https://doi.org/10.1038/nature07321.

[33] K. Safeen, V. Micheli, R. Bartali, G. Gottardi, A. Safeen, H. Ullah, Influence of intrinsic defects on

the electrical and optical properties of TiO2:Nb films sputtered at room temperature, Thin Solid Films 645 (2018) 173–179. https://doi.org/10.1016/j.tsf.2017.10.028.

[34] J. Tao, H. Pan, L.M. Wong, T.I. Wong, J.W. Chai, J. Pan, S.J. Wang, Mechanism of insulator-to-metal transition in heavily Nb doped anatase TiO2, Mater. Res. Express 015911 (2014). https://doi.org/10.1088/2053-1591/1/1/015911.

[35] B.G. Lewis, D.C. Paine, Applications and Processing of Transparent Conducting Oxides, MRS Bull. (2000) 22–27. https://doi.org/10.1557/mrs2000.147.

[36] H. Lee, J. Robertson, Doping and compensation in Nb-doped anatase and rutile TiO2, J. Appl. Phys. 113 (2013). https://doi.org/10.1063/1.4808475.

[37] T. Hitosugi, N. Yamada, S. Nakao, Y. Hirose, T. Hasegawa, T. Hitosuji, N. Yamada, S. Nakao, Y. Hirose, T. Hasegawa, Properties of TiO2-based transparent conducting oxides, Phys. Status Solidi Appl. Mater. Sci. 207 (2010) 1529–1537. https://doi.org/10.1002/pssa.200983774pss.

[38] IDTechEx, K. Ghaffarzadeh, R. Das, Transparent Conductive Films (TCF) 2017-2027: Forecasts, Markets, Technologies, 2017. https://www.idtechex.com/research/reports/transparent-conductive-films-tcf-2017-2027-forecasts-markets-technologies-000524.asp?viewopt=desc.

[39] IDTechEx, P. Harrop, R. Das, Thermoelectric Energy Harvesting 2018-2028: Applications, Markets, Players, 2018. https://www.idtechex.com/research/reports/thermoelectric-energy-harvesting-2018-2028-applications-markets-players-000582.asp.

[40] K.B. Spooner, A.M. Ganose, D.O. Scanlon, Assessing the limitations of transparent conducting oxides as thermoelectrics, J. Mater. Chem. A (2020). https://doi.org/10.1039/d0ta02247k.

[41] B.M.M. Faustino, D. Gomes, J. Faria, T. Juntunen, G. Gaspar, C. Bianchi, A. Almeida, A. Marques, I. Tittonen, I. Ferreira, CuI p-type thin films for highly transparent thermoelectric p-n modules, 2018. https://doi.org/10.1038/s41598-018-25106-3.

[42] L.C. Ding, A. Akbarzadeh, L. Tan, A review of power generation with thermoelectric system and its alternative with solar ponds, Renew. Sustain. Energy Rev. 81 (2018) 799–812. https://doi.org/10.1016/j.rser.2017.08.010.

[43] K. Wasa, Handbook of Sputter Deposition Technology, 2012. https://doi.org/10.1017/CBO9781107415324.004.

[44] S.M. Rossnagel, Thin film deposition with physical vapor deposition and related technologies, J. Vac. Sci. Technol. A Vacuum, Surfaces, Film. 21 (2003) S74–S87. https://doi.org/10.1116/1.1600450.

[45] A. Mubarak, E. Hamzah, M.R.M. Toff, Review of physical vapour deposition (PVD) techniques for

hard coating, J. Mek. (2005) 42–51. https://api.semanticscholar.org/CorpusID:45550647.

[46] S. Shahidi, B. Moazzenchi, M. Ghoranneviss, A review-application of physical vapor deposition (PVD) and related methods in the textile industry, EPJ Appl. Phys. 71 (2015) 1–13. https://doi.org/10.1051/epjap/2015140439.

[47] M. Ohring, Materials Science of Thin Films, 2002. https://doi.org/10.1017/CBO9781107415324.004.

[48] M. Ohring, Substrate Surfaces and Thin-Film Nucleation, Mater. Sci. Thin Film. (2002) 357–415. https://doi.org/10.1016/b978-012524975-1/50010-0.

[49] D.M. Mattox, Handbook of Physical Vapor Deposition (PVD) Processing, 2009. https://doi.org/10.1016/B978-0-8155-2037-5.00025-3.

[50] J.E. Mahan, Physical Vapor Deposition of Thin Films, Wiley-Interscience, 2000. https://www.wiley.com/en-us/Physical+Vapor+Deposition+of+Thin+Films-p-9780471330011.

[51] A. Ferreira, C. Lopes, N. Martin, S. Lanceros-Méndez, F. Vaz, Nanostructured functional Ti-Ag electrodes for large deformation sensor applications, Sensors Actuators, A Phys. 220 (2014) 204–212. https://doi.org/10.1016/j.sna.2014.09.031.

[52] P. Pedrosa, D. Machado, J. Borges, M.S. Rodrigues, E. Alves, N.P. Barradas, N. Martin, M. Evaristo, A. Cavaleiro, C. Fonseca, F. Vaz, Agy:TiNx thin films for dry biopotential electrodes: the effect of composition and structural changes on the electrical and mechanical behaviours, Appl. Phys. A Mater. Sci. Process. 119 (2015) 169–178. https://doi.org/10.1007/s00339-014-8943-9.

[53] J.F.V. Vaz, Preparação e Caracterização de Filmes Finos de Ti1-xSixNy, crescidos por Pulverização Catódica Reativa em Magnetrão, Universidade do Porto, 2000. https://catalogo.up.pt/F/?func=direct&doc_number=000259292&local_base=UPB01.

[54] J.N.P. Borges, Otimização do processo de deposição de oxinitretos metálicos por pulverização reativa magnetrão, Universidade do Minho, 2013. https://hdl.handle.net/1822/25553.

[55] P.J. Kelly, R.D. Arnell, Magnetron sputtering: a review of recent developments and applications, Vacuum 56 (2000) 159–172. https://doi.org/10.1016/S0042-207X(99)00189-X.

[56] K.S. Sree Harsha, Principles of Vapor Deposition of Thin Films, Elsevier Sci. (2006). https://doi.org/10.1016/B978-0-08-044699-8.X5000-1.

[57] G.B. Bronner, S.A. Cohen, D.M. Dobuzinsky, J.P. Gambino, H.L. Ho, K.P. Madden, High dielectric TiO2-SiN composite films for memory applications, US005876788A, 1999.

[58] K.F. Albertin, M.A. Valle, I. Pereyra, Study Of MOS Capacitors With TiO2 And SiO2/TiO2 Gate

Dielectric, J. Integr. Circuits Syst. 2 (2007) 89–93. https://www.researchgate.net/publication/285020579_Study_of_MOS_capacitors_with_TiO2_and_SiO2TiO2_gate_dielectric.

[59] R. Riedel, Handbook of Ceramic Hard Materials, Darmstadt, 2000. https://doi.org/10.1002/9783527618217.ch22.

[60] K. Okimura, Low temperature growth of rutile TiO2 films in modified rf magnetron sputtering, Surf. Coatings Technol. 135 (2001) 286–290. https://doi.org/10.1016/S0257-8972(00)00999-3.

[61] A. Fujishima, X. Zhang, Titanium dioxide photocatalysis: present situation and future approaches, Comptes Rendus Chim. 9 (2006) 750–760. https://doi.org/10.1016/j.crci.2005.02.055.

[62] N.R. Yogamalar, A.C. Bose, Burstein – Moss shift and room temperature near-band-edge luminescence in lithium-doped zinc oxide, (2011) 33–42. https://doi.org/10.1007/s00339-011-6304-5.

[63] A. Walsh, J.L.F. Da Silva, S.-H. Wei, Origins of band-gap renormalization in degenerately doped semiconductors, Phys. Rev. B 78 (2008) 075211. https://doi.org/10.1103/PhysRevB.78.075211.

[64] M.M. Abdel-aziz, I.S. Yahia, L.A. Wahab, M. Fadel, M.A. Afifi, Determination and analysis of dispersive optical constant of TiO2 and Ti2O3 thin films, Appl. Surf. Sci. 252 (2006) 8163–8170. https://doi.org/10.1016/j.apsusc.2005.10.040.

[65] M.M. Hasan, A.S.M.A. Haseeb, R. Saidur, H.H. Masjuki, Effects of Annealing Treatment on Optical Properties of Anatase TiO2 Thin Films, Int. J. Mech. Ind. Manuf. Eng. 2 (2008) 410–414. https://doi.org/10.5281/zenodo.1058617.

[66] Q. Hao, H. Zhao, D. Xu, Thermoelectric Studies of Nanoporous Thin Films with Adjusted Pore-Edge Charges, J. Appl. Phys. 121 (2017) 1–3. https://doi.org/10.1063/1.4977871.

[67] J. Yang, J. Zhang, H. Zhang, Y. Zhu, Thermal conductivity measurement of thin films by a dc method, Rev. Sci. Instrum. 81 (2010) 1–5. https://doi.org/10.1063/1.3481787.

[68] C.J. Tavares, M.V. Castro, E.S. Marins, A.P. Samantilleke, S. Ferdov, L. Rebouta, M. Benelmekki, M.F. Cerqueira, P. Alpuim, E. Xuriguera, J.-P. Rivière, D. Eyidi, M.-F. Beaufort, A. Mendes, Effect of hot-filament annealing in a hydrogen atmosphere on the electrical and structural properties of Nb-doped TiO2 sputtered thin films, Thin Solid Films 520 (2012) 2514–2519. https://doi.org/10.1016/j.tsf.2011.10.031.

[69] A. Zaleska, Doped-TiO2: A Review, Recent Patents Eng. (2008) 157–164. https://doi.org/10.2174/187221208786306289.

[70] X.D. Liu, E.Y. Jiang, Z.Q. Li, Q.G. Song, Electronic structure and optical properties of Nb-doped anatase TiO2, Appl. Phys. Lett. 92 (2008) 3–5. https://doi.org/10.1063/1.2949070.

[71] S. Luo, B. Yan, J. Shen, Enhancement of photoelectric and photocatalytic activities: Mo doped TiO2 thin films deposited by sputtering, Thin Solid Films 522 (2012) 361–365. https://doi.org/10.1016/j.tsf.2012.07.121.

[72] M.V. Castro, L. Rebouta, P. Alpuim, M.F. Cerqueira, M. Benelmekki, C.B. Garcia, E. Alves, N.P. Barradas, E. Xuriguera, C.J. Tavares, Optimisation of surface treatments of TiO2:Nb transparent conductive coatings by a post-hot-wire annealing in a reducing H2 atmosphere, Thin Solid Films 550 (2014) 404–412. https://doi.org/10.1016/j.tsf.2013.11.044.

[73] J.M. Ribeiro, F.C. Correia, A. Kuzmin, I. Jonane, M. Kong, A.R. Goñi, J.S. Reparaz, A. Kalinko, E. Welter, C.J. Tavares, Influence of Nb-doping on the local structure and thermoelectric properties of transparent TiO2:Nb thin films, J. Alloys Compd. 838 (2020) 155561. https://doi.org/10.1016/j.jallcom.2020.155561.

[74] T. Hitosugi, A. Ueda, S. Nakao, N. Yamada, Y. Furubayashi, Y. Hirose, T. Shimada, T. Hasegawa, Fabrication of highly conductive Ti1-x Nbx O2 polycrystalline films on glass substrates via crystallization of amorphous phase grown by pulsed laser deposition, Appl. Phys. Lett. 90 (2007) 20–23. https://doi.org/10.1063/1.2742310.

[75] T. Hitosugi, A. Ueda, S. Nakao, N. Yamada, Y. Furubayashi, Y. Hirose, S. Konuma, T. Shimada, T. Hasegawa, Transparent conducting properties of anatase Ti0.94Nb0.06O2 polycrystalline films on glass substrate, Thin Solid Films 516 (2008) 5750–5753. https://doi.org/10.1016/j.tsf.2007.10.028.

[76] N. Yamada, T. Shibata, K. Taira, Y. Hirose, S. Nakao, N.L.H. Hoang, T. Hitosugi, T. Shimada, T. Sasaki, T. Hasegawa, Enhanced carrier transport in uniaxially (001)-oriented anatase Ti 0.94Nb0.06O2 films grown on nanosheet seed layers, Appl. Phys. Express 4 (2011). https://doi.org/10.1143/APEX.4.045801.

[77] S. Murai, R. Kamakura, K. Fujita, Y. Daido, K. Tanaka, Preparation of Nb-doped anatase type TiO2 epitaxial thin films and excitation of surface plasmon polaritons, Funtai Oyobi Fummatsu Yakin/Journal Japan Soc. Powder Powder Metall. 64 (2017) 23–27. https://doi.org/10.2497/jjspm.64.23.

[78] Y. Sato, H. Akizuki, T. Kamiyama, Y. Shigesato, Transparent conductive Nb-doped TiO2 films deposited by direct-current magnetron sputtering using a TiO2 - x target, Thin Solid Films 516 (2008) 5758–5762. https://doi.org/10.1016/j.tsf.2007.10.047.

[79] A.H. Simon, Sputter Processing, Handb. Thin Film Depos. Tech. Process. Technol. Third Ed. (2012) 55–88. https://doi.org/10.1016/B978-1-4377-7873-1.00004-8.

[80] P. Sigmund, Theory of Sputtering. I. Sputtering Yield of Amorphous and Polycrystalline Targets, Phys. Rev. 184 (1969) 383–416. https://doi.org/10.1177/1362361310366314.

[81] P. Sigmund, Mechanisms and theory of physical sputtering by particle impact, Nucl. Inst. Methods Phys. Res. B 27 (1987) 1–20. https://doi.org/10.1016/0168-583X(87)90004-8.

[82] A.H. Simon, Sputter Processing, Handb. Thin Film Depos. Fourth Ed. (2018) 195–230. https://doi.org/10.1016/B978-0-12-812311-9.00007-4.

[83] J.S. Chapin, Sputtering Process and Apparatus, US4166018A, 1979.

[84] D. Depla, S. Mahieu, J.E. Greene, Sputter Deposition Processes, Handb. Depos. Technol. Film. Coatings (2010) 253–296. https://doi.org/10.1016/B978-0-8155-2031-3.00005-3.

[85] C. V. Thompson, Structure Evolution During Processing of Polycrystalline Films, Mater. Sci. 30 (2000) 159–190. https://doi.org/10.1146/annurev.matsci.30.1.159.

[86] I. Petrov, P.B. Barna, L. Hultman, J.E. Greene, Microstructural evolution during film growth, J. Vac. Sci. Technol. A Vacuum, Surfaces, Film. 21 (2003) S117–S128. https://doi.org/10.1116/1.1601610.

[87] S. Mahieu, P. Ghekiere, D. Depla, R. De Gryse, Biaxial alignment in sputter deposited thin films, Thin Solid Films 515 (2006) 1229–1249. https://doi.org/10.1016/j.tsf.2006.06.027.

[88] G. Bräuer, B. Szyszka, M. Vergöhl, R. Bandorf, Magnetron sputtering - Milestones of 30 years, Vacuum 84 (2010) 1354–1359. https://doi.org/10.1016/j.vacuum.2009.12.014.

[89] M.V. Castro, M.F. Cerqueira, L. Rebouta, P. Alpuim, C.B. Garcia, G.L. Júnior, C.J. Tavares, Influence of hydrogen plasma thermal treatment on the properties of ZnO:Al thin films prepared by dc magnetron sputtering, Vacuum 107 (2014) 145–154. https://doi.org/10.1016/j.vacuum.2014.04.022.

[90] M.V. Castro, C.J. Tavares, Dependence of Ga-doped ZnO thin film properties on different sputtering process parameters: Substrate temperature, sputtering pressure and bias voltage, Thin Solid Films 586 (2015) 13–21. https://doi.org/10.1016/j.tsf.2015.04.036.

[91] J.M. Ribeiro, F.C. Correia, P.B. Salvador, L. Rebouta, L.C. Alves, E. Alves, N.P. Barradas, A. Mendes, C.J. Tavares, Compositional analysis by RBS, XPS and EDX of ZnO:Al,Bi and ZnO:Ga,Bi thin films deposited by d.c. magnetron sputtering, Vacuum 161 (2019) 268–275. https://doi.org/10.1016/j.vacuum.2018.12.038.

[92] K.M. Reddy, S. V. Manorama, A.R. Reddy, Bandgap studies on anatase titanium dioxide

nanoparticles, Mater. Chamestry Phys. 78 (2002) 239–245. https://doi.org/10.1016/S0254-0584(02)00343-7.

[93] J. He, Y. Du, Y. Bai, J. An, X. Cai, Y. Chen, P. Wang, X. Yang, Q. Feng, Facile Formation of Anatase/Rutile TiO2 Nanocomposites with Enhanced Photocatalytic Activity, Molecules 24 (2019) 2996. https://doi.org/10.3390/molecules24162996.

[94] R.N.S. Sodhi, Time-of-flight secondary ion mass spectrometry (TOF-SIMS):—versatility in chemical and imaging surface analysis, Analyst 129 (2004) 483–487. https://doi.org/10.1039/B402607C.

[95] M. Stamm, Polymer Surfaces and Interfaces, Springer Berlin Heidelberg, Berlin, Heidelberg, 2008. https://doi.org/10.1007/978-3-540-73865-7.

[96] E. Welter, R. Chernikov, M. Herrmann, R. Nemausat, A beamline for bulk sample x-ray absorption spectroscopy at the high brilliance storage ring PETRA III, AIP Conf. Proc. 2054 (2019) 1–6. https://doi.org/10.1063/1.5084603.

[97] J.T.M. De Hosson, N.J.M. Carvalho, Y. Pei, D. Galvan, Electron Microscopy Characterization of Nanostructured Coatings, 2007. https://doi.org/10.1007/0-387-48756-5_5.

[98] D.K. Schroder, Semiconductor Material and Device characterization, Third, 2006. https://doi.org/10.1063/1.2810086.

[99] B.W. Schueler, Microscope imaging by time-of-flight secondary ion mass spectrometry, Microsc. Microanal. Microstruct. 3 (1992) 119–139. https://doi.org/10.1051/mmm:0199200302-3011900.

[100] M.K. Miller, R.G. Forbes, The Local Electrode Atom Probe, in: Atom-Probe Tomogr., Springer US, Boston, MA, 2014: pp. 229–258. https://doi.org/10.1007/978-1-4899-7430-3_5.

[101] D.J. Larson, T.J. Prosa, R.M. Ulfig, B.P. Geiser, T.F. Kelly, Local Electrode Atom Probe Tomography, Springer New York, New York, NY, 2013. https://doi.org/10.1007/978-1-4614-8721-0.

[102] W. Lefebvre-Ulrikson, F. Vurpillot, X. Sauvage, Atom Probe Tomography: Put Theory Into Practice, 1st ed., Academic Press, 2016. https://shop.elsevier.com/books/atom-probe-tomography/lefebvre/978-0-12-804647-0.

[103] B. Gault, M.P. Moody, J.M. Cairney, S.P. Ringer, Atom Probe Tomography, in: R. Hull, C. Jagadish, J. R.M. Osgood, J. Parisi, Z.M. Wang (Eds.), Springer Ser. Mater. Sci., Springer, 2009: p. 160. https://link.springer.com/book/10.1007/978-1-4614-3436-8.

[104] Cameca, Atom Probe Tomography Tutorial: Essential Knowledge Briefings, (2017).

https://www.cameca.com/learning-zone/tutorials/apt-tuto.

[105] T.F. Kelly, M.K. Miller, Atom probe tomography, Rev. Sci. Instrum. 78 (2007). https://doi.org/10.1063/1.2709758.

[106] M.K. Miller, R.G. Forbes, The Local Electrode Atom Probe, in: Atom-Probe Tomogr., Springer US, Boston, MA, 2014: pp. 229–258. https://doi.org/10.1007/978-1-4899-7430-3_5.

[107] D.J. Larson, T.J. Prosa, R.M. Ulfig, B.P. Geiser, T.F. Kelly, Local Electrode Atom Probe Tomography, Springer New York, New York, NY, 2013. https://doi.org/10.1007/978-1-4614-8721-0.

[108] S.K. O'Leary, S.R. Johnson, P.K. Lim, The relationship between the distribution of electronic states and the optical absorption spectrum of an amorphous semiconductor: An empirical analysis, J. Appl. Phys. 82 (1997) 3334–3340. https://doi.org/10.1063/1.365643.

[109] C.C. Kim, J.W. Garland, H. Abad, P.M. Raccah, Modeling the optical dielectric function of semiconductors: Extension of the critical-point parabolic-band approximation, Phys. Rev. B 45 (1992) 11749–11767. https://doi.org/10.1103/PhysRevB.45.11749.

[110] M. Fox, Optical Properties of Solids, Second, Elsevier, 1972. https://doi.org/10.1016/C2013-0-07656-6.

[111] J. Tauc, R. Grigorovici, A. Vancu, Optical Properties and Electronic Structure of Amorphous Germanium, Phys. Status Solidi 15 (1966) 627–637. https://doi.org/10.1002/pssb.19660150224.

[112] A.J. Schmidt, R. Cheaito, M. Chiesa, A frequency-domain thermoreflectance method for the characterization of thermal properties A frequency-domain thermoreflectance method for the characterization, Rev. Sci. Instrum. 80 (2009). https://doi.org/10.1063/1.3212673.

[113] M. Yoshiizumi, N. Oikawa, K. Shimada, S. Endo, M. Sugiyama, H. Mikami, R. Maeda, T. Hayakawa, Thermal Conductivity Evaluation of Polymer Thin Film, Trans. Mater. Res. Soc. Japan 38 (2014) 555–559. https://doi.org/10.14723/tmrsj.38.555.

[114] J. Martin, W. Wong-ng, M.L. Green, Seebeck Coefficient Metrology: Do Contemporary Protocols Measure Up?, Miner. Met. Mater. Soc. (2015). https://doi.org/10.1007/s11664-015-3640-9.

[115] J. Timoshenko, A. Kuzmin, J. Purans, EXAFS study of hydrogen intercalation into ReO3 using the evolutionary algorithm, J. Phys. Condens. Matter 26 (2014). https://doi.org/10.1088/0953-8984/26/5/055401.

[116] A. Kuzmin, J. Chaboy, EXAFS and XANES analysis of oxides at the nanoscale, IUCrJ 1 (2014) 571–589. https://doi.org/10.1107/S2052252514021101.

[117] C.J. Howard, T.M. Sabine, F. Dickson, Structural and thermal parameters for rutile and anatase, Acta Crystallogr. Sect. B Struct. Sci. 47 (1991) 462–468. https://doi.org/10.1107/S010876819100335X.

[118] A.L. Ankudinov, B. Ravel, J.J. Rehr, S.D. Conradson, Real-space multiple-scattering calculation and interpretation of x-ray-absorption near-edge structure, Phys. Rev. B 58 (1998) 7565–7576. https://doi.org/10.1103/PhysRevB.58.7565.

[119] J.J. Rehr, R.C. Albers, Theoretical approaches to x-ray absorption fine structure, Rev. Mod. Phys. 72 (2000) 621–654. https://doi.org/10.1103/RevModPhys.72.621.

[120] L. Hedin, B.I. Lundqvist, Explicit local exchange-correlation potentials, J. Phys. C Solid State Phys. 4 (1971) 2064–2083. https://doi.org/10.1088/0022-3719/4/14/022.

[121] Y. Joly, X-ray absorption near-edge structure calculations beyond the muffin-tin approximation, 63 (2001) 1–10. https://doi.org/10.1103/PhysRevB.63.125120.

[122] O. Bunau, Y. Joly, Self-consistent aspects of x-ray absorption, (2009). https://doi.org/10.1088/0953-8984/21/34/345501.

[123] O. Keski-Rahkonen, M.O. Krause, Total and partial atomic-level widths, At. Data Nucl. Data Tables 14 (1974) 139–146. https://doi.org/10.1016/S0092-640X(74)80020-3.

[124] P. Giannozzi, S. Baroni, N. Bonini, M. Calandra, R. Car, C. Cavazzoni, D. Ceresoli, G.L. Chiarotti, M. Cococcioni, I. Dabo, A. Dal Corso, S. De Gironcoli, S. Fabris, G. Fratesi, R. Gebauer, U. Gerstmann, C. Gougoussis, A. Kokalj, M. Lazzeri, L. Martin-Samos, N. Marzari, F. Mauri, R. Mazzarello, S. Paolini, A. Pasquarello, L. Paulatto, C. Sbraccia, S. Scandolo, G. Sclauzero, A.P. Seitsonen, A. Smogunov, P. Umari, R.M. Wentzcovitch, QUANTUM ESPRESSO: A modular and open-source software project for quantum simulations of materials, J. Phys. Condens. Matter 21 (2009) 1–20. https://doi.org/10.1088/0953-8984/21/39/395502.

[125] P. Giannozzi, O. Andreussi, T. Brumme, O. Bunau, M. Buongiorno Nardelli, M. Calandra, R. Car, C. Cavazzoni, D. Ceresoli, M. Cococcioni, N. Colonna, I. Carnimeo, A. Dal Corso, S. De Gironcoli, P. Delugas, R.A. Distasio, A. Ferretti, A. Floris, G. Fratesi, G. Fugallo, R. Gebauer, U. Gerstmann, F. Giustino, T. Gorni, J. Jia, M. Kawamura, H.Y. Ko, A. Kokalj, E. Kücükbenli, M. Lazzeri, M. Marsili, N. Marzari, F. Mauri, N.L. Nguyen, H. V. Nguyen, A. Otero-De-La-Roza, L. Paulatto, S. Poncé, D. Rocca, R. Sabatini, B. Santra, M. Schlipf, A.P. Seitsonen, A. Smogunov, I. Timrov, T. Thonhauser, P. Umari, N. Vast, X. Wu, S. Baroni, Advanced capabilities for materials modelling with Quantum ESPRESSO, J. Phys. Condens. Matter 29 (2017). https://doi.org/10.1088/1361-648X/aa8f79.

[126] D.R. Hamann, Optimized norm-conserving Vanderbilt pseudopotentials, Phys. Rev. B - Condens.

Matter Mater. Phys. 88 (2013) 1–10. https://doi.org/10.1103/PhysRevB.88.085117.

[127] G. Prandini, A. Marrazzo, I.E. Castelli, N. Mounet, N. Marzari, Precision and efficiency in solid-state pseudopotential calculations, Npj Comput. Mater. 4 (2018) 1–13. https://doi.org/10.1038/s41524-018-0127-2.

[128] A.C.R. Fernández, A.B. Schvval, M.J. Jiménez, G.F. Cabeza, C.I.N. Morgade, Comparative study of the effect of the Hubbard coefficient U on the properties of TiO2 and ZnO, Mater. Today Commun. 27 (2021) 1–12. https://doi.org/10.1016/j.mtcomm.2021.102368.

[129] K. Momma, F. Izumi, VESTA 3 for three-dimensional visualization of crystal, volumetric and morphology data, J. Appl. Crystallogr. 44 (2011) 1272–1276. https://doi.org/10.1107/S0021889811038970.

[130] A. Kokalj, XCrySDen-a new program for displaying crystalline structures and electron densities, J. Mol. Graph. Model. 17 (1999) 176–179. https://doi.org/10.1016/S1093-3263(99)00028-5.

[131] G.K.H. Madsen, J. Carrete, M.J. Verstraete, BoltzTraP2, a program for interpolating band structures and calculating semi-classical transport coefficients, Comput. Phys. Commun. 231 (2018) 140–145. https://doi.org/10.1016/j.cpc.2018.05.010.

[132] A.J. Schmidt, R. Cheaito, M. Chiesa, A frequency-domain thermoreflectance method for the characterization of thermal properties, Rev. Sci. Instrum. 80 (2009). https://doi.org/10.1063/1.3212673.

[133] M.Z.Z. Atashbar, H.T.T. Sun, B. Gong, W. Wlodarski, R. Lamb, XPS study of Nb-doped oxygen sensing TiO2 thin films prepared by sol-gel method, Thin Solid Films 326 (1998) 238–244. https://doi.org/10.1016/S0040-6090(98)00534-3.

[134] M.C. Biesinger, L.W.M. Lau, A.R. Gerson, R.S.C. Smart, Resolving surface chemical states in XPS analysis of first row transition metals, oxides and hydroxides: Sc, Ti, V, Cu and Zn, Appl. Surf. Sci. 257 (2010) 887–898. https://doi.org/10.1016/j.apsusc.2010.07.086.

[135] A. Mattsson, M. Leideborg, K. Larsson, G. Westin, L. Österlund, Adsorption and Solar Light Decomposition of Acetone on Anatase TiO_2 and Niobium Doped TiO_2 Thin Films, J. Phys. Chem. B 110 (2006) 1210–1220. https://doi.org/10.1021/jp055656z.

[136] Y. Joly, D. Cabaret, H. Renevier, C.R. Natoli, Electron population analysis by full-potential X-ray absorption simulations, Phys. Rev. Lett. 82 (1999) 2398–2401. https://doi.org/10.1103/PhysRevLett.82.2398.

[137] D.S.J. Kim, D.S.J. Kim, S. Cho, S.W. Kim, S.H. Lee, J.C. Kim, Measurement of thermal conductivity of TiO2 thin films using 3ω method, Int. J. Thermophys. 25 (2004) 281–289.

https://doi.org/10.1023/B:IJOT.0000022340.65615.22.

[138] M.-H. Hong, S.-Y. Jung, T.-J. Ha, W.-S. Seo, Y.S. Lim, S. Shin, H.H. Cho, H.-H. Park, Thermoelectric properties of mesoporous TiO2 thin films through annealing temperature and ratio of surfactant, Surf. Coatings Technol. 231 (2013) 370–373. https://doi.org/10.1016/j.surfcoat.2012.07.035.

[139] L. Xu, M.P. Garrett, B. Hu, Doping effects on internally coupled seebeck coefficient, electrical, and thermal conductivities in aluminum-doped TiO 2, J. Phys. Chem. C 116 (2012) 13020–13025. https://doi.org/10.1021/jp302652c.

[140] D. Kurita, S. Ohta, K. Sugiura, H. Ohta, K. Koumoto, Carrier generation and transport properties of heavily Nb-doped anatase TiO[sub 2] epitaxial films at high temperatures, J. Appl. Phys. 100 (2006) 096105. https://doi.org/10.1063/1.2362990.

[141] S. Ohta, T. Nomura, H. Ohta, M. Hirano, H. Hosono, K. Koumoto, Large thermoelectric performance of heavily Nb-doped SrTiO3 epitaxial film at high temperature, Appl. Phys. Lett. 87 (2005) 1–4. https://doi.org/10.1063/1.2035889.

[142] L. Sheppard, T. Bak, J. Nowotny, C.C. Sorrell, S. Kumar, A.R. Gerson, M.C. Barnes, C. Ball, Effect of niobium on the structure of titanium dioxide thin films, Thin Solid Films 510 (2006) 119–124. https://doi.org/10.1016/j.tsf.2005.12.272.

[143] A. Janotti, C.G. Van De Walle, Fundamentals of zinc oxide as a semiconductor, Reports Prog. Phys. 72 (2009). https://doi.org/10.1088/0034-4885/72/12/126501.

[144] A. Fujishima, T. Rao, D. Tryk, Titanium dioxide photocatalysis, J. Photochem. Photobiol. C Photochem. Rev. 1 (2000) 1–21. https://doi.org/10.1016/S1389-5567(00)00002-2.

[145] E. Burstein, Anomalous Optical Absorption Limit in InSb, Am. Phys. Soc. 93 (1954) 632. https://doi.org/10.1103/PhysRev.93.632.

[146] J.M. Ribeiro, F.C. Correia, F.J. Rodrigues, J.S. Reparaz, A.R. Goñi, C.J. Tavares, Transparent niobium-doped titanium dioxide thin films with high Seebeck coefficient for thermoelectric applications, Surf. Coatings Technol. 425 (2021) 127724. https://doi.org/10.1016/j.surfcoat.2021.127724.

[147] N. Matsunami, Y. Yamamura, Y. Itikawa, N. Itoh, Y. Kazumata, S. Miyagawa, K. Morita, R. Shimizu, H. Tawara, Energy dependence of the ion-induced sputtering yields of monatomic solids, At. Data Nucl. Data Tables 31 (1984) 1–80. https://doi.org/10.1016/0092-640X(84)90016-0.

[148] V. V. Atuchin, I.E. Kalabin, V.G. Kesler, N. V. Pervukhina, Nb 3d and O 1s core levels and chemical bonding in niobates, J. Electron Spectros. Relat. Phenomena 142 (2005) 129–134. https://doi.org/10.1016/J.ELSPEC.2004.10.003.

[149] M.C. Biesinger, B.P. Payne, A.P. Grosvenor, L.W.M. Lau, A.R. Gerson, R.S.C. Smart, Resolving surface chemical states in XPS analysis of first row transition metals, oxides and hydroxides: Cr, Mn, Fe, Co and Ni, Appl. Surf. Sci. 257 (2011) 2717–2730. https://doi.org/10.1016/j.apsusc.2010.10.051.

[150] L. Zhu, Q. Lu, L. Lv, Y. Wang, Y. Hu, Z. Deng, Z. Lou, Y. Hou, F. Teng, Ligand-free rutile and anatase TiO2 nanocrystals as electron extraction layers for high performance inverted polymer solar cells, RSC Adv. Invert. 7 (2017) 20084–20092. https://doi.org/10.1039/c7ra00134g.

[151] J. Ovenstone, K. Yanagisawa, Effect of Hydrothermal Treatment of Amorphous Titania on the Phase Change from Anatase to Rutile during Calcination, Chem. Mater. 11 (1999) 2770–2774. https://doi.org/10.1021/cm990172z.

[152] M. Park, J. Li, A. Kumar, G. Li, Y. Yang, Doping of the Metal Oxide Nanostructure and its Influence in Organic Electronics, Adv. Funct. Mater. 18 (2009) 1241–1246. https://doi.org/10.1002/adfm.200801639.

[153] T.S. Moss, The Interpretation of the Properties of Indium Antimonide, Proc. Phys. Soc. Sect. B 67 (1954) 775–782. https://doi.org/10.1088/0370-1301/67/10/306.

[154] H. Tang, K. Prasad, R. Sanjinès, P.E. Schmid, F. Lévy, Electrical and optical properties of TiO2 anatase thin films, J. Appl. Phys. 75 (1994) 2042–2047. https://doi.org/10.1063/1.356306.

[155] V. Pfeifer, P. Erhart, S. Li, K. Rachut, J. Morasch, J. Bro, P. Reckers, T. Mayer, S. Ru, A. Zaban, M. Sero, J. Bisquert, W. Jaegermann, A. Klein, Energy Band Alignment between Anatase and Rutile TiO 2, J. Phys. Chem. Lett. 4 (2013) 4182–4187. https://doi.org/10.1021/jz402165b |.

[156] A. Billard, D. Mercs, F. Perry, C. Frantz, Influence of the target temperature on a reactive sputtering process, Surf. Coatings Technol. 116–119 (1999) 721–726. https://doi.org/10.1016/S0257-8972(99)00261-3.

[157] Y. Wang, H. Zhang, P. Liu, X. Yao, H. Zhao, Engineering the band gap of bare titanium dioxide materials for visible-light activity: A theoretical prediction, RSC Adv. 3 (2013) 8777–8782. https://doi.org/10.1039/c3ra40239h.

[158] J.K. Burdett, T. Hughbanks, G.J. Miller, J. V. Smith, J.W. Richardson, Structural-Electronic Relationships in Inorganic Solids: Powder Neutron Diffraction Studies of the Rutile and Anatase Polymorphs of Titanium Dioxide at 15 and 295 K, J. Am. Chem. Soc. 109 (1987) 3639–3646. https://doi.org/10.1021/ja00246a021.

[159] O.A. López-Galán, M. Ramos, J. Nogan, A. Ávila-García, T. Boll, M. Heilmaier, The electronic states of ITO–MoS2: Experiment and theory, MRS Commun. 12 (2022) 137–144.

https://doi.org/10.1557/s43579-021-00126-9.

[160] H. Peng, J. Li, S.S. Li, J.B. Xia, First-principles study of the electronic structures and magnetic properties of 3d transition metal-doped anatase TiO2, J. Phys. Condens. Matter 20 (2008) 1–5. https://doi.org/10.1088/0953-8984/20/12/125207.

[161] H. Tian, W. Ahn, K. Maize, M. Si, P. Ye, M.A. Alam, A. Shakouri, P. Bermel, Thermoreflectance imaging of electromigration evolution in asymmetric aluminum constrictions, J. Appl. Phys. 123 (2018). https://doi.org/10.1063/1.5005938.

[162] K. Zeb, S.M. Ali, B. Khan, C.A. Mehmood, N. Tareen, W. Din, U. Farid, A. Haider, 2 A survey on waste heat recovery: Electric power generation and potential prospects within Pakistan, Renew. Sustain. Energy Rev. 75 (2017) 1142–1155. https://doi.org/10.1016/j.rser.2016.11.096.

[163] Y. Gaillard, V.J. Rico, E. Jimenez-Pique, A.R. González-Elipe, Nanoindentation of TiO2 thin films with different microstructures, J. Phys. D. Appl. Phys. 42 (2009). https://doi.org/10.1088/0022-3727/42/14/145305.

[164] D. Kaczmarek, D. Wojcieszak, J. Domaradzki, E. Prociow, F. Placido, S. Lapp, R. Dylewicz, Influence of nanocrystalline structure and composition on hardness of thin films based on TiO2, Cent. Eur. J. Phys. 9 (2011) 349–353. https://doi.org/10.2478/s11534-010-0112-y.

[165] A.J. Perry, H.K. Pulker, Hardness, adhesion and abrasion resistance of TiO2 films on glass, Thin Solid Films 124 (1985) 323–333. https://doi.org/10.1016/0040-6090(85)90283-4.

[166] B.G.N. Fernandes, Thermoelectric transparent micro-arrays for thermal energy harvesting, University of Minho, 2023. https://hdl.handle.net/1822/85237.

[167] Merck, AZ® P4000 Series Positive Tone Photoresist - Thechnical datasheet, 2016. https://www.microchemicals.com/products/photoresists/az_p4110.html (accessed June 5, 2024).

[168] EMD Performance Materials, AZ® 400K Developer, SDS: 70MDGM184432 (Version 3.6) - Technical datasheet, 2020. www.emdgroup.com/electronics.

[169] J.M. Ribeiro, F.J. Rodrigues, F.C. Correia, I. Pudza, A. Kuzmin, A. Kalinko, E. Welter, N.P. Barradas, E. Alves, A.P. LaGrow, O. Bondarchuk, A. Welle, A. Telfah, C.J. Tavares, The influence of Sb doping on the local structure and disorder in thermoelectric ZnO:Sb thin films, J. Alloys Compd. 939 (2023) 168751. https://doi.org/10.1016/j.jallcom.2023.168751.

APPENDIX A – SEM-EDX ANALYSIS

EDX experiments were performed to determine the composition of Ti:Nb and TiO_2:Nb thin films.

Figure A 1 presents measurements performed on the Ti(96)Nb(4) wt.% target, and corresponding TiO_2:Nb thin films deposited with 7.5 sccm, 8 sccm, 8.5 sccm and 9 sccm of reactive O_2 flow, detailed in **Chapter 4**.

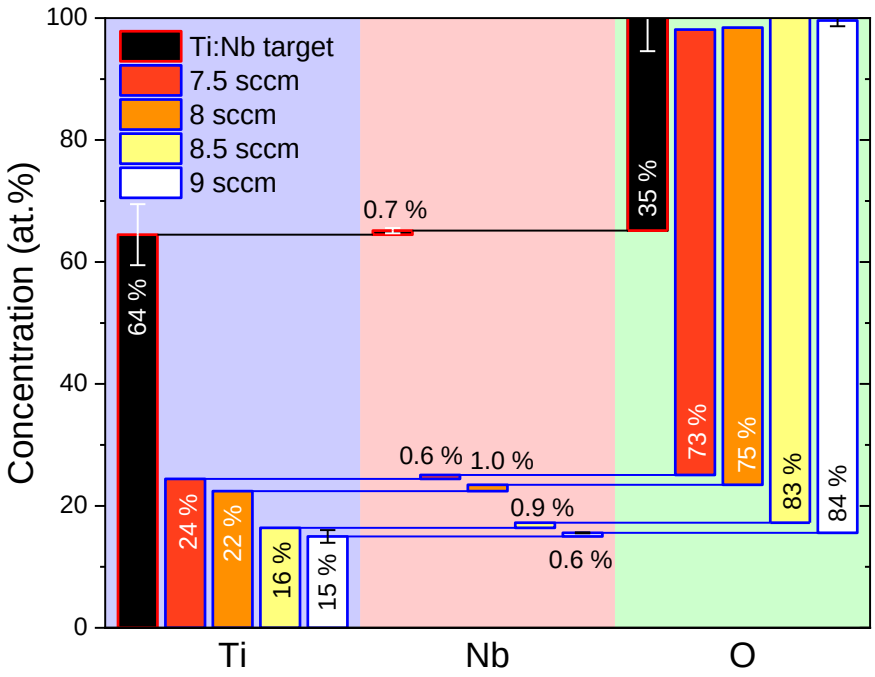

Figure A 1. EDX analysis of the Ti, Nb and O atomic concentration in TiO_2:Nb thin films, deposited with 7.5 sccm, 8 sccm, 8.5 sccm and 9 sccm of reactive Oxygen flow, and the used Ti(96)Nb(4) wt.% target (99.9 % of purity, FHR) (*black*).

As expected, the oxygen concentration increases for higher oxygen flows and seems to decrease the Nb content. The composition of the deposited thin films differs considerably from that of the Ti:Nb target, which measured lower Nb content (0.7 at.%) than expected (1.2 at.%) but is still within experimental error.

Figure A 2 presents EDX measurements on Ti:Nb (without reactive Oxygen during sputtering) and TiO_2:Nb thin films (with 7 sccm of O_2), deposited for 5 min with and without the use of substrate heating during sputtering detailed in **Chapter 5**.

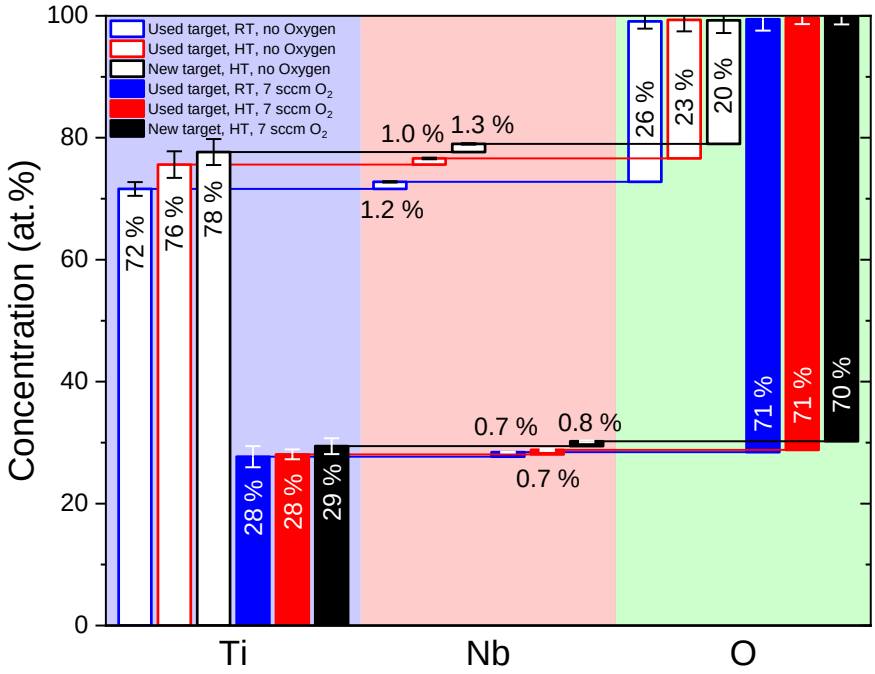

Figure A 2. EDX analysis of the Ti, Nb and O atomic concentration in Ti:Nb (no Oxygen, *lined columns*) and TiO_2:Nb (7 sccm of reactive Oxygen flow, *full columns*) thin films, deposited without substrate heating *(RT, blue)* and with substrate heating *(HT, red)* and using a new (previously unused) target *(HT, black)*.

The use of 7 sccm of O_2 during sputtering increases the Oxygen content present in the thin film, with it being slightly decreased when using substrate heating and the presence of Oxygen decreases the Nb content. Substrate heating has a clear influence in the Nb content present in the TiO_2:Nb thin films, as does the presence of oxygen inside the chamber during sputtering. With no added oxygen, the Nb content is higher when no substrate heating was used, but there is no clear distinction with 7 sccm of O_2. Depositions with substrate heating showed higher content of Ti, with more substantial differences in non-reactive mode. The new target deposited thin films with higher Ti and Nb atomic concentrations in both reactive and non-reactive cases.

EDX was also used to study the homogeneity of Nb incorporation during reactive sputtering on Al foil mounted to a circular 5 cm radius substrate holder (**Figure A 3**). The substrate was analysed in 5 distinct zones, with 1 to 4 along the edge and 5 in the centre of the substrate. Zone 1 is closest to the vacuum chamber wall and zone 3 is located closer to the centre.

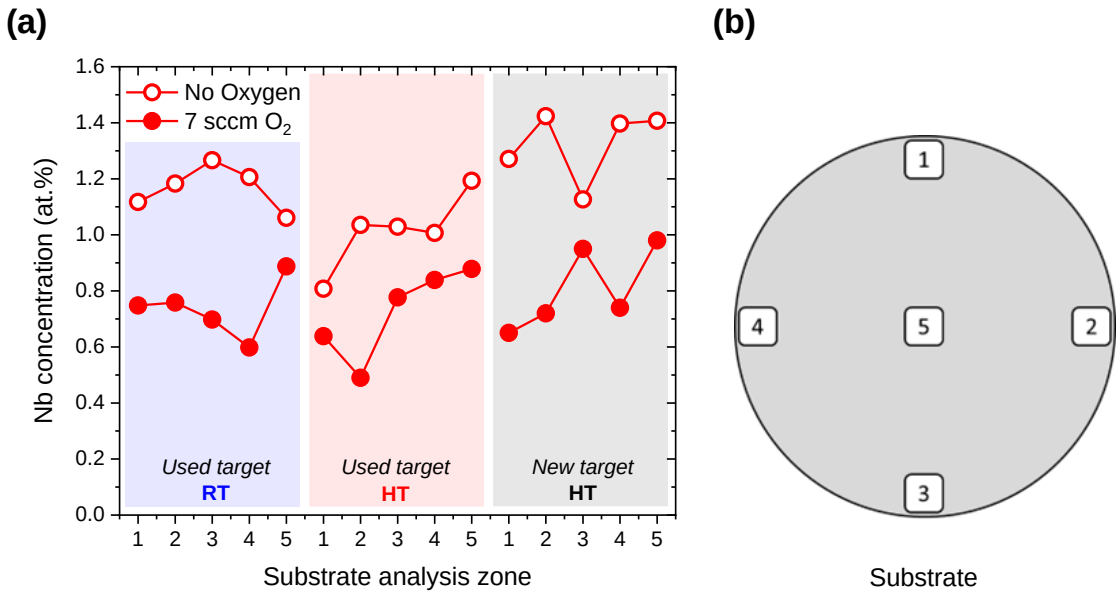

Figure A 3. EDX analysis of the Nb atomic concentration in Ti:Nb (no Oxygen, *open circles*) and TiO_2:Nb (7 sccm of reactive Oxygen flow, *closed circles*) thin films deposited on Al foil without substrate heating *(RT, blue)* and with substrate heating *(HT, red)* and with a new target *(HT, black)* **(a)**, carried out in 5 different substrate zones **(b)**.

When analysing the 5 substrate zones deposited using the used target and with 7 sccm of O_2, the Nb content is the highest in the centre (zone 5) of the substrate. While the same is seen when the chamber is heated with or without oxygen, it is lowest in the case where no heating was used.

With the new target with 7 sccm of O_2, the central zone (zone 5) and the region of the substrate farthest away from the vacuum chamber wall observed the higher atomic concentration of Nb. The same is not seen when no oxygen is used during deposition, where a higher Nb content was observed at the central zone (zone 5) and the three adjacent sides (zones 2, 3 and 4) of the substrate closest to the chamber wall.

It is clear that the positioning of the substrate and its distance to the chamber wall influences the composition, but because of the observed variations no clear relation can be established.

APPENDIX B – XRR ANALYSIS

XRR experiments were performed to determine the film thickness, roughness and density of TiO_2 (undoped) and TiO_2:Nb thin films, with varying deposition times and oxygen flow rates, detailed in **Chapter 4**. Samples deposited for 10 sec, 30 sec, 1 min, 2 min and 3 min and with 6, 7 and 7.5 sccm were measured by XRR, however, not all fits were successful. **Figure B 1** show the XRR experimental results and respective fits for a TiO_2 thin film and a TiO_2:Nb thin film, both deposited for 2 min with reactive oxygen flow rates of 6 sccm. The XRR results for the all the successfully measured samples are presented in **Table B 1**.

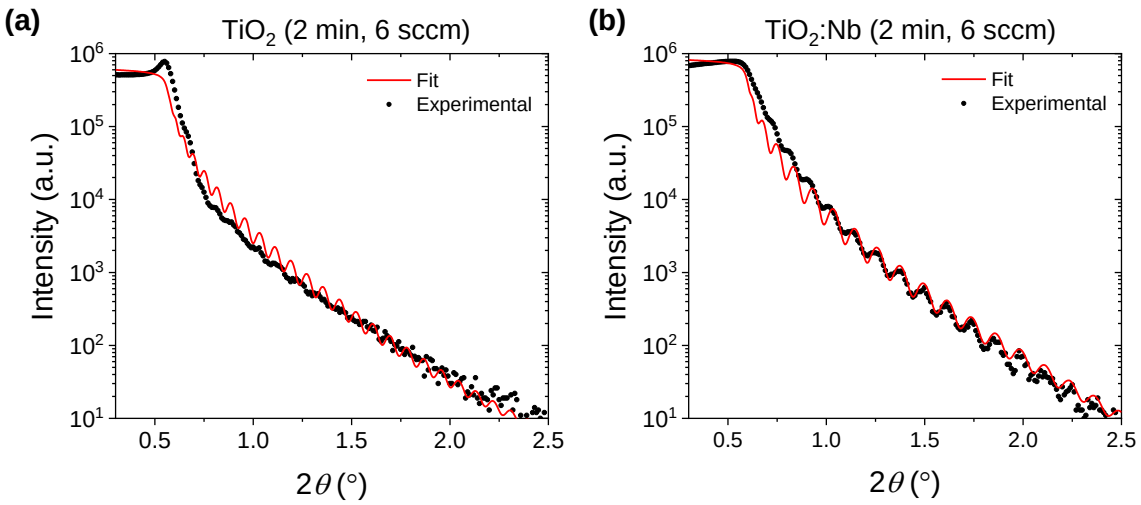

Figure B 1. XRR measurement results and fits of a TiO_2 **(a)** and TiO_2:Nb **(b)** thin film, deposited for 2 min with a reactive oxygen flow of 6 sccm.

Table B 1. Thickness (d), roughness and density (D), obtained by XRR, and average transmittance in the (400 to 700) nm range, obtained by UV-vis, for as-deposited TiO_2 and TiO_2:Nb thin films with varying deposition times and reactive oxygen flows.

Type	t_{dep}	O_2 flow (sccm)	d (nm)	Roughness (nm)	D (g·cm^3)	$\overline{T}_{vis}$ (%)
TiO_2	2 min	6	97	1.3	3.9	75
TiO_2:Nb	30 sec	6	14	0.7	3.5	93
	1 min	6	28	1.2	3.2	82
	2 min	6	68	1.2	4.4	73
	30 sec	7	8	0.8	4.2	96
	3 min	7	83	1.0	4.2	65
	1 min	7.5	25	0.8	4.2	83
	2 min	7.5	57	1.0	4.3	72

APPENDIX C – XPS SPECTRA AND FITS

XPS experiments were performed on TiO_2 (undoped) and TiO_2:Nb thin films to determine the chemical bonding state and film composition detailed in **Chapter 4**.

Figure C 1, **Figure C 2** and **Figure C 3** show the XPS spectra and respective fits for the Ti 2p and Nb 3d core levels for TiO_2:Nb thin films deposited with reactive oxygen flow rates of 7 sccm (measured as-deposited), 7.5 sccm (measured as-deposited and after annealing) and 9 sccm (measured as-deposited) and an undoped TiO_2 thin film deposited with a reactive oxygen flow rate of 7.5 sccm (measured as-deposited).

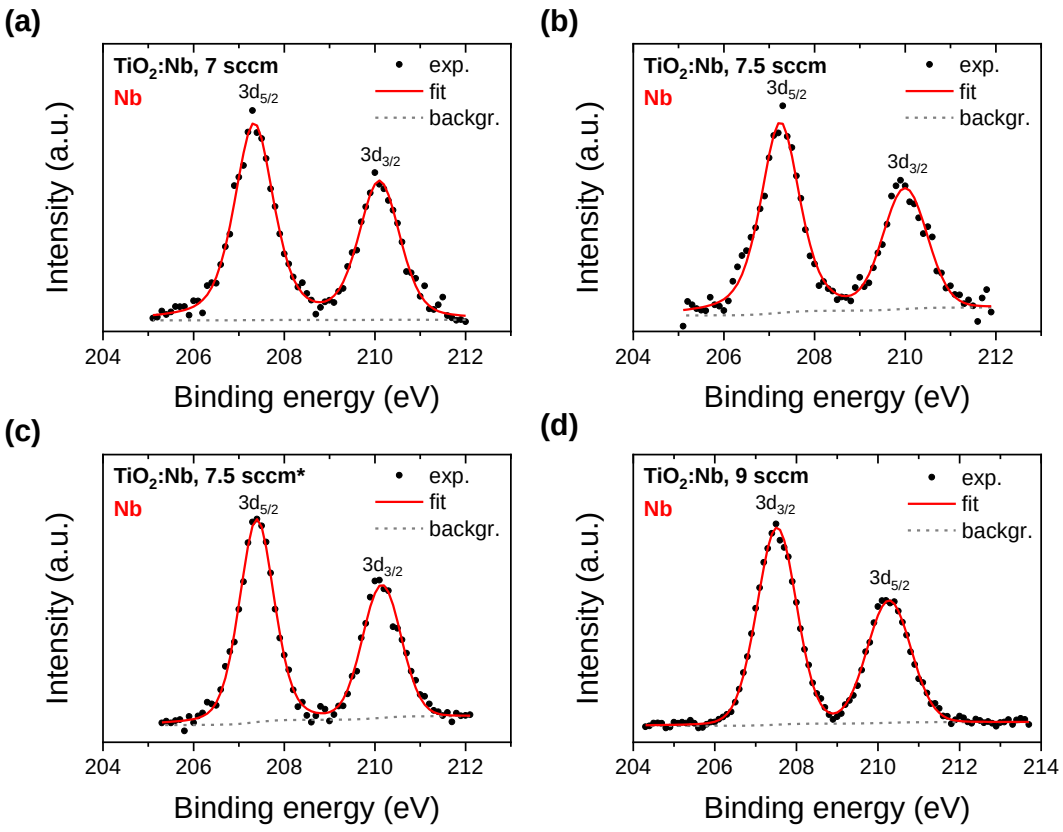

Figure C 1. XPS spectra and respective fits for the Nb 3d core lines for as-deposited TiO_2:Nb thin film with a reactive oxygen flow rate of 7 sccm **(a)**, as-deposited TiO_2:Nb with 7.5 sccm **(b)**, TiO_2:Nb with 7.5 sccm after annealing (*) **(c)** and as-deposited TiO_2:Nb with 9 sccm **(d)**.

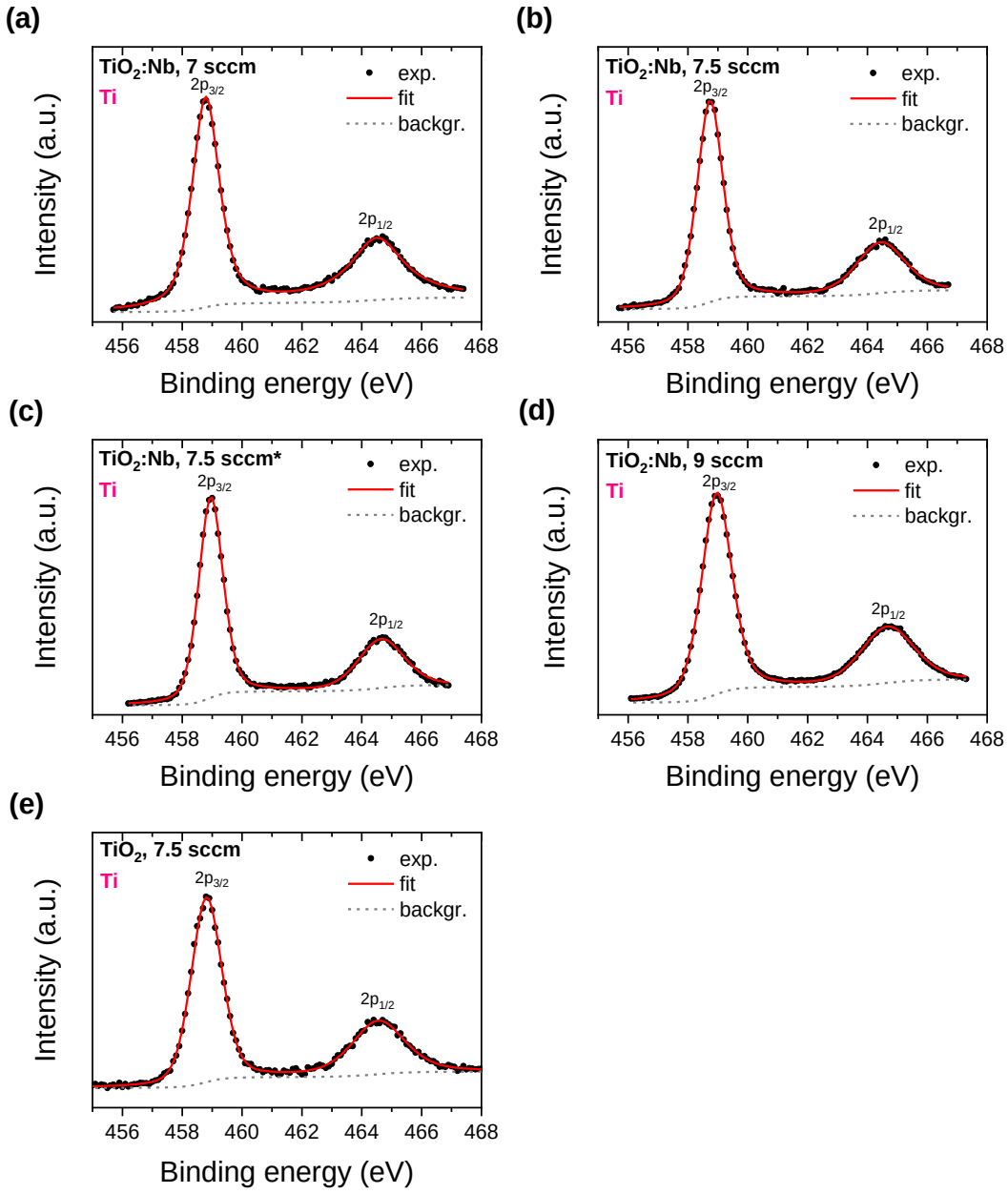

Figure C 2. XPS spectra and respective fits for the Ti 2p core lines for as-deposited TiO_2:Nb thin film with a reactive oxygen flow rate of 7 sccm **(a)**, as-deposited TiO_2:Nb with 7.5 sccm **(b)**, TiO_2:Nb with 7.5 sccm after annealing (*) **(c)**, as-deposited TiO_2:Nb with 9 sccm **(d)** and as-deposited undoped TiO_2 with a reactive oxygen flow rate of 7.5 sccm **(e)**.

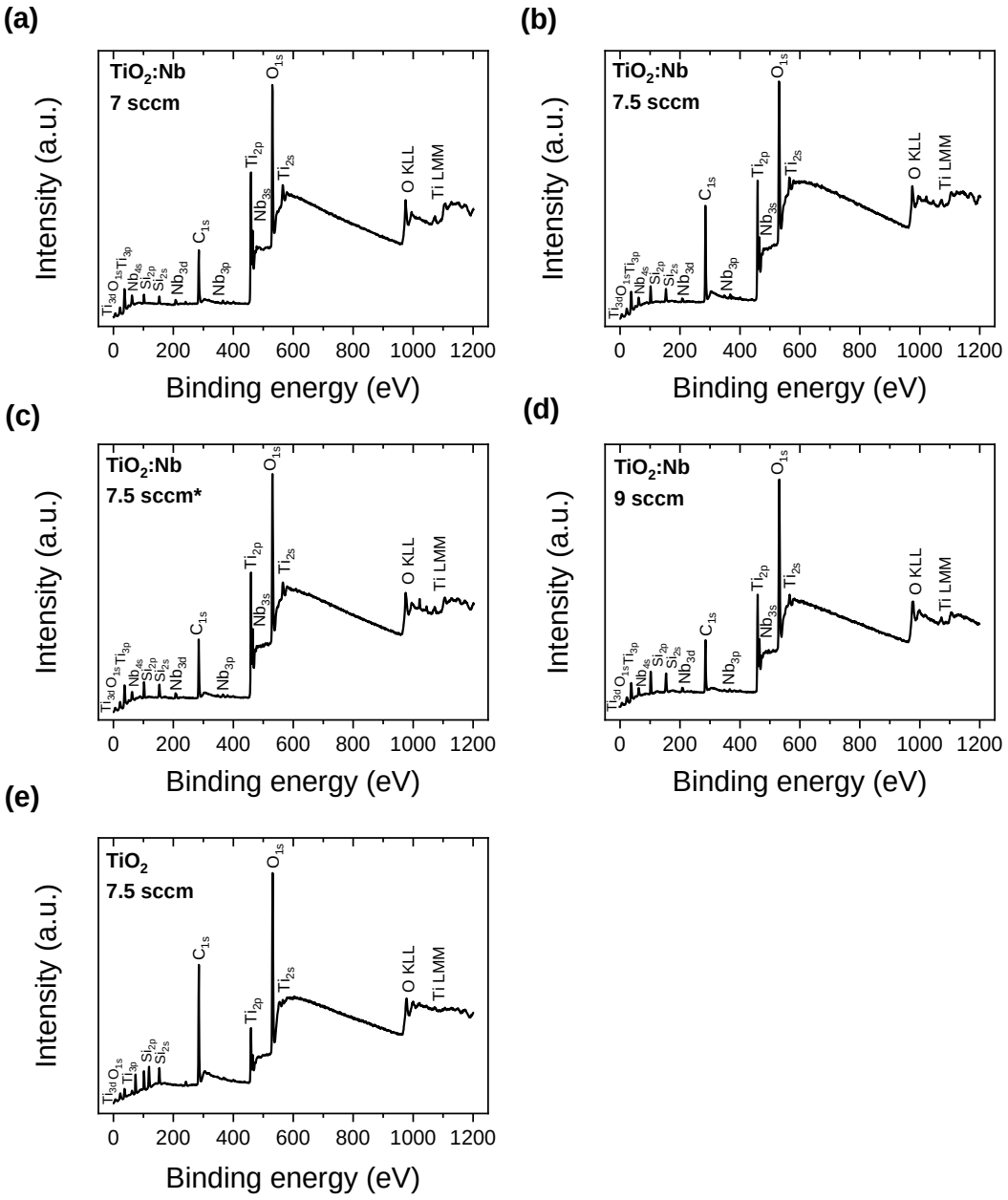

Figure C 3. Survey XPS spectra for as-deposited TiO_2:Nb thin film deposited with a reactive oxygen flow rate of 7 sccm **(a)**, as-deposited TiO_2:Nb with 7.5 sccm **(b)**, TiO_2:Nb with 7.5 sccm after annealing (*) **(c)**, as-deposited TiO_2:Nb with 9 sccm **(d)** and as-deposited undoped TiO_2 with a reactive oxygen flow rate of 7.5 sccm **(e)**.

APPENDIX D – TRANSMITTANCE AND REFLECTANCE SPECTRA

The transmittance and reflectance of TiO_2:Nb thin films was measured to evaluate the optical properties, using the glass substrate and the calibration mirrors as baseline, respectively.

Figure D 1 presents the optical transmittance and specular reflectance spectra for TiO_2:Nb thin films deposited for 5 min with varying reactive oxygen flow rates (measured as-deposited), discussed in **Chapter 4**.

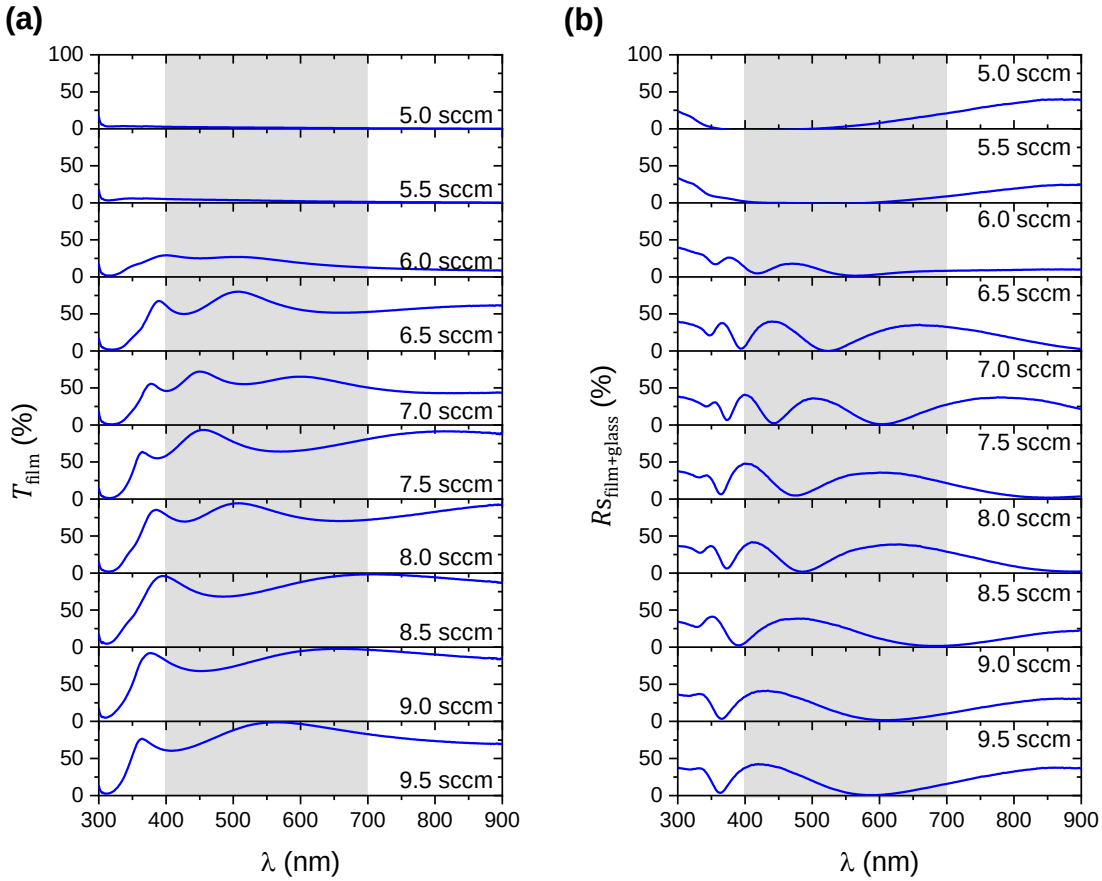

Figure D 1. Transmittance **(a)** and specular reflectance spectra **(b)** for as-deposited TiO_2:Nb thin films deposited for 5 min with varying oxygen flow rates.

Figure D 2 presents the optical transmittance and specular reflectance spectra for TiO_2:Nb thin films deposited with 7.5 sccm of reactive oxygen flow rates for 5 min, with (HT) and without (RT) substrate heating and with increasing deposition temperate (A thought E), measured as-deposited (Ad) and after annealing at 500 °C (TT), discussed in **Chapter 5**.

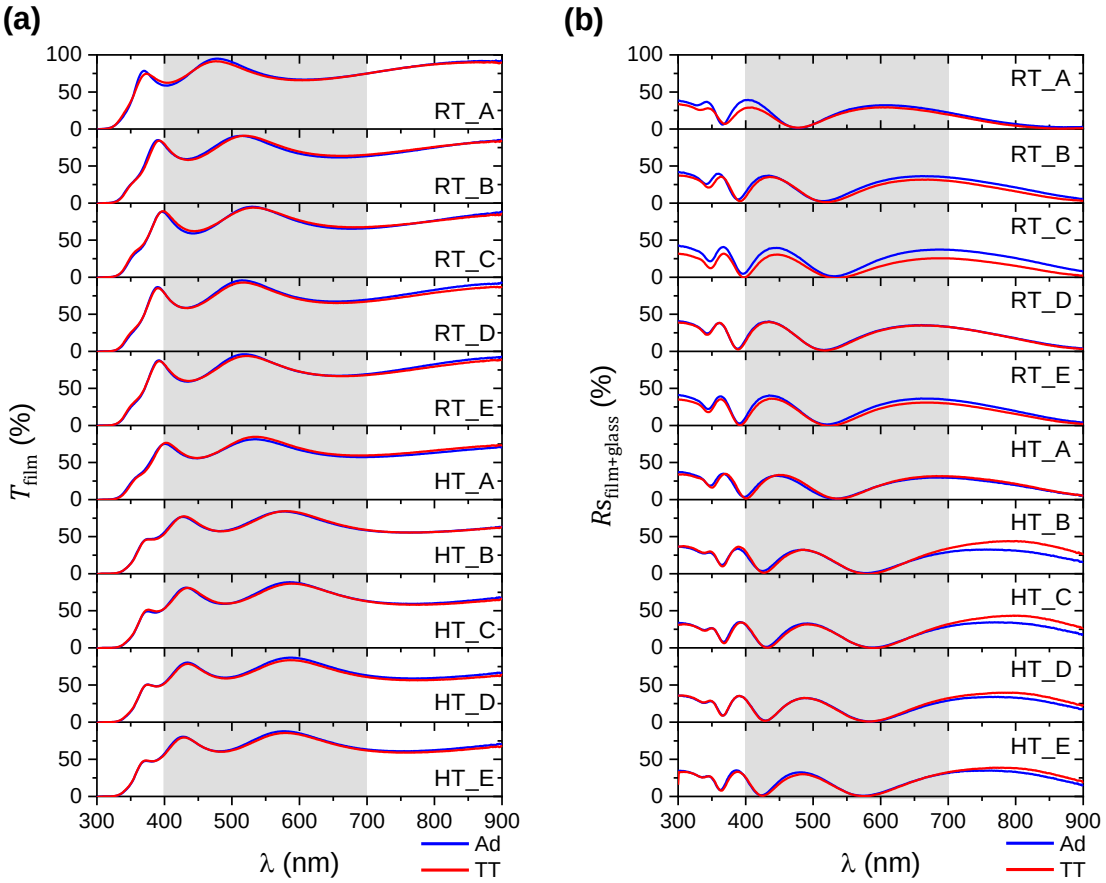

Figure D 2. Transmittance **(a)** and specular reflectance spectra **(b)** for TiO_2:Nb thin films deposited for 5 min with 7.5 sccm of oxygen flow rate measured as-deposited *(Ad, blue)* and after annealing *(TT, red)*.

APPENDIX E – APT ANALYSIS

APT analysis was performed on Ti:Nb (without reactive oxygen during sputtering) and TiO_2:Nb thin films (with 7 sccm of O_2), with and without the post-deposition annealing at 500° C, detailed in **Chapter 6**.

Figure E 1 illustrates the tip number and positions relative to the Si coupon used for APT analysis.

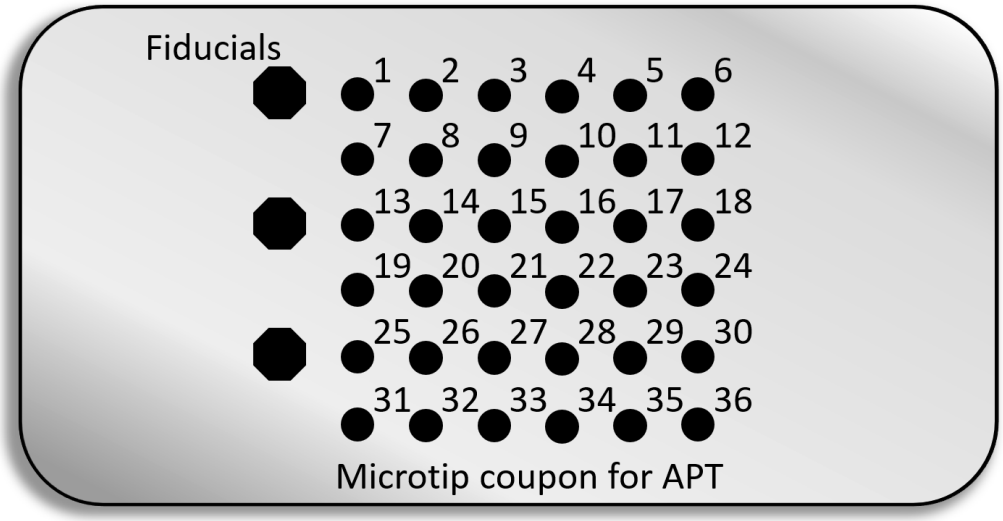

Figure E 1. APT microtip array. The fiducials are used as references for sample positioning during measurements.

Full data concerning all measured tips is displayed in **Table E 1**.

Table E 1. APT tip measurements for sample A, B and C measured in a local electrode atom probe (LEAP 4000X HR) in UV-laser mode with variable laser energy (E_{laser}), pulse frequency (f), temperature (T_{A} and T_{B}) and detection rate (DR).

Sample	APT Measurement Conditions					
	Tip	**Data**	E_{laser} **(pJ)**	f_{pulse} **(kHz)**	$T_{\mathrm{A}} - T_{\mathrm{B}}$ **(K)**	DR **(%)**
A	M2	16667	30	100	40 – 44.7	0.3
	M7	16668	30	100	40 – 44.7	0.3
	M9	16669	30	100	40 – 44.7	0.3
	M4*	**16758**	**30**	**100**	**40 – 44.7**	**0.3**
	M5*	16759	30	100	40 – 44.7	0.5
	M10*	**16760**	**30**	**100 – 200**	**40 – 44.7**	**0.3 – 0.5**
	M6*	16761	30	100 – 200	40 – 44.7	0.3 – 0.5
	M11*	**16772**	**30**	**100**	**40 – 44.7**	**0.3**
	M12*	**16762**	**30**	**100 – 200**	**40 – 44.7**	**0.3 – 0.5**
B	M2	16673	30	100	40 – 44.6	0.3
	M4	**16677**	**30**	**100**	**40 – 44.6**	**0.3 – 0.5**
	M6	16678	30	100 – 200	40 – 44.6	0.3
	M11	**16679**	**20**	**100 – 200**	**40 – 44.6**	**0.3**
	M9	**16680**	**10**	**100 – 200**	**40 – 44.6**	**0.3**
	M7	16682	20	100	40 – 44.6	0.4
	M1*	16773	30	100	40 – 44.6	0.3
	M3*	16774	30	100	40 – 44.6	0.3
	M5*	16775	30	100	40 – 44.6	0.3
	M8*	16777	30	100	40 – 44.6	0.3
	M10*	16778	30	100	40 – 44.6	0.3
	M12*	16779	30	100	40 – 44.6	0.3
C	**M25**	**5112**	**30**	**100 – 200**	**50 – 55.7**	**0.3**
	M27	**5113**	**30**	**100 – 200**	**50 – 55.7**	**0.3**
	M32	5114	30	100 – 200	50 – 55.7	0.3
	M34	5115	30	100	50 – 55.7	0.2
	M29	**5116**	**30**	**100**	**50 – 55.7**	**0.3**
	M36	5117	20	100 – 200	50 – 55.7	0.3
	M26*	**15394**	**20**	**100 – 200**	**50 – 55.7**	**0.2**
	M28*	**15395**	**30**	**100**	**50 – 55.7**	**0.3**
	M31*	15398	30	100	50 – 55.7	0.3
	M33*	**15401**	**30**	**100**	**50 – 55.7**	**0.3**
	M35*	15402	30	100	50 – 55.7	0.3

* Second analysis batch

E.1. Sample A

A total of 9 tips were analysed for sample A (**Figure E 2**), M2 (16667), M7 (16668) and M9 (16669) correspond to the first batch and M4* (16758), M5* (16759), M10* (16760), M6* (16761), M11* (16772) and M12* (16762) correspond to the second batch (eroded during FIB preparation).

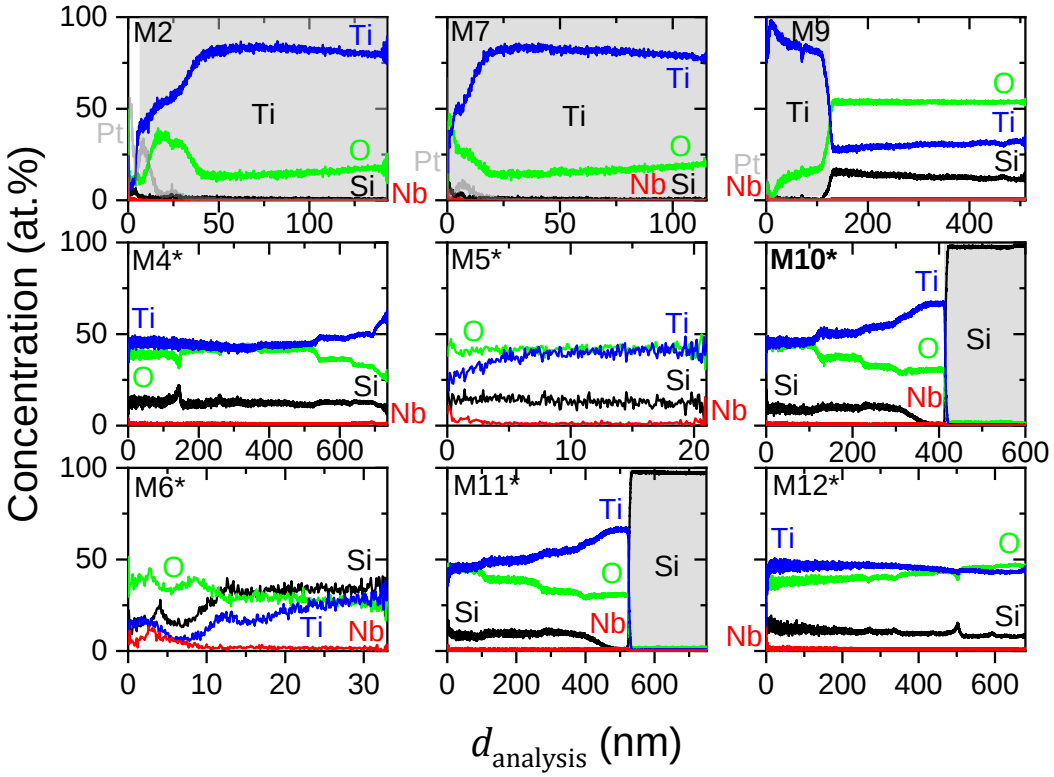

Figure E 2. 1D concentration profiles of all analysed tips in the z-axis (parallel to the film growth) of a Ti:Nb/TiO_2:Nb film (Sample A), obtained by APT.

None of the first set of measurements were able to reach the interface to the Si substrate and still had Pt at the top of the tip from the FIB sample preparation. The measurement on tip M9 was able to reach the TiO_2:Nb layer just below the topmost Ti layer but the tip eventually fractured. This was most probably due to the high electrical resistivity difference between the topmost Ti layer and the following TiO_2:Nb layer (11 sccm of Oxygen flow). Most measurements were very short and could only analyse 1 to 3 layers, with the exceptions being M4*, M10* and M11*, presenting with visible layers of different compositions. The ionic maps are presented for tips M4* (**Figure E 3**), M10* (**Figure E 4**), and M11* (**Figure E 5**).

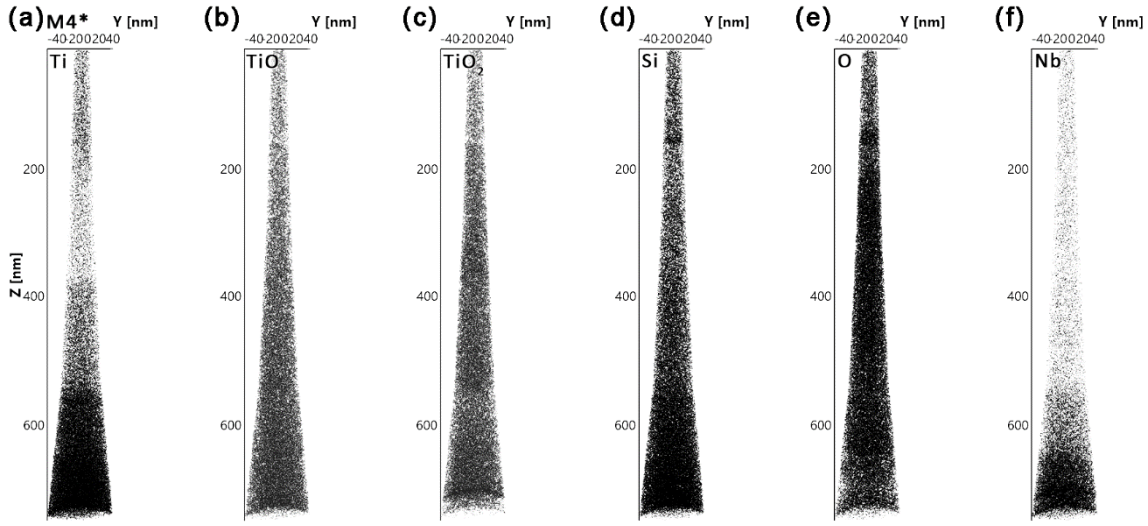

Figure E 3. APT profile viewed ionic maps of Ti **(a)**, TiO **(b)**, TiO_2 **(c)**, Si **(d)**, O **(e)** and Nb **(f)** signals of the 3D reconstruction of tip M4* (16758) of a Ti:Nb/TiO_2:Nb film (Sample A).

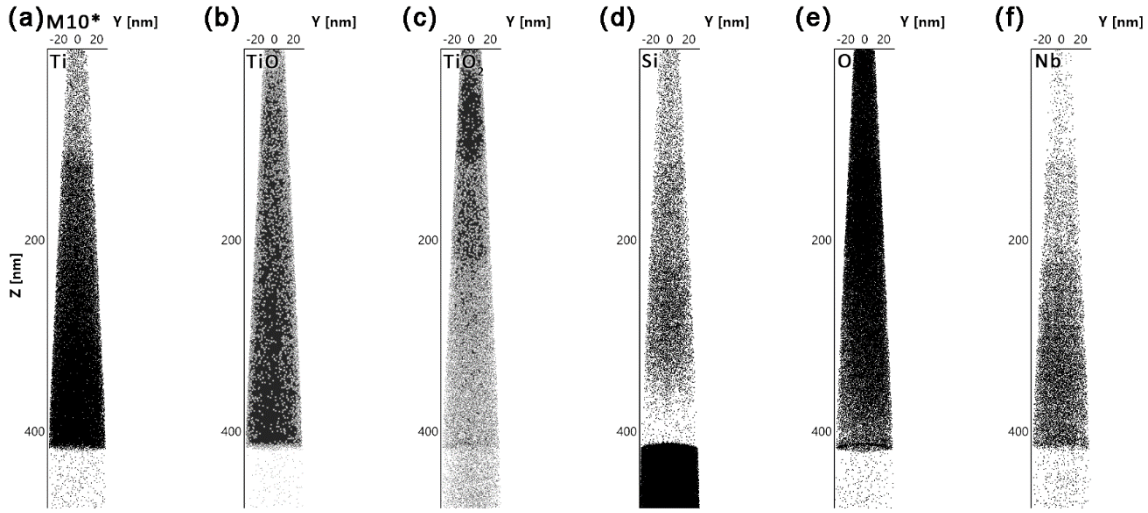

Figure E 4. APT profile viewed ionic maps of Ti **(a)**, TiO **(b)**, TiO_2 **(c)**, Si **(d)**, O **(e)** and Nb **(f)** signals of the 3D reconstruction of tip M10* (16760) of a Ti:Nb/TiO_2:Nb film (Sample A).

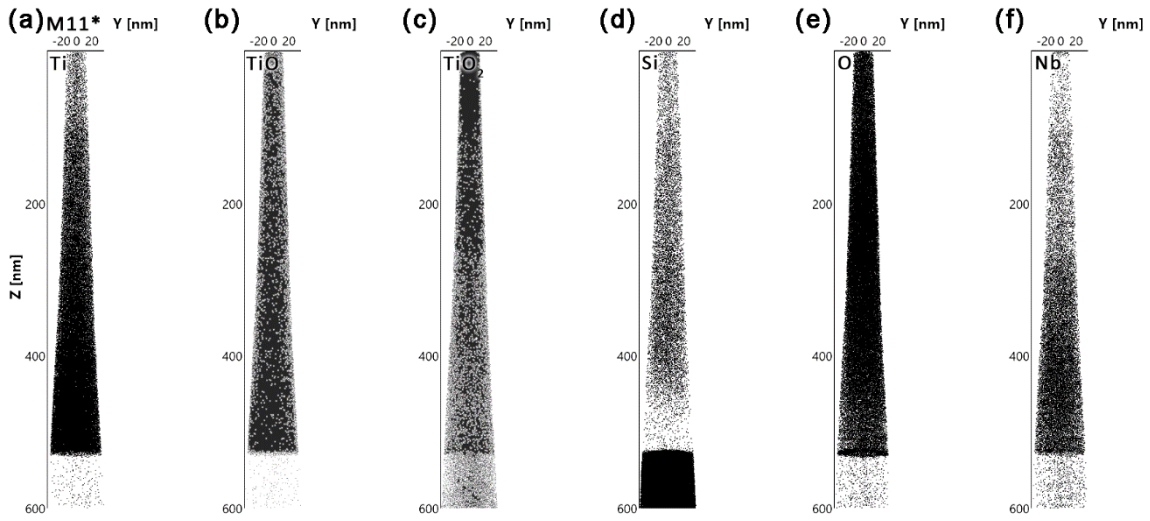

Figure E 5. APT profile viewed ionic maps of Ti **(a)**, TiO **(b)**, TiO_2 **(c)**, Si **(d)**, O **(e)** and Nb **(f)** signals of the 3D reconstruction of tip M11* (16772) of a Ti:Nb/TiO_2:Nb film (Sample A).

Figure E 6 shows the side-viewed rendered volumes of decomposed atomic Ti, Si, O and Nb concentration, for tip M10* of sample A.

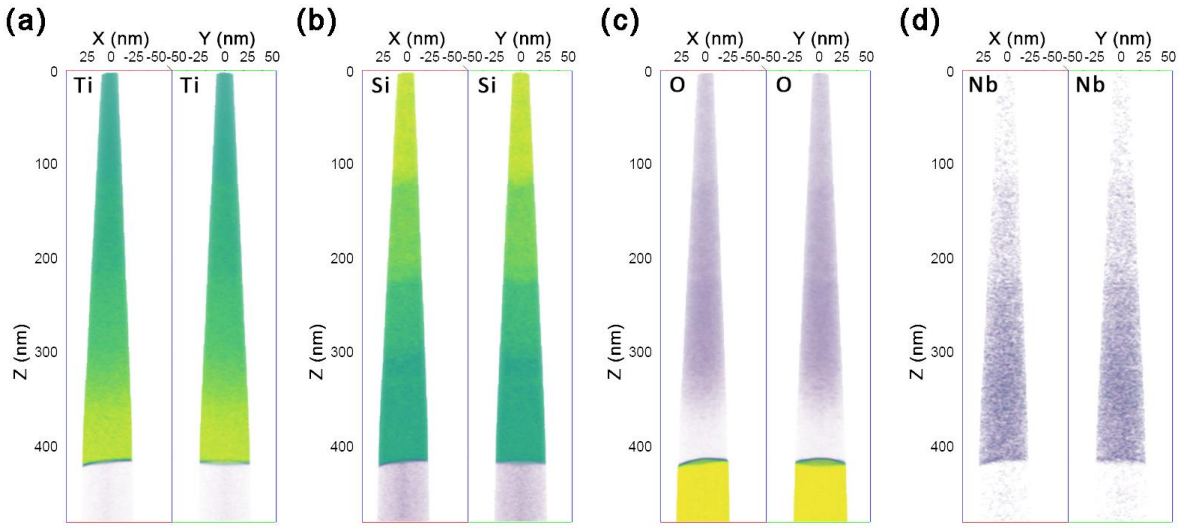

Figure E 6. Volume rendered side-views of decomposed atomic Ti concentration **(a)**, O concentration **(b)**, Ti density **(c)** and O density **(d)** for tip M10* (16760) of a Ti:Nb/TiO_2:Nb film (Sample A). Sample count threshold at 0 %, with confidence sigma of 0. Opacity is at half value and a darker color value relates to a higher atomic concentration/density value.

E.2. Sample B

A total of 11 tips were analysed for sample B (**Figure E 7**), M2 (16673), M4 (16677), M6 (16678), M11 (16679), M9 (16680) and M7 (16682) correspond to the first batch and M1* (16773), M3* (16774), M5* (16775), M8* (16777), M10* (16778) and M12* (16779) correspond to the second batch (eroded during FIB preparation).

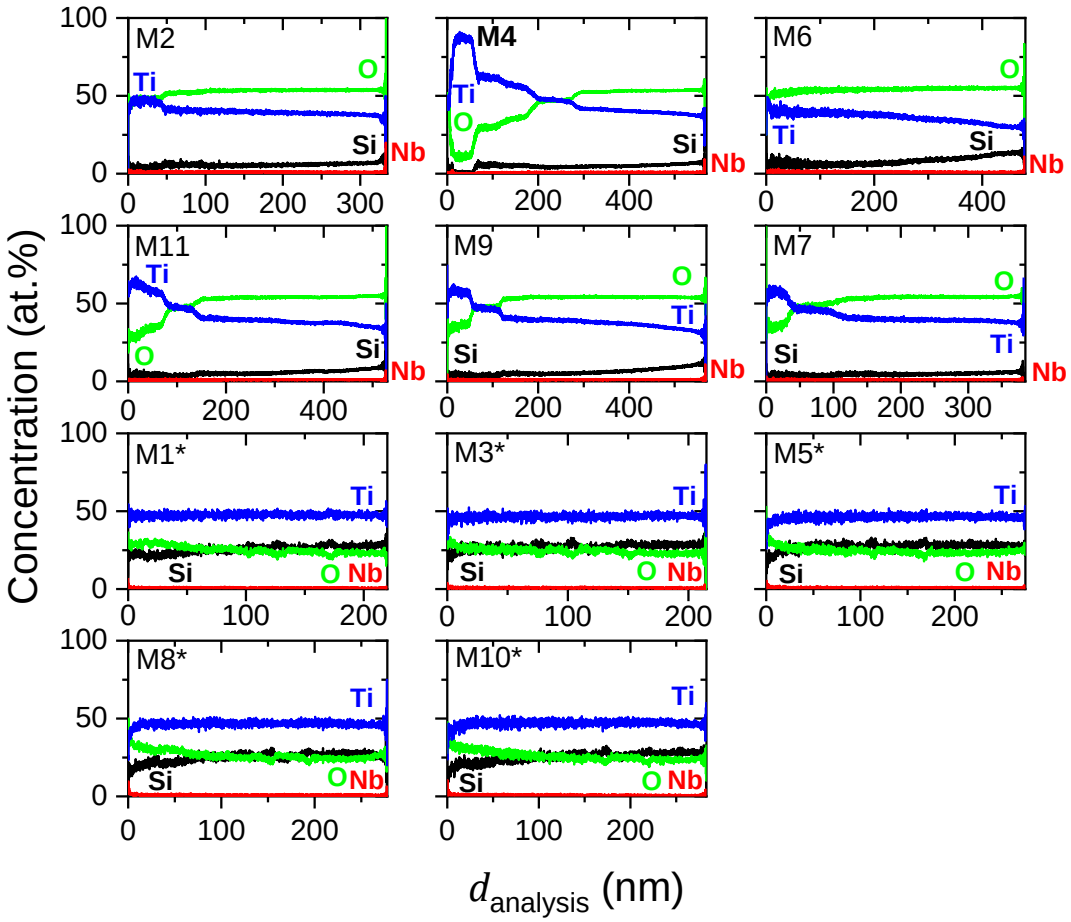

Figure E 7. 1D concentration profile of all analysed tips in the z-axis (parallel to the film growth) of a Ti:Nb/TiO_2:Nb film (Sample B), obtained by APT.

The first set of measured tips yielded better results due to the higher electrical conductivity of the analysed layers, with tips M4, M11 and M9 displaying layers. The ionic maps are presented for tips M4 (**Figure E 8**), M11 (**Figure E 9**), and M9 (**Figure E 10**).

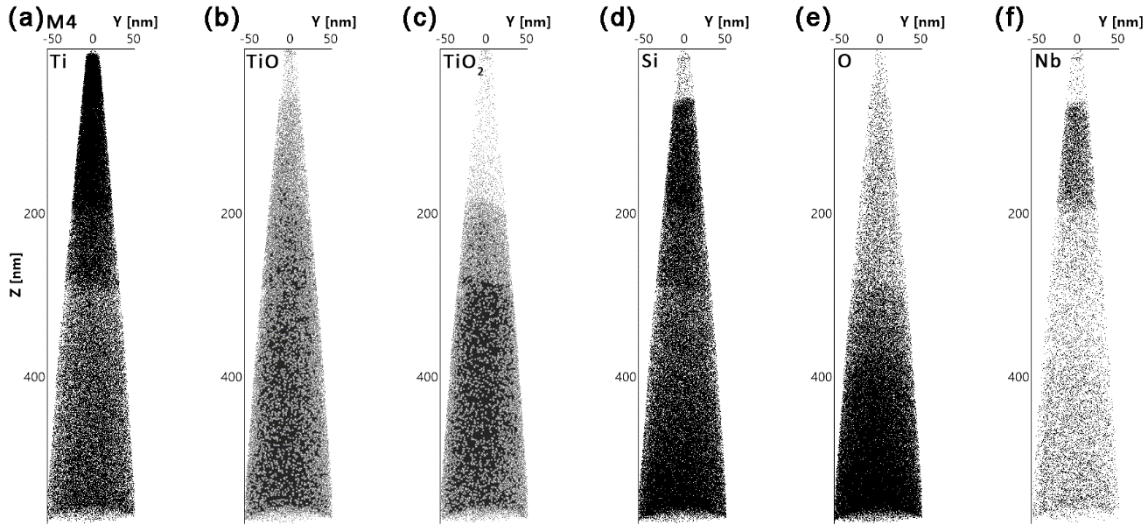

Figure E 8. APT profile viewed ionic maps of Ti **(a)**, TiO **(b)**, TiO_2 **(c)**, Si **(d)**, O **(e)** and Nb **(f)** signals of the 3D reconstruction of tip M4 (16677) of a Ti:Nb/TiO_2:Nb film (Sample B).

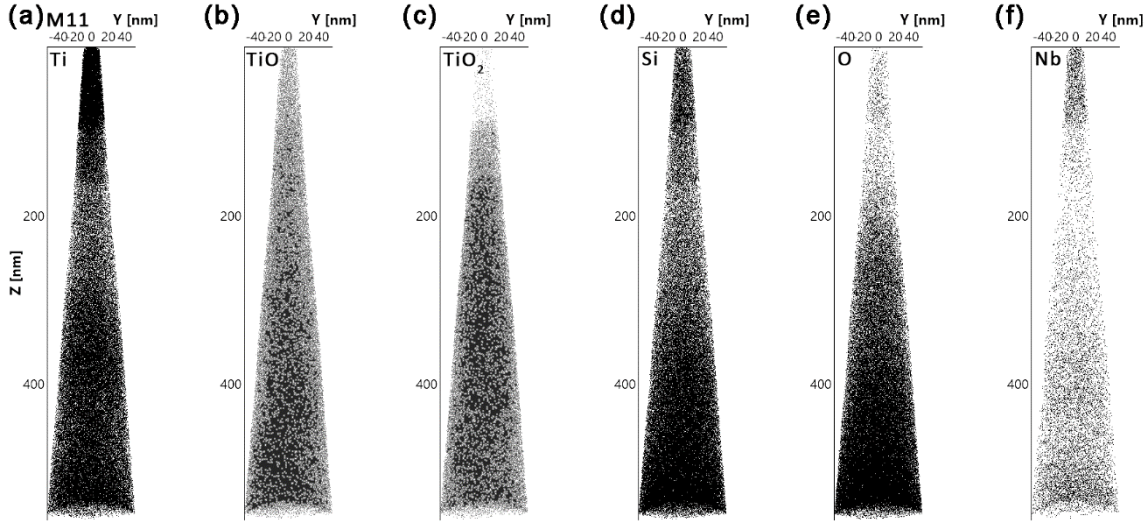

Figure E 9. APT profile viewed ionic maps of Ti **(a)**, TiO **(b)**, TiO_2 **(c)**, Si **(d)**, O **(e)** and Nb **(f)** signals of the 3D reconstruction of tip M11 (16679) of a Ti:Nb/TiO_2:Nb film (Sample B).

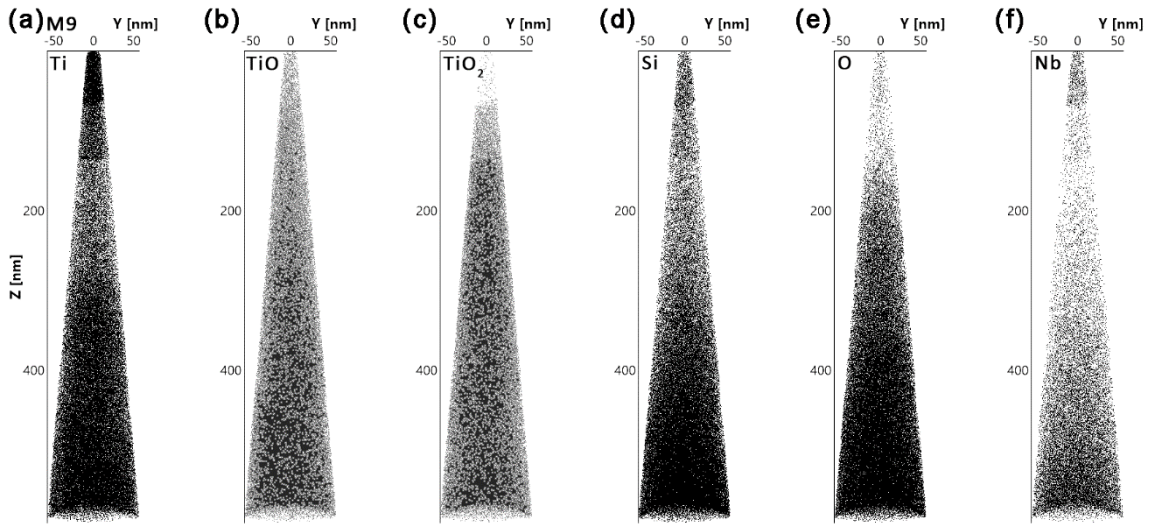

Figure E 10. APT profile viewed ionic maps of Ti **(a)**, TiO **(b)**, TiO_2 **(c)**, Si **(d)**, O **(e)** and Nb **(f)** signals of the 3D reconstruction of tip M9 (16680) of a Ti:Nb/TiO_2:Nb film (Sample B).

Figure E 11 shows the side-viewed rendered volumes of decomposed atomic Ti and O concentration and density, for tip M9 of sample B.

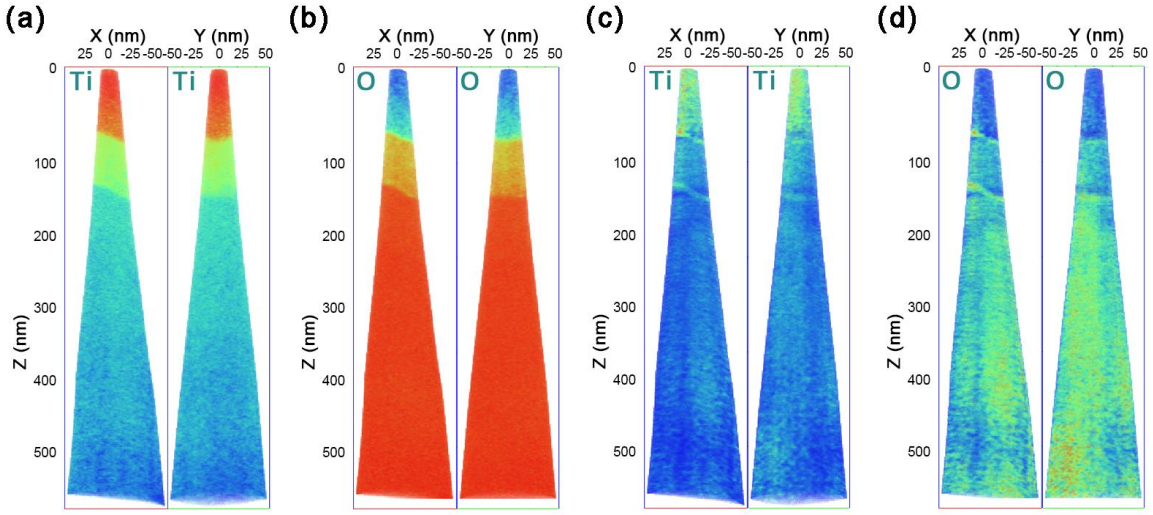

Figure E 11. APT volume rendered side-views of decomposed atomic Ti concentration **(a)**, O concentration **(b)**, Ti density **(c)** and O density **(d)** for tip M9 (16680) of a Ti:Nb/TiO_2:Nb film (Sample B). Sample count threshold at 0 %, with confidence sigma of 0. Opacity is at half value and a darker color value relates to a higher atomic concentration/density value.

E.3. Sample C

A total of 11 tips were analysed for sample C, M25, M27, M32, M34, M29 and M36 correspond to the first batch (measured as-deposited) and M26*, M28*, M31*, M33* and M35* correspond to the second

batch (measured after annealing at 500 °C in vacuum). Because all tips contained Ga at the top from the FIB preparation, a reconstruction region of interest (ROI) was created excluding the beginning of the measurement.

Tips M32 (5114), M31* (15398) and M35* (15402) resulted in bad measurements due to a damaged local electrode and were not considered for reconstruction. Tips M34 (5115) and M36 (5117) were not included in the results as they present Ga contamination on considerable regions of the samples, possibly due to Ga implantation during FIB preparation.

Tips M25 (5112), M27 (5113), M29 (5116), M26* (15394), M28* (15395) and M33* (15401) yielded good measurement runs and presented useful results. The bulk concentration of decomposed atomic Ti, Nb and O over the remaining 6 tip measurements can be seen in **Figure E 12**, both for total sample volume **Figure E 12(a)** and measured over a (10 × 10) nm cylinder over total sample depth **Figure E 12(b)**. The respective total 1D concentration profiles are presented in **Figure E 13**.

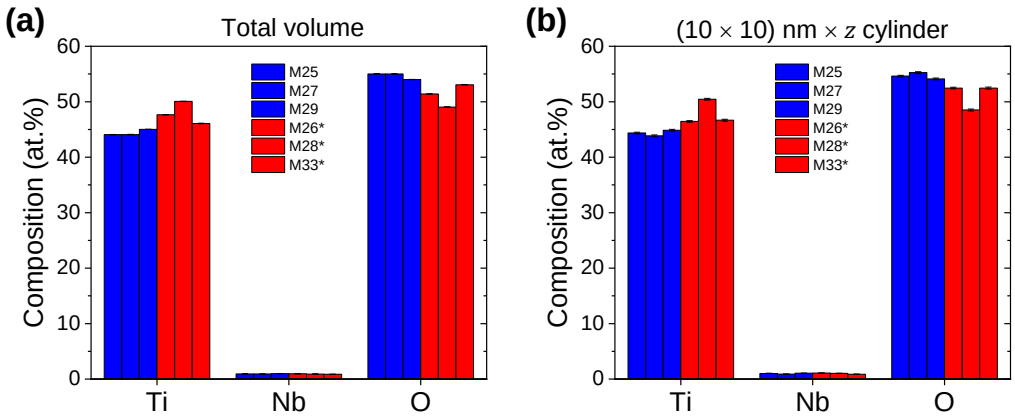

Figure E 12. Atomic concentration of Ti, O and Nb in a TiO_2:Nb thin film (sample C) obtained by APT, over 3 tip measurements as-deposited *(Ad, in blue)* and 3 after annealing at 500 °C *(TT, in red)*.

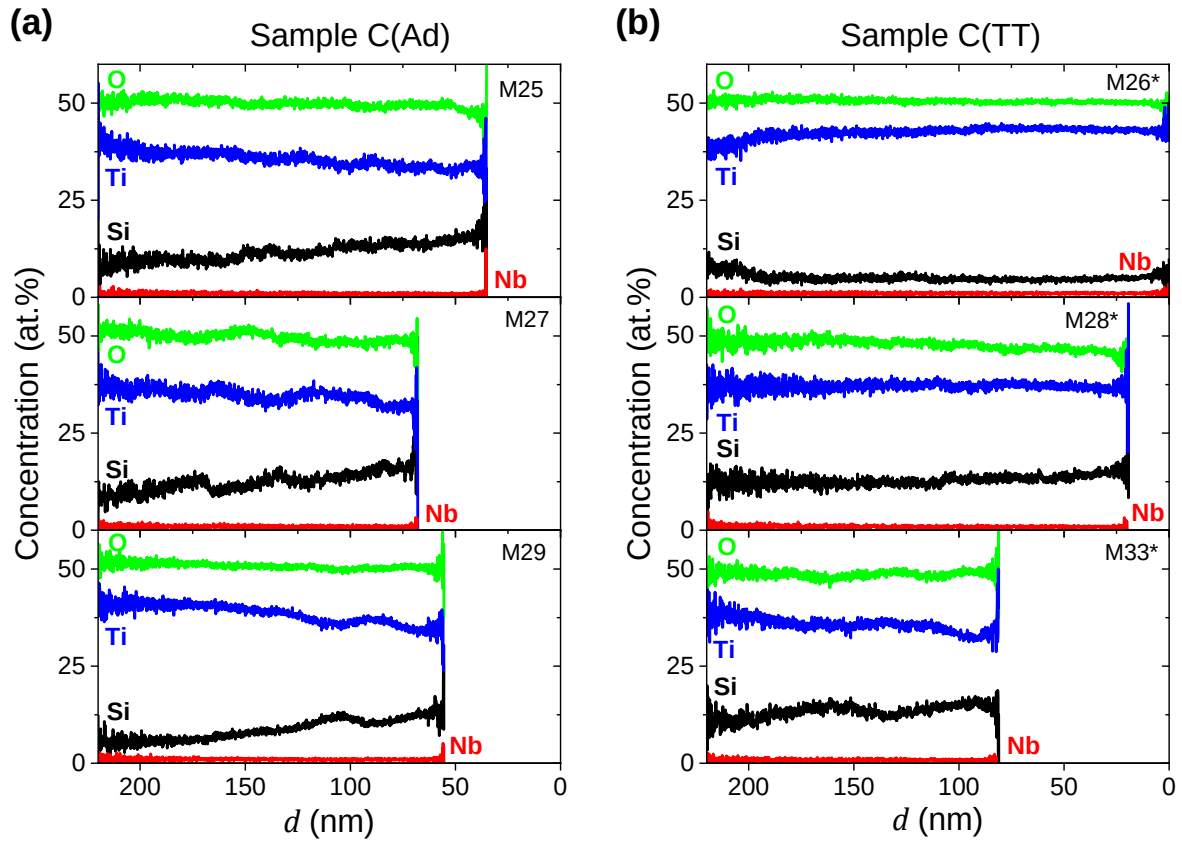

Figure E 13. 1D concentration profile in the z-axis (parallel to the film growth) of Ti, O and Nb in a TiO_2:Nb thin film (sample C) obtained by APT, over 3 tip measurements as-deposited *(Ad)* **(a)** and 3 after annealing at 500 °C *(TT)* **(b)**.

The ionic maps are presented for tips M25 (**Figure E 14**), M27 (**Figure E 15**), M29 (**Figure E 16**) M26* (**Figure E 17**), M28* (**Figure E 18**) and M33* (**Figure E 19**).

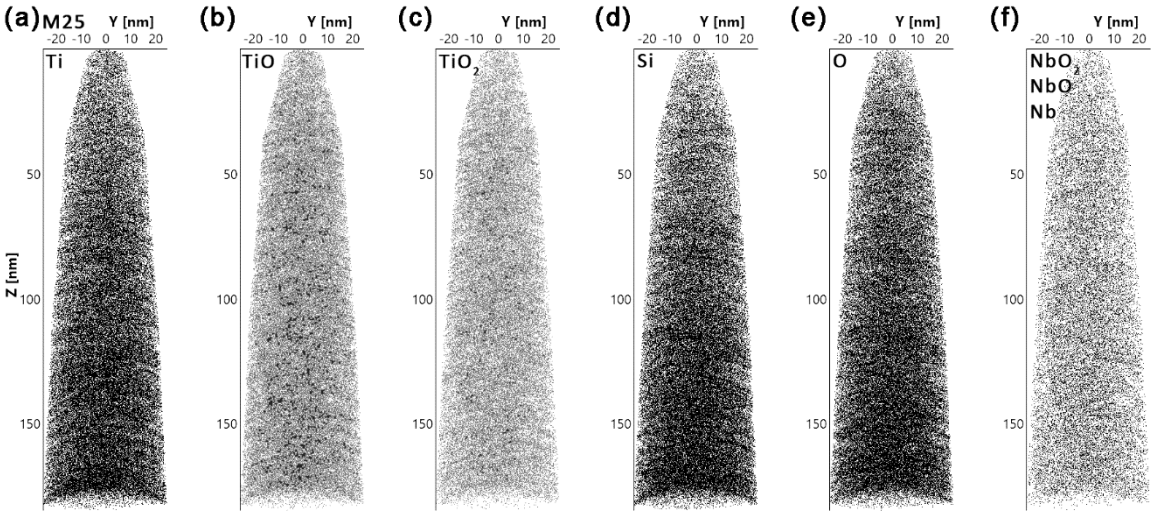

Figure E 14. APT profile viewed ionic maps of Ti **(a)**, TiO **(b)**, TiO_2 **(c)**, Si **(d)**, O **(e)** and a combination of Nb, NbO and NbO_2 **(f)** signals of the 3D reconstruction of tip M25 (5112) of a TiO_2:Nb thin film (Sample C(Ad)).

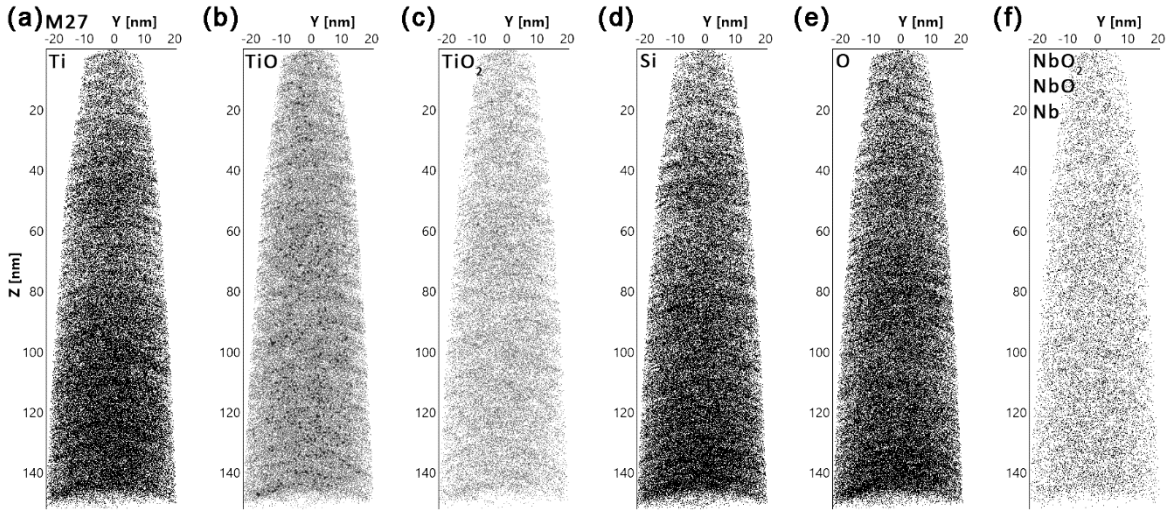

Figure E 15. APT profile viewed ionic maps of Ti **(a)**, TiO **(b)**, TiO_2 **(c)**, Si **(d)**, O **(e)** and a combination of Nb, NbO and NbO_2 **(f)** signals of the 3D reconstruction of tip M27 (5113) of a TiO_2:Nb thin film (Sample C(Ad)).

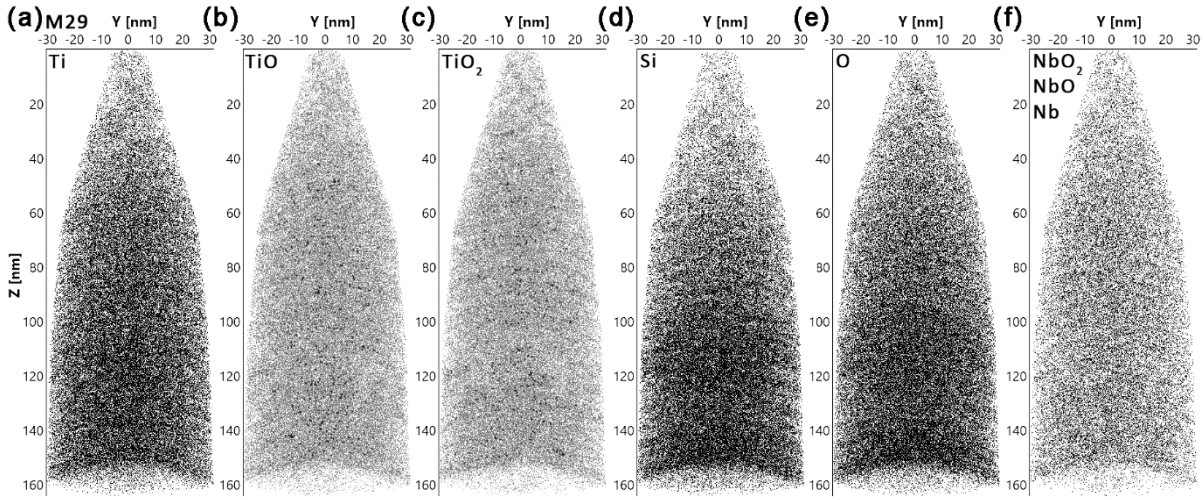

Figure E 16. APT profile viewed ionic maps of Ti **(a)**, TiO **(b)**, TiO_2 **(c)**, Si **(d)**, O **(e)** and a combination of Nb, NbO and NbO_2 **(f)** signals of the 3D reconstruction of tip M29 (5116) of a TiO_2:Nb thin film (Sample C(Ad)).

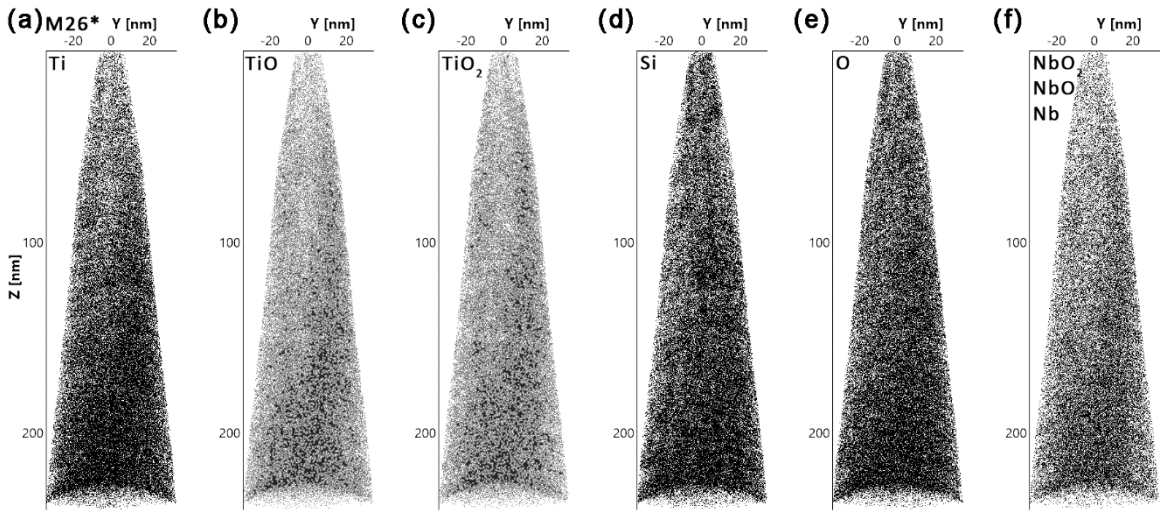

Figure E 17. APT profile viewed ionic maps Ti **(a)**, TiO **(b)**, TiO_2 **(c)**, Si **(d)**, O **(e)** and a combination of Nb, NbO and NbO_2 **(f)** signals of the 3D reconstruction of tip M26* (15394) of a TiO_2:Nb thin film measured after annealing at 500 °C (Sample C(TT)).

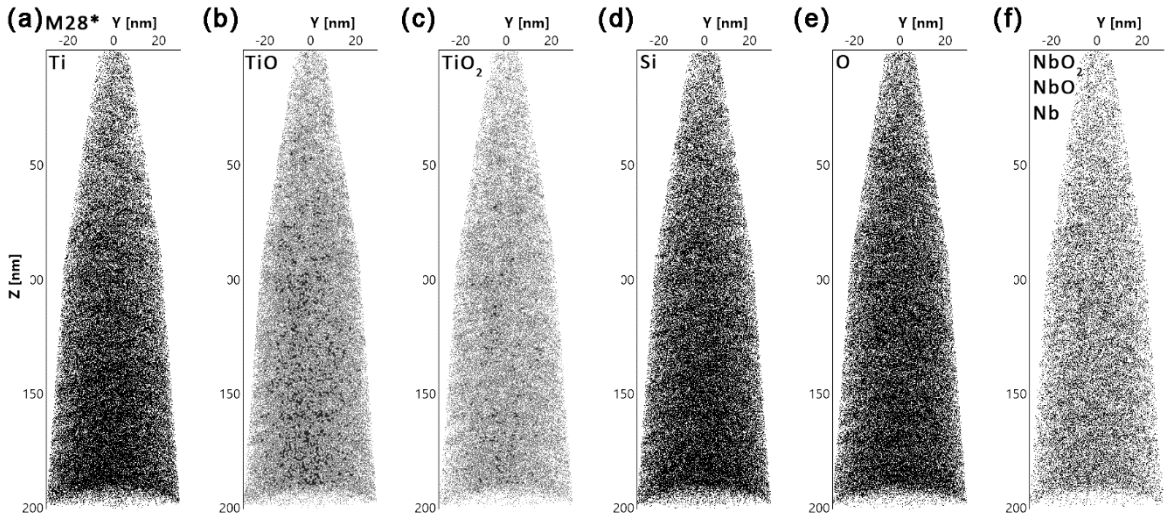

Figure E 18. APT profile viewed ionic maps of Ti **(a)**, TiO **(b)**, TiO_2 **(c)**, Si **(d)**, O **(e)** and a combination of Nb, NbO and NbO_2 **(f)** signals of the 3D reconstruction of tip M28* (15395) of a TiO_2:Nb thin film measured after annealing at 500 °C (Sample C(TT)).

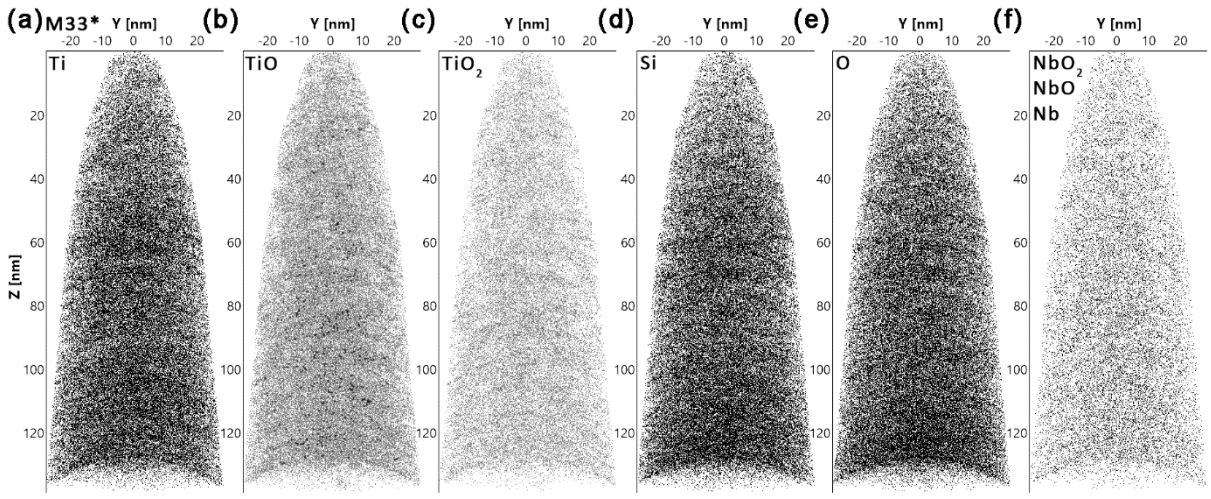

Figure E 19. APT profile viewed ionic maps of Ti **(a)**, TiO **(b)**, TiO_2 **(c)**, Si **(d)**, O **(e)** and a combination of Nb, NbO and NbO_2 **(f)** signals of the 3D reconstruction of tip M33* (153401) of a TiO_2:Nb thin film measured after annealing at 500 °C (Sample C(TT)).

The iso-surfaces of decomposed Ti, Si, O and Nb atomic concentration for tip M25 (measured as-deposited) are presented in **Figure E 20**. A top-viewed slice can be seen in **Figure E 21**.

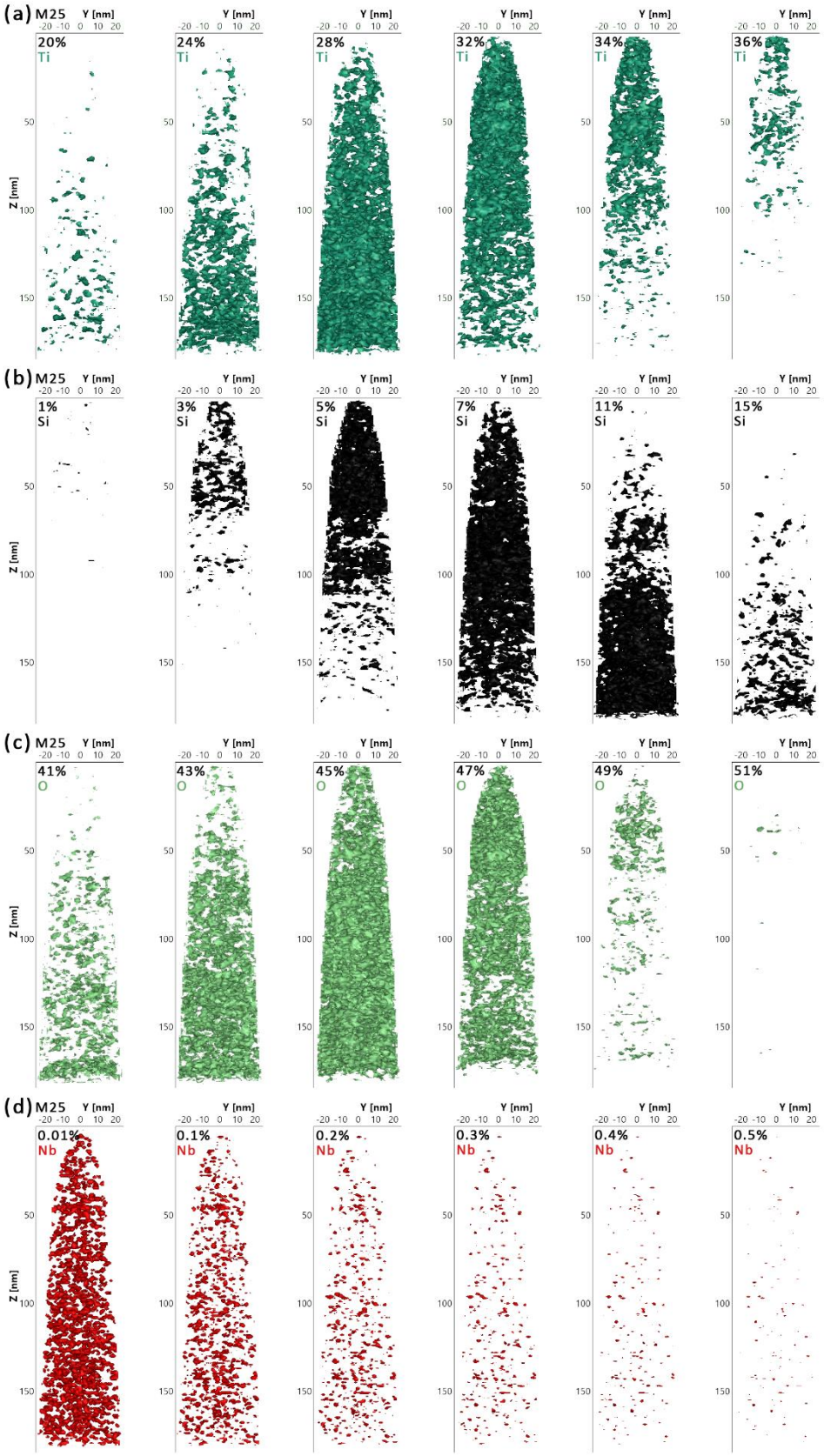

Figure E 20. APT profile view of the 3D reconstruction of tip M25 (5112) of a TiO_2:Nb thin film (Sample C(Ad)), with decomposed atomic concentration iso-surfaces of Ti at 20 %, 24 %, 28 %, 32 %, 34 % and 36 % **(a)**, Si at 1 %, 3 %, 5 %, 7 %, 11 % and 15 % **(b)**, O at 41 %, 43 %, 45 %, 47 %, 49 % and 51 % **(c)** and Nb at 0.01 %, 0.1 %, 0.2 %, 0.3 %, 0.4 % and 0.5 % **(d)**. Sample count threshold at 1 % for Si and Nb and 5 % for Ti and O, with confidence sigma of 1.

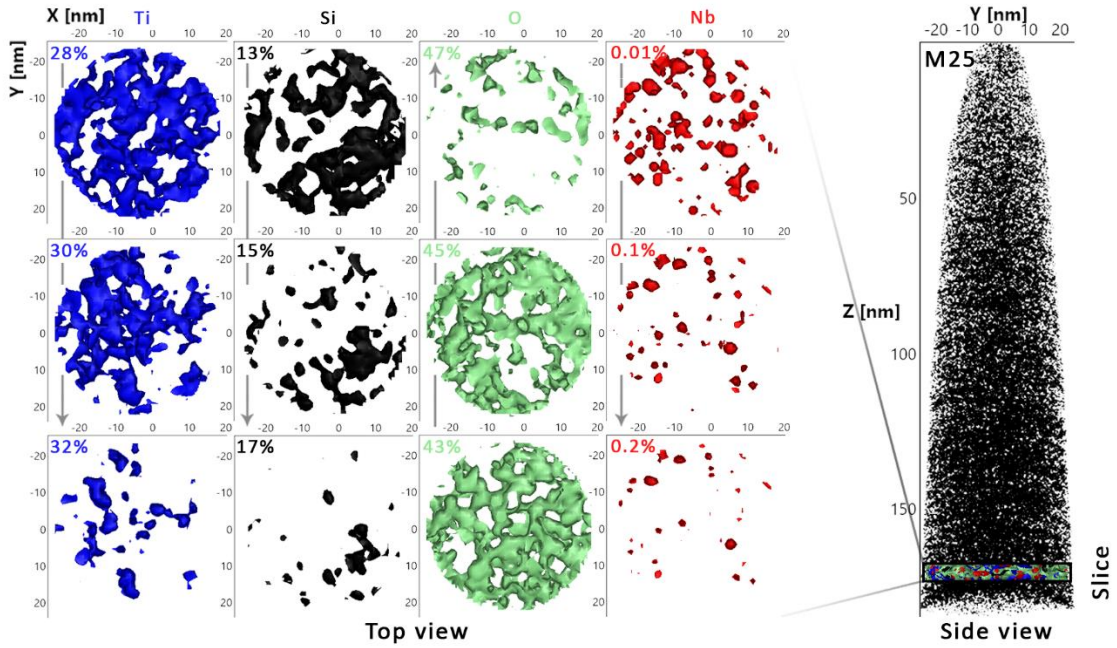

Figure E 21. APT sliced top view of the 3D reconstruction of tip M25 (5112) of a TiO_2:Nb thin film (Sample C(Ad)), decomposed atomic Ti (*blue*, at 28 %, 30 % and 32 %), Si (*black*, at 13 %, 15 % and 17 %), O (*green*, at 47 %, 45 % and 43 %) and Nb (*red*, at 0.01 %, 0.1 % and 0.2 %) concentration iso-surfaces. Sample count threshold at 1 % for Si and Nb and 5 % for Ti and O, with confidence sigma of 1.

The iso-surfaces of decomposed Ti, Si, O and Nb atomic concentration for tip M27 (measured as-deposited) are presented in **Figure E 22**. A top-viewed slice can be seen in **Figure E 23**.

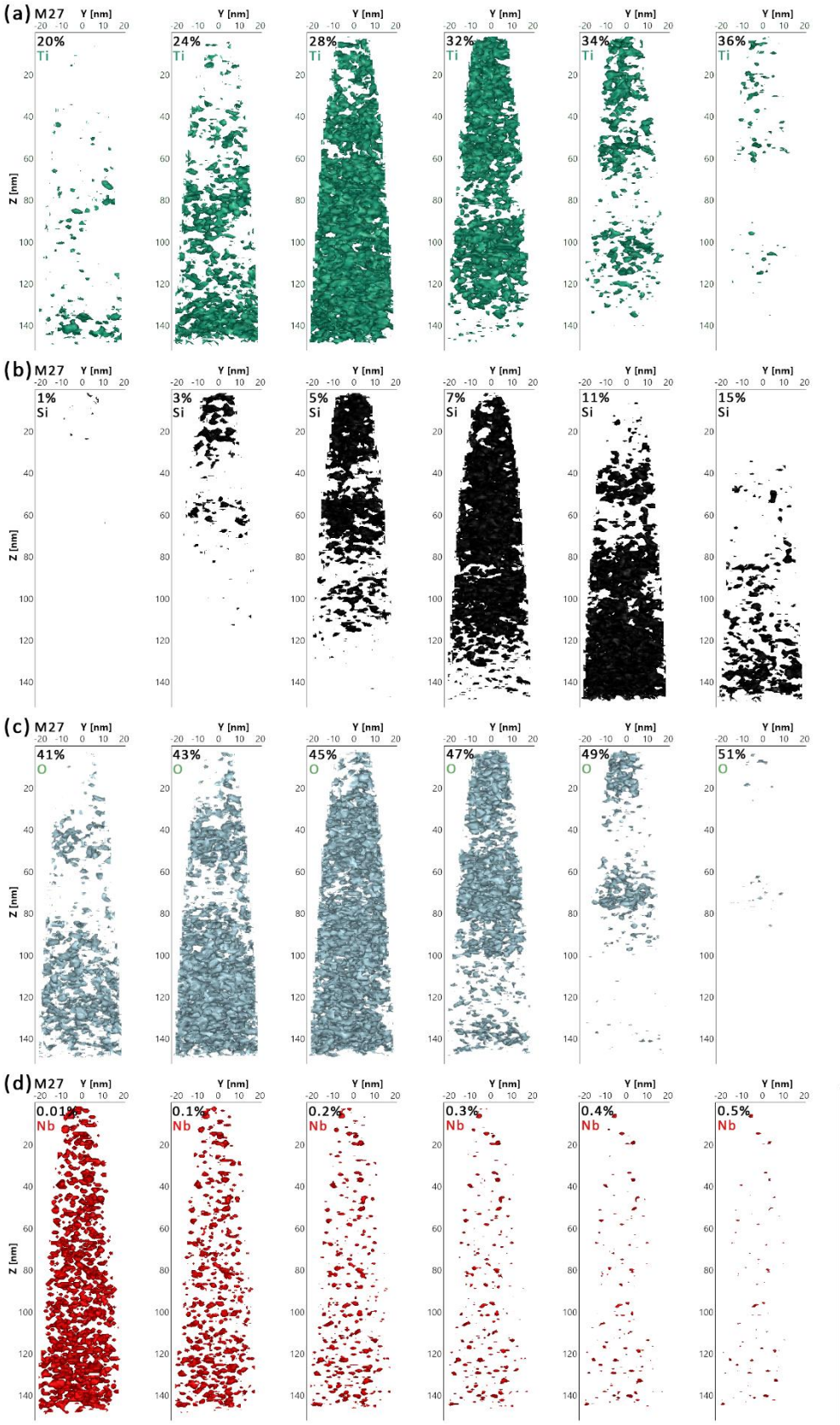

Figure E 22. APT profile view of the 3D reconstruction of tip M27 (5113) of a TiO_2:Nb thin film (Sample C(Ad)), with decomposed atomic concentration iso-surfaces of Ti at 20 %, 24 %, 28 %, 32 %, 34 % and 36 % **(a)**, Si at 1 %, 3 %, 5 %, 7 %, 11 % and 15 % **(b)**, O at 41 %, 43 %, 45 %, 47 %, 49 % and 51 % **(c)** and Nb at 0.01 %, 0.1 %, 0.2 %, 0.3 %, 0.4 % and 0.5 % **(d)**. Sample count threshold at 1 % for Si and Nb and 5 % for Ti and O, with confidence sigma of 1.

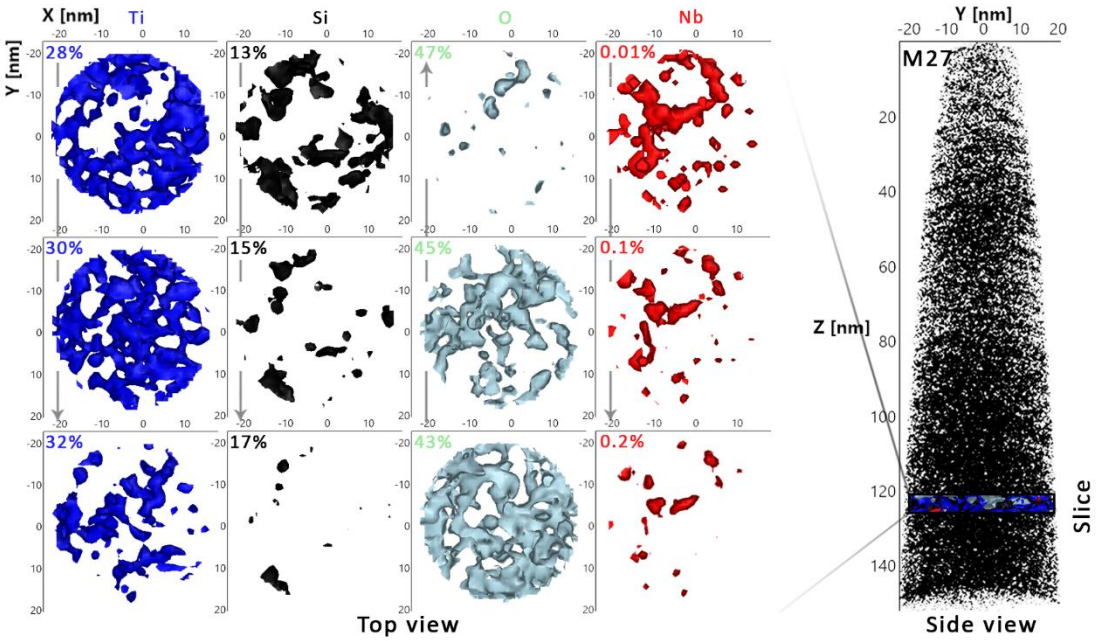

Figure E 23. APT sliced top view of the 3D reconstruction of tip M27 (5113) of a TiO_2:Nb thin film (Sample C(Ad)), decomposed atomic Ti (*blue*, at 28 %, 30 % and 32 %), Si (*black*, at 13 %, 15 % and 17 %), O (*green*, at 47 %, 45 % and 43 %) and Nb (*red*, at 0.01 %, 0.1 % and 0.2 %) concentration iso-surfaces. Sample count threshold at 1 % for Si and Nb and 5 % for Ti and O, with confidence sigma of 1.

The iso-surfaces of decomposed Ti, Si, O and Nb atomic concentration for tip M29 (measured as-deposited) are presented in **Figure E 24**. A combined side profile can be seen in **Figure E 25**, and a top-viewed slice is presented in **Figure E 26**.

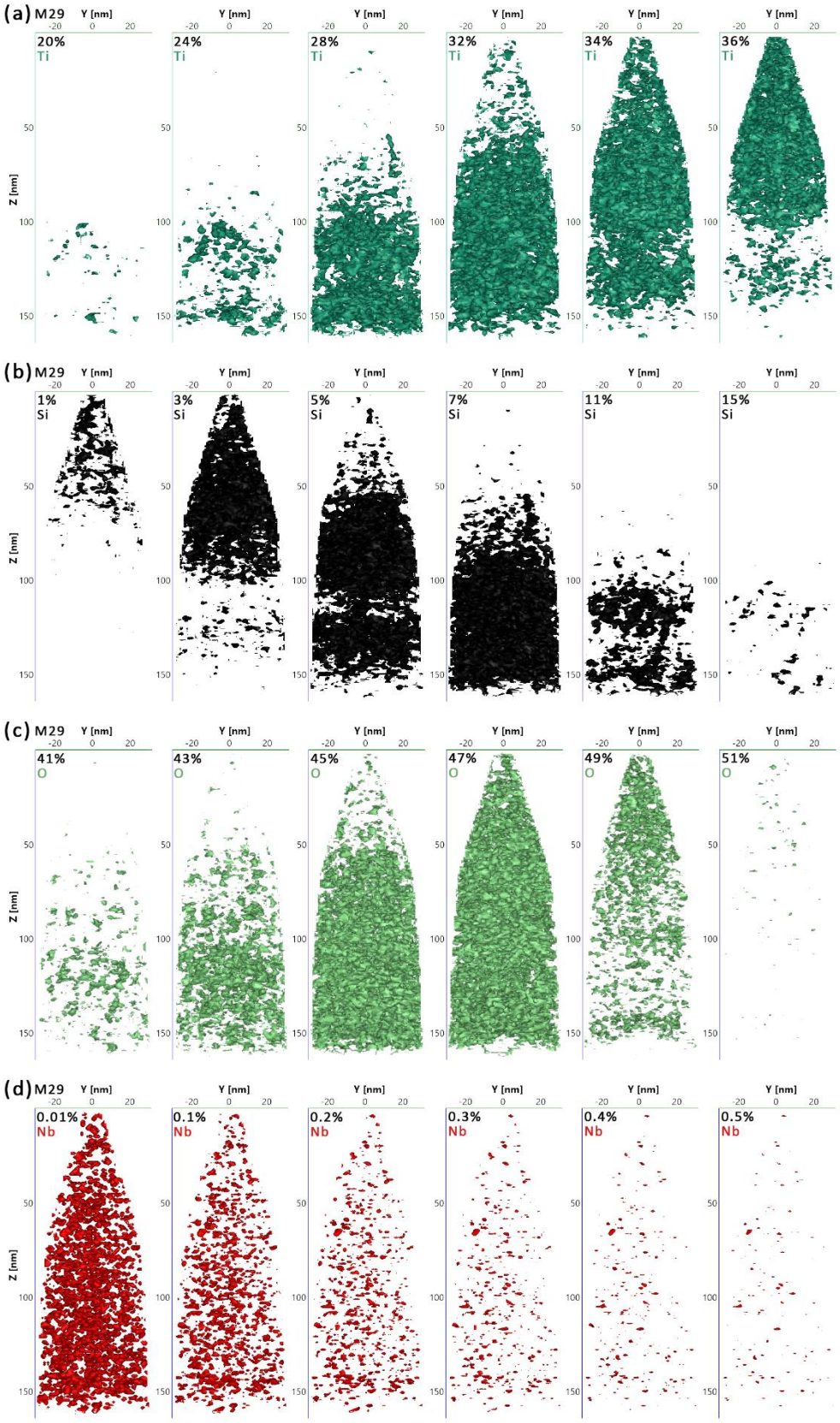

Figure E 24. APT profile view of the 3D reconstruction of tip M29 (5116) of a TiO_2:Nb thin film (Sample C(Ad)), with decomposed atomic concentration iso-surfaces of Ti at 20 %, 24 %, 28 %, 32 %, 34 % and 36 % **(a)**, Si at 1 %, 3 %, 5 %, 7 %, 11 % and 15 % **(b)**, O at 41 %, 43 %, 45 %, 47 %, 49 % and 51 % **(c)** and Nb at 0.01 %, 0.1 %, 0.2 %, 0.3 %, 0.4 % and 0.5 % **(d)**. Sample count threshold at 1 % for Si and Nb and 5 % for Ti and O, with confidence sigma of 1.

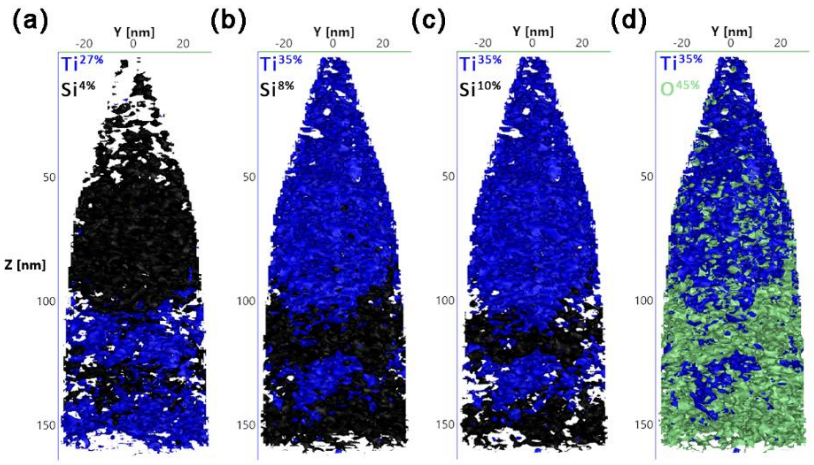

Figure E 25. APT profile view of the 3D reconstruction of tip M29 (5116) of a TiO_2:Nb thin film (Sample C(Ad)), with decomposed atomic concentration iso-surfaces of Ti (*blue*, 27 %) and Si (*black*, 4 %) **(a)**, Ti (35 %) and Si (8 %) **(b)**, Ti (35 %) and Si (10 %) **(c)** and Ti (35 %) and O (*green*, 45) **(d)**. Sample count threshold at 1 % for Si and 5 % for Ti and O, with confidence sigma of 1.

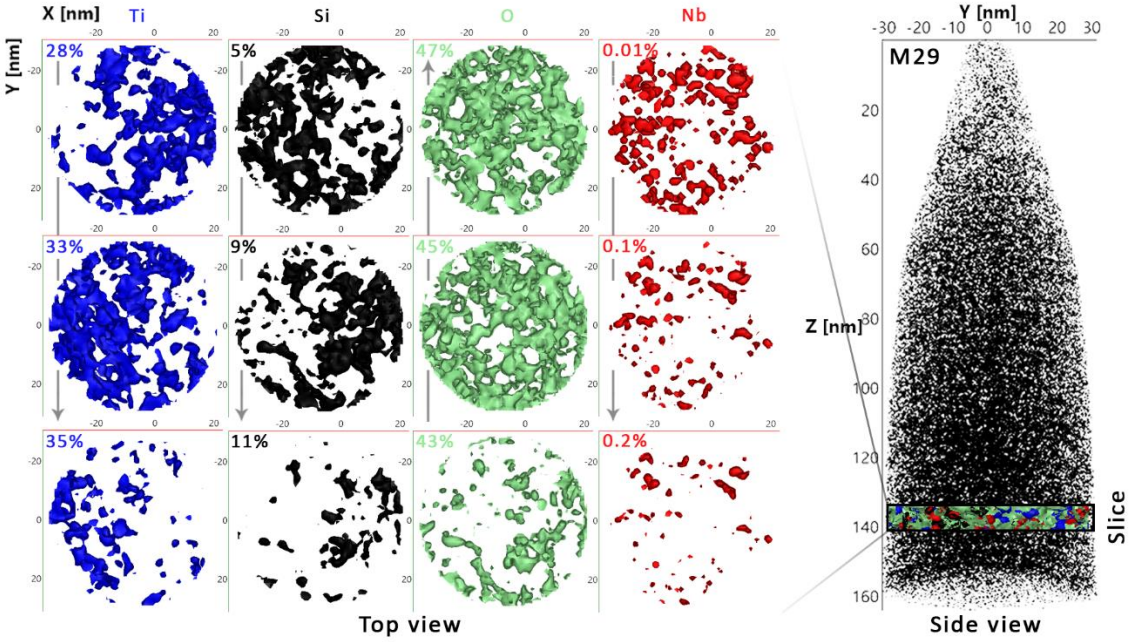

Figure E 26. APT sliced top view of the 3D reconstruction of tip M29 (5116) of a TiO_2:Nb thin film (Sample C(Ad)), decomposed atomic Ti (*blue*, at 28 %, 33 % and 35 %), Si (*black*, at 5 %, 9 % and 11 %), O (*green*, at 47 %, 45 % and 43 %) and Nb (*red*, at 0.01 %, 0.1 % and 0.2 %) concentration iso-surfaces. Sample count threshold at 1 % for Si and Nb and 5 % for Ti and O, with confidence sigma of 1.

The iso-surfaces of decomposed Ti, Si, O and Nb atomic concentration for tip M26*, M28* and M33* (measured after annealing) are presented in **Figure E 27**, **Figure E 28** and **Figure E 29**, respectively.

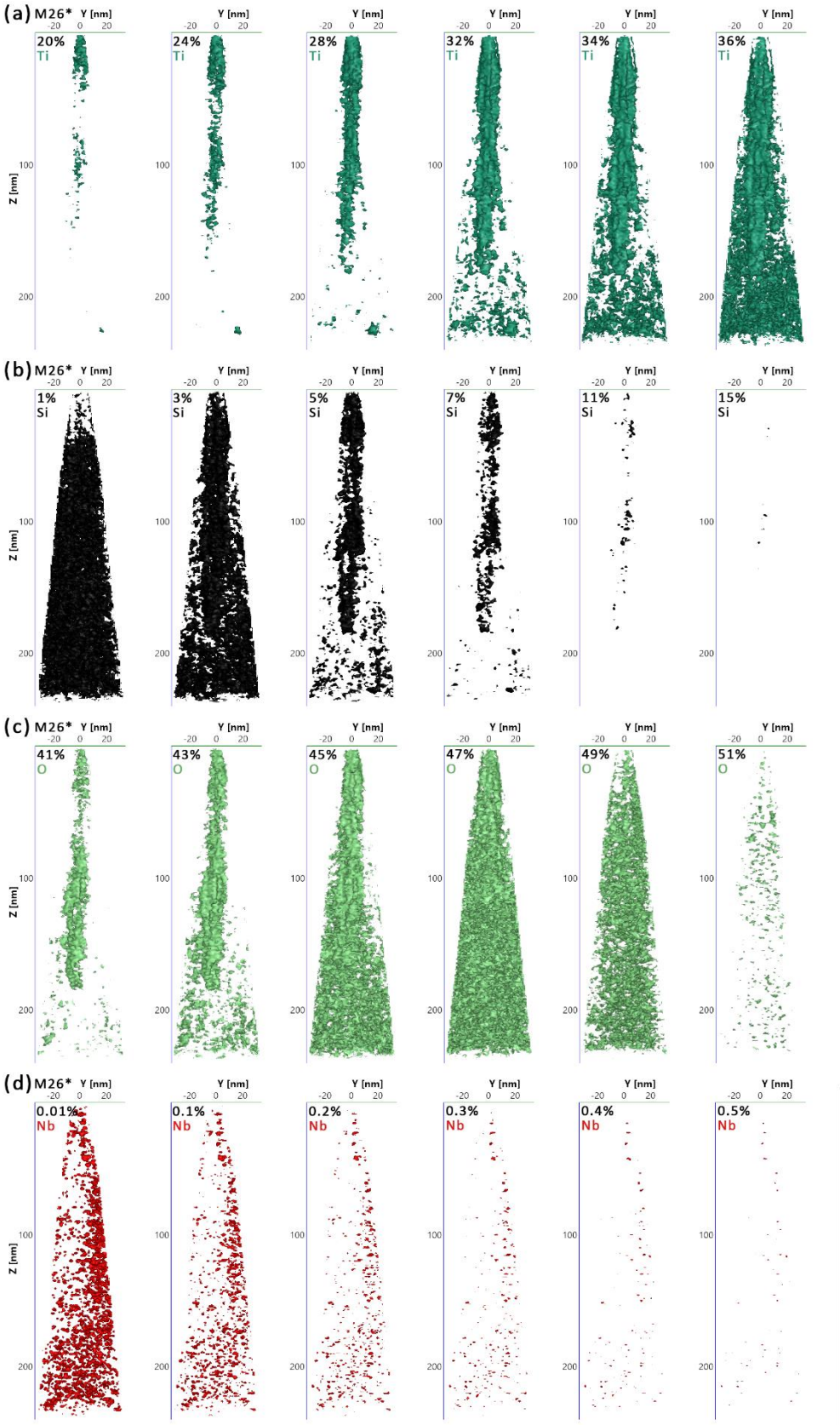

Figure E 27. APT profile view of the 3D reconstruction of tip M26* (15394) of a TiO_2:Nb thin film after annealing at 500 °C (Sample C(TT)), with decomposed atomic concentration iso-surfaces of Ti at 20 %, 24 %, 28 %, 32 %, 34 % and 36 % **(a)**, Si at 1 %, 3 %, 5 %, 7 %, 11 % and 15 % **(b)**, O at 41 %, 43 %, 45 %, 47 %, 49 % and 51 % **(c)** and Nb at 0.01 %, 0.1 %, 0.2 %, 0.3 %, 0.4 % and 0.5 % **(d)**. Sample count threshold at 1 % for Si and Nb and 5 % for Ti and O, with confidence sigma of 1.

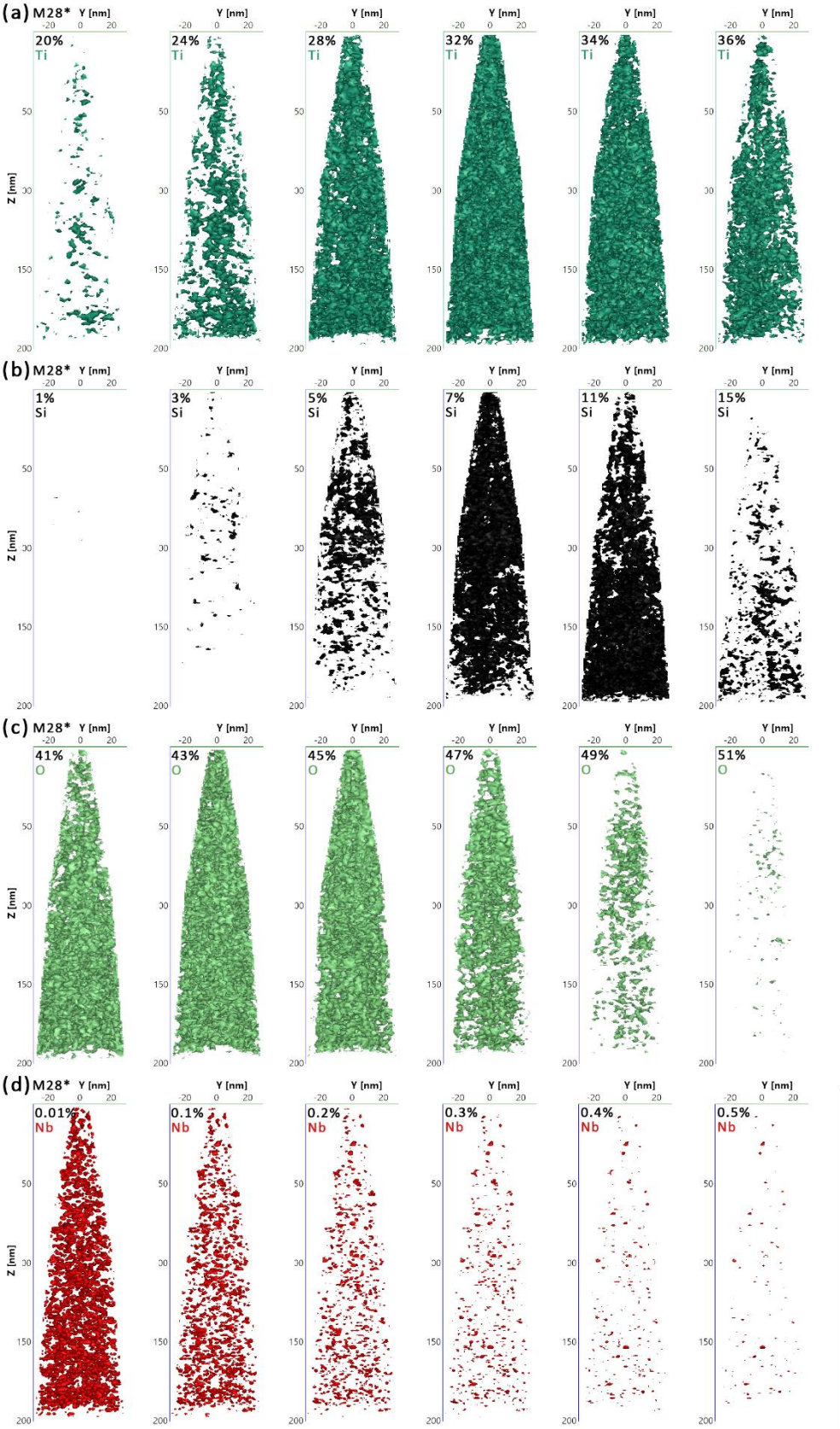

Figure E 28. APT profile view of the 3D reconstruction of tip M28* (15395) of a TiO_2:Nb thin film after annealing at 500 °C (Sample C(TT)), with decomposed atomic concentration iso-surfaces of Ti at 20 %, 24 %, 28 %, 32 %, 34 % and 36 % **(a)**, Si at 1 %, 3 %, 5 %, 7 %, 11 % and 15 % **(b)**, O at 41 %, 43 %, 45 %, 47 %, 49 % and 51 % **(c)** and Nb at 0.01 %, 0.1 %, 0.2 %, 0.3 %, 0.4 % and 0.5 % **(d)**. Sample count threshold at 1 % for Si and Nb and 5 % for Ti and O, with confidence sigma of 1.

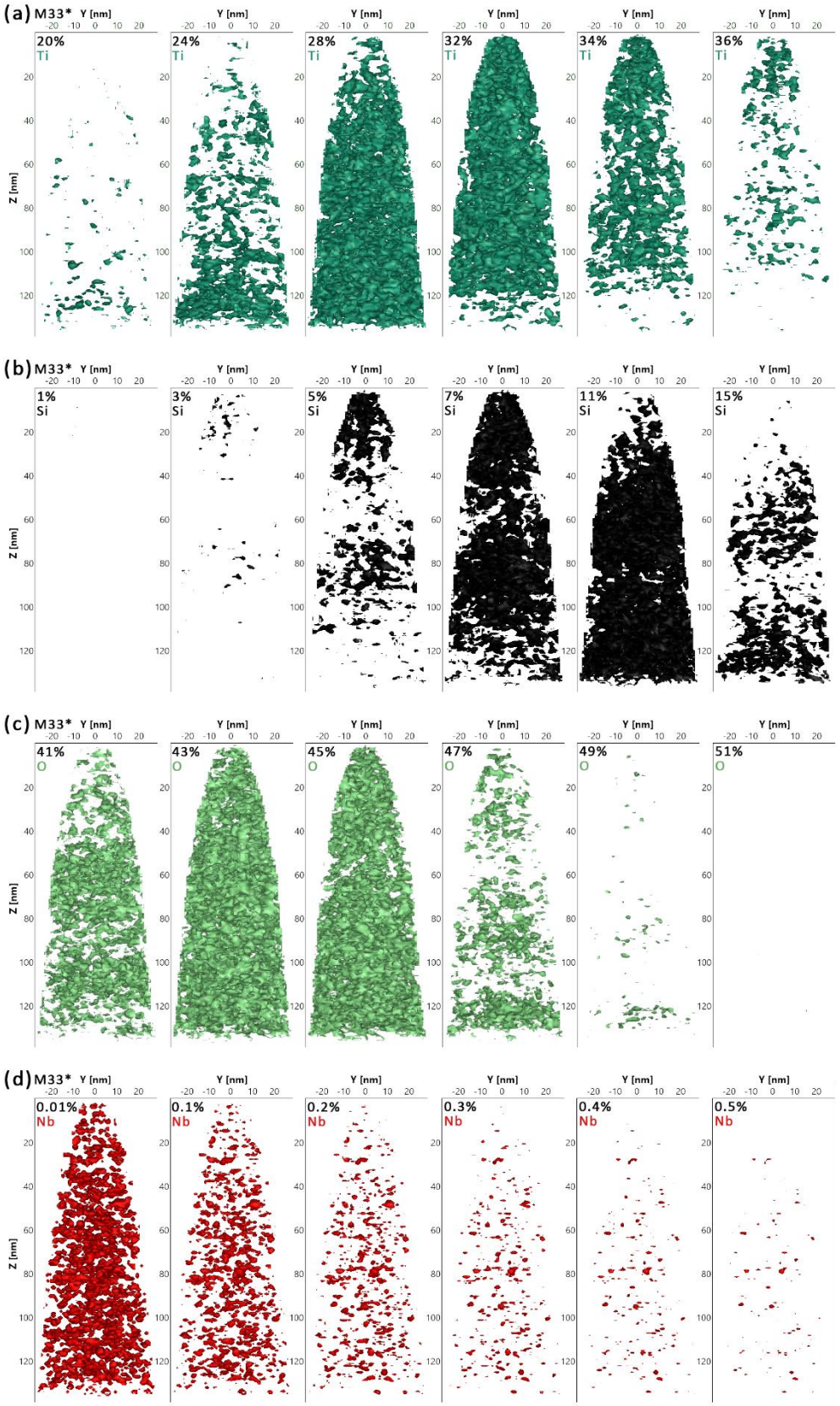

Figure E 29. APT profile view of the 3D reconstruction of tip M33* (15401) of a TiO_2:Nb thin film after annealing at 500 °C (Sample C(TT)), with decomposed atomic concentration iso-surfaces of Ti at 20 %, 24 %, 28 %, 32 %, 34 % and 36 % **(a)**, Si at 1 %, 3 %, 5 %, 7 %, 11 % and 15 % **(b)**, O at 41 %, 43 %, 45 %, 47 %, 49 % and 51 % **(c)** and Nb at 0.01 %, 0.1 %, 0.2 %, 0.3 %, 0.4 % and 0.5 % **(d)**. Sample count threshold at 1 % for Si and Nb and 5 % for Ti and O, with confidence sigma of 1.

APPENDIX F – HAADF-STEM ANALYSIS

HAADF-STEM analysis was performed on a TiO_2:Nb thin film (**Figure F 1**) after annealing at 500 °C to assess the morphology, composition, phase and grain boundary information, detailed in **Chapter 6**.

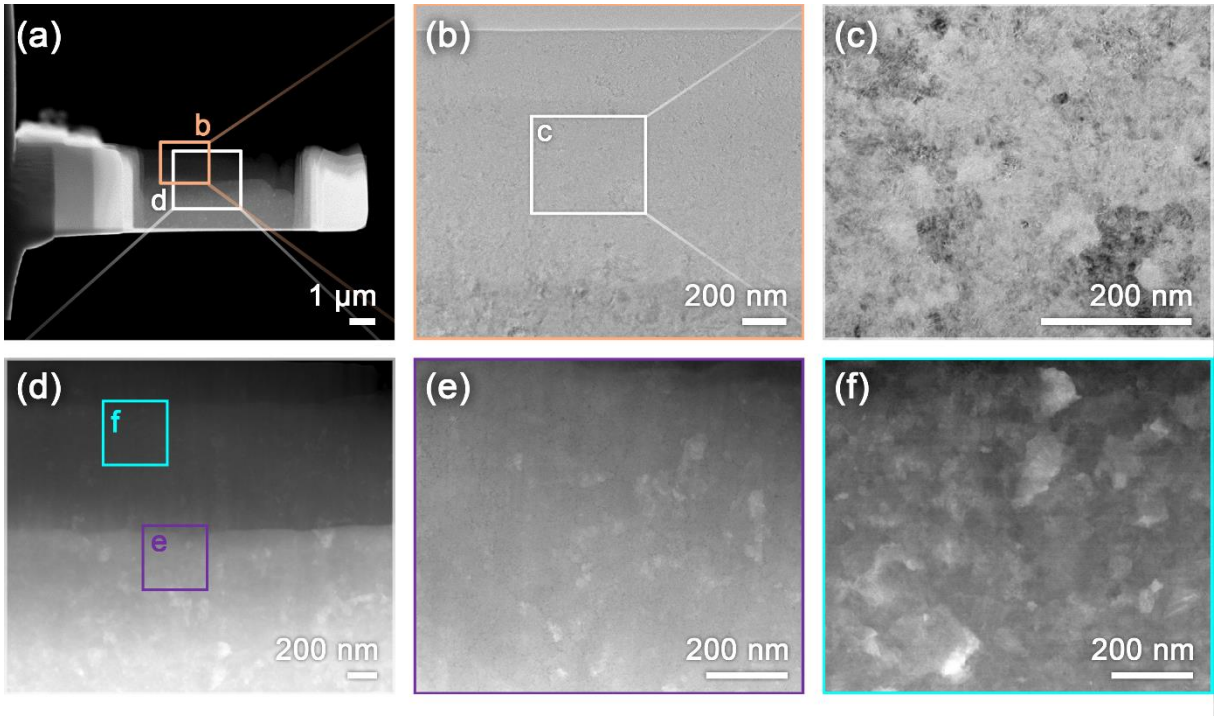

Figure F 1. HAADF-STEM of the TiO_2:Nb thin film (after thermal annealing at 500 °C) lamella **(a)**. **(b)** and **(d)** are zoomed-in magnifications of b-ROI and d-ROI in (a), **(c)** is a magnification of the c-ROI (b) and **(e)** and **(f)** (ROI#1) are magnifications of the e-ROI and f-ROI in (d), indicated by their respective coloured squares.

Figure F 2 and **Figure F 3** show the HAADF-STEM and respective Nb, Ti and O compositional EDX maps for various analysed ROI, from analysis areas of around (200 × 200) nm to around (800 × 800) nm), while smaller areas, around (10 × 10) nm to around (20 × 20) nm), were analysed for the micrographs in **Figure F 4**, **Figure F 5** and **Figure F 6**. ROI#4 (**Figure F 5**) is a magnification of a region of ROI#240 (**Figure F 4**). The EDX spectra and results are displayed in **Figure F 7**, **Figure F 8** and **Figure F 9**.

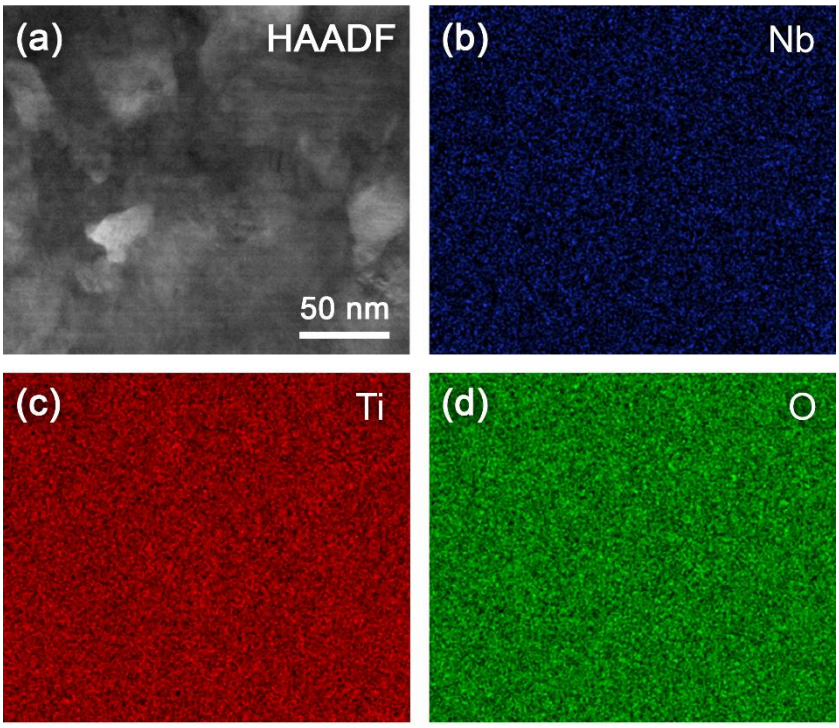

Figure F 2. HAADF-STEM (ROI#2) **(a)** and respective Nb **(b)**, Ti **(c)** and O **(d)** EDX maps of a TiO_2:Nb thin film after thermal annealing at 500 °C.

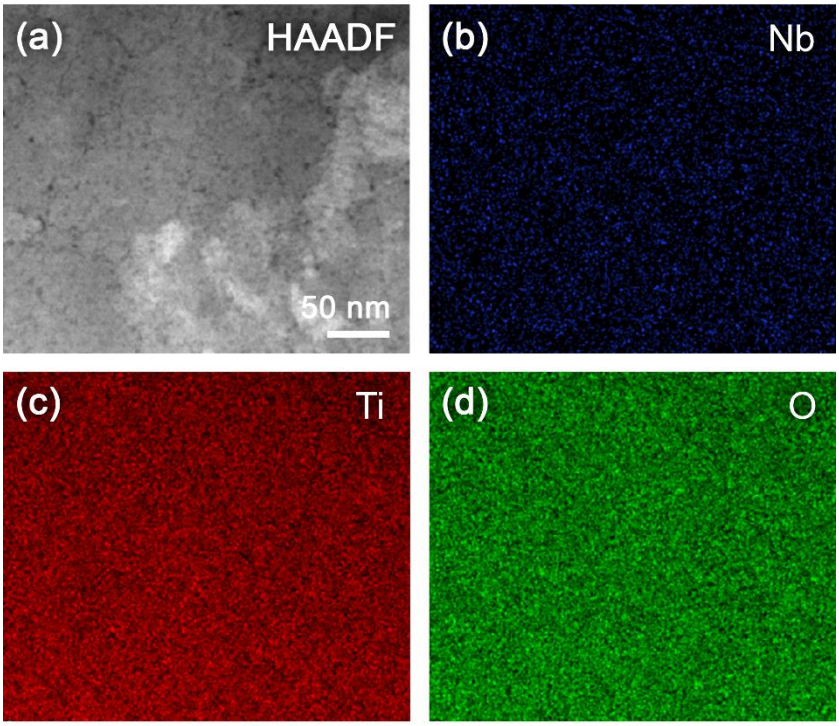

Figure F 3. HAADF-STEM (ROI#3) **(a)** and respective Nb **(b)**, Ti **(c)** and O **(d)** EDX maps of a TiO_2:Nb thin film after thermal annealing at 500 °C.

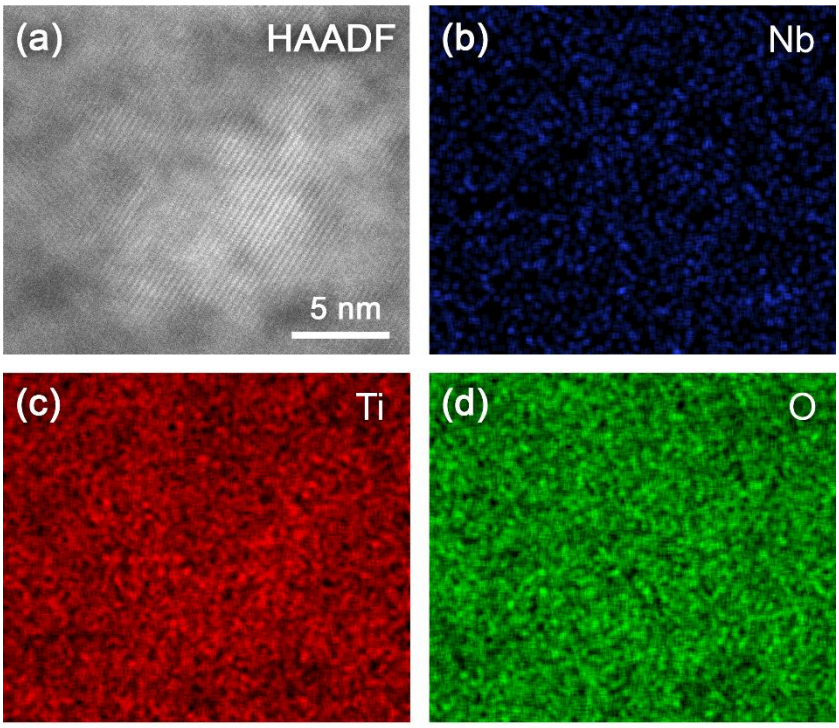

Figure F 4. HAADF-STEM (ROI#240) **(a)** and respective Nb **(b)**, Ti **(c)** and O **(d)** EDX maps of a TiO_2:Nb thin film after thermal annealing at 500 °C.

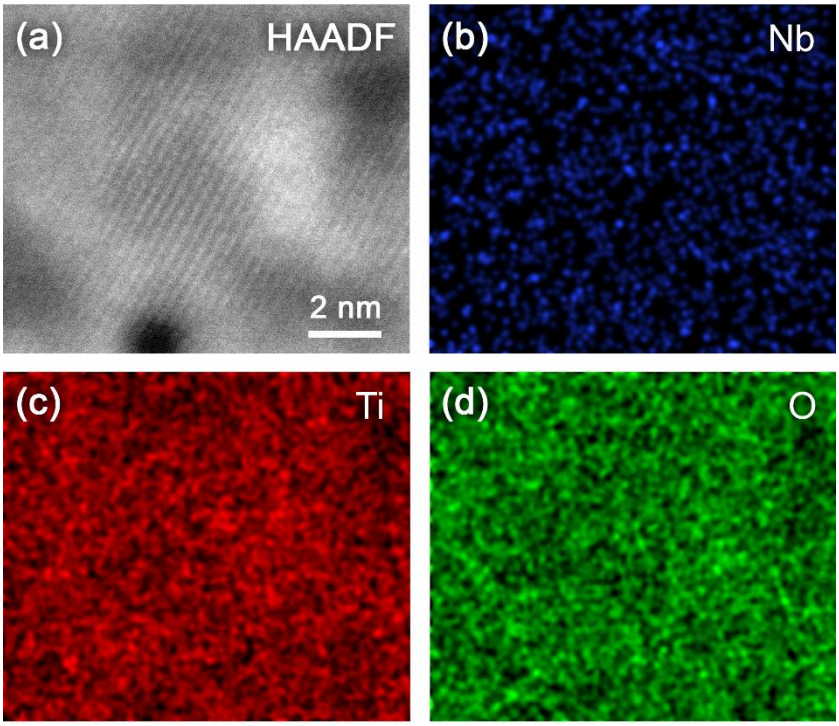

Figure F 5. HAADF-STEM (ROI#4) **(a)** and respective Nb **(b)**, Ti **(c)** and O **(d)** EDX maps of a TiO_2:Nb thin film after thermal annealing at 500 °C.

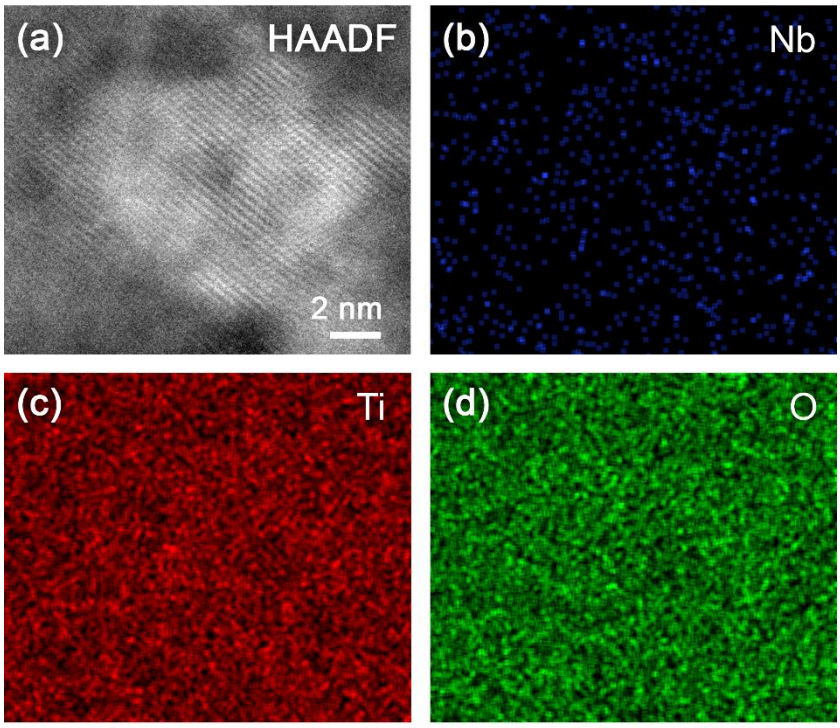

Figure F 6. HAADF-STEM (ROI#36) **(a)** and respective Nb **(b)**, Ti **(c)** and O **(d)** EDX maps of a TiO_2:Nb thin film after thermal annealing at 500 °C.

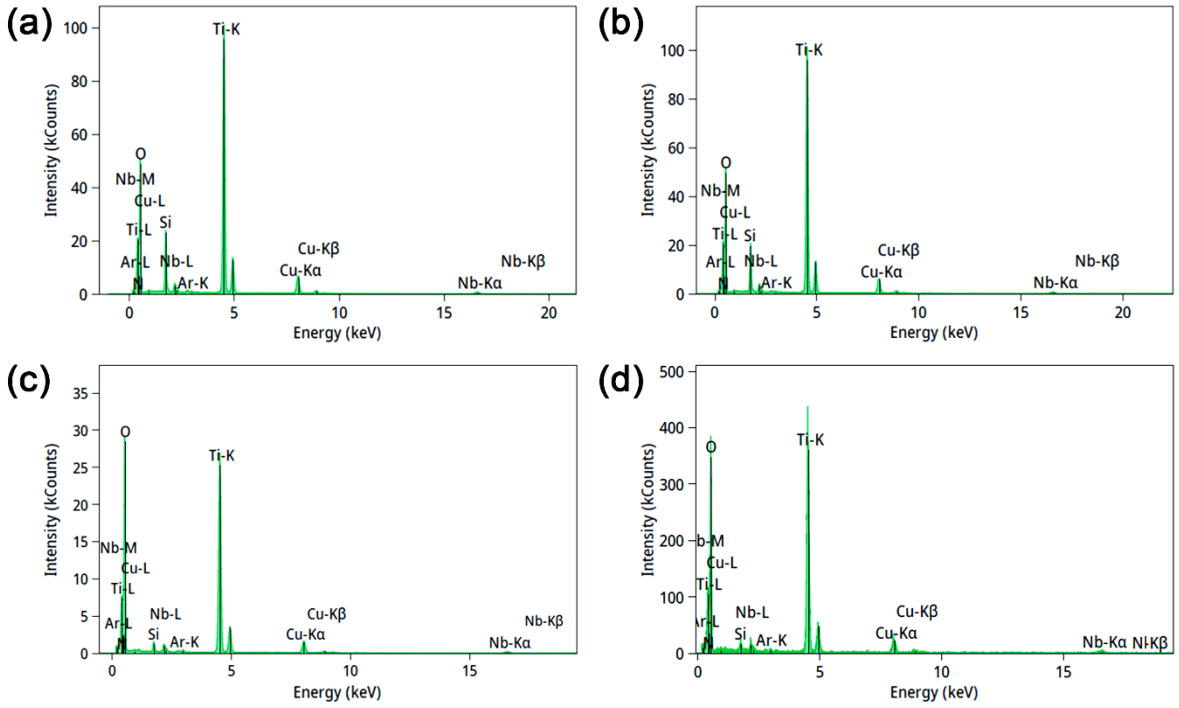

Figure F 7. HAADF-STEM EDX spectra for ROI#1 **(a)**, ROI#2 **(b)**, ROI#3 **(c)** and ROI#4 **(d)** of a TiO_2:Nb thin film after thermal annealing at 500 °C.

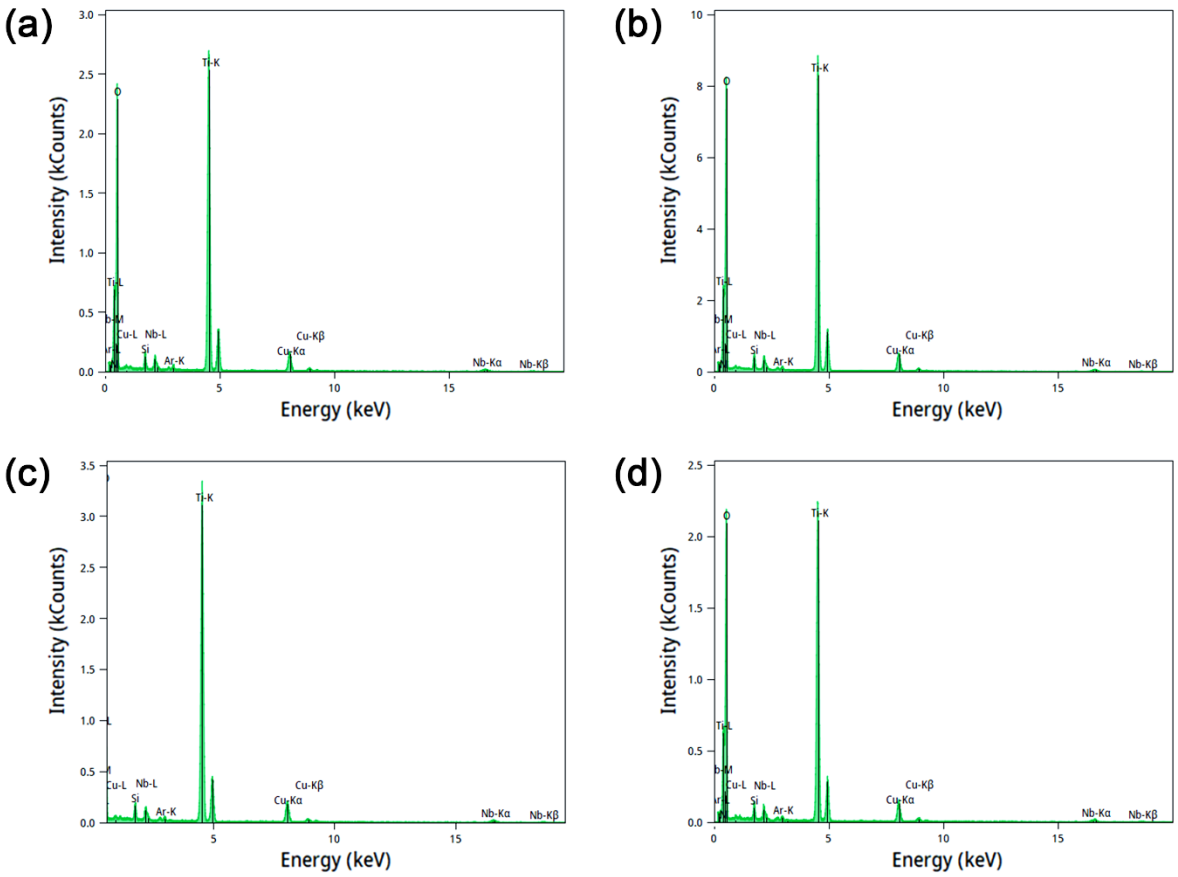

Figure F 8. HAADF-STEM EDX spectra for ROI#53 **(a)**, ROI#240 **(b)**, ROI#43 **(c)** and ROI#36 **(d)** of a TiO_2:Nb thin film after thermal annealing at 500 °C.

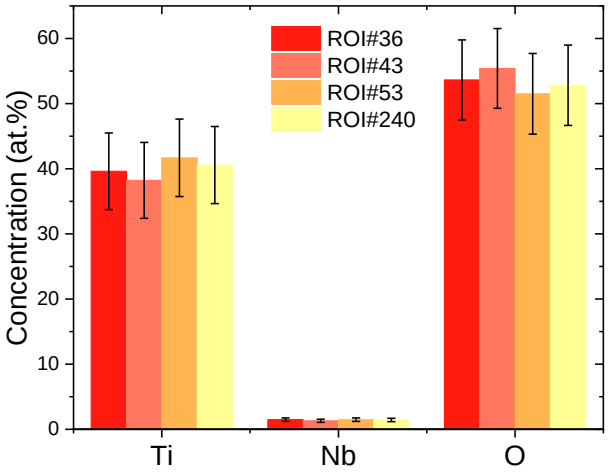

Figure F 9. Atomic concentration of Ti, O and Nb in a TiO_2:Nb thin film after thermal annealing at 500 °C obtained by STEM-EDX, over measurements in 4 zones: ROI#36, ROI#43, ROI#53 and ROI#240.

APPENDIX G – PROPAGATION OF UNCERTAINTY

Excluding errors given by measurement equipment, graphical functions fitting and statistics, here are represented the error equations by propagation of uncertainty. The uncertainties of ZT and PF, calculated throughout this work, obtained from equations **(8)** and **(9)**, respectively, were attained by

$$\begin{aligned}\Delta_{ZT} &= \left|\frac{\mathrm{d}ZT}{\mathrm{d}S}\right| \cdot |\Delta_S| + \left|\frac{\mathrm{d}ZT}{\mathrm{d}\sigma}\right| \cdot |\Delta_\sigma| + \left|\frac{\mathrm{d}ZT}{\mathrm{d}T}\right| \cdot |\Delta_T| + \left|\frac{\mathrm{d}ZT}{\mathrm{d}\kappa}\right| \cdot |\Delta_\kappa| \\ &= \left|\frac{2S\sigma T}{\kappa}\right| \cdot |\Delta_S| + \left|\frac{S^2 T}{\kappa}\right| \cdot |\Delta_\sigma| + \left|\frac{S^2 \sigma}{\kappa}\right| \cdot |\Delta_T| + \left|\frac{S^2 \sigma T}{\kappa^2}\right| \cdot |\Delta_\kappa|\end{aligned}$$

and

$$\begin{aligned}\Delta_{PF} &= \left|\frac{\mathrm{d}PF}{\mathrm{d}S}\right| \cdot |\Delta_S| + \left|\frac{\mathrm{d}PF}{\mathrm{d}\sigma}\right| \cdot |\Delta_\sigma| \\ &= |2S\sigma| \cdot |\Delta_S| + S^2 \cdot |\Delta_\sigma| \,.\end{aligned}$$

In **Section 7.3**, the electrical conductivity σ was not measured by the hall effect equipment described in **Section 2.3.3** and was instead calculated using equation **(30)**. The uncertainty is given by

$$\begin{aligned}\Delta_\sigma &= \left|\frac{\mathrm{d}\sigma}{\mathrm{d}R}\right| \cdot |\Delta_R| + \left|\frac{\mathrm{d}\sigma}{\mathrm{d}A}\right| \cdot |\Delta_A| + \left|\frac{\mathrm{d}\sigma}{\mathrm{dL}}\right| \cdot |\Delta_L| \\ &= \left|\frac{L}{AR^2}\right| \cdot |\Delta_R| + \left|\frac{L}{RA^2}\right| \cdot |\Delta_A| + \left|\frac{L}{RA}\right| \cdot |\Delta_L| \,,\end{aligned}$$

where

$$\begin{aligned}\Delta_A &= \left|\frac{\mathrm{d}A}{\mathrm{d}r}\right| \cdot |\Delta_r| \\ &= |2\pi r| \cdot |\Delta_r| \,.\end{aligned}$$

APPENDIX H – SCIENTIFIC CONTRIBUTION

This work gave way to 8 articles Published in Scientific Journals, 10 oral and 6 poster presentations in international conferences, 1 national patent and 2 awards for poster presentations in international conferences.

H.1. Articles Published in Scientific Journals

L. Dias, F. C. Correia, **J. M. Ribeiro**, C. J. Tavares, "Photocatalytic Bi_2O_3/TiO_2:N thin films with enhanced surface area and visible light activity", **Coatings. 10** (2020) 445. (https://doi.org/10.3390/coatings10050445)

J. M. Ribeiro, F. C. Correia, A. Kuzmin, I. Jonane, M. Konge, A. R. Goñie, J. S. Reparaz, A. Kalinko, E. Welter, C. J. Tavares, "Influence of Nb-doping on the local structure and thermoelectric properties of transparent TiO_2:Nb thin films", **Journal of Alloys and Compounds. 838** (2020) 155561. (https://doi.org/10.1016/j.jallcom.2020.155561)

F. C. Correia, **J. M. Ribeiro**, A. Kuzmin, I. Pudza, A. Kalinko, E. Welter, A. Mendes, Joana Rodrigues, Nabiha Ben Sedrine, Teresa Monteiro, Maria Rosário Correia, C. J. Tavares, "The role of Ga and Bi doping on the local structure of transparent zinc oxide thin films", **Journal of Alloys and Compounds. 870** (2021) 159489. (https://doi.org/10.1016/j.jallcom.2021.159489)

J. M. Ribeiro, F. C. Correia, F. J. Rodrigues, J. S. Reparaz, A. R. Goñi, C. J. Tavares, "Transparent niobium-doped titanium dioxide thin films with high Seebeck coefficient for thermoelectric applications", **Surface & Coatings Technology. 425** (2021) 127724. (https://doi.org/10.1016/j.surfcoat.2021.127724)

F. C. Correia, **J. M. Ribeiro**, A. Ferreira, J. S. Reparaz, A. R. Goñi, T. Boll, A. Mendes, and C. J. Tavares, "The effect of Bi doping on the thermal conductivity of ZnO and ZnO:Al thin films", **Vacuum. 207** (2023) 111572. (https://doi.org/10.1016/j.vacuum.2022.111572)

J. M. Ribeiro, F. J. Rodrigues, F. C. Correia, I. Pudza, A. Kuzmin, A. Kalinko, E. Welter, N. P. Barradas, E. Alves, A. P. LaGrow, O. Bondarchuk, A. Welle, A. Telfah, C. J. Tavares, "The influence of Sb doping on the local structure and disorder in thermoelectric ZnO:Sb thin films", **Journal of Alloys and Compounds. 939** (2023) 168751. (https://doi.org/10.1016/j.jallcom.2023.168751)

M. Isram, R. Magrin Maffei, V. Demontis, L. Martini, S. Forti, C. Coletti, V. Bellani, A. Mescola, G. Paolicelli, A. Rota, S. Benedetti, A. D. Bona, **J. M. Ribeiro**, C. J. Tavares, F. Rossella, "Thermoelectric and

Structural Properties of Sputtered AZO Thin Films with Varying Al Doping Ratios", **Coatings. 13** (2023) 691. (https://doi.org/10.3390/coatings13040691)

H. F. Faria, **J. M. Ribeiro**, T. Boll, C. J. Tavares, "Thermoelectric and Structural Properties of Transparent Sb-doped ZnO Thin Films Sputtered in a Confocal Geometry", **Coatings. 13** (2023) 735. (https://doi.org/10.3390/coatings13040735)

H.2. Oral presentations in international conferences

J. M. Ribeiro, F. C. Correia, C. J. Tavares, "Transparent TiO_2:Nb thin films for thermal energy harvesting", **Virtual Conference on Thermoelectrics 2020 (VCT2020)**, Virtual, 21–23 Jully 2020. (https://conferences.mines.edu/vct2020/)

J. M. Ribeiro, F. C. Correia, C. J. Tavares, "Transparent Niobium-doped Titanium Dioxide Thin Films with high Seebeck coefficient for thermoelectric applications", **Society of Vacuum Coaters 64th Annual Technical Conference 2021 (SVC TechCon 2021)**, Virtual, 3–7 May 2021. (https://www.flipsnack.com/svcdigitalpublications/2021-svc-techcon-proceedings.html/)

J. M. Ribeiro, F. C. Correia, F. J. Rodrigues, J. S. Reparaz, A. R. Goñi, C. J. Tavares, "Transparent Niobium-doped Titanium Dioxide Thin Films with high Seebeck coefficient for thermoelectric applications", **Iberian Vacuum Online Meeting 2021 (RIVA Online 2021)**, Virtual, 4–6 October 2021. (https://aseva.es/conferences/riva-online/)

J. M. Ribeiro, F. C. Correia, F. J. Rodrigues, J. S. Reparaz, A. R. Goñi, C. J. Tavares, "Transparent Niobium-doped Titanium Dioxide Thin Films with high Seebeck coefficient for thermoelectric applications", **XII Iberian Vacuum and Applications Conference (RIVA 2022)**, Braga, Portugal, 15–17 May 2022. (https://www.riva2022.pt/)

J. M. Ribeiro, F. C. Correia, F. J. Rodrigues, J. S. Reparaz, A. R. Goñi, C. J. Tavares, "Transparent Niobium-Doped Titanium Dioxide Thin Films with high Seebeck coefficient for thermoelectric applications", **48th International Conference on Metallurgical Coatings and Thin Films 2022 (ICMCTF 2022)**, San Diego, USA, 22–27 May 2022. (https://icmctf2022.avs.org/)

J. M. Ribeiro, F. C. Correia, F. J. Rodrigues, J. S. Reparaz, A. R. Goñi, C. J. Tavares, "Development of TiO_2:Nb thin films for transparent thermoelectric modules", **Junior EuroMAT 2022**, Coimbra, Portugal, 19–22 July 2022. (https://junioreuromat.org/)

J. M. Ribeiro, F. C. Correia, A. Welle, T. Boll, and C. J. Tavares, "Doping impact on thermal and electrical properties of transparent ZnO and TiO_2 thin films for thermoelectric applications", **International Conference on Atom Probe Tomography & Microscopy 2022 (APT&M 2022)** and **59th International Field Emission Symposium**, Nanjing, China/Virtual, 11–14 October 2022. (https://aptm2022.scievent.com/)

J. M. Ribeiro, F. C. Correia, F. J. Rodrigues, J. S. Reparaz, A. R. Goñi, A. Welle, T. Boll, C. J. Tavares, "Development of transparent TiO_2:Nb thin films for thermoelectric modules", **VÁCUO 2022 Workshop**, Aveiro, Portugal, 25 November 2022 (http://www.soporvac.pt/files/Vacuo2022/VACUO%202022.pdf)

J. M. Ribeiro, F. C. Correia, F. J. Rodrigues, J. S. Reparaz, A. R. Goñi, A. Welle, T. Boll, C. J. Tavares, "Development of transparent TiO_2:Nb thin films by Reactive Magnetron Sputtering for thermoelectric modules", **XXI Congresso da Sociedade Portuguesa de Materiais (Materiais 2023)** and **XII International Symposium on Materials**, Guimarães, Portugal, 3–6 April 2023. (https://congressomateriais.pt/)

J. M. Ribeiro, A. Welle, T. Boll, C. J. Tavares, "Transparent Niobium-doped Titanium Dioxide thin films by Reactive Magnetron Sputtering for thermoelectric modules", **19th International Conference on Thin Films (ICTF'19)**, Burgos, Spain, 26–29 September 2023. (https://ictf2023.com/)

J. M. Ribeiro, O. A. López-Galán, A. Welle, T. Boll and C. J. Tavares, "Transparent Thermoelectric Titanium Dioxide-based Thin Films for Thermal Energy Harvesting", **General Conference of the Condensed Matter Division (CMD31)**, Braga, Portugal, 2–6 September 2024. (https://cmd31.sci-meet.net/)

H.3. Poster communications in International Conferences

J. M. Ribeiro, F. C. Correia, C. J. Tavares, "Transparent Niobium-doped Titanium Dioxide Thin Films with high Seebeck coefficient for thermoelectric applications", **Jornadas Physics Centre of Minho and Porto Universities 2019** (Jornadas CF-UM-UP 2019), Braga, Portugal, 13 December 2019. (https://www.fisicauminho.pt/index.php/pt/divulgacao/eventos/191-jornadas-cf-um-up-2019/)

J. M. Ribeiro, F. C. Correia, T. Boll, C. J. Tavares, "Study of Transparent Thermoelectric ZnO-based Thin Films for Energy Harvesting through Atom Probe Tomography", **1st Workshop of LaPMET**, Virtual, 23–24 September 2021. (https://indico.cern.ch/event/1064329/)

J. M. Ribeiro, F. C. Correia, T. Boll, C. J. Tavares, "Transparent Thermoelectric ZnO-Thin Films for Energy Harvesting applications", **Atom Probe Tomography & Microscopy Virtual Conference 2021 (APTM2021)**, Virtual, 27–30 September 2021. (https://pnnl.cventevents.com/event/b37eba2c-bebf-40a8-9c36-6bf87cae10c0/summary/)

J. M. Ribeiro, F. C. Correia, F. J. Rodrigues, J. S. Reparaz, A. R. Goñi, C. J. Tavares, "Transparent Niobium-doped Titanium Dioxide Thin Films with high Seebeck coefficient for thermoelectric applications", **16th European Vacuum Conference (EVC-16)**, Marseille, France, 21–26 November 2021. (https://www.evc16.org/)

J. M. Ribeiro, F. C. Correia, F. J. Rodrigues, J. S. Reparaz, A. R. Goñi, C. J. Tavares, "Transparent Niobium-doped titanium Dioxide Thin Films with high Seebeck coefficient for thermoelectric applications", **Junior EuroMAT 2022**, Coimbra, Portugal, 19–22 July 2022. (https://junioreuromat.org/)

J. M. Ribeiro, F. C. Correia, A. Welle, T. Boll, C. J. Tavares, "Doping impact on thermal and electrical properties of transparent ZnO and TiO_2 thin films for thermoelectric applications", **19th International Conference on Thin Films (ICTF'19)**, Burgos, Spain, 26–29 September 2023. (https://ictf2023.com/)

H.4. Schools and Training Courses

Training course on Atom Probe Tomography, Karlsruhe Institute of Technology's Institute for Applied Materials, Karlsruhe, Germany, 21–25 October 2019.

Training course on Kelvin Probe Atomic Force Microscopy, International Iberian Nanotechnology Laboratory (INL), Braga, Portugal, January 2020.

13th School on Atom Probe Tomography, Groupe de Physique des Matériaux, University of Rouen, France, 25–29 October 2021.

H.5. Patents

Carlos José Tavares, Filipe Correia Costa, **Joana Margarida Ribeiro,** *"Filme Termoelétrico transparente e respetivo método de obtenção",* PT 110639/2021, Universidade do Minho, Portugal. National patent published by the INPI – Instituto Português de Propriedade Intelectual.

H.6. Awards

IUVSTA Elsevier Best Poster Award, issued by the International Union for Vacuum Science, Technique And Applications (IUVSTA), for a Poster presentation in "Transparent niobium-doped titanium dioxide thin films with high Seebeck coefficient for thermoelectric applications", at the 16th European Vacuum Conference (EVC-16), Marseille, France, 21–26 November 2021. (https://www.evc16.org/IUVSTA-Elsevier-Awards/)

ICTF-AUSE Runner-up Best Poster Award, issued by the Spanish Association of Synchrotron Radiation Users (AUSE), for a Poster presentation in "Doping impact on thermal and electrical properties of transparent ZnO and TiO_2 thin films for thermoelectric applications", at the 19th International Conference on Thin Films (ICTF'19), Burgos, Spain, 26–29 September 2023. (https://ictf2023.com/prizes-grants/)